Title
Development of Inter- and Intra-cellular Components of Direction Selectivity in The Mammalian Retina

Permalink
https://escholarship.org/uc/item/9r1061mw

Author
Morrie, Ryan David

Publication Date
2018

Development of Inter- and Intra-cellular Components of Direction Selectivity in The Mammalian Retina

by

Ryan D. Morrie

A dissertation submitted in partial satisfaction of the
requirements for the degree of
Doctor of Philosophy

in

Molecular and Cell Biology

in the

Graduate Division

of the

University of California, Berkeley

Committee in charge:
Professor Marla B. Feller, Chair
Professor Ehud Y. Isacoff
Professor Hillel Adesnik
Professor Michael DeWeese

Spring 2018

Development of Inter- and Intra-cellular Components of Direction Selectivity in The Mammalian Retina

Abstract

Development of Inter- and Intra-cellular Components of Direction Selectivity in The Mammalian Retina

by

Ryan D. Morrie

Doctor of Philosophy in Molecular and Cell Biology

University of California, Berkeley

Professor Marla B. Feller, Chair

The mouse brain contains over 70 million neurons that form around a trillion connections, or synapses, with one another. Different synaptically connected networks of neurons are organized with varying circuit motifs to receive information and transform that information into a relevant output for the animal. The visual system, and in particular the retina, has served as a classic model for elucidating how neuronal circuits perform these computations. The focus of this dissertation was to understand how the inter-neuronal and sub-neuronal aspects of the direction selective circuit in the retina develop and operate to extract the directions of object motion from the milieu of information in the visual scene. The key neuron in this circuit is the starburst amacrine cell. The dendrites of starburst cells exhibit specific responses to motion in the visual scene that depend upon the dendrite's orientation within the retina. These signals are then propagated through a stereotyped asymmetric arrangement of synaptic connections from multiple starburst cells onto direction selective ganglion cells, which transmit this directional information to the brain. I begin by summarizing the current understanding of how the direction selective circuit develops and operates in Chapter I. Then, experimental evidence is provided that seeks to answer outstanding questions regarding the development of direction selective circuit components and their roles within the mature circuit. First, in Chapter II, I investigate how the asymmetric synaptic connections between starburst cells and direction selective ganglion cells develop. I find that the mature direction selective circuit wiring diagram results from a subcellularly specified synaptogenesis program, rather than synaptic pruning or strengthening. Next, in Chapter III I investigate how the direction selective responses within the starburst cell dendrites are generated. I find that a skewed distribution of excitatory inputs onto the dendrite is sufficient to produce these responses. In Chapter IV, I explore how starburst cell dendritic morphology influences direction selective circuit computations. I find that starburst cell morphology aligns the subcellular starburst cell computation with the appropriate post-synaptic ganglion cell and that the dense plexus of starburst dendrites is required to produce directionally discriminate responses in the ganglion cell. In addition, I find that the subcellular directional computation in starburst cells is performed at the end of the bipolar cell input distribution along the dendrite identified in Chapter III. In Chapter V I seek to identify the molecular determinants of the asymmetric wiring program identified in Chapter II. These preliminary results will provide a basis for further exploration of direction selective circuit development. Together, these results reveal how the morphology, connectivity,

and biophysical properties of neurons are arranged during development to generate the amazing computational abilities of neuronal circuits.

For everyone who has helped me get here, and everyone who will help me go further.

Contents

Acknowledgements

I am eternally grateful to multiple people for being able to show you the results presented below. Throughout this dissertation the imprint of all my advisors and labmates past and present can be felt. In addition, I would be remiss to exclude the amazing contribution of the American (and French) taxpayers that have funded this work.

For Chapter I, we thank Anna Vlasits for helpful comments on this manuscript. Support was provided by National Science Foundation (NSF) Grant DGE 1106400 and NIH ROI1EY019498 and RO1EY013528.

For Chapter II, I want to acknowledge Wei Wei, without whose previous work and generosity these experiments would not have been fathomed, much less accomplished. This work was supported by NIH Grants R01EY019498 and R01EY013528 and NSF Graduate Research Fellowship DGE 1106400.

For Chapter III, I want to acknowledge Anna Vlasits, without whom I would be a much lesser scientist. Your skepticism, supportiveness, and overall brilliance certainly made this and all dissertation chapters better. In addition, we are grateful to Kevin Briggman for providing previously published SBEM data, members of the Feller lab and DiGregorio lab for discussion and technical support, Rachel Wong for helpful comments on the manuscript and Melissa Panlasigui for microscopy support. This work was supported by numerous grants. In no particular order they were: NSF Grant No. DGE 1106400, NIH F31 NS089197-01, NIH ROI1EY019498, RO1EY013528, P30EY003176, NIH EY10699, the French National Agency for Research (ANR-2010-BLANC-1411, ANR-13-SAMA-0006-05, ANR-13-BSV4-0016), the Fondation de Recherche Medicale (Team grant), the Ecole des Neurosciences de Paris, EMBO Long-Term Fellowship 1582-2011, a Roux-Howard-Cantarini post-doctoral fellowship, a Marie Curie Individual Fellowship 301362 within the 7th European Community Framework Program (FP7-PEOPLE-2011-IEF), P30EY003176, and the France-Berkeley Fund.

For Chapter IV, I want to thank Alex Kolodkin for the generous gift of the Sema6A$^{-/-}$ mice, Keven Laboy-juarez for help with circular regression analysis, Benjamin E. Smith for help with Ca^{2+} imaging data analysis, Stephen G. Brohawn for lending his microforge, and the Berkeley Molecular Imaging Center for image analysis software. This work was supported by National Science Foundation (NSF) Grant DGE 1106400, the UC Dissertation Fellowship, and by NIH grants ROI1EY019498, RO1EY013528, and P30EY003176.

For Chapter V, I want to thank Hector Nolla and Alma Valeros for their help and guidance with FAC sorting, Justin Choi and the rest of the Berkeley Functional Genomics Lab for their molecular biology assistance, Rachel Kjølby for continued consultation throughout the project, and Jeremy Kay for cell dissociation guidance. In addition, Shaw Hsu was an outstanding mentee, whose great work in the lab I hope will one day be deservedly published. This work was supported by National Science Foundation (NSF) Grant DGE 1106400, the UC Dissertation Fellowship, and by NIH grants ROI1EY019498, RO1EY013528, and P30EY003176.

Of course, none of these chapters would have been possible without the amazing mentorship of

Marla Feller. I feel immeasurably lucky to have been your student. Under your tutelage I have learned some of the essentials for being a rigorous scientist, such as doing the right experiment to answer the question I am asking and treating every talk like a 'job talk'. Your dedication to your mentee's success has made it easy for me to both continue to push through difficult experiments and confusing data and also celebrate and be proud of accomplishments when they happen.

I would also like to especially thank my thesis committee of Udi Isacoff, Hillel Adesnik, and Mike DeWeese, who have always provided prescient advice about both my science and my future scientific endeavors.

Many others have made my grad school experience both intellectually stimulating and fun. All of my Feller Lab mates, classmates, students, and question asking colleagues have contributed towards making me a better scientist and person.

Penultimately, I want to thank my family. You have instilled a sense of wonder and drive in me that has enabled my pursuit down a path that we were not even dreaming of just 10 years ago. Although that path has moved me far away from home, my mind never drifts from the values that I have inherited from you or the sacrifices you have made for me. I love you all.

Finally, no acknowledgements section would be legitimate without thanking the person who has been by my side throughout graduate school, Rachel Kjølby. No matter how bad (or good) my data were, you were always there to talk me through it, and offer a trip to Smitten to pick me up (or celebrate). I'm so happy to become Drs. with you and can't wait to begin our next set of life experiments together. *Ti amo.*

Chapter I

Development of synaptic connectivity in the retinal direction selective circuit.

This chapter is a full reprint of Morrie & Feller, *Current Opinion in Neurobiology* (2016), in which I was the primary author. This work is included with permission from all authors.

Relevant Publication:

Morrie, R. D., & Feller, M. B. (2016). Development of synaptic connectivity in the retinal direction selective circuit. *Current Opinion in Neurobiology*, *40*, 45–52.

Abstract

Direction selectivity is a classic neuronal computation that has been described in many different sensory systems. The circuit basis of this computation is perhaps best understood in the retina, where direction selectivity is the result of asymmetric connectivity patterns between excitatory and inhibitory circuit components. Retinal direction selective circuits emerge prior to eye-opening, though components of the circuit undergo refinement after vision begins. These features make the direction selective circuit a rich model in which to investigate neuronal circuit assembly. In this Opinion, we highlight recent experiments investigating the contribution of various molecular cues, as well as neuronal activity, to the development of the retinal direction selective circuit.

Introduction: Organization of the retinal direction selective circuit

A classic goal in developmental neurobiology is to understand how molecular markers and neuronal activity interact to instruct the emergence of functional circuits (reviewed in [1]). To tease apart these contributions, it is vital that the detailed wiring diagram of the circuit and its computation are well understood. To this end, the retinal direction selective circuit is an excellent system to examine this developmental puzzle.

There are two key features of direction selective circuits that emerge during development. First is their tuning. Direction selective ganglion cells (DSGCs) fire robustly to stimuli moving in a preferred direction and weakly to stimuli moving in the opposite, or null direction. (Though there are several types of DSGCs, in this review we focus on one class, On-Off DSGCs, whose members respond to both increments and decrements in luminance). Second, the preferred directions of DSGCs are not randomly distributed, but rather cluster tightly along particular directions of motion [2,3]. This results in DSGCs subpopulations with preferred directions along four axes: nasal, temporal, dorsal, and ventral, which we refer to as the cardinal directions (Figure 1B,D).

The circuit components that underlie DSGC tuning are well identified at the cellular level: a class of inhibitory interneurons, called starburst amacrine cells (SACs), provide GABAergic inhibition, while a class of excitatory interneurons, called bipolar cells, provide glutamatergic excitation (Figure 1A). Directional tuning arises predominantly via asymmetric inhibitory signaling; when inhibition from SACs is abolished using GABA-A antagonists [4], ablation of SACs [5], or reversible pharmacogenetic silencing [6] DSGCs fire to stimuli moving in their null direction, eliminating direction selectivity. A role for excitation in generating direction selectivity is more controversial. Calcium imaging in bipolar cell terminals [7,8] and imaging of glutamate released from bipolar cells [9] in response to visual stimulation indicate that bipolar cells do not encode direction. However, a recent studied implicated a role for excitation in direction selectivity. In a transgenic mouse with significantly reduced GABA release from SACs, a substantial number of DSGCs remained [10]; the DSGCs that retained direction selectivity did so via an asymmetric excitatory input [10], demonstrating a role for excitation in this computation in at least a subset of DSGCs. Indeed, transgenic manipulations of cone bipolar cell (cBC) release and connectivity can have large effects on the direction selective circuit [11,12].

Importantly, the bipolar cell subtypes, SACs, and DSGCs that comprise On-Off direction selective circuits are all symmetric in their morphology (see Figure 1D for exception) and therefore direction selectivity emerges as the result of selective wiring. Several experimental approaches have converged onto a consistent description of the inhibitory wiring scheme that underlies direction selectivity. Paired SAC-DSGC recordings revealed that SACs located on the null side of a DSGC have a stronger GABAergic synaptic conductance than SACs located on the preferred side [13-15]. Serial electron microscopy reconstructions revealed the subcellular connectivity pattern underlying this asymmetry; the orientations of individual SAC processes strongly correlated with the null direction of the DSGC with which they formed synapses. Thus, null-oriented SAC processes form more synapses with DSGCs than preferred-oriented SAC processes [16] (Figure 1C). Moreover, the clustering of DSGC preferred directions along cardinal axes functions as a constraint on this antiparallel wiring of SACs onto DSGCs (Figure 1D). The asymmetric inhibitory input from SACs is further enhanced by the intrinsic direction selectivity of the SAC process itself to centrifugal motion [7,17-19]. Antiparallel wiring (Figure 1D) dictates that null direction motion provides centrifugal stimulation for null oriented SAC processes. Hence, these subcellular mechanisms work together to ensure object motion in the null direction induces a larger release of GABA from SACs onto DSGCs than motion in the preferred direction.

Although the basis of excitation-driven direction selectivity is not well understood, a variety of approaches, including EM reconstructions [20], viral tracing [7], and electrophysiological recordings [8], have revealed asymmetries in bipolar cell inputs between SACs and DSGCs, despite their similar stratification patterns. For example, cone bipolar cell type 7 (cBC7) contacts ON SACs but not DSGCs. In addition, the centrifugal direction selectivity of SACs themselves may be partially determined by specific subcellular connectivity patterns with cBCs [21-23].

Despite recent advances in our detailed understanding of the mature DS circuit [3,24], an essential developmental question remains: what instructs the selective synaptic connectivity that underlies the antiparallel wiring of SACs onto DSGCs? Here we describe recent progress in elucidating when direction selective circuit elements emerge, the molecular cues that are involved in their development, and evidence that neuronal activity may play an important role in direction selective circuit maturation.

Timeline of DS circuit development

DS circuits emerge early in retinal development. Using MEA and cell attached recordings, direction selective responses have been observed at eye opening (end of the second postnatal week in mice), and even a few days prior [14,25-28]. At this time bipolar cells are beginning to link photoreceptors to the rest of the retina, indicating that the antiparallel wiring of SACs onto DSGCs exists prior to the maturation of bipolar cell synapses.

When does asymmetric SAC-DSGC wiring emerge? Transgenic mouse lines that label specific subpopulations of DSGCs (reviewed in [29], Figure 1D) enable identification of DSGCs with particular preferred directions prior to the establishment of functional light responses in the retina. Paired whole cell recordings between transgenically labeled DSGCs and SACs revealed that asymmetries in inhibition begin near the end of the second postnatal week [14,30] and channelrhodopsin activation of SACs showed asymmetric connectivity with DSGCs as early as P9 [31]. By isolating quantal GABA release events from SAC-DSGC pairs, we found that this asymmetric conductance emerges due to an increase in the number of synapses from null-oriented SAC processes, rather than a change in synaptic strength [30]. Hence, the early development of the DS circuit involves a process of rapid and selective synaptogenesis between SACs and DSGCs prior to light response maturation.

Towards a molecular understanding of direction selectivity

Specific genetic fingerprints are postulated to exist for each of the different DSGC subpopulations that have been identified in transgenic mice [32]. Indeed, microarray expression profiling identified candidate genes hypothesized to be specifically expressed in ventral motion preferring DSGCs (BD) [33] or SACs [34]. After analyzing the expression of these candidates in two mouse lines that labeled nasal motion preferring DSGCs (Drd4-GFP, W9-YFP) [34,35], Kay et al., found that among DSGCs, MMP17 was expressed exclusively by nasal preferring cells, while Cdh6 and Col25a1 were expressed exclusively by ventral and dorsal preferring DSGCs. These molecular signatures were present a week before eye opening [34] and in some cases immediately following differentiation [36], further indicating that DSGCs differentiate into cardinal direction subpopulations with specific genetic fingerprints long before the maturation of light responses.

The presence of specific genetic markers for DSGC subpopulations leads to the hypothesis that each DSGC subpopulation has a unique molecular signature that is recognized by antiparallel SAC processes expressing the requisite complementary molecular cues (Figure 1D). Here we describe multiple molecules that are essential for the proper development of components of the direction selective circuit.

Molecularly induced alterations in SAC morphology

In looking for SAC-DSGC synaptogenesis factors, members of two classic synaptogenesis gene families were found to be highly expressed in SACs, the protocadherin-γ cluster [37] and the semaphorin *Sema6A* [38]. Both of these genes are essential for proper SAC morphological development and function.

Protocadherins are responsible for dendritic self-avoidance in SACs and cerebellar Purkinje cells [37]. The protocadherin-γ cluster has a unique genetic structure whereby different extracellular variants of protocadherin-γ proteins are expressed stochastically in individual cells. The model is that homotypic interactions between protocadherin isoforms cause self-avoidance but heterotypic interactions do not [39]. Protocadherin-γ cluster deletion in SACs (*Pcdhg*$^{-/-}$) resulted in a collapse of SAC 'starburst' morphology and increased SAC-SAC connectivity (Figure 2B), presumably via an absence of self-avoidance. In contrast, directed SAC expression of a single protocadherin-γ isoform (*Pcdhg*^{3}) in the *Pcdhg*$^{-/-}$ background resulted in a restoration of self avoidance, but an absence of SAC-SAC synapses because of increased non-self avoidance (Figure 2C) [37,40]. Thus, Pcdhg heterogeneity amongst SACs is required for normal development of SAC–SAC connectivity.

What is the impact of altered SAC-SAC connectivity on direction selectivity? Ventral motion preferring DSGCs (HB9-GFP) in the *Pcdhg*$^{-/-}$ mouse have reduced directional tuning and a wider distribution of preferred directions (Figure 2B). In contrast, in *Pcdhg*^{3} mice the ventral motion preference was maintained, but the strength of direction selectivity was reduced (Figure 2C). The reduced direction selectivity in both cases resulted from weaker and more symmetric SAC-DSGC inhibition [40]. Hence, these data indicate that disrupting SAC-SAC connectivity results in reduced directional tuning.

Semaphorin mutants also link a change in SAC morphology to reduced direction selectivity. Semaphorins are a class of transmembrane proteins with multiple roles in synapse development and axon guidance, especially within the retina (reviewed in [41]). Sema6A is essential for the ON/OFF segregation found in the inner plexiform layer of the retina [42] and signals through PlexinA2 to achieve proper lamination of ON and OFF SAC dendrites [38]. In *Sema6A*$^{-/-}$ mice, ON, but not OFF, SACs lose their morphological symmetry, and nasal preferring DSGCs (TrHr-GFP) exhibit reduced DS for bright, but not dark, moving edges [38] (Figure 3D).

These studies demonstrate that morphological alterations in SACs and/or SAC-SAC signaling results in compromised direction selectivity, likely via reduced direction selectivity in SACs themselves. Both mouse models exhibit degraded DS in genetically identified subpopulations of DSGCs due to increased null direction-evoked spiking activity. However, neither Pcdhg nor Sema6A has been implicated in patterning the asymmetric SAC-DSGC connectivity fundamental to the direction selective computation. Thus, it is predicted that loss of direction selective tuning in these mice is not specific to a particular subpopulation of DSGC.

Molecular determinants of horizontal preferred directions

A recent study identified for the first time a gene that selectively affects the development of some direction selective axes while others remain intact. Based on the observation that ablation of SACs abolishes the optokinetic reflex [5], Yonehara and colleagues studied mice with mutations in *FRMD7*, a gene linked to infantile idiopathic nystagmus, a disorder characterized by a loss of horizontal optokinetic reflexes in humans [43]. Mice with a hypomorphic mutation in *FRMD7 (FRMD7*^{tm}*)* completely lack the optokinetic reflex and retinal DS responses along the horizontal axes, but retain normal responses along the vertical axes [44] (Figure 2E).

FRMD7 is expressed exclusively in SACs [44,45], but unlike in other mouse models with reduced direction selectivity [38,40], SACs in *FRMD7*^{tm} mice appeared morphologically and functionally normal [44]. Furthermore, temporal motion preferring DSGCs (Hoxd10-GFP) in *FRMD7*^{tm} mice lost directional tuning due to a lack of spiking to temporally moving stimuli, instead of the increases in spiking to null direction stimuli observed in *Pcdhg*$^{-/-}$ and *Sema6A*$^{-/-}$ mice. Thus, these DSGCs in *FRMD7*^{tm} mice experience strong but symmetric GABAergic inhibition to horizontal motion stimulation [44] .

The symmetric inhibition phenotype in *FRMD7*^{tm} mice leads to the hypothesis of a distinct developmental mechanism in which DSGCs may provide repulsive signals to preferred-oriented SAC dendrites, rather than attractive signals to null-oriented ones. FRMD7 itself is most likely not instructional for asymmetric wiring of SACs to DSGCs because it is expressed symmetrically in SAC dendrites [44]. However, it may be involved in the trafficking of other proteins to the correct subcellular location due to its interactions with actin cytoskeleton organizers [46].

The role of activity in direction selective circuit development

Thus far we have described roles for molecules involved in the wiring of inhibitory synapses that underlie direction selectivity. However, activity also influences the establishment, subcellular localization, and persistence of GABAergic synapses [47] in many parts of the brain. Hence, neuronal activity could affect three components of SAC-DSGC wiring in the DS circuit: 1) SAC-DSGC synaptogenesis, 2) symmetry breaking to produce anti-parallel SAC-DSGC wiring, or 3) refinement of SAC-DSGC wiring.

Strong SAC-DSGC inhibition emerges early in development, prior to the maturation of the light response [14,31], when the primary source of activity in the retina is retinal waves. Do retina waves play a role in SAC-DSGC synaptogenesis? Several studies based on pharmacological blockades [14,28] or genetic alterations [25,48] of retinal waves have not revealed an effect on direction selective responses at eye opening, indicating that SAC-DSGC synapses are not influenced by the patterned activity of retinal waves [49,50]. However, one can never be sure that the activity manipulations are functioning at all times (see Discussion in [48]) and therefore these negative results do not rule out a potential role for SAC-DSGC signaling in synaptogenesis.

The emergence of asymmetric SAC-DSGC synaptic connectivity also occurs prior to eye-opening. Therefore, the symmetry-breaking step is either "hard-wired" or influenced by spontaneous activity. In a recent study in hippocampus, it was shown that activity-dependent transcription factors played a role in the establishment of a subcellular GABAergic connectivity pattern onto pyramidal cells [51]. We speculate that a similar model may occur in the retina in which the presence of neuronal activity is required for the production of specific proteins in SACs that are then trafficked to specific SAC processes.

Importantly, the process of direction selective circuit development does not end at eye-opening. The strength of direction selective tuning is higher in retinas from adult mice than at eye opening [25,40,52,53,54] (but see [27]) and most strikingly, DSGC preferred directions do not cluster along the cardinal directions in young mice [25,52,54] (Figure 3A). This clustering is a process of refinement; population calcium imaging of nasal preferring GFP$^+$ DSGCs has shown that their preferred directions are less clustered at eye opening compared to adults, but are never tuned to a direction more than 90^o from nasal (Figure 3A, inset) [54]. Furthermore, Bos et al., found that visual activity is required for this refinement process, as animals reared in the dark also exhibit a lack of DSGC preferred direction clustering (Figure 3A) [54]. Whether this reduced clustering in the absence of visual activity is a result of fewer postsynaptic GABAergic sites on bistratified RGCs [55], a failure to refine SAC-SAC connectivity (Figure 3C) [40], or imprecise SAC-DSGC connectivity remains to be determined.

Conclusion

The retinal DS circuit provides a powerful model in which to study the patterning of synapses in neural circuits due to our strong understanding of the cell types and their connectivity patterns that comprise the circuit in the adult [3,24]. Thus far, only a small number of molecules that identify DSGC subpopulations, that are crucial for the normal development of SACs, or that are necessary for the development of direction selectivity of certain DSGC subpopulations have been identified. Thus, the question of what instructs the antiparallel wiring of individual SACs processes to DSGCs remains to be answered.

We end with a framework for determining how asymmetric SAC-DSGC wiring develops. In this hypothetical scenario, SACs sense one of the many molecular gradients that are found along cardinal axes in the developing retina (reviewed in [56,57]) and use them to traffic different proteins to their processes oriented in different directions. These proteins then interact with proteins expressed by the different classes of DSGCs in either a repulsive or attractive manner to prevent or induce synapse formation. Our hope is that novel candidates will be identified in unbiased screens, such as a recent one designed to look for cell surface recognition partners that identified a novel set of proteins governing SAC and DSGC dendritic lamination [58]. To probe effects on synaptic connectivity, candidate genes can be tested using cell specific manipulations to express or delete them presynaptically in bipolar cells and SACs (such as in[12,59]) or postsynaptically in subtypes of DSGCs (such as in [60]). Lastly, activity manipulations targeted to SAC-DSGCs signaling will be necessary to determine whether neuronal activity plays a role in the expression, trafficking or function of these candidate proteins. Only through such a multipronged approach will the puzzle of direction selective wiring be solved.

References

1. Yogev S, Shen K: **Cellular and molecular mechanisms of synaptic specificity.** *Annu. Rev. Cell Dev. Biol.* 2014, **30**:417–437.

2. Oyster CW, BARLOW HB: **Direction-Selective Units in Rabbit Retina: Distribution of Preferred Directions**. *Science* 1967, **155**:841–842.

3. Vaney DI, Sivyer B, Taylor WR: **Direction selectivity in the retina: symmetry and asymmetry in structure and function.** *Nat Rev Neurosci* 2012, **13**:194–208.

4. Wyatt HJ, Day NW: **Specific effects of neurotransmitter antagonists on ganglion cells in rabbit retina.** *Science* 1976, **191**:204–205.

5. Yoshida K, Watanabe D, Ishikane H, Tachibana M, Pastan I, Nakanishi S: **A key role of starburst amacrine cells in originating retinal directional selectivity and optokinetic eye movement.** *Neuron* 2001, **30**:771–780.

6. Vlasits AL, Bos R, Morrie RD, Fortuny C, Flannery JG, Feller MB, Rivlin-Etzion M: **Visual stimulation switches the polarity of excitatory input to starburst amacrine cells.** *Neuron* 2014, **83**:1172–1184.

7. Yonehara K, Farrow K, Ghanem A, Hillier D, Balint K, Teixeira M, Jüttner J, Noda M, Neve RL, Conzelmann K-K, et al.: **The first stage of cardinal direction selectivity is localized to the dendrites of retinal ganglion cells.** *Neuron* 2013, **79**:1078–1085.

8. Chen M, Lee S, Park SJH, Looger LL, Zhou ZJ: **Receptive field properties of bipolar cell axon terminals in the direction-selective sublaminas of the mouse retina**. *J. Neurophysiol.* 2014, **112**:jn.00283.2014.

9. Park SJH, Kim IJ, Looger LL, Demb JB, Borghuis BG: **Excitatory Synaptic Inputs to Mouse On-Off Direction-Selective Retinal Ganglion Cells Lack Direction Tuning**. *J. Neurosci.* 2014, **34**:3976–3981.

10. •Pei Z, Chen Q, Koren D, Giammarinaro B, Ledesma HA, Wei W: **Conditional Knock-Out of Vesicular GABA Transporter Gene from Starburst Amacrine Cells Reveals the Contributions of Multiple Synaptic Mechanisms Underlying Direction Selectivity in the Retina**. *J. Neurosci.* 2015, **35**:13219–13232.

    This study demonstrates a key role of excitatory signaling in the generation of DS. The authors found a substantial number of DSGCs remained in a transgenic mouse in which VGAT was specifically knocked out of SACs.

11. •Shi Z, Trenholm S, Zhu M, Buddingh S, Star EN, Awatramani GB, Chow RL: **Vsx1 Regulates Terminal Differentiation of Type 7 ON Bipolar Cells**. *J. Neurosci.* 2011, **31**:13118–13127.

The authors localize expression of Vsx1 in ON bipolar cells to cBC7. They then show that the ON direction selectivity of DSGCs is decreased in Vsx1$^{-/-}$ mice due to increased null direction spiking, while OFF direction selective tuning remains normal.

12. ••Duan X, Krishnaswamy A, la Huerta De I, Sanes JR: **Type II Cadherins Guide Assembly of a Direction-Selective Retinal Circuit.** *Cell* 2014, **158**:793–807.

This study uses optogenetic and molecular characterization of bipolar cell connectivity in the DS circuit to show that cadherins instruct the lamination of bipolar cells axons and their synaptic connections with SACs and DSGCs.

13. Fried SI, Münch TA, Werblin FS: **Mechanisms and circuitry underlying directional selectivity in the retina.** *Nature* 2002, **420**:411–414.

14. Wei W, Hamby AM, Zhou K, Feller MB: **Development of asymmetric inhibition underlying direction selectivity in the retina.** *Nature* 2011, **469**:402–406.

15. Lee S, Kim K, Zhou ZJ: **Role of ACh-GABA cotransmission in detecting image motion and motion direction.** *Neuron* 2010, **68**:1159–1172.

16. Briggman KL, Helmstaedter M, Denk W: **Wiring specificity in the direction-selectivity circuit of the retina.** *Nature* 2011, **471**:183–188.

17. Euler T, Detwiler PB, Denk W: **Directionally selective calcium signals in dendrites of starburst amacrine cells.** *Nature* 2002, **418**:845–852.

18. Lee S, Zhou ZJ: **The synaptic mechanism of direction selectivity in distal processes of starburst amacrine cells.** *Neuron* 2006, **51**:787–799.

19. Hausselt SE, Euler T, Detwiler PB, Denk W: **A dendrite-autonomous mechanism for direction selectivity in retinal starburst amacrine cells.** *Plos Biol* 2007, **5**:e185.

20. Helmstaedter M, Briggman KL, Turaga SC, Jain V, Seung HS, Denk W: **Connectomic reconstruction of the inner plexiform layer in the mouse retina.** *Nature* 2013, **500**:168–174.

21. Kim JS, Greene MJ, Zlateski A, Lee K, Richardson M, Turaga SC, Purcaro M, Balkam M, Robinson A, Behabadi BF, et al.: **Space–time wiring specificity supports direction selectivity in the retina**. *Nature* 2014, doi:10.1038/nature13240.

22. Greene MJ, Kim JS, Seung HS, EyeWirers: **Analogous Convergence of Sustained and Transient Inputs in Parallel On and Off Pathways for Retinal Motion Computation.** *CellReports* 2016, doi:10.1016/j.celrep.2016.02.001.

23. Vlasits AL, Morrie RD, Tran-Van-Minh A, Bleckert A, Gainer CF, DiGregorio DA, Feller MB: **A Role for Synaptic Input Distribution in a Dendritic Computation of Motion Direction in the Retina.** *Neuron* 2016, **89**:1317–1330.

24. Helmstaedter M, Borst A: **Common circuit design in fly and mammalian motion vision**. *Nat Neurosci* 2015, doi:10.1038/nn.4050.

25. Elstrott J, Anishchenko A, Greschner M, Sher A, Litke AM, Chichilnisky EJ, Feller MB: **Direction selectivity in the retina is established independent of visual experience and cholinergic retinal waves.** *Neuron* 2008, **58**:499–506.

26. Chan Y-C, Chiao C-C: **Effect of visual experience on the maturation of ON-OFF direction selective ganglion cells in the rabbit retina.** *Vision Res.* 2008, **48**:2466–2475.

27. Chen M, Weng S, Deng Q, Xu Z, He S: **Physiological properties of direction-selective ganglion cells in early postnatal and adult mouse retina**. *The Journal of Physiology* 2009, **587**:819–828.

28. Sun L, Han X, He S: **Direction-selective circuitry in rat retina develops independently of GABAergic, cholinergic and action potential activity.** *PLoS ONE* 2011, **6**:e19477.

29. Dhande OS, Stafford BK, Lim J-HA, Huberman AD: **Contributions of Retinal Ganglion Cells to Subcortical Visual Processing and Behaviors**. *Annu. Rev. Vis. Sci.* 2015, **1**:291–328.

30. Morrie RD, Feller MB: **An Asymmetric Increase in Inhibitory Synapse Number Underlies the Development of a Direction Selective Circuit in the Retina.** *J. Neurosci.* 2015, **35**:9281–9286.

31. Yonehara K, Balint K, Noda M, Nagel G, Bamberg E, Roska B: **Spatially asymmetric reorganization of inhibition establishes a motion-sensitive circuit.** *Nature* 2011, **469**:407–410.

32. Elstrott J, Feller MB: **Vision and the establishment of direction-selectivity: a tale of two circuits.** *Current Opinion in Neurobiology* 2009, **19**:293–297.

33. Kim I-J, Zhang Y, Meister M, Sanes JR: **Laminar restriction of retinal ganglion cell dendrites and axons: subtype-specific developmental patterns revealed with transgenic markers.** *J. Neurosci.* 2010, **30**:1452–1462.

34. ••Kay JN, la Huerta De I, Kim I-J, Zhang Y, Yamagata M, Chu MW, Meister M, Sanes JR: **Retinal ganglion cells with distinct directional preferences differ in molecular identity, structure, and central projections.** *J. Neurosci.* 2011, **31**:7753–7762.

This study was the first to identify genetic markers specific to different subpopulations of DSGCs using microarray analysis.

35. Huberman AD, Wei W, Elstrott J, Stafford BK, Feller MB, Barres BA: **Genetic identification of an On-Off direction-selective retinal ganglion cell subtype reveals a layer-specific subcortical map of posterior motion.** *Neuron* 2009, **62**:327–334.

36. la Huerta De I, Kim I-J, Voinescu PE, Sanes JR: **Direction-selective retinal ganglion cells arise from molecularly specified multipotential progenitors.** *Proceedings of the National Academy of Sciences* 2012, **109**:17663–17668.

37. Lefebvre JL, Kostadinov D, Chen WV, Maniatis T, Sanes JR: **Protocadherins mediate dendritic self-avoidance in the mammalian nervous system**. *Nature* 2012, **488**:517–521.

38. ••Sun LO, Jiang Z, Rivlin-Etzion M, Hand R, Brady CM, Matsuoka RL, Yau KW, Feller MB, Kolodkin AL: **On and Off Retinal Circuit Assembly by Divergent Molecular Mechanisms**. *Science* 2013, **342**:1241974–1241974.

This study found that ON SACs, but not OFF SACs, express the transmembrane protein Sema6A, and that this expression pattern mediates the different dendritic stratification patterns of the two SAC populations via repulsive signaling with PlexA2. Furthermore, the authors show that Sema6A is required for proper ON SAC dendritic morphology and that DSGCs have reduced ON, but not OFF, direction selectivity in Sema6A$^{-/-}$ mice.

39. Lefebvre JL, Sanes JR, Kay JN: **Development of Dendritic Form and Function.** *Annu. Rev. Cell Dev. Biol.* 2015, doi:10.1146/annurev-cellbio-100913-013020.

40. ••Kostadinov D, Sanes JR: **Protocadherin-dependent dendritic self-avoidance regulates neural connectivity and circuit function.** *Elife* 2015, **4**.

This study demonstrates an essential role for SAC self/non-self discrimination in DS using transgenic mouse lines to manipulate Pcdhg expression in SACs. In addition, the authors are the first to show a refinement in GABAergic SAC-SAC connectivity during development.

41. Koropouli E, Kolodkin AL: **Semaphorins and the dynamic regulation of synapse assembly, refinement, and function.** *Current Opinion in Neurobiology* 2014, **27C**:1–7.

42. Matsuoka RL, Nguyen-Ba-Charvet KT, Parray A, Badea TC, Chédotal A, Kolodkin AL: **Transmembrane semaphorin signalling controls laminar stratification in the mammalian retina.** *Nature* 2011, **470**:259–263.

43. Thomas S, Proudlock FA, Sarvananthan N, Roberts EO, Awan M, McLean R, Surendran M, Anil Kumar AS, Farooq SJ, Degg C, et al.: **Phenotypical characteristics of idiopathic infantile nystagmus with and without mutations in FRMD7**. *Brain* 2007, **131**:1259–1267.

44. ••Yonehara K, Fiscella M, Drinnenberg A, Esposti F, Trenholm S, Krol J, Franke F,

Scherf BG, Kusnyerik A, Müller J, et al.: **Congenital Nystagmus Gene FRMD7 Is Necessary for Establishing a Neuronal Circuit Asymmetry for Direction Selectivity.** *Neuron* 2015, doi:10.1016/j.neuron.2015.11.032.

This pioneering study found that the lack of horizontal optokinetic reflexes in human patients with FRMD7 mutations was phenocopied by mice with a hypomorphic mutation in FRMD7. The authors explained this phenotype by demonstrating a specific loss of horizontal DSGCs in Frmd7^{tm} mice using MEA recordings of explanted retinas. Genetically labeled horizontal DSGCs lost DS due to an increase in preferred direction inhibition, which prevents spiking to all directions of moving stimuli.

45. Siegert S, Cabuy E, Scherf BG, Kohler H, Panda S, Le Y-Z, Fehling HJ, Gaidatzis D, Stadler MB, Roska B: **Transcriptional code and disease map for adult retinal cell types**. *Nat Neurosci* 2012, **15**:487–495.

46. Pu J, Mao Y, Lei X, Yan Y, Lu X, Tian J, Yin X, Zhao G, Zhang B: **FERM domain containing protein 7 interacts with the Rho GDP dissociation inhibitor and specifically activates Rac1 signaling.** *PLoS ONE* 2013, **8**:e73108.

47. Huang ZJ: **Activity-dependent development of inhibitory synapses and innervation pattern: role of GABA signalling and beyond.** *The Journal of Physiology* 2009, **587**:1881–1888.

48. Hamby AM, Rosa JM, Hsu C-H, Feller MB: **CaV3.2 KO mice have altered retinal waves but normal direction selectivity.** *Vis. Neurosci.* 2015, **32**:E003.

49. Elstrott J, Feller MB: **Direction-selective ganglion cells show symmetric participation in retinal waves during development.** *J. Neurosci.* 2010, **30**:11197–11201.

50. Stafford BK, Sher A, Litke AM, Feldheim DA: **Spatial-temporal patterns of retinal waves underlying activity-dependent refinement of retinofugal projections.** *Neuron* 2009, **64**:200–212.

51. Bloodgood BL, Sharma N, Browne HA, Trepman AZ, Greenberg ME: **The activity-dependent transcription factor NPAS4 regulates domain-specific inhibition.** *Nature* 2013, **503**:121–125.

52. Chan Y-C, Chiao C-C: **The distribution of the preferred directions of the ON-OFF direction selective ganglion cells in the rabbit retina requires refinement after eye opening**. *Physiol Rep* 2013, **1**:e00013.

53. Chen H, Liu X, Tian N: **Subtype-Dependent Postnatal Development of Direction- and Orientation-Selective Retinal Ganglion Cells in Mice**. *J. Neurophysiol.* 2014, **112**:2092–2101.

54. ••Bos R, Gainer C, Feller MB: **Role for Visual Experience in the Development of Direction-Selective Circuits**. *Current Biology* 2016, doi:10.1016/j.cub.2016.03.073.

Using 2-photon calcium imaging, the authors find that at eye opening and in dark reared adults DSGC preferred directions are diffusely distributed, demonstrating a key role for visual signaling in the clustering of DSGC preferred directions to the cardinal axes.

55. Bleckert A, Parker ED, Kang Y, Pancaroglu R, Soto F, Lewis R, Craig AM, Wong ROL: **Spatial Relationships between GABAergic and Glutamatergic Synapses on the Dendrites of Distinct Types of Mouse Retinal Ganglion Cells across Development.** *PLoS ONE* 2013, **8**:e69612.

56. McLaughlin T, O'Leary DDM: **Molecular gradients and development of retinotopic maps.** *Annu. Rev. Neurosci.* 2005, **28**:327–355.

57. Clandinin TR, Feldheim DA: **Making a visual map: mechanisms and molecules.** *Current Opinion in Neurobiology* 2009, **19**:174–180.

58. Visser JJ, Cheng Y, Perry SC, Chastain AB, Parsa B, Masri SS, Ray TA, Kay JN, Wojtowicz WM: **An extracellular biochemical screen reveals that FLRTs and Unc5s mediate neuronal subtype recognition in the retina**. *Elife* 2015, **4**:e08149.

59. Krishnaswamy A, Yamagata M, Duan X, Hong YK, Sanes JR: **Sidekick 2 directs formation of a retinal circuit that detects differential motion**. *Nature* 2015, **524**:466–470.

60. Tang JCY, Szikra T, Kozorovitskiy Y, Teixiera M, Sabatini BL, Roska B, Cepko CL: **A nanobody-based system using fluorescent proteins as scaffolds for cell-specific gene manipulation.** *Cell* 2013, **154**:928–939.

61. Kim I-J, Zhang Y, Yamagata M, Meister M, Sanes JR: **Molecular identification of a retinal cell type that responds to upward motion.** *Nature* 2008, **452**:478–482.

62. Baden T, Berens P, Franke K, Rosón MR, Bethge M, Euler T: **The functional diversity of retinal ganglion cells in the mouse**. *Nature* 2016, **529**:345–350.

63. Joesch M, Meister M: **A neuronal circuit for colour vision based on rod–cone opponency**. *Nature* 2016, **532**:236–239

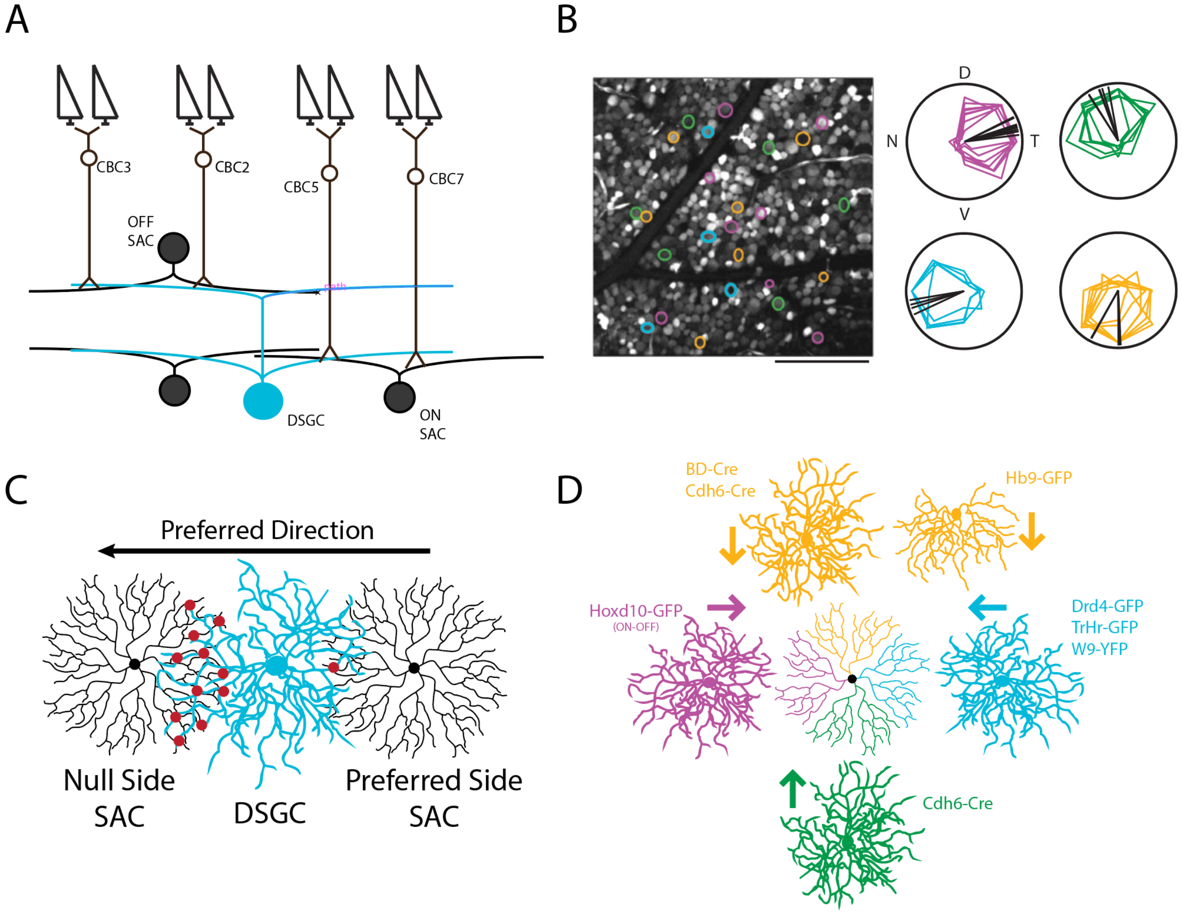

Figure 1. Major components of the direction selective circuit.

A. Schematic of the identified cellular components in the direction selective circuit. Photoreceptors (top) synapse onto OFF bipolar cells (cone bipolar cell, cBC2 and cBC3) through sign-conserving synapses and onto ON bipolar cells (cBC5 and cBC7) through sign-inverting synapses. Bipolar cells provide excitatory gluatamatergic input to SACs and DSGCs: cBC2 provides about half the overall excitatory input onto DSGC OFF arbors while cBC5 provides the majority of excitatory input onto DSGC ON arbors [12]. Different bipolar cell subtypes contact different SACs at the subcellular locations shown [21,22]. Note the lack of bipolar cell contact on the distal portions of SAC processes [23]. SACs provide lateral GABAergic inhibition onto other SACs and feedforward GABAergic inhibition onto DSGCs. Note, SACs also provide cholinergic excitation to DSGCs. The role of this cholinergic synapse in the DS computation is an area of active research and is not covered in this review.

B. There are 4 subpopulations of On-Off DSCGs whose preferred directions cluster along the cardinal axes. *Left* Retina loaded with the calcium indicator OGB via electroporation. Circled cells demarcate ON-OFF DSGCs, with color representing the preferred direction cluster. Scale bar: 100 µm. *Right* Tuning curves and respective vector sums of Ca^{2+} signals in DSGCs in response to moving bar stimuli. N = nasal, D = dorsal, T = temporal, V = ventral in retinal coordinates. *Figure adapted from* [16].

C. SACs on the null side of DSGCs form more GABAergic synapses than SACs on the preferred side. Schematic depicting wiring diagram underlying directional GABA release onto DSGCs. The null-oriented processes of the null side SAC form many GABAergic synapses with the DSGC, while the preferred-oriented processes of the preferred side SAC rarely form GABAergic synapses with the DSGC.

D. Summary of proposed antiparallel SAC-DSGC wiring diagram. Each color represents specific molecular marker expressed by one of the four subpopulations of DSGCs, as well as the corresponding molecular markers expressed by antiparallel-oriented SAC processes. The transgenic mouse lines listed express GFP or Cre in specific subpopulations of DSGCs. (Note we are not discussing ON DSGCs, which compute DS like ON-OFF DSGCS via GABA release from SACs, or OFF DSGCs, which compute DS through a mechanism independent of SACs [3,61-63]).

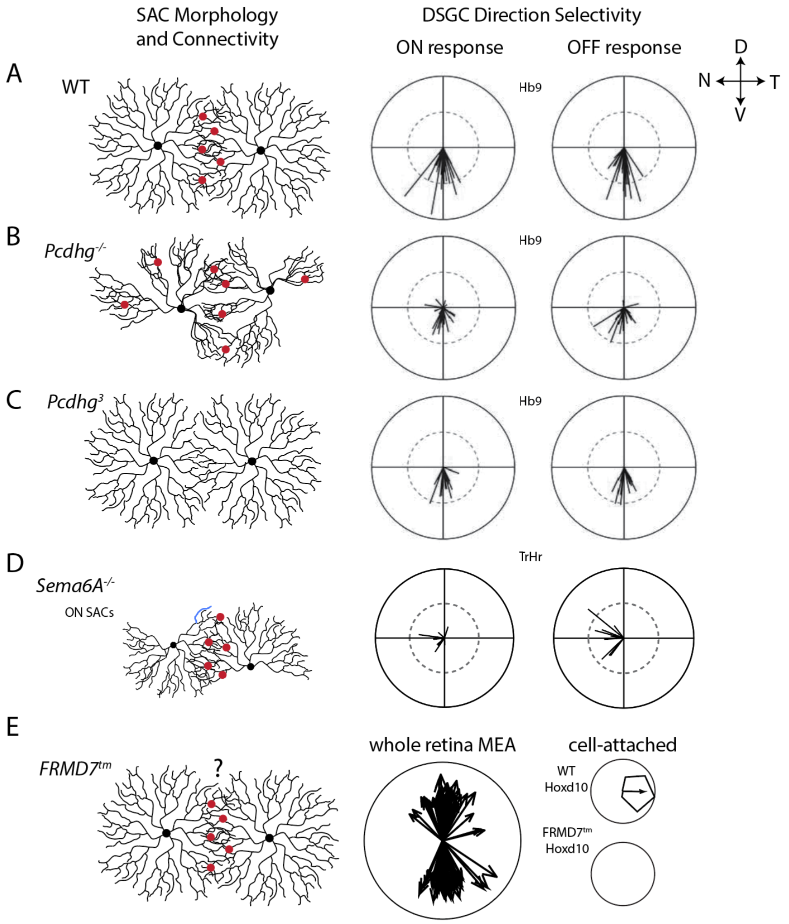

Figure 2. Summary of SAC morphology and connectivity defects in various mutant mouse lines and consequences for direction selectivity.

A. *Left:* SACs in WT mice have radially symmetric dendrites and form GABAergic synaptic connections onto other SACs. SAC connections onto DSGCs are not pictured. *Right*: Tuning curve vector sums with amplitude representing strength of tuning and the angle representing the preferred direction. For Hb9-GFP$^+$ DSGCs, which prefer ventral motion, both ON and OFF responses are strongly tuned. *Figure adapted from* [40].

B. SACs in mice lacking the entire *γ-Protocadherin* cluster do not exhibit self-avoidance, resulting in loss of radially symmetric morphology, and form GABAergic synapses with other SACs, as well as autapses. Both ON and OFF DS responses from Hb9-GFP$^+$ DSGCs are weaker than in WT mice and are not consistently tuned toward the ventral direction. *Figure adapted from* [40].

C. SACs in mice expressing only one *γ-Protocadherin* isoform have radially symmetric morphology but display little dendritic overlap and rarely form GABAergic synapses with other SACs. Both ON and OFF DS responses from Hb9-GFP$^+$ DSGCs are weaker than in WT but generally tuned to the ventral direction. *Figure adapted from* [40].

D. ON SACs in mice lacking *Sema6A* do not have radially symmetric morphology, exhibit reduced self-avoidance, and have smaller overall dendritic arbors. They still receive GABAergic inhibition but SAC-SAC connectivity has not been tested. OFF SACs in this mouse have slightly smaller dendritic field areas but are otherwise normal (not shown). In Trhr-GFP$^+$ DSGCs, which prefer nasal motion, ON DS responses are weaker than in WT but generally tuned to the nasal direction, while OFF DS responses remain strongly tuned. *Figure adapted from* [38].

E. SACs in mice with a hypomorphic mutation in *FRMD7* have normal morphology, but precise SAC-SAC connectivity has not been tested.

Middle: DS responses from MEA recordings of FRMD7^{tm} retina explants show only ventrally and dorsally tuned DSGCs.

Right: Hoxd10-GFP$^+$ DSGCs, which prefer temporal motion in WT mice, do not fire action potentials in response to moving bars in *FRMD7^{tm}* mice. *Figure adapted from* [44].

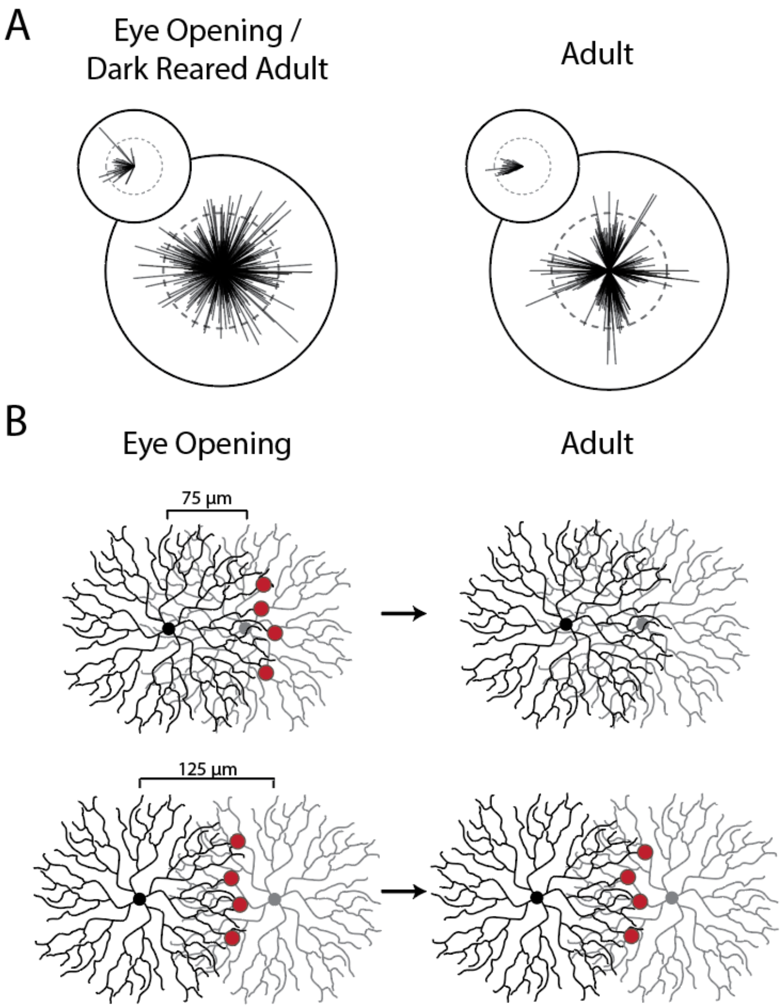

Figure 3. Development of DS circuit components.
A. DSGC preferred directions do not cluster along cardinal directions in young and dark reared animals [52,54]. Tuning curve vector sums of calcium responses to moving bars for all DSGCs, with amplitude representing strength of tuning and the angle representing the preferred direction. *Insets:* Preferred directions of nasal preferring Drd4-GFP$^+$ DSGCs are less clustered along the nasal axis in young and dark reared animals. *Figure adapted from* [54].
B. SAC-SAC GABAergic synapses are refined during development. Although both SACs will form GABAergic synapses onto the other, for simplicity the red circles only indicate synapses from the black SAC onto the grey SAC.
Left: In young animals, SACs form GABAergic synapses onto other SACs regardless of inter-soma distance.
Right: In adult animals, SACs only form GABAergic synapses onto other SACs with an inter-soma distance >100 µm. Schematic based on results from [40].

Chapter II

An Asymmetric Increase in Inhibitory Synapse Number Underlies the Development of a Direction Selective Circuit in the Retina

This chapter is a full reprint of Morrie & Feller, *The Journal of Neuroscience* (2015), in which I was the primary author. This work is included with permission from all authors.

Relevant Publication:

Morrie, R. D., & Feller, M. B. (2015). An Asymmetric Increase in Inhibitory Synapse Number Underlies the Development of a Direction Selective Circuit in the Retina. *The Journal of Neuroscience*, *35*(25), 9281–9286.

Abstract

Neural circuits rely upon a precise wiring of their component neurons to perform meaningful computations. To compute the direction of motion in the visual scene, the direction selective circuit in the mouse retina depends on an asymmetry in the inhibitory neurotransmission from starburst amacrine cells (SACs) to direction selective ganglion cells (DSGCs). Specifically, depolarization of a SAC on the null side of a DSGC causes a threefold greater unitary inhibitory conductance than depolarization of a SAC on the preferred side. This asymmetry emerges during the second postnatal week of development, but its basis remains unknown. To determine the source of this asymmetry in inhibitory conductance, we conducted paired recordings between SACs and DSGCs at the beginning and end of the second postnatal week. We replaced calcium with strontium to promote asynchronous neurotransmitter release and produce quantal events. During the second postnatal week the quantal frequency but not the quantal amplitude of synaptic events increased more than threefold for null side SAC-DSGC pairs but remained constant for preferred side pairs. In addition, paired pulse depression did not differ between SACs located on the null and preferred sides of DSGCs, indicating that all inhibitory SAC synapses onto a DSGC exhibit the same probability of release. Thus, the higher quantal frequency seen in null-side pairs results from a greater number of inhibitory synapses, revealing that an asymmetry in synapse number between SACs and DSGCs underlies the development of an essential component in the retina's direction selective circuit.

Introduction

Direction-selective circuits in the mouse retina depend on a precise wiring of inhibitory connections. Retinal direction selective ganglion cells (DSGCs) respond maximally to stimuli moving in their preferred direction and minimally to stimuli moving in the opposite, or null, direction. This spiking difference results from greater synaptic inhibition onto the DSGC during null direction motion (Fried et al., 2002; Taylor and Vaney, 2002), while the excitatory input is constant regardless of stimulus direction (Yonehara et al., 2013; Park et al., 2014). Several lines of evidence demonstrate that starburst amacrine cells (SACs) are the source of this inhibition. First, eliminating SACs with immunotoxin leads to a loss of direction selectivity (Yoshida et al., 2001). Second, transiently hyperpolarizing SACs reduces direction selective responses in DSGCs (Vlasits et al., 2014). Third, paired recordings between SACs and DSGCs reveal that SACs located on the null side of a DSGC have a stronger overall inhibitory conductance than those located on the preferred side (Fried et al., 2002; Lee et al., 2010; Wei et al., 2011; Yonehara et al., 2011). Based on a serial EM reconstruction, it has been postulated that the asymmetry in inhibitory input onto DSGCs results from SAC processes pointing in a DSGC's null direction being more likely to form synapses with the DSGC than SAC processes pointing in the preferred direction (Briggman et al., 2011). Yet, when this wiring diagram arises during development is not known. Furthermore, the relative contributions of synaptic strength and functional synapse number to the overall asymmetry in inhibitory synaptic transmission between SACs and DSGCs remain to be determined.

Here we compare the quantal properties of null side versus preferred side SAC inputs onto DSGCs across the developmental period when asymmetric inhibitory wiring emerges (Wei et al., 2011; Yonehara et al., 2011). We performed paired voltage clamp recordings from genetically identified DSGCs and SACs under conditions that favor asynchronous release of neurotransmitter and analyzed the quantal properties of events from the null and preferred side pairs during the second postnatal week. We found that the asymmetric increase in SAC inhibitory synaptic conductance is due, not to a change in release probability or quantal size, but rather to an increase in the number of synapses from null oriented SAC processes.

Materials and Methods

Mice

To target SACs and posterior-motion preferring DSGCs for recording, we used ChAT-Cre/TdTomato/Drd4 mice generated by crossing together three mouse lines: *1)* B6.129S6-ChATtm1(cre)lowl/J (Jackson Labs) with Cre driven by the endogenous choline acetyltransferase promoter, *2)* B6.129S6-Gt(ROSA)26Sortm9(CAG-tdTomato)Hze/J (Jackson Labs) with a floxed TdTomato gene, and *3)* Tg(Drd4-EGFP)W18Gsat/Mmnc (Mutant Mouse Regional Resource Centers) to label posterior-preferring DSGCs with GFP (Gong et al., 2003; Huberman et al., 2009). All animal procedures were approved by the UC Berkeley Institutional Animal Care and Use Committee and conformed to the NIH Guide for the Care and Use of Laboratory Animals, the Public Health Service Policy, and the SFN Policy on the Use of Animals in Neuroscience Research.

Electrophysiology

Mice (p7-p14) of either sex were anesthetized with isoflurane and decapitated. Retinas were dissected from enucleated eyes in oxygenated (95% O_2/ 5% CO_2) Ca^{2+}-ACSF containing (in mM) 119 NaCl, 2.5 KCl, 1.3 $MgCl_2$, 1 K_2HPO_4, 26.2 $NaHCO_3$, 11 d-glucose, and 2.5 $CaCl_2$. Retinal orientation was determined as described previously (Wei et al., 2010). Isolated retinas were cut into dorsal and ventral halves, mounted over a 1-2 mm^2 hole in nitrocellulose filter paper (Millipore) with the photoreceptor layer side down, and stored in oxygenated ACSF until use (maximum 8 h).

For quantal recordings, filter paper-mounted retinas were perfused with 30-32°C oxygenated Sr^{2+}-ACSF (5mM Sr^{2+}, 2.5mM EGTA replaces 2.5mM Ca^{2+}) containing the following excitatory synaptic blockers (in μM): 50 AP-5, 20 DNQX, and 8 dihydro-β-erythroidine (DhβE) (Tocris Bioscience). GFP^+ and $TdTomato^+$ cells were identified using an epiflourescent microscope (Olympus BX51). The inner limiting membrane above targeted cells was dissected with a glass pipette. Whole cell voltage clamp recordings were achieved for a given DSGC before targeting multiple SACs on either side of the DSGC in succession, removing the pipette from the previous SAC before targeting a new SAC. For whole cell recordings, borosillicate glass capilary tubes pulled to a 4-5 mΩ tip were filled with an internal solution containing (in mM) 110 $CsMeSO_3$, 2.8 NaCl, 4 EGTA, 5 TEA-Cl, 4 ATP (magnesium salt), 0.3 GTP (trisodium salt), 20 HEPES, 10 Na_2-phosphocreatine, and 0.025 Alexa 488. SACs exhibit asynchronous neurotransmitter release upon depolarization in the voltage clamp configuration (Fried et al., 2002; Zheng et al., 2004; Lee et al., 2010) which may be at least partially attributed to an inadequate space clamp of the distal neurotransmitter release sites (Miller and Bloomfield, 1983; Zhou, 1998; Hausselt et al., 2007). However, by lowering the Ca^{2+} buffering capacity of the internal solution for SACs (0.1 versus 4 mM EGTA) and using tail currents to elicit responses, we could enhance the synchrony of GABA release from SACs upon depolarization

(Figure 1A, grey trace). Due to a lower activation threshold in younger mice P7-8 SACs were depolarized to 0 mV for 3 ms to induce tail currents. Prolonged tail currents in Sr^{2+}-ACSF increased release duration from SACs (Figure 1A, red trace) and may result from a lack of Ca^{2+}-dependent inactivation of VGCCs (data not shown).

Paired-pulse recordings were performed in Ca^{2+}-ACSF. Although SAC tail currents varied between pulses, IPSCs remained consistent between sweeps (Figure 3A). $MgCl_2$ replaced $CaCl_2$ when lowering Ca^{2+} concentration (Figure 3C) to maintain $[Cl^-]_{out}$ and osmolarity.

Data were acquired at 10 kHz and filtered at 2 kHz with a Multiclamp 700B amplifier using pCLAMP 10 recording software and a Digidata 1440 digitizer (Molecular Devices). Reported holding potentials have been corrected for the junction potential (-10 mV). Series resistance (<65 mΩ for all DSGCs) was not compensated, but the current divider effect of the series resistance, $(R_{series}+R_{input})/R_{input}$, was similar across all recordings (range = 1.05-1.27, SD = .049).

Data Analysis

Data analysis was performed in IgorPro (WaveMetrics) and MATLAB (MathWorks). The Taro Tools (sites.google.com/site/tarotoolsregister/) plug-in for IgorPro was used to detect and analyze quantal events (Figure 1B). Events were detected manually for each trace because some traces had multiple overlapping events, preventing the use of amplitude thresholds for event detection. The decay time parameter was 2.5 ms (default) to separate overlapping events. Frequency, amplitude, rise time, and average event calculations were computed with “Further Analysis” and “Event Cut Out” options. Large (>60 pA) initial IPSCs after SAC stimulation resulting from synchronous neurotransmitter release were excluded from analysis. Frequency histograms were fit with a double exponential (Figure 1C, red line). Evoked asynchronous miniature IPSCs (a-mIPSCs) were separated from spontaneous mIPSCs when the curve reached baseline frequency plus two standard deviations (Figure 1C, red dashed line). Mean a-mIPSC frequency was calculated from 50 to 968 ms post-stimulation (the average time when frequency decayed to baseline for p7-8 SAC-DSGC pairs). Frequency measures were normalized by subtracting the baseline mIPSC frequency to isolate a-mIPSCS specific to the depolarized SAC. Paired pulse ratio was calculated by dividing the amplitude of the second IPSC by the amplitude of the first IPSC after averaging at least 3 traces for a given inter-stimulus interval.

Results

Pre-synaptic mechanisms mediate changes in SAC-DSGC connectivity during development

The asymmetry in inhibitory conductance present in the mature direction selective circuit emerges during the second postnatal week in mice (Wei et al., 2011; Yonehara et al., 2011), but whether it manifests as an increase in synapse strength or synapse number is unknown. Previous recordings have demonstrated that from p7 to p14 mIPSCs measured in DSGCs increase in frequency but not in amplitude (Wei et al., 2011), indicating a presynaptic change in SAC-DSGC connectivity during development. However, it has been estimated that each DSGC can receive inputs from roughly 35 different SACs distributed on all sides (Keeley et al., 2007) and therefore changes in mIPSC frequency cannot by attributed to null side SACs alone.

Thus, we first sought to isolate quantal events recorded in DSGCs from single SACs whose somas were located on the null and preferred sides of the DSGC. We conducted paired recordings in solutions in which we replaced Ca^{2+} with Sr^{2+} to increase the asynchronous component of neurotransmitter release and generate IPSCs that are quantal in nature (Goda and Stevens, 1994; Xu-Friedman and Regehr, 1999; 2000). We used brief, strong depolarizations (5 msec, 120 mV) to trigger release from calcium tail currents (Singer and Diamond, 2003; Singer et al., 2004) which led to a primarily synchronous release of neurotransmitter when recordings were performed in Ca^{2+}-ACSF (Figure 1A, grey trace). In contrast, depolarization of SACs in Sr^{2+}-ACSF induced a prolonged asynchronous release of GABA onto DSGCs (Figure 1A, red trace). During this prolonged release, individual asynchronous miniature IPSCs (a-mIPSCs) evoked from the depolarized SAC could be resolved (Figure 1B, see Methods). a-mIPSCs were considered quantal events because a-mIPSCs and mIPSCs displayed similar amplitudes and kinetics (Figure 1D,E).

To determine whether a pre- or post-synaptic change in SAC-DSGC synapses produces the asymmetry in inhibitory conductance, we analyzed the frequency and amplitude of a-mIPSCs evoked from SACs located on the null and preferred sides of DSGCs (e.g. Figure 2A). At p7-8, null and preferred side pairs displayed similar a-mIPSC frequencies and amplitudes (Figure 2B,C, n=5 DSGCs, 6 null SACs, 5 preferred SACs), consistent with the similar inhibitory currents observed at this point in development (Wei et al., 2011; Yonehara et al., 2011). By p13-14 the average a-mIPSC frequency was over 3 times greater for null side pairs than preferred side pairs (Figure 2B,C, n=5 DSGCs, 8 null SACs, 8 preferred SACs), matching the previously observed asymmetry in overall inhibitory conductance (Wei et al., 2011). Null side pairs also trended toward having larger a-mIPSC amplitudes at this age, but this difference was not significant (Figure 2B,C). Therefore, the asymmetry in inhibitory conductance emerges via a presynaptic mechanism at null side SAC-DSGC synapses, with postsynaptic mechanisms (e.g. increases in $GABA_AR$ expression per synapse) at most a minor contributor to the development of asymmetric inhibitory input.

Null and preferred side SACs exhibit similar paired pulse depression throughout development

The asymmetric increase in a-mIPSC frequency during development indicates that either null side SACs form more synapses with DSGCs or that synapses from null side SACs increase their probability of vesicle release during the second postnatal week. To distinguish between these possibilities, we performed paired pulse recordings with SAC-DSGC pairs in Ca^{2+}-ACSF (Figure 3A). Importantly, our paired pulse ratio altered inversely with external Ca^{2+} concentration, demonstrating reliability in our measure of relative vesicle release probability via tail currents (Singer et al., 2004) (Figure 3C, for each $[Ca^{2+}]$ in mM: 0.625 n=3 DSGCs, 7 pairs; 1.25 n=3 DSGCs, 6 pairs; 2.5 n=6 DSGCs, 14 pairs; 5.0 n=2 DSGCs, 5 pairs). Paired pulse recordings of SAC-DSGC pairs at the beginning and end of the second postnatal week showed the average paired pulse ratio did not differ between null and preferred side pairs at either age, or between pairs at different ages (Figure 3D, p7-8 n=4 DSGCs, 4 null SACs, 3 preferred SACs; p13-14 6 DSGCs, 12 null SACs, 5 preferred SACs). Thus the asymmetric increase in a-mIPSC frequency (Figure 2) is not due to an increase in vesicle release probability, but is rather a result of null side SACs forming more synapses onto DSGCs from p7-p14.

Null side SACs form synapses closer to the DSGC soma.

It has been suggested that null oriented SAC processes (Figure 4A, red shading) are more likely to form synapses with DSGCs than preferred oriented SAC processes, regardless of SAC somatic location relative to the DSGC (Briggman et al., 2011). This would lead to the following synaptic configuration: for null side pairs the null oriented SAC processes overlap extensively with the DSGC dendrites (form synapses at proximal and distal locations) while for preferred side pairs, the null oriented SAC processes only overlap, and thus only form synapses, with DSGC dendrites at very distal locations (Figure 4A). This proposed arrangement would result in increased dendritic filtering of synaptic events from preferred side SACs, prolonging the rise times of synaptic events when recording at the DSGC soma (Rall, 1967).

To test for this scenario physiologically, we analyzed the average a-mIPSC rise times for null and preferred side pairs at p13-14 (Figure 4B). To ensure the same overall degree of SAC-DSGC dendritic overlap between null and preferred side pairs, we statistically compared the rise times of null and preferred side SAC-DSGC pairs with inter-soma distances <100 μm. We found that the distribution of a-mIPSC rise times for preferred side pairs is shifted to higher values than the distribution for null side pairs (Figure 4C, n=5 DSGCs, 6 null SACs, 8 preferred SACs). This shift in the distribution is reflected in significantly longer average a-mIPSC rise times for preferred side pairs than null side pairs (Figure 4D). Furthermore, this effect was also present in Ca^{2+}-ACSF, where the average rise times for the initial IPSCs in the paired pulse protocol were longer for preferred side pairs than null side pairs (Figure 4E, n=10 DSGCs, 17 null SACs, 7 preferred SACs). Thus, our data is consistent with a model in which, by p13-14, SAC-DSGC synapses are primarily located at sites of overlap between DSGC dendrites and null oriented SAC processes. From our findings we conclude that during the second postnatal week, null oriented SAC processes form more synapses with DSGCs than preferred oriented SAC processes, establishing the asymmetry in inhibitory conductance required for direction selectivity.

Discussion

By comparing the properties of quantal events in DSGCs from null and preferred side SACs during the second postnatal week, we have found that quantal event frequency, but not amplitude, dramatically increases solely for null side SAC-DSGC pairs. We have also demonstrated that SAC-DSGC synapses are usually found at sites of overlap with null oriented SAC processes and all exhibit similar probabilities of release. Thus, we conclude that during development there is a specific increase in functional inhibitory synapse number from null oriented SAC processes to DSGCs. Our results provide the first unambiguous and physiological explanation for the development of the asymmetric inhibitory conductance required for direction selectivity in the mouse retina.

A model in which synapses are formed at sites of overlap between null oriented SAC processes and DSGC dendrites also provides an explanation for the lone preferred side SAC-DSGC pair with a high a-mIPSC frequency (Figure 2C, 20.2 Hz). This preferred side SAC was the only depolarized SAC located within 50 μm of a DSGC, allowing extensive overlap of its null oriented processes with the dendritic arbor of the DSGC, despite the preferred side somatic location. When we recorded from this same DSGC while depolarizing a preferred side SAC further away, the average a-mIPSC frequency dropped to 1.4 Hz (Figure 2C), as this more distant SAC had many fewer null oriented processes overlapping with the DSGC's dendrites.

The present study identifies synapse formation from null oriented processes as the driving force behind the development of retinal direction selectivity. However, how this specificity is achieved remains unresolved. SAC-DSGC connectivity is hypothesized to be hard-wired, relying on each of the four classes of ON-OFF DSGCs expressing a particular synaptogenic marker while complimentary markers are expressed on SAC processes oriented in the null direction (Elstrott and Feller, 2009). If different SAC processes do express different synaptogenic factors during a specified time in development, how each SAC robustly achieves this expression pattern remains to be determined. Interestingly, from p7-14 SAC processes grow extensively and develop varicosities (Zheng et al., 2004; Wei et al., 2011), the sites of neurotransmitter release (Famiglietti, 1991; Briggman et al., 2011). Analyzing the emergence and interactions of these structures with DSGC dendrites during development may provide insight into the preferential association of DSGCs with null oriented SAC processes. Thus, the retinal direction selective circuit will continue to enhance our understanding of the mechanisms underlying inhibitory circuit development.

References

Briggman KL, Helmstaedter M, Denk W (2011) Wiring specificity in the direction-selectivity circuit of the retina. Nature 471:183–188.

Elstrott J, Feller MB (2009) Vision and the establishment of direction-selectivity: a tale of two circuits. Current Opinion in Neurobiology 19:293–297.

Famiglietti EV (1991) Synaptic organization of starburst amacrine cells in rabbit retina: analysis of serial thin sections by electron microscopy and graphic reconstruction. J Comp Neurol 309:40–70.

Fried SI, Münch TA, Werblin FS (2002) Mechanisms and circuitry underlying directional selectivity in the retina. Nature 420:411–414.

Goda Y, Stevens CF (1994) Two components of transmitter release at a central synapse. Proc Natl Acad Sci USA 91:12942–12946.

Gong S, Zheng C, Doughty ML, Losos K, Didkovsky N, Schambra UB, Nowak NJ, Joyner A, Leblanc G, Hatten ME, Heintz N (2003) A gene expression atlas of the central nervous system based on bacterial artificial chromosomes. Nature 425:917–925.

Hausselt SE, Euler T, Detwiler PB, Denk W (2007) A dendrite-autonomous mechanism for direction selectivity in retinal starburst amacrine cells. Plos Biol 5:e185.

Huberman AD, Wei W, Elstrott J, Stafford BK, Feller MB, Barres BA (2009) Genetic identification of an On-Off direction-selective retinal ganglion cell subtype reveals a layer-specific subcortical map of posterior motion. Neuron 62:327–334.

Keeley PW, Whitney IE, Raven MA, Reese BE (2007) Dendritic spread and functional coverage of starburst amacrine cells. J Comp Neurol 505:539–546.

Lee S, Kim K, Zhou ZJ (2010) Role of ACh-GABA cotransmission in detecting image motion and motion direction. Neuron 68:1159–1172.

Miller RF, Bloomfield SA (1983) Electroanatomy of a unique amacrine cell in the rabbit retina. Proc Natl Acad Sci USA 80:3069–3073.

Park SJH, Kim IJ, Looger LL, Demb JB, Borghuis BG (2014) Excitatory Synaptic Inputs to Mouse On-Off Direction-Selective Retinal Ganglion Cells Lack Direction Tuning. J Neurosci 34:3976–3981.

Rall W (1967) Distinguishing theoretical synaptic potentials computed for different soma-dendritic distributions of synaptic input. J Neurophysiol 30:1138–1168

Rivlin-Etzion M, Zhou K, Wei W, Elstrott J, Nguyen PL, Barres BA, Huberman AD, Feller MB (2011) Transgenic mice reveal unexpected diversity of on-off direction-selective retinal ganglion cell subtypes and brain structures involved in motion processing. J Neurosci 31:8760–8769.

Singer JH, Diamond JS (2003) Sustained Ca2+ entry elicits transient postsynaptic currents at a retinal ribbon synapse. J Neurosci 23:10923–10933.

Singer JH, Lassová L, Vardi N, Diamond JS (2004) Coordinated multivesicular release at a mammalian ribbon synapse. Nat Neurosci 7:826–833.

Taylor WR, Vaney DI (2002) Diverse synaptic mechanisms generate direction selectivity in the rabbit retina. J Neurosci 22:7712–7720.

Vlasits AL, Bos R, Morrie RD, Fortuny C, Flannery JG, Feller MB, Rivlin-Etzion M (2014) Visual stimulation switches the polarity of excitatory input to starburst amacrine cells. Neuron 83:1172–1184.

Wei W, Elstrott J, Feller MB (2010) Two-photon targeted recording of GFP-expressing neurons for light responses and live-cell imaging in the mouse retina. Nat Protoc 5:1347–1352.

Wei W, Hamby AM, Zhou K, Feller MB (2011) Development of asymmetric inhibition underlying direction selectivity in the retina. Nature 469:402–406.

Xu-Friedman MA, Regehr WG (1999) Presynaptic strontium dynamics and synaptic transmission. Biophys J 76:2029–2042.

Xu-Friedman MA, Regehr WG (2000) Probing fundamental aspects of synaptic transmission with strontium. J Neurosci 20:4414–4422.

Yonehara K, Balint K, Noda M, Nagel G, Bamberg E, Roska B (2011) Spatially asymmetric reorganization of inhibition establishes a motion-sensitive circuit. Nature 469:407–410.

Yonehara K, Farrow K, Ghanem A, Hillier D, Balint K, Teixeira M, Jüttner J, Noda M, Neve RL, Conzelmann K-K, Roska B (2013) The first stage of cardinal direction selectivity is localized to the dendrites of retinal ganglion cells. Neuron 79:1078–1085.

Yoshida K, Watanabe D, Ishikane H, Tachibana M, Pastan I, Nakanishi S (2001) A key role of starburst amacrine cells in originating retinal directional selectivity and optokinetic eye movement. Neuron 30:771–780.

Zheng J-J, Lee S, Zhou ZJ (2004) A Developmental Switch in the Excitability and Function of the Starburst Network in the Mammalian Retina. Neuron 44:851–864

Zhou ZJ (1998) Direct participation of starburst amacrine cells in spontaneous rhythmic activities in the developing mammalian retina. J Neurosci 18:4155–4165.

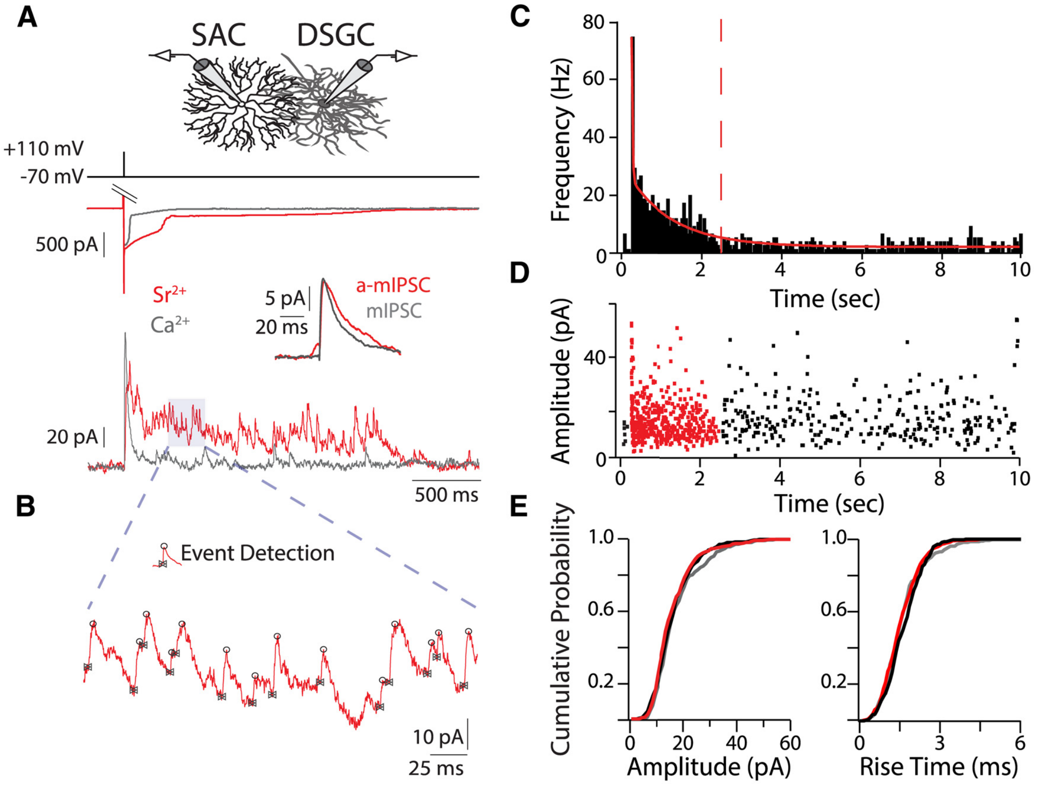

Figure 1 Isolation of quantal events from single starburst amacrine cells.

A, Voltage clamp recordings in calcium (grey) and strontium (red) from two different SAC (top traces)-DSGC (bottom traces) pairs show prolonged asynchronous neurotransmitter release from SACs in Sr2+-ACSF upon tail current activation. DSGC is held at 0 mV. Inset: average evoked asynchronous miniature IPSC (a-mIPSC) in Sr2+-ACSF and average mIPSC in Ca2+-ACSF. **B**, Example of manual event detection with Taro Tools. IPSC events are marked at their onset (bowties) and peak (circles). **C**, Frequency histogram (50 ms bins) of IPSC events in Sr2+-ACSF for SAC-DSGC pair in A. Stimulus occurred at 250 ms. Solid red line is a double exponential fit to the histogram; dashed red line demarcates a-mIPSCs from mIPSCs (see Methods). Note: C and D display the full 10 seconds of the sweeps, unlike A. **D**, Amplitude of IPSCs in Sr2+-ACSF for SAC-DSGC pair in A. Red events are a-mIPSCs evoked by a single SAC. Black events are mIPSCs from all SACs. **E**, Cumulative probability distributions of amplitudes and rise times for a-mIPSCs (red) and mIPSCs (black) in Sr2+-ACSF and mIPSCs (grey) in Ca2+-ACSF for the SAC-DSGC pairs in A.

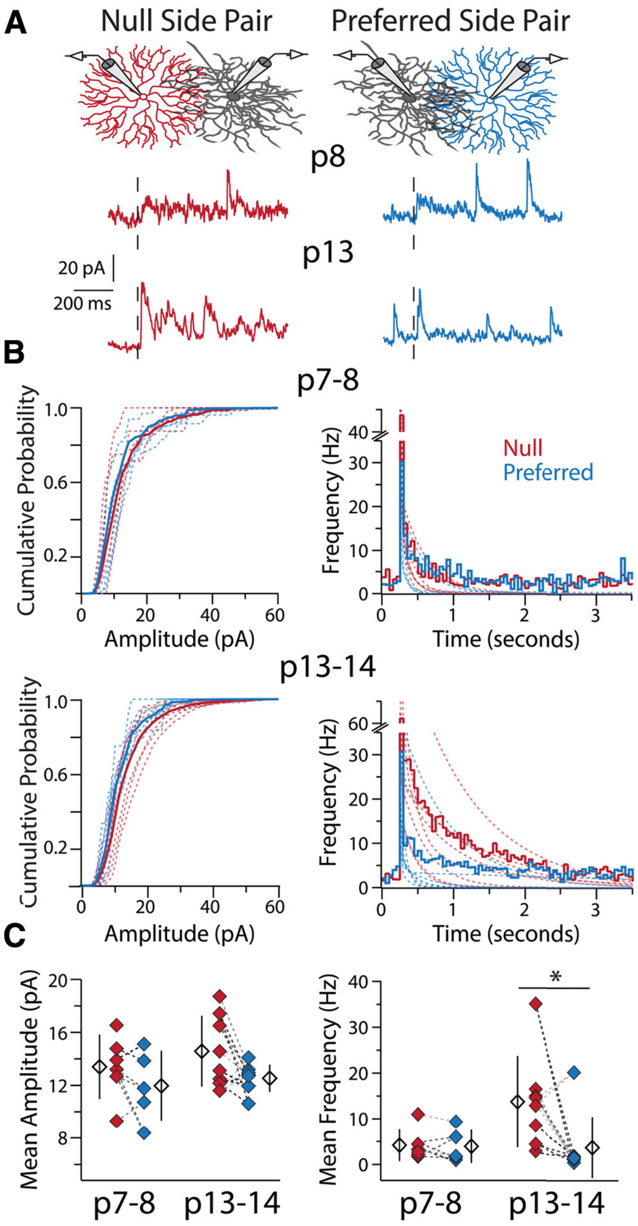

Figure 2. Pre-synaptic mechanisms underlie the changes in SAC-DSGC connectivity during development.

A, Example recordings in Sr^{2+}-ACSF from two DSGCs at different ages upon stimulation (black dashed line) of a null and a preferred side SAC connected to each DSGC. Stimulation of the null side SAC at p13 produces a greater frequency of a-mIPSCs. **B,** Average cumulative probability distributions of a-mIPSC amplitudes (left) and average peristimulus frequency histograms (right) for null and preferred side pairs at p7-8 (top) and p13-14 (bottom). Dashed lines are cumulative probability distributions of a-mIPSC amplitudes or double exponential fits to frequency histograms (as per Figure 1C) for individual pairs. **C,** Mean a-mIPSC amplitude (left) and mean a-mIPSC frequency (right, see Methods) for each SAC-DSGC pair. Amplitude and frequency measures recorded in the same DSGC for preferred and null side pairs are connected via dashed lines of the same color. Average a-mIPSC amplitudes are not significantly different between groups (one-way ANOVA, $p = 0.18$, df = 26) while a-mIPSC frequency is significantly different at p13-14, but not p7-8, between null and preferred side pairs (Kruskal-Wallis one-way ANOVA $p = 0.006$, df = 3, Dunn-Holland-Wolfe post-hoc $p = 0.007$ (Null p13-14 vs Pref p13-14)). Note, the one preferred side SAC-DSGC pair with a high a-mIPSC frequency was the only SAC-DSGC pair in this study with an inter-soma distance of <50 µm (see Discussion). Open diamonds are population averages, error bars show SD, and * highlights significant difference between groups for this and all subsequent figures.

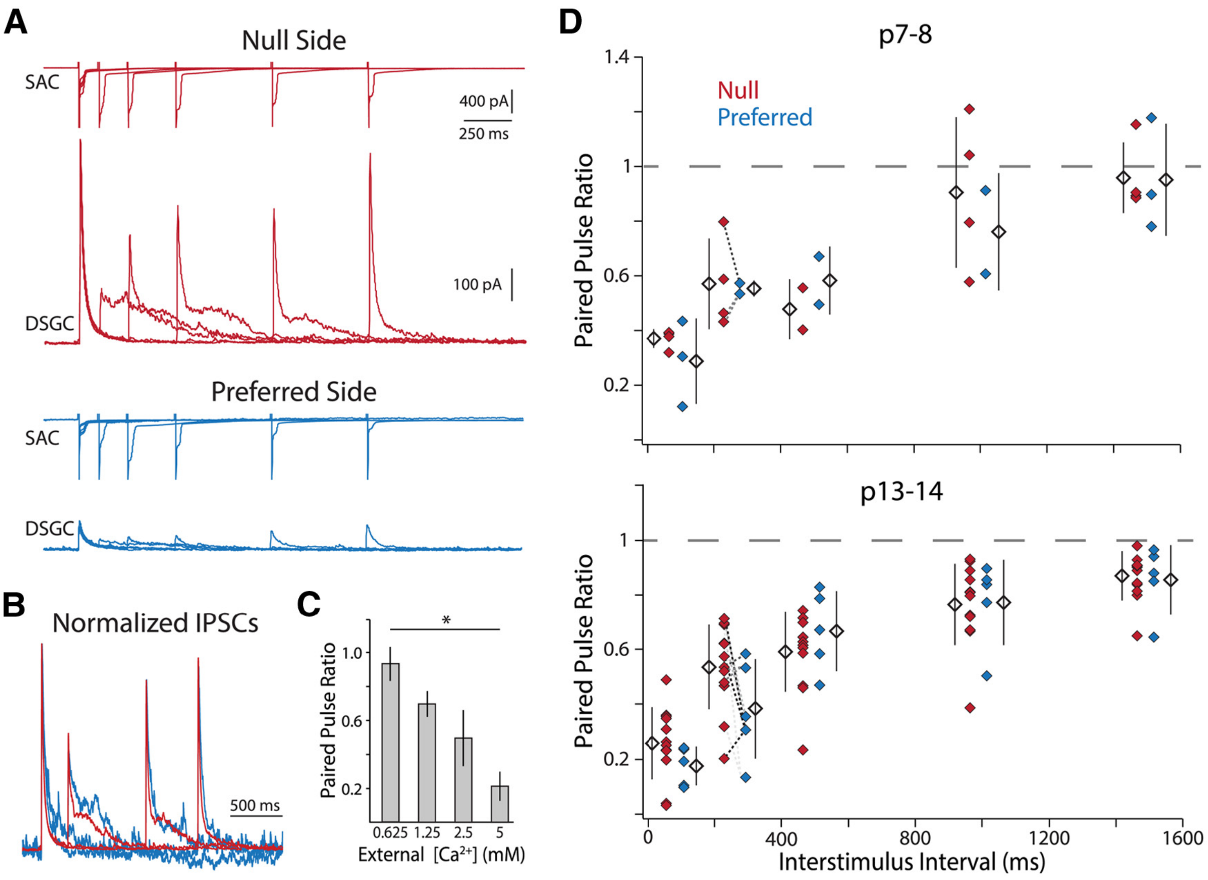

Figure 3. Null and preferred side SAC-DSGC synapses display similar paired pulse depression throughout development.

A, Example traces from paired pulse protocol. Top traces of each color show tail currents elicited from a null (red) and a preferred side (blue) p14 SAC at varying inter-stimulus time intervals (100, 250, 500, 1000, 1500 ms) in Ca^{2+}-ACSF. Bottom traces show responses of their shared postsynaptic DSGC held at 0 mV. **B,** IPSCs evoked from preferred and null side SACs display the same kinetics. Peak normalized traces from (A) for 250, 1000, and 1500 ms inter-stimulus intervals. **C,** The average paired pulse ratio for p13-14 SAC-DSGC pairs decreases as external Ca^{2+} increases for the 250 ms inter-stimulus interval. All groups are significantly different from each other (one way ANOVA, $p = 2.2x10^{-9}$, df = 35, Tukey-Kramer post-hoc, $p<0.05$). **D,** Paired pulse ratio at the beginning and end of the second postnatal week as a function of inter-stimulus interval. Data points for the 250 ms inter-stimulus interval recorded in the same DSGC are connected via dashed lines of the same color.

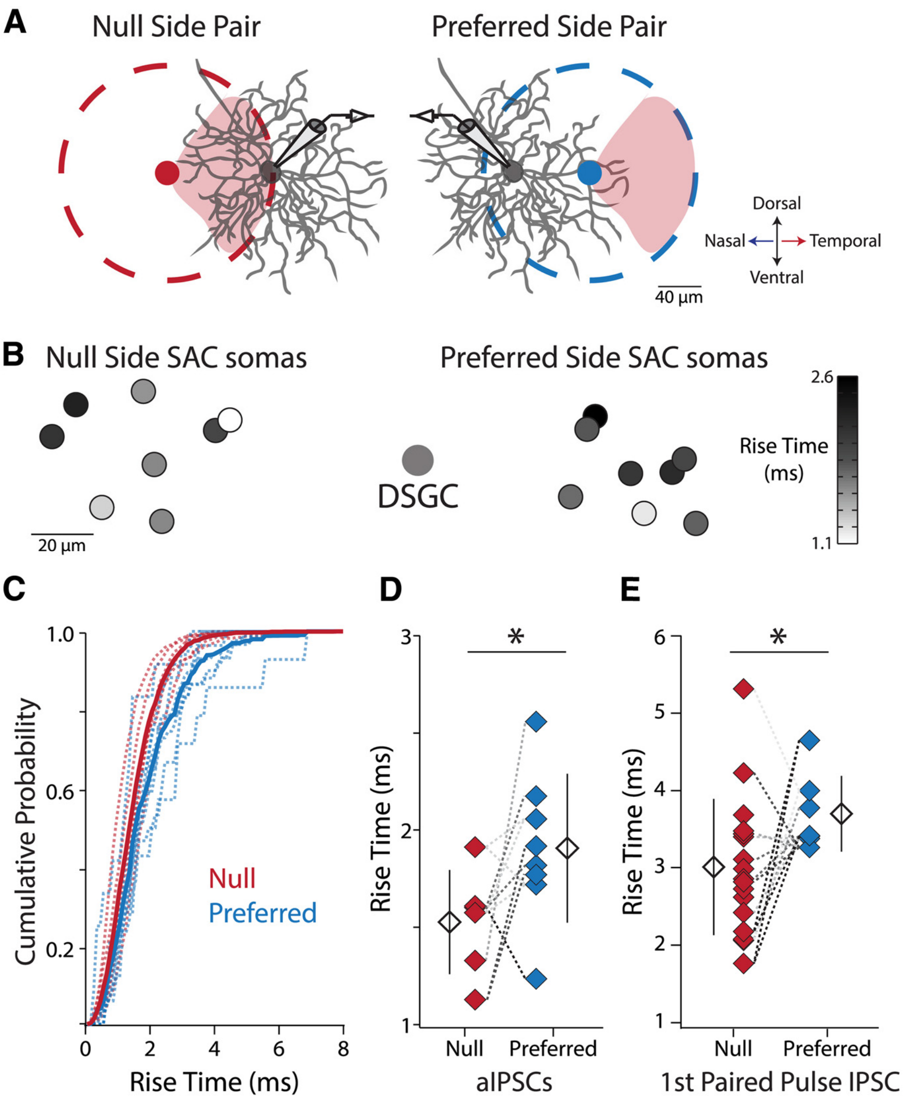

Figure 4. Synapses from null side SACs are located closer to the DSGC soma than synapses from preferred side SACs at p13-14.

A, Model in which SAC-DSGC synapses are located where the DSGC's dendrites overlap with the portion of the SAC dendritic arbor (dashed circles) oriented in the DSGC's null direction (red shading, temporal retinal direction for Drd4-GFP$^+$ cells) (Briggman et al., 2011). The null oriented portion of the null side SAC's dendritic arbor overlaps extensively with the DSGC's dendrites at both proximal and distal locations. In contrast, the null oriented portion of the preferred side SAC's dendritic arbor only overlaps with DSGC dendrites at very distal locations. Thus, upon depolarization of the preferred side SAC signals from synaptic events will experience greater dendritic filtering when recording at the DSGC soma. All diagrams are to scale based on average dendritic arbor size at p14 (Wei et al., 2011) but note that DRD4-GFP$^+$ cells often have asymmetric dendritic fields (Rivlin-Etzion et al., 2011). Null and preferred side SAC somata are located 89 and 70 µm away from the DSGC soma respectively, the average inter-soma distance for the two groups at p13-14. **B,** Heat map of average a-mIPSC rise times. Small circles are SAC soma locations relative to the DSGC soma. Null side SACs close to the DSGC have the fastest rise times, while preferred side SACs the same distance away have slower rise times. **C,** Average cumulative probability distributions of 10-90% a-mIPSC rise times for null side and preferred side SAC-DSGC pairs with inter-soma distances <100 µm (6 null side pairs, 8 preferred side pairs). Dashed lines are cumulative probability distributions for individual pairs. **D,** Average 10-90% a-mIPSC rise times for SAC-DSGC pairs in (C) (Welch's t-test, p=0.049, df =11.98).**E,** Average 10-90% IPSC rise times for SAC-DSGC pairs for the initial IPSCs in the paired pulse protocol (Figure 2A) (Welch's t-test, p=0.025, df = 19.5). Rise times measured from the same DSGC are connected via dashed lines of the same color for D and E.

Chapter III

A Role for Synaptic Input Distribution in a Dendritic Computation of Motion Direction in the Retina

This chapter is a full reprint of Vlasits et al, *Neuron* (2016), in which I was the secondary author. This work is included with permission from all authors.

Relevant Publication:

Vlasits, A. L., Morrie, R. D., Tran-Van-Minh, A., Bleckert, A., Gainer, C. F., DiGregorio, D. A., & Feller, M. B. (2016). A Role for Synaptic Input Distribution in a Dendritic Computation of Motion Direction in the Retina. *Neuron*, *89*(6), 1317–1330.

Author contributions

RDM, ATVM, and AB contributed substantially and equally to this work. ALV and MBF designed the receptive field experiments. ALV performed receptive field mapping and analysis. ALV, DD, ATVM and MBF designed uncaging experiments. ALV and ATVM performed uncaging experiments. ALV analyzed uncaging experiments. *RDM*, ALV and CG performed Ca^{2+} imaging. *RDM* and ALV designed and analyzed Ca^{2+} imaging. AB designed, performed, and analyzed the PSD95 experiments. AB and ALV performed comparison of output sites, PSD95 and uncaging data. ATVM and DD created the starburst cell simulation. All authors wrote the manuscript.

Summary

The starburst amacrine cell in the mouse retina presents an opportunity to examine the precise role of sensory input location on neuronal computations. Using visual receptive field mapping, glutamate uncaging, two-photon Ca^{2+} imaging, and genetic labeling of putative synapses, we identify a unique arrangement of excitatory inputs and neurotransmitter release sites on starburst amacrine cell dendrites: the excitatory input distribution is skewed away from the release sites. By comparing computational simulations with Ca^{2+} transients recorded near release sites, we show that this anatomical arrangement of inputs and outputs supports a dendritic mechanism for computing motion direction. Direction selective Ca^{2+} transients persist in the presence of a GABA-A receptor antagonist, though the directional tuning is reduced. These results indicate a synergistic interaction between dendritic and circuit mechanisms for generating direction selectivity in the starburst amacrine cell.

Introduction

Starburst amacrine cells (SACs) are axonless GABAergic interneurons, whose release sites are located in the distal tips of their processes. SACs play a critical in the computations of direction selectivity by providing asymmetric inhibition onto direction selective ganglion cells (DSGCs), which fire selectively to motion in one direction and very little to motion in the other direction (Amthor et al., 2002; Fried et al., 2002, 2005; Vlasits et al., 2014; Yoshida et al., 2001). The mechanism of direction selective inhibition from SACs has been widely studied. DSGCs receive greater inhibitory input from SACs located on their "null side" (Fried et al., 2002; Wei et al., 2011; Yonehara et al., 2011) due to selective wiring of inhibitory synapses from SAC dendrites pointed in the DSGC's null direction (Beier et al., 2013; Briggman et al., 2011; Morrie and Feller, 2015). But wiring cannot by itself explain direction selective inhibition, because DSGCs exhibit DS even when moving stimuli are restricted to a small region of the receptive field (Fried et al., 2002). Therefore, GABA release from SAC dendrites must also be DS. Indeed, individual SAC dendrites prefer motion in different directions. Specifically, Ca^{2+} transients in SAC dendrites are larger in response to motion outward from the soma to the end of the dendrite compared to motion inward from the end of the dendrite to the soma (Euler et al., 2002; Hausselt et al., 2007; Lee and Zhou, 2006; Yonehara et al., 2013). SACs receive excitatory input from bipolar cells, glutamatergic interneurons that are the major feed-forward circuit component in the retina. But bipolar cell axon terminals exhibit neither DS Ca^{2+} transients (Chen et al., 2014; Yonehara et al., 2013) nor DS glutamate release onto DSGCs (Park et al., 2014). This suggests that the first computation of motion direction takes place in SAC dendrites.

Currently, there are three hypotheses of how direction selective calcium signals arise in SAC dendrites. The first hypothesis is that integration of spatially-offset bipolar cell inputs with different release kinetics produces DS (Kim et al., 2014). The second is that circuit-level reciprocal lateral inhibition between SACs creates a preference for outward motion in the absence of dendrite-intrinsic asymmetries (Lee and Zhou, 2006; Münch and Werblin, 2006). The third is a dendrite-intrinsic mechanism, which proposes that passive properties of SAC dendrites, combined with non-linear conductances, are capable of computing motion direction (see Vaney et al., 2012 for review). However, the precise dendritic computations would depend on the arrangement of input and output sites. Outputs (GABA release sites) are located in the distal 1/3 of the SAC dendrite, where widenings called varicosities contact DSGCs (Briggman et al., 2011; Famiglietti, 1991). On the other hand, different distributions of excitatory inputs have been proposed in the SAC dendritic arbor: either inputs cover the entire arbor (Famiglietti, 1991; Koizumi et al., 2011) or there are fewer inputs in the distal dendrites (Greene et al., 2016; Kim et al., 2014).

Here, we determined the dendritic locations of excitatory synaptic inputs to elucidate the dendrite-intrinsic mechanisms that play a role in SAC computations. We utilized several methods to examine the excitatory input distribution: visual receptive field mapping, localized glutamate uncaging, and labeling of the PSD95 distribution. In addition, we modeled the SAC to explore the effect of changing the input distribution on the voltage responses in different regions of the dendrite. Finally, we used two-photon Ca^{2+} imaging of varicosities to determine the relative contributions of excitation and lateral inhibition to the direction selective computation in SAC dendrites.

Results

The starburst amacrine cell excitatory receptive field is excluded from distal dendrites

A neuron's input distribution relative to its outputs can make a difference in the nature of the dendrite-intrinsic computation the cell can perform. If inputs and outputs are comingled, *local* dendritic computations would dominate. On the other hand, if inputs are skewed or segregated away from output sites, *global* computations within each dendrite would dominate (**Fig. 1A**). Modeling studies thus far have assumed inputs are near to output sites (Taylor and Smith, 2012; Tukker et al., 2004), and achieving DS in this case requires strong nonlinear mechanisms.

To determine the functional map of excitatory inputs onto SAC dendrites in the retina, we first measured the excitatory receptive field using visual stimulation of the retina with small spots (25 μm diameter) whose size was chosen to roughly match the receptive field size of cone bipolar cells (Berntson and Taylor, 2000) (**Fig 1B).** We performed voltage clamp recordings from SACs to measure light-evoked excitatory currents (**Fig. 1C**) and quantified the charge transfer as a function of the position of the stimulation spot relative to the dendritic radius. We observed a decrease in charge transfer as spots were presented further from the soma, with spots centered at ≥74±13% of the dendritic radius producing <5% of the maximum charge transfer recorded in the cell (**Fig. 1D-E**, n = 15 cells). On the other hand, we did not observe differences in the spot response kinetics at different locations on the dendritic tree, suggesting that phasic vs. sustained bipolar cell release kinetics may not play a role in generating DS in On-SACs (**Fig. S1**; see **Discussion** and Kim et al., 2014). We repeated our receptive field measurements using 24 μm wide ring stimuli to stimulate all of the SAC dendrites at a certain radius on the arbor at once (**Fig. 1F**). Similar to the stimulation with small spots of light, the charge transfer in response to rings decreased to <5% of the maximum response with rings centered at ≥77±10% (average±S.D. for 6 cells) of the maximum dendritic radius (**Fig. 1I**). In addition, during stimulation outside of the dendritic field we observed a decrease in the tonic excitatory current that coincided with an inhibitory current; the inhibitory receptive field extended beyond the excitatory receptive field (**Fig. S1**). Thus, based on ring and spot stimulation, the excitatory receptive field appears to exclude the most distal dendrites. So far, we have determined the excitatory receptive field using voltage clamp recordings from the soma, but SACs are thought to release neurotransmitter from varicosities in their distal dendrites. To determine the impact of proximal vs. distal visual stimulation at SAC release sites, we performed two-photon imaging of Ca^{2+} transients from varicosities in SACs filled with OGB-1 (**Fig. 2A**). Consistent with our voltage clamp recordings (**Fig. 1**), we observed larger Ca^{2+} transients in varicosities in response to spots centered at proximal compared to distal locations, despite the distal spots' closer proximity to the varicosities being imaged (**Fig. 2B-E**). Together, these findings suggest that the excitatory receptive field does not include distal regions of the dendrites, but nevertheless has a strong influence on the Ca^{2+} concentration there.

Glutamate uncaging reveals absence of excitatory synapses in distal dendrites

To directly characterize the distribution of excitatory inputs on SAC dendrites, we used 2-photon fluorescence imaging, glutamate uncaging by single-photon photolysis of MNI-glutamate (2 mM, bath-applied) (DiGregorio et al., 2007), and somatic voltage clamp recordings (**Fig. 3A-B**). Locations along the dendrite where uncaging-evoked EPSCs were detected were assumed to result from the presence of AMPAR clusters (Abrahamsson et al., 2012). We selected uncaging-evoked EPSCs with locally-maximal amplitudes as the location of putative postsynaptic sites (**Fig. S2**). In 20 dendrites from 15 cells, the majority of putative synapses were in the more proximal region of the dendritic tree (**Fig. 3C-D)**, resulting in an excitatory receptive field that extended to 69±9% of the dendritic field, similar to that determined using visual stimulation (**Fig. 3E**). We confirmed that the lack of responses in distal dendritic regions was not due to alterations in the uncaging resolution or cable filtering (**Fig. S3**), and therefore not below the sensitivity of our measurements. Taken together, these results are consistent with the conclusion that synaptic inputs are absent from the outer third of the SAC dendritic tree.

PSD95 puncta are skewed away from output sites

We next used an anatomical approach to confirm our functional estimates of the distribution of glutamate receptors in SAC dendrites. Retinas were biolistically transfected with plasmids encoding post-synaptic density 95 fused to YFP (PSD95-YFP) to label putative sites of glutamatergic input and tdTomato for identification of transfected SACs (**Fig. 4A, C**). We then took confocal images of SAC processes that did not overlap with other labeled cells and identified the locations of PSD95-YFP puncta (**Fig. 4B**; see Methods and **Fig. S4)**. We found that PSD95-YFP puncta were at the highest density near the soma, while the density decreased more distally with a profile similar to the putative postsynaptic sites detected with uncaging (**Fig. 4D**, n = 8 cells from 5 retinas).

To establish the locations of inputs relative to outputs, we plotted putative postsynaptic locations determined from uncaging or PSD95 labeling and release sites. We took advantage of data from a previous study that used serial block-face electron microscopy (SBEM) to characterize the dendritic locations of On and Off SAC contacts with DSGCs (Briggman et al., 2011). We found that synaptic input and output distributions were significantly skewed away from one another (**Fig. 4E**; $p<0.05$, Wilcoxon Rank test). Similarly, only 25% of the output sites overlapped with the excitatory receptive field predicted from uncaging (**Fig. 4E**, orange dotted line is the mean radial distance of the last postsynaptic site predicted from uncaging). This arrangement of inputs and outputs suggests that computations in the SAC most likely rely on a global mechanism of dendritic integration (**Fig. 1A**), and may underlie a dendrite-intrinsic DS computation.

Skewed synaptic input distributions enhance DS of simulated dendritic voltage

How does the skewed distribution of inputs contribute to direction selectivity of SAC outputs? To address this question, we turned to a computer simulation based on a passive "ball and stick" representation of the SAC dendrite (**Fig. 5A, D** and **Fig. S5**). The dendritic morphology was based on the average lengths of dendritic branches measured from SACs imaged by 2-photon microscopy (data not shown). We compared the dendritic voltage responses produced by several different input distributions: the skewed distribution determined by uncaging (**Fig. 5A**), the higher density skewed distribution determined by PSD95 labeling (**Fig. S5A**), a regular distribution covering the entire dendritic length (**Fig. 5D**, **Fig. S5D**), and a regular distribution covering the proximal 71% of the dendritic length, which is the extent of the excitatory receptive field predicted from uncaging (calculated from **Fig. 3C**). These different distributions allowed us to assess separately the impact of skewed synapse distributions and the effect of the absence of any inputs to the distal region of the SAC.

We simulated voltage along the dendrite during outward and inward stimulation of inputs at an apparent velocity of 500 μm/s and report the results both at specific sites (**Fig. 5B, E**) as well as continuously along the entire dendrite (**Fig. 5C, F**). To quantify the strength of DS, we computed the difference in peak depolarization between outward and inward stimulation (**Fig. 5H**, **J**). There were three primary predictions from the model. First, we found that input distributions restricted to the proximal 71% of the dendrite (whether skewed distributions or regular distributions) produced the strongest DS for outward motion. Second, input distributions restricted to the proximal 71% of the dendrites also led to lower DS values for varicosities located within the receptive field of the SAC process compared to varicosities located outside the receptive field. Third, the degree of DS was constant over a long section at the end of the dendrite (>30 μm for the uncaging distribution; >45 μm for the PSD95 distribution) only for input distributions restricted to the proximal 71% of the dendrites. The uniform depolarization along the distal dendrite is the result of inputs localized to the proximal portion of the dendritic tree acting in combination with the sealed cable effect of the dendrite (see **Discussion**). In contrast, stimulating a regular synapse distribution covering the whole dendrite produced DS values that became steadily stronger with increasing distance from the soma, although DS remained much weaker than for input distributions restricted to the proximal 71%, even at the most distal sites (**Fig. 5G-J)**. These results were consistent at a faster velocity of stimulation (1000 μm/s, data not shown). Our passive model simulations suggest that a proximal-weighted input distribution promotes a prominent direction selective depolarization in the distal dendritic tips, where the majority of release sites are located.

DS of varicosities depends on varicosity location

Our simulations predict that varicosities in the distal region of the dendrite will have similar strength DS, in contrast to weaker DS at more proximal release sites (**Fig. 5**). To test this prediction directly, we performed 2-photon Ca^{2+} imaging of varicosities in SACs while stimulating the retina with moving squares of light (25 μm^2). Note, there are two important differences from previous measurements that used Ca^{2+} imaging to assess DS in SAC dendrites (Euler et al., 2002; Hausselt et al., 2007; Lee and Zhou, 2006; Yonehara et al., 2013). First, we stimulated the retina with small moving squares, rather than circular gratings or stimuli larger than the size of the SAC dendritic field, to observe single motion-evoked events and isolate the contribution from a single process. Second, we restricted the moving square to 75% of the dendritic radius to optimally stimulate the excitatory receptive field (**Fig. 6A**). Similar to previous studies, we observed distal varicosities that responded with Ca^{2+} transients that were larger for outward compared to inward motion (**Fig. 6B, C**) and a large variance in the DS across varicosities (Euler et al., 2002; Hausselt et al., 2007; Lee and Zhou, 2006; Yonehara et al., 2013) (**Fig. 6F-G**). We believe this variance to be due to the complex dendritic structure being stimulated (**Fig. S6**) or to off-axis tuning of varicosities, as described previously (Euler et al., 2002; Yonehara et al., 2013).

Next, we examined how the DS of a varicosity related to its location along the SAC dendrite. Because our model predicts strong DS of varicosities over the last ~30% of the SAC dendrite, we split the imaged varicosities into two groups using the average path length to the last synapse predicted from uncaging (71% of the dendritic path from the soma, calculated from **Fig. 3C**). We found that varicosities located distal to the last synapse predicted from uncaging (examples in **Fig. 6B, C**) were significantly more direction selective than varicosities located within the region where synapses were detected (examples in **Fig. 6D, E**, summary in **Fig. 6F, G**; mean DSI = 0.34±0.23 for 25 varicosities outside receptive field and 0.11±0.18 for 8 varicosities inside receptive field; Student's t-test: $p<0.05$). These results demonstrate that the DSI of varicosity Ca^{2+} transients depends on location in a manner consistent with the voltage responses predicted by a purely passive dendrite model.

Excitatory and inhibitory inputs cooperate to enhance DS

While we have demonstrated that the excitatory input distribution can enable a dendrite-intrinsic computation of motion direction, some studies have proposed that lateral inhibition from other SACs is the origin of DS in SAC dendrites (Lee and Zhou, 2006; Münch and Werblin, 2006). Note, lateral inhibition between SACs in adult mice is mostly provided by SAC processes oriented in antiparallel directions (**Fig. S7**, Kostadinov and Sanes, 2015; Lee and Zhou, 2006). Given this geometry, inward light stimulation for the SAC being recorded would correspond to outward motion for neighboring presynaptic SACs (**Fig. S7**). Hence, the dendrite-intrinsic computation described above would maximally drive GABA release from the neighboring SAC onto the SAC being recorded, enabling lateral inhibition, which we predict will enhance DS by suppressing responses to inward light stimulation.

To test this model, we conducted two manipulations. First we compared DS in distal varicosities in response to motion stimuli that ended at 75% of the dendritic radius (as in **Fig. 6**) to those that ended at 100% of the dendritic radius, which is likely to induce a more robust activation of inhibitory inputs because the stimulus travels over a larger portion of the neighboring SACs' dendrites **(Fig. S7**). Indeed, we observed larger DSIs in response to 100% stimulation compared to 75% stimulation (**Fig. 7B, E**; paired t-test: $p<0.05$ [Bonferroni corrected], n=22 varicosities). This difference is due primarily to a reduction in Ca^{2+} transients evoked by 100% inward stimulation (**Fig. 7D**).

Second, we repeated these experiments in the $GABA_A$ receptor antagonist, gabazine (5 μM). Though there was an overall reduction in DSI across varicosities (**Fig. 7E**; repeated measures ANOVA: $p<0.05$ for control vs. gabazine groups), the majority of varicosities still exhibited larger responses to outward motion compared to inward motion (e.g. **Fig. 7C**). The weakened DSI in the absence of GABAergic inhibition is primarily attributable to an increase in the response to inward motion (**Fig. 7D**), suggesting that in control conditions inhibition is more pronounced during inward stimulation. Notably, in the absence of GABAergic network interactions, the enhanced DS observed for 100% stimulation over 75% was eliminated (**Fig. 7F**; mean $\Delta DSI_{control} = 0.16\pm0.1$; $\Delta DSI_{gabazine} = 0.02\pm0.23$). Thus, both excitatory and inhibitory inputs cooperate to compute motion direction in SAC dendrites, and both are greatly enhanced by the differential dendritic distributions of inputs and outputs. Taken together, our results suggest that DS is achieved through a dendrite-intrinsic computation, which determines the outward preference as well as the circuit-level lateral inhibition of the response to inward motion (**Fig. S7**).

Discussion

Directly linking neural connectivity to neuronal computations is a major goal of contemporary neuroscience. We studied the relationship between excitatory input locations and the motion direction computation that SACs perform. We found that the excitatory inputs are localized to the proximal two-thirds of the dendritic tree, mostly segregated from output sites, and that their distribution can determine the region of the dendrite where varicosities are direction selective. This differential distribution enhances the mechanisms influencing DS; both the intrinsic dendritic mechanism and the lateral inhibition mechanism. These results allowed us to determine the relative contributions from dendrite-intrinsic and circuit-level mechanisms to DS in SAC dendrites. Our findings highlight the critical importance of synaptic input placement and distribution within the dendrite in determining the types of neuronal computations performed.

Excitatory inputs to starburst amacrine cells

We used several approaches to demonstrate that the excitatory input distribution is mostly separated from the varicosity-rich distal dendrites. We observed this distribution in three ways: as a restricted visual receptive field using either voltage clamp recordings from the soma (**Fig. 1**) or two-photon Ca^{2+} imaging in distal processes (**Fig. 2**), as a paucity of synapses in distal dendrites detected with glutamate uncaging (**Fig. 3**), and as a decreased density of PSD95-YFP expression in distal dendrites (**Fig. 4**). These findings are consistent with two SBEM studies that found fewer bipolar cell contacts in the most distal dendrites in both On- and Off-layer SACs (Greene et al., 2016; Kim et al., 2014).

Our results indicate that there may be a different distribution of glutamate receptors in mice than in rabbit, where several studies determined that excitatory inputs are present throughout the entire SAC dendritic tree. These studies also used a variety of methods, including visual receptive field mapping with ring stimuli and voltage clamp recordings (Lee and Zhou, 2006), electron microscopy (Famiglietti, 1991), and PSD95-GFP labeling (Koizumi et al., 2011). Hence, it appears that a different combination of excitatory and inhibitory distributions may account for DS in rabbit.

Mechanisms of dendritic integration in starburst amacrine cell dendrites

Overall, our findings suggest that the distribution of excitatory inputs in SACs can produce a dendrite-intrinsic DS response, with outward motion producing a larger depolarization in distal varicosities compared to inward motion (**Fig. 5-6**). We found that DS was strongest for varicosities located outside of the excitatory receptive field and that more proximal varicosities are less direction selective (**Fig. 6F,G**). Two properties of SAC dendrites are the basis of this effect: the high input impedance of narrow diameter dendrites and the sealed-end of the distal dendritic compartment, which retards current flow (the "end effect", see Rall, 1964, 1967).

High input impedance of narrow diameter dendrites contributes to DS in the following way. In somatic recordings of uncaging-evoked currents, we observed a tendency of the rise time to increase and the amplitude to decrease with increasing distance along the dendrite (**Fig. S2**), although our simulations suggest that the filtering-induced reduction in amplitude is similar for inputs placed 85 or 150 μm from the soma (**Fig. S3**). Thus, it is highly unlikely that the decreased probability of detecting events in distal dendrites resulted from dendritic filtering. The narrow diameter of the dendrite (<0.3 μm) is likely to account for this filtering over the short distances in SAC dendrites (<150 μm). Numerical simulations indicate that dendritic filtering is critical for producing the slow-rising and -decaying EPSPs in varicosities during stimulation of inputs proximal to the soma (**Fig. 5**). This filtering produces the sensitivity to outward stimulation, in which larger peak depolarizations are achieved because the proximal inputs, which are distant from release sites, produce slow depolarizations in the release compartments. Outward DS results from activation of synapses progressively closer to release sites, which produces a depolarization that summates on previous EPSPs more distant from release sites, thus achieving a larger absolute peak depolarization, as opposed to stimulation in the inward direction (Rall, 1964). This effect is maximized when the output sites are not intermingled with inputs within the same compartment (**Fig. 5D, E, I**). If they were intermingled, the voltage drive of inputs close to the release sites dominates, thereby masking any slow accumulation of depolarization from more distal synapses. Thus, the separation of inputs and outputs is a global dendritic strategy used to compute motion direction (**Fig. 1A**).

The second feature, the “end effect”, is the property of the closed end of the dendritic compartment that essentially reflects current flow in the outward direction and leads to less voltage attenuation in the direction of the distal compartment. This is in contrast to locations near branch points or the soma, which act as current sinks. The end effect is critical for ensuring that large segments of dendrite containing release sites are subjected to a similar depolarization, despite the increased distance from the last activated input, which in turn leads to a large region of the dendrite exhibiting DS (**Fig. 5**). This could also be a mechanism for synchronizing release from varicosities at different distances from the end of the dendrite.

In this study, we created a simulation based on passive membrane properties to examine the role of the excitatory input distribution. The principle prediction is that direction selectivity of distal dendritic voltage is enhanced if inputs are segregated away from release sites (**Fig. 5**). We confirmed this enhancement by monitoring calcium responses to motion stimuli as a proxy for voltage integration at release sites (**Fig. 6**). However, it is difficult to test empirically whether the alternative case, the regular distribution of inputs located all along the dendrite, produces weaker DS at release sites. Therefore it remains to be shown directly that exclusion of synaptic inputs near release sites is necessary, as our simulations suggest, to produce DS at most of the release sites.

It is likely that non-linearities also contribute to DS. SACs express the voltage-gated potassium channel Kv3.1, which is localized to proximal dendrites and which probably enhances the electrical isolation of dendrites pointing in different directions (Ozaita et al., 2004). SACs also exhibit TTX-insensitive voltage-gated sodium channel conductances (Oesch and Taylor, 2010), which might amplify the direction selective voltage observed in our model (**Fig. 5**). Voltage-gated Ca^{2+} channels could also amplify direction selective voltage—both P/Q and N-type channels are expressed in SACs (Lee et al., 2010; Xu et al., 2003) and adding voltage-gated Ca^{2+} channels to the varicosities in our model resulted in a significant amplification of DS in SAC varicosities (data not shown). Our evidence of the presence of nonlinearities is that we observe an outward preference of the somatic voltage in response to moving square stimuli, while a purely passive model would predict a small inward direction preference for voltage recorded at the soma (**Fig. S5;** Euler et al., 2002; Gavrikov et al., 2003, 2006; Hausselt et al., 2007; Oesch and Taylor, 2010; Ozaita et al., 2004). Directly measuring voltage in SAC dendrites would provide a basis for determining the contribution of each non-linearity to the amplification of passive DS. Finally, the cooperative binding of neurotransmitter release sensors (e.g. Kochubey et al., 2009) will likely contribute to amplification of DS release of GABA onto DSGCs.

A unifying model of SAC DS

So far, three models of how DS arises in SAC dendrites have been proposed. First, the space-time wiring model by Kim et al. (2014) proposes that bipolar cells with phasic vs. sustained release kinetics synapsing onto different regions of the dendrite produce a delay-line computation of DS. As shown in **Figure S1**, our voltage clamp recordings do not show detectable differences in bipolar cell release kinetics at different sites along the dendrite. However, the ideal experiment to test this model would be to record from bipolar cell-SAC pairs to test directly for differences in release kinetics.

Second, the lateral inhibition model postulates that DS in SACs arises due to lateral inhibition from other SACs. SACs release GABA onto one another (Kostadinov and Sanes, 2015; Lee and Zhou, 2006; Zheng et al., 2004) and a previous study demonstrated that the DS of Ca^{2+} responses in proximal varicosities requires surround stimulation in rabbit SACs (Lee and Zhou, 2006). This inhibition mechanism relies on the ability of GABA receptor activation to shunt excitation when inhibition arrives first (Münch and Werblin, 2006). However, other studies in rabbit retina have found that blocking GABA receptors did not affect direction selective responses in one example of dendritic Ca^{2+} imaging (Euler et al., 2002) or in direction selective responses as measured by voltage clamp recordings at the soma (Hausselt et al., 2007; Oesch and Taylor, 2010).

We found that lateral inhibition enhanced, but was not required for, DS in distal varicosities (**Fig. 7**). First, stimulating out to 100% of the dendritic tree, which maximally stimulates antiparallel presynaptic SAC processes, led to a larger DS than stimulation to 75% of the dendritic tree. Second, blockade of $GABA_A$ signaling reduced DS in distal varicosities, primarily by increasing the dendritic response to inward motion. It is important to note that a bath application of gabazine not only affects SAC-SAC interactions, but will also affect wide-field amacrine cell inputs to SACs (Hoggarth et al., 2015) as well as the amount of glutamate released from bipolar cells, due to a relief of synaptic inhibition (Pei et al., 2015). However, GABA release from wide-field amacrine cells should not be DS, and the distribution of bipolar cell inputs on SACs allows them to maintain DS despite potential increases in glutamate release.

Our data are more in favor of a third model in which DS arises through a dendrite-intrinsic mechanism. In this model, the excitatory input distribution and passive cable properties described here contribute to the direction selectivity of dendritic voltage, and hence synaptic output. In addition, the differential distribution of inputs and outputs contributes to a circuit-based mechanism of DS in which lateral inhibition from neighboring SACs enhances DS. Overall, our findings suggest a model where the dendrite-intrinsic direction preference is enhanced by lateral inhibition from other SACs, a circuit-level interaction that itself requires the presence of the dendrite-intrinsic mechanism, leading to robust DS in SAC processes (**Fig. S7**).

Experimental Procedures

Visual stimulation and calcium imaging

Ethics statement

All animal procedures were approved by the UC Berkeley Institutional Animal Care and Use Committee and conformed to the NIH Guide for the Care and Use of Laboratory Animals, the Public Health Service Policy, and the SFN Policy on the Use of Animals in Neuroscience Research.

Tissue preparation

Adult mice (P21-P40) of either sex were anesthetized with isoflurane and decapitated. Retinas were dissected from enucleated eyes under infrared illumination and isolated retinas were mounted over a 1-2 mm^2 hole in filter paper (Millipore) with the photoreceptor layer side down. Mounted retinas were stored in oxygenated Ames' media (US Biological or Sigma) in the dark at room temperature prior to imaging and recording. To target SACs for whole cell recordings, we used two mouse lines that express fluorescent proteins in SACs: *mGluR2-GFP* mice that contain a transgene insertion of the interleukin-2 receptor fused to GFP under control of the mGluR2 promoter (Watanabe et al., 1998); and *ChAT-Cre/nGFP* mice generated by crossing a mouse in which *IRES-Cre* recombinase was knocked in downstream of the endogenous choline acetyltransferase gene (Ivanova et al., 2010) (B6.129S6-*ChAT*$^{tm2(cre)Lowl}$*/J*; Jackson Labs) (Chat-cre) with a mouse line containing a *loxP*-flanked STOP cassette upstream of the GFP gene containing a nuclear-localization sequence (Stoller et al., 2008) (B6.129-*Gt(ROSA)26Sor*^{tm1Joe}/J; Jackson Labs). For some experiments, ChAT-Cre mice without the nGFP transgene or wild-type (C57BL/6J; Jackson Labs) mice were used. In these experiments SAC identity was confirmed by fluorescence imaging of dye-filled cells at the end of the experiment.

Whole cell recordings

All recordings in this study were performed from displaced (On-layer) SACs. Retinas mounted on filter paper were placed under the microscope and perfused with oxygenated (95% O_2 – 5% CO_2), bicarbonate-buffered Ames' media at 32-34°C. For calcium imaging experiments, L-ascorbic acid (Sigma) was added to Ames' media to achieve a final concentration of 0.5 mM. For experiments in **Figure 7**, SR 95531 hydrobromide (GABAzine, Tocris Bioscience), was added to Ames' media to achieve a final concentration of 5 µM. Retinas were bathed in GABAzine-containing Ames' media for $\geq$ 10 minutes before recording from SACs.

To avoid bleaching the photoreceptors, fluorescently labeled retinal cells were targeted for whole cell recordings using two-photon microscopy (see *2-photon imaging* below) (Wei et al., 2010). For placing the patch pipette on the cell soma, the tissue was visualized using transmitted infrared illumination with an IR-LED (Thor Labs) and an IR1000 camera (DAGE-MTI). The inner limiting membrane and Müller cell endfeet above the targeted fluorescent cell were removed using a glass pipette before targeting a new pipette for recording. In all instances a gigaohm seal was obtained before breaking in.

For whole cell voltage clamp recordings, borosilicate glass electrodes pulled to a 5-7MΩ tip were filled with an internal solution containing (in mM): 110 CsMeSO3, 2.8 NaCl, 4 EGTA, 5 TEA-Cl, 4 adenosine 5'-triphosphate (magnesium salt), 0.3 guanosine 5'-triphosphate (trisodium salt), 20 HEPES, 10 phosphocreatine (disodium salt), and CsOH to pH 7.2. Alexa

Fluor 594 hydrazide (0.03 mM, Life Technologies, #A-10438) was included in internal solution for collecting 2-photon images of dendritic morphology after the visual stimulation protocol was complete. Voltage clamp recordings were acquired at 10 kHz and filtered at 2 kHz with a Multiclamp 700A amplifier (Molecular Devices) using pCLAMP 10 recording software and a Digidata 1440 digitizer. Currents were recorded at only one holding potential (-72 mV). The holding potentials reported throughout are after correction for the junction potential (-12 mV).

For calcium imaging experiments, electrodes were filled with an internal solution containing (in mM): 116 D-gluconic acid (K+ salt), 6 KCl, 2 NaCl, 20 HEPES, 4 adenosine 5'-triphosphate (magnesium salt), 0.3 guanosine 5'-triphosphate (trisodium salt), 10 phosphocreatine (disodium salt), 0.15 Oregon Green 488 BAPTA-1 hexapostassium salt (OGB-1; Life Technologies) and KOH to pH 7.25. Membrane potentials reported here are after correction for the liquid junction potential (-8.6mV) Cells were held in current clamp for calcium imaging experiments and recordings were acquired at 10kHz. Cells resting above -48 mV were injected with negative current (maximum -150 pA) to achieve a resting potential < -48mV. Cells that did not hyperpolarize below -48mV upon current injection were discarded from analysis.

2-photon imaging

Targeted patching of GFP-expressing cells and imaging of Alexa-594 and OGB-1 dye-filled SACs were performed using a custom-built two-photon microscope. We used a Chameleon Ultra II laser (Coherent) tuned to 810 nm (for Alexa-594 dye imaging) or 930 nm (for GFP and OGB-1 imaging) focused through a 60x LUMPlanFL N water-immersion objective (1.00 NA, Olympus). A 20x UMPlanFL N water-immersion objective (0.50 NA, Olympus) was used for imaging the entire SAC dendritic tree. Laser intensity was controlled using a Pockels cell (Conoptics), scanning was performed using a 3 mm XY Galvanometer scanner (Edmund Optics), and the fluorescence was collected with photomultiplier tubes (H10770PA-40, Hamamatsu). The average sample plane laser power measured after the objective was 6.5-13 mW. The imaging system was controlled by ScanImage software (www.scanimage.org).

For Ca^{2+} imaging experiments, OGB-1 visualization was performed at 930 nm to reduce the light response of the retina during scanning (Denk and Detwiler, 1999). After break-in, the distal end of a dendrite, as well as a single varicosity on that dendrite, were identified as quickly as possible with minimal exposure to the 2-photon laser (6±2 minutes after break in). A small region of interest (2-6 μm^2) that included the varicosity was imaged at either 5.92 or 11.84 Hz (64 x 64 pixels) (see *Visual Stimulation* below). Unlike Hausselt et al. (2007), we saw that a majority (61%) of our patched SACs had Ca^{2+} responses to light stimuli, although long whole cell recording times (>~20 minutes), as well as prolonged laser and/or visual stimulation exposure, often led to unreliable Ca^{2+} responses. These included changes in SAC response polarity (Vlasits et al., 2014), as assessed by the electrical current clamp recording, as well as reduction in fluorescent signal and light responsiveness. Cells were discarded from analysis if the response polarity changed during the imaging session or if the responses to stimuli were lower than 2 S.D. above the noise. Overall, 39% of cells for which a recording was achieved were discarded for the reasons stated above.

Visual Stimulation

For visual receptive field mapping using voltage clamp, visual stimuli were generated using a computer running an Intel core duo processor with Windows XP running a monochromatic organic light-emitting display (OLED-XL, eMagin, 800 x 600 pixel resolution, 85 Hz refresh rate). For simultaneous calcium imaging and visual stimulation, visual stimuli were generated using a computer running an Intel core duo processor with Ubuntu (v. 14.04.2, "Trusty Tahr") running a DMD projector (Cel5500-Fiber, Digital Light Innovations, 1024 x 768 pixel resolution, 60 Hz refresh rate) and an LED light source (M470L2, Thorlabs, Inc.). Visual stimuli were filtered to project only wavelengths between 480-490 nm. The OLED or DMD was projected through a condenser lens onto the photoreceptor-side of the sample. For the OLED, the maximum size of the projected image on the retina was 800 x 600 µm. For the DMD, the maximum size of the projected image on the retina was 670 µm x 500 µm. Custom stimuli were developed using Matlab or GNU Octave and the Psychophysics Toolbox. Proper alignment of stimuli in all planes was checked each day prior to performing the experiment. First, a pipette filled with fluorescent dye was inserted into the bath at the focal plane of the retinal photoreceptors in our chamber (empirically measured using IR imaging (see *Whole Cell Recordings*)). The tip of the pipette was used to find the center of the 2-photon image and align it to a point in the image from the IR1000 camera used for patching. A 5 µm radius spot was then projected through the condenser and detected directly with the IR1000 camera. To align the stimulus to the tip of the pipette (center point of the 2-photon image) any misalignments in the z-plane were corrected by focusing the condenser, while those in the x-y plane were corrected by shifting the condenser along the horizontal axes.

For visual receptive field mapping with voltage clamp, we presented 4 repetitions of each stationary spot (12.5 µm radius) position at maximum intensity (2.9 x 10^5 R*/rod/s) on a black background (1.4 x 10^4 R*/rod/s) for 1 s with 2 s between each spot. For rings, we presented 4 repetitions of each ring radius at maximum intensity (2.9 x 10^5 R*/rod/s) on a dark grey background (8.3 x 10^4 R*/rod/s) for 1 s with 2 s between each ring. For rings and spots, we allowed the retina to adapt to the background illumination for 30 s before beginning data collection. After the experiment was performed a 1 µm/slice z-stack of the dye-filled dendritic arbor was acquired to determine stimuli locations.

For simultaneous calcium imaging and visual stimulation, we first calculated the dendritic radius of a SAC using measurement tools in ImageJ on images of the dye-filled arbor and soma taken within 15 minutes of break-in (See *Data Analysis* for radius calculations). For **Fig. 2**, we presented 3 repetitions of the same sized stationary spot (12.5µm radius) (1.9 x 10^5 R*/rod/s) on a black background for 1 s with 6 s between each spot. Spots were centered on the 25-100% dendritic radius locations previously calculated from ImageJ. For measuring direction selectivity (**Fig. 6**), we presented a 25 µm x 25µm square moving at 500 µm/s. For outward moving squares, the stimulus originated centered on the soma and moved a distance of 75 or 100% of the dendritic radius. Inward stimuli began centered at either 75% or 100% of the dendritic radius and moved inward to the soma. For both these experiments, the relative visual stimulus location along the SAC arbor was verified, and post-hoc corrected if necessary, using a maximum intensity projection image of a 0.5 um/slice z-stack of the quadrant of the filled SAC containing the region of interest imaged. The stack was acquired with the laser tuned to 800 nm (16 mW sample plane power) to take advantage of the larger 2-photon cross-section of OGB at this wavelength. For all visual stimulation experiments, stimuli were presented in pseudorandom order.

Data analysis

Data analysis of physiological recordings was performed in IgorPro (WaveMetrics) running Neuromatic functions. Reported responses are the averages over the 4 repetitions of each stimulus position/radius. The excitatory charge transfer of visually-evoked events was calculated by integrating the average current over the entire 1 s period of the stimulus and subtracting the background charge measured during the 1 s prior to stimulus presentation. For spots, the charge transfer was normalized to the charge transfer measured at the soma as this was usually the maximum response (**Fig. 1B-E**). For rings, the charge transfer was normalized to the maximum charge transfer (**Fig. 1F-I**). For spots, the receptive field was defined as the % of the dendritic field at which the normalized charge transfer reached <5% of the charge transfer at the soma. For rings, the receptive field was defined as the % of the dendritic field at which the normalized charge transfer reached <0% of the maximum charge transfer.

Measurements of the extent of the SAC dendritic field were performed in ImageJ. Measurements were taken from the maximum intensity projection of images of the SAC. The dendritic field with stationary spot stimuli (**Fig. 1B-E**) was the radius from the center of the soma to the edge of the longest dendrite within the region of the cell covered by the stimuli. The dendritic field with ring stimuli (**Fig. 1F-I**), was the radius from the center of the soma to the end of the longest dendrite in the entire dendritic tree. The dendritic field for Ca^{2+} imaging experiments was the radius from the center of the soma through the imaged varicosity to the edge of the longest dendrite within the region of the cell covered by the stimuli. Path lengths were calculated using the segmented line function in ImageJ to trace the dendritic path from the soma through the imaged varicosity to the tip of that dendrite.

Analysis of the calcium imaging experiments was performed in MATLAB and IgorPro using custom procedures. Images of varicosities were segmented by Multi Otsu's method. In brief, time-lapse images from a single stimulation experiment were combined by maximum intensity projection. The bottom class of each thresholded projection was then assigned as background, while the top class was used as a mask for further analysis. The pixel intensities for pixels within a mask were averaged at each time step. The average background intensity was subtracted and the change in fluorescence responses shown here were calculated as

$$\frac{\Delta F}{F} = \frac{F - F_0}{F_0}$$

where F is the fluorescence during visual stimulation and F_0 is the average fluorescence during the 3 s preceding visual stimulation. The maximum ΔF/F for each average response was used to calculate the direction selectivity index as follows (with direction of visual stimulation relative to SAC soma indicated by the subscript):

$$DSI = \frac{\frac{\Delta F}{F}_{out} - \frac{\Delta F}{F}_{in}}{\frac{\Delta F}{F}_{out} + \frac{\Delta F}{F}_{in}}$$

Glutamate Uncaging

Ethics statement

Animal experiments were performed in accordance with the guidelines of Institut Pasteur.

Tissue preparation

Tissue was prepared as described for visual stimulation (above) with the exception that dissections of the retina were done in ambient light and tissue was stored in oxygenated ACSF containing (in mM): 125 NaCl, 2.5 KCl, 1 $CaCl_2$, 1 $MgCl_2$, 1.25 NaH_2PO_4, 25 $NaHCO_3$, and 25 glucose. We recorded from wild type (C57Bl/6) mice. To target On-SACs in wild type mice, we filled cells with small, round somas (Petit-Jacques et al., 2005) with Alexa Fluor 594 in the internal solution and imaged the dendritic morphology using a 2-photon microscope to determine cell identity before proceeding.

Voltage clamp recordings

Whole-cell recordings were made from SACs at -72 mV at near physiological temperatures (32°C) using a Multiclamp 700B amplifier (Axon Instruments, Foster City, Ca, USA) with thick-walled glass patch-electrodes (tip resistances of 5-8 MΩ) that were backfilled with either a K^+-based internal solution containing (in mM): 117 K-$MeSO_3$, 40 HEPES, 6 NaOH, 5 EGTA, 1.78 $CaCl_2$, 4 MgCl2, 0.3 NaGTP, 4 NaATP, and 0.03 Alexa 594 or a Cs^+- based internal solution containing (in mM): 90 Cs-$MeSO_3$, 40 HEPES, 6 NaOH, 10 BAPTA, 3.4 $CaCl_2$, 5 $MgCl_2$, 10 TEA-Cl, 0.3 NaGTP, 4 NaATP, and 0.03 Alexa 594, adjusted to ~305 mOsm and pH 7.3. The series resistance was typically below 35 MΩ and was not compensated. Unless otherwise noted, for recording, the ACSF was supplemented with 2 μM L-AP4 and 1.2 μM LY341495 to block the light response from photoreceptors (Ala-Laurila et al., 2011) in addition to 2 mM MNI-glutamate. Uncaging-evoked events were filtered at 10 kHz and digitized at 100-500 kHz using an analogue-to-digital converter (model NI USB 6259, National Instruments, Austin, TX, USA) and acquired with Nclamp (www.neuromatic.thinkrandom.com).

2-photon imaging

SAC somata were identified and whole-cell patched using infrared Dodt contrast (Luigs and Neumann, Ratingen, Germany) and a frame transfer CCD camera (Scion Corporation, Cairn Research Ltd, Faversham, UK). These components were mounted on an Ultima two-photon laser scanning head (Prairie Technologies, Middleton, WI, USA) based on an Olympus BX61W1 microscope, equipped with a water- immersion objective (60x, 1.1 numerical aperture, Olympus Optical, Tokyo, Japan). Two-photon excitation was performed with a pulsed Ti:Sapphire laser (DeepSee, Spectra-Physics, Evry, France) tuned to 810 nm. The SAC morphology was visualized from maximal intensity projections of 2PLSM images (0.261 μm/pixel, and 1 μm in Z-dimension) to find isolated dendrites for uncaging. 100 nm diameter fluorescent beads (Invitrogen, Carlsbad, CA, USA) were used to estimate the point spread function (PSF) of the microscope system as previously described (Abrahamsson et al., 2012; DiGregorio et al., 2007). The measured PSF had lateral and axial dimensions of 390 ± 5 nm (FWHM, n = 15) and 1430 ± 40 nm (n = 14), respectively.

Glutamate uncaging

The caged compound 4-methoxy-7-nitroindolinyl-caged L-glutamate (MNI-glutamate, Tocris Bioscience) was bath applied at a concentration of 2 mM (in ACSF). The custom photolysis system was coupled into the photolysis pathway of the Ultima two-photon scanhead. A 405 nm diode laser (Omicron Lasers, Rodgau, Germany) beam was coupled to the microscope using a single mode optical fiber (Oz Optics, Ottawa, Ontario, Canada) similar to a previously described setup (DiGregorio et al., 2007), except additional optics were used to adjust the convergence angle to both backfill the objective and match the focal plane of the two photon excitation for imaging (810 nm). Parfocality of the two wavelengths was verified previously (Abrahamsson et al., 2012). Photolysis laser powers were 2.55 mW.

To map putative postsynaptic sites along a dendrite (**Fig. 3**), we uncaged at dendritic locations 2.5-4 μm apart at 100 or 200 ms intervals and measured current responses to uncaging in voltage clamp. In one cell, we uncaged inward from the distal dendrite to the soma and did not observe any differences in measured parameters (data not shown). Uncaging-based mapping was performed using 100 μs duration laser pulses, a duration shown to optimize event detection and resolution (see **Fig. S2**). The effective uncaging resolution was measured by uncaging systematically in locations 0.5 – 1 μm along a line perpendicular to a synaptic location determined via mapping (**Fig. S3**). For all experiments, uncaging pulses in neighboring locations were timed 100 or 200 ms apart, which was enough time to ensure that nearby glutamate receptors were no longer desensitized (**Fig. S2**). Depending on flatness of the sample, the objective was refocused between bouts of uncaging to only uncage on in-focus sections of the dendrite. Because SAC dendrites lie in a relatively flat plane, tissue depth was fairly constant across uncaging locations, though because of slight changes in depth of the dendrites in the inner plexiform layer, we cannot make major conclusions about receptor number or dendritic filtering using amplitudes of events measured here.

Data analysis

Data analysis of uncaging-evoked events was performed in IgorPro (WaveMetrics) running Neuromatic functions. Using event detection combined with selection of events with locally-maximal amplitudes, we determined the events we thought were putative postsynaptic sites (**Fig. S2**).

For event detection, uncaging-evoked events were defined as having an amplitude greater than 6 times the S.D. measured during the 3 ms prior to uncaging. This criterion was found to be sufficient to exclude noise due to spontaneous activity from being included. The amplitude was defined as the maximum current during the 10 ms after uncaging. The rise time was the time period from 10% to 90% of the amplitude.

For analyzing the resolution of uncaging, we evaluated the event found to have the maximum amplitude to determine the time point for evaluating the amplitude of other events in the series. These amplitudes were then fit to a Gaussian distribution and the FWHM of the distribution was measured to determine the resolution of uncaging.

The paired-pulse ratio was defined as the amplitude of the second uncaging event divided by the first event.

To determine the location of putative postsynaptic sites from uncaging-evoked events, we selected the events of local maximal amplitude within 5 μm from the set of events detected using the event detection procedure described above (**Fig. S2**). For events proximal to the soma, events with locally maximal amplitude almost always had locally minimal rise times, while for events distal to the soma this was not the case (**Fig. S2**).

The path length from the soma to the location of the uncaging sites was determined in ImageJ. Measurements were taken from the maximum intensity projection of images of the SAC (stacks taken in 1 μm z-steps). We traced the path from the center of the soma to most distal uncaging site recorded in an image during the experiment identified based on the local anatomical features. Then, we extrapolated backward from this site to the soma to determine the location of all other sites using our records of the distance between sites measured during the experiment. For analyses using the radius from the soma to distal uncaging sites, we measured the radius using a straight line from the soma center to the anatomical location of the most distal uncaging site. The dendritic field was measured from a straight line from soma center to the end of the dendrite uncaged upon. The receptive field was defined as the % of the dendritic field at which the last synaptic site was detected.

PSD95 Labeling and Imaging

Ethics statement
This study was conducted with the approval of the University of Washington Institutional Animal Care and Use Committee (Protocol 4122-01). Mice were euthanized by isoflurane overdose followed by decapitation.

Tissue preparation
Mice of postnatal day 22 were euthanized and enucleated and the eyes immersed in oxygenated mouse artificial cerebral spinal fluid (mACSF) containing the following in (mM): 119 NaCl, 2.5 KCl, 2.5 $CaCl_2$, 1.3 $MgCl_2$, 1 NaH_2PO_4, 11 glucose, and 20 HEPES, and brought to pH 7.42 with NaOH. To obtain retinal whole mounts, retinas were isolated in mACSF and mounted flat, ganglion cell side up, onto filter paper (Millipore).

Biolistic transfection
Plasmids for which a cytomegalovirus (CMV) promoter drives expression of tandem dimer Tomato (tdTomato) or postsynaptic density protein 95 fused to yellow fluorescent protein (PSD95-YFP) were coprecipitated onto gold particles (Bio-Rad) (Morgan and Kerschensteiner, 2012). Gold particles were propelled into whole mount retinas using a Helios Gene Gun (Bio-Rad), and the tissue then incubated at ~34°C in oxygenated mACSF in a humidified chamber for 24 hr to allow for expression of PSD95-YFP and tdTomato. We have found that 18-24 hour incubation is sufficient for detection of fluorescent protein expression in peripheral processes (Morgan et al., 2008), and minimizes overexpression of exogeneous PSD95-YFP, which is accompanied by accumulation of fluorescent protein in the nucleus, indicative of overexpression, and is known to alter synaptic dynamics (El-Husseini et al., 2000; Prange et al., 2004). Afterwards, retinas were fixed in 4% paraformaldehyde in mACSF for 20-30 min, rinsed in PBS, and flat mounted in vectashield (Vector Laboratories) for confocal imaging.

Image acquisition
Image stacks were acquired on an Olympus FV-1000 laser scanning confocal microscope with an oil-immersion 60x objective (Olympus, 1.35 NA). Voxel dimensions were (x-y-z in μm) 0.103-0.103-0.3 for images of isolated single starburst amacrine cells (SACs) in whole mount retinas. Images were median filtered to remove noise and compressed to 8-bits for analysis after normalization of the entire stack histogram using Fiji(Schindelin et al., 2012).

Quantification of SAC dendrites
The branching patterns of SAC dendrites were skeletonized using the filament function of Imaris (Bitplane). Total dendritic length was calculated from the skeletonized filament. A skeleton of an entire SAC traced in Imaris was used to create the schematic in **Figure S6**.

Identification and quantification of postsynaptic PSD95 puncta
Potential PSD95YFP puncta were identified using custom MATLAB scripts previously described(Morgan et al., 2008). Briefly, fluorescence signals within the PSD95 channel were

iteratively thresholded, filtered by size and contrast, and their ratio of fluorescence to cytosolic fluorescence intensity. We then calculated the log ratio of YFP to tdTomato fluorescence intensity within each punctum in order to evaluate potential bleedthrough between the two channel (Torborg and Feller, 2004). To compare across cells, for each cell, the minimum value for the log ratio for each cell was set to zero (but log ratio distributions were not normalized). A log ratio threshold of 1 was used for simulations and comparison to uncaging and output distributions because it minimized bleedthrough while allowing for a clear designation of PSD95 puncta (see **Fig. S4** for details). For figures in which a log ratio threshold is used, only puncta with a log ratio greater than the threshold value were included in analysis.

Path length and radial density analysis

We first determined the path length distance from the soma for every node of the skeletonized dendritic filament. The path length distance for each PSD95 puncta was assigned from its nearest node of the skeletonized dendritic filament. We determined the path length puncta linear density by dividing the total number of identified PSD95 puncta by the total dendritic length of the skeletonized dendrite within a sliding window of 10 µms, incrementally by 1 µm, from the soma to the longest path length distance. For radial distributions in **Figure 4E** and **Figure S4C**, the number of inputs across cells was summed in 1 µm bins. To exclude the cell body and vertical dendritic segments the initial 15 µm were omitted.

Simulation of SAC

Passive cable simulations of EPSC propagation or EPSP integration within an idealized SAC model were performed using Neuron v7.3 (Carnevale and Hines, 2006). The SAC morphology was approximated as a ball-and-stick model (**Fig. 5**, **Fig S3, and Fig. S5**).

To test the effect of dendritic filtering on voltage-clamp recordings, we modeled one 150 µm-long main dendritic branch, each with 3 branch points at 15, 35 and 65 µm **(Fig. S3)**. This length was chosen to correspond to the longest SAC dendrites measured (3% of 95 dendrites of SACs patch-loaded with Alexa Fluor 594 and imaged on a two-photon microscope), for which distal events would be the most filtered.

For the integration experiments, we wanted to establish an average dendritic branching representative of SAC morphology **(Fig. 5, Fig. S5)**. Out of the 95 dendrites of SACs imaged and measured, 66% had 4 or 5 orders of branching, so we implemented those two morphologies in the model. We modeled one 105 µm-long main dendritic branch, with 4 branch points at 10.9, 35.2 and 67.2 and 73.7 µm, and another 115 µm-long main dendritic branch, with 3 branch points at 21.9, 53.6 and 69.1 µm. Synapses were distributed along one of the main branches with regular spacing or as a density gradient that matched experimental findings. The initial 10 µm of the dendrite was set to 400 nm in diameter, which represents the dendritic segment linking the soma in the ganglion cell layer to the dendrites in the inner plexiform layer. The diameter of subsequent dendrites were set at a constant value of 200 nm (Kim et al., 2014). Varicosities were inserted in the most distal third of the dendrites, equally spaced, and modeled as a cylinder of 500 nm length and 500 nm diameter.

Passive properties were assumed uniform across the cell. Specific membrane capacitance (C_m) was set to 1 pF/cm^2. R_m was set to 21700 Ω-cm^2 based on an electrophysiological estimate of the membrane time constant□($□_m$ = 21.7±2.4ms, n=5 cells, data not shown). $□_m$ was measured from the slowest decay time constant of the voltage response to a brief 0.5 ms negative current pulse injection, which produced hyperpolarizations of 30 mV. R_i was set to either 100 Ω-cm or 200 Ω-cm to match a range of values used in modeling studies of SACs and other amacrine cells (Grimes et al., 2010; Singer et al., 2004; Tukker et al., 2004). In all simulations, the resting potential of the cell was set at -70 mV.

All synaptic responses were modeled using the Exp2syn function. The AMPA conductance was set to match the amplitude (313 pS) and time course ($□_{\mathrm{rise}}$ = 0.14ms, $□_{\mathrm{decay}}$ = 0.54ms) of fast rising miniatures EPSCs (< 0.175 ms rise-time, data not shown), as they are likely to represent synapses converging on proximal dendritic compartments, which are space-clamped. For direction selectivity simulations, however, the value of the synaptic conductance was increased to model the release of three vesicles (939 pS) to account for multivesicular release from bipolar cell terminals (Grimes et al., 2010). We plotted the simulated dendritic voltage at 25, 55, 75, 95 and 105 or 115 µm from the soma, in response to the inward or outward activation of synapses at a speed of 500 µm/s. This speed is within the range of velocity tuning of direction-selective ganglion cells (Sivyer et al., 2010) and matches the speed of visual stimulation from experiments in **Figures 6** and **7**.

References

Abrahamsson, T., Cathala, L., Matsui, K., Shigemoto, R., and Digregorio, D.A. (2012). Thin dendrites of cerebellar interneurons confer sublinear synaptic integration and a gradient of short-term plasticity. Neuron *73*, 1159–1172.

Amthor, F.R., Keyser, K.T., and Dmitrieva, N.A. (2002). Effects of the destruction of starburst-cholinergic amacrine cells by the toxin AF64A on rabbit retinal directional selectivity. Vis. Neurosci. *19*, 495–509.

Beier, K.T., Borghuis, B.G., El-Danaf, R.N., Huberman, a. D., Demb, J.B., and Cepko, C.L. (2013). Transsynaptic Tracing with Vesicular Stomatitis Virus Reveals Novel Retinal Circuitry. J. Neurosci. *33*, 35–51.

Berntson, A., and Taylor, W.R. (2000). Response characteristics and receptive field widths of on-bipolar cells in the mouse retina. J. Physiol. *524*, 879–889.

Briggman, K.L., Helmstaedter, M., and Denk, W. (2011). Wiring specificity in the direction-selectivity circuit of the retina. Nature *471*, 183–188.

Carnevale, N.T., and Hines, M.L. (2006). The NEURON book (Cambridge, UK: Cambridge University Press).

Chen, M., Lee, S., Park, S.J.H., Looger, L.L., and Zhou, Z.J. (2014). Receptive field properties of bipolar cell axon terminals in the direction-selective sublaminas of the mouse retina. J. Neurophysiol.

DiGregorio, D.A., Rothman, J.S., Nielsen, T.A., and Silver, R.A. (2007). Desensitization properties of AMPA receptors at the cerebellar mossy fiber granule cell synapse. J. Neurosci. *27*, 8344–8357.

Euler, T., Detwiler, P.B., and Denk, W. (2002). Directionally selective calcium signals in dendrites of starburst amacrine cells. Nature *418*, 845–852.

Famiglietti, E. V (1991). Synaptic organization of starburst amacrine cells in rabbit retina: analysis of serial thin sections by electron microscopy and graphic reconstruction. J. Comp. Neurol. *309*, 40–70.

Fried, S.I., Münch, T. a, and Werblin, F.S. (2002). Mechanisms and circuitry underlying directional selectivity in the retina. Nature *420*, 411–414.

Fried, S.I., Münch, T. a, and Werblin, F.S. (2005). Directional selectivity is formed at multiple levels by laterally offset inhibition in the rabbit retina. Neuron *46*, 117–127.

Gavrikov, K.E., Dmitriev, A. V, Keyser, K.T., and Mangel, S.C. (2003). Cation-chloride cotransporters mediate neural computation in the retina. Proc. Natl. Acad. Sci. U. S. A. *100*, 16047–16052.

Gavrikov, K.E., Nilson, J.E., Dmitriev, A. V, Zucker, C.L., and Mangel, S.C. (2006). Dendritic compartmentalization of chloride cotransporters underlies directional responses of starburst amacrine cells in retina. Proc. Natl. Acad. Sci. U. S. A. *103*, 18793–18798.

Greene, M.J., Kim, J.S., and Seung, H.S. (2016). Analogous Convergence of Sustained and Transient Inputs in Parallel On and Off Pathways for Retinal Motion Computation. Cell Rep.

Hausselt, S.E., Euler, T., Detwiler, P.B., and Denk, W. (2007). A dendrite-autonomous mechanism for direction selectivity in retinal starburst amacrine cells. PLoS Biol. *5*, e185.

Hoggarth, A., McLaughlin, A.J., Ronellenfitch, K., Trenholm, S., Vasandani, R., Sethuramanujam, S., Schwab, D., Briggman, K.L., and Awatramani, G.B. (2015). Specific Wiring of Distinct Amacrine Cells in the Directionally Selective Retinal Circuit Permits Independent Coding of Direction and Size. Neuron *86*, 276–291.

Kim, J.S., Greene, M.J., Zlateski, A., Lee, K., Richardson, M., Turaga, S.C., Purcaro, M., Balkam, M., Robinson, A., Behabadi, B.F., et al. (2014). Space–time wiring specificity supports direction selectivity in the retina. Nature *509*, 331–336.

Kochubey, O., Han, Y., and Schneggenburger, R. (2009). Developmental regulation of the intracellular Ca2+ sensitivity of vesicle fusion and Ca2+-secretion coupling at the rat calyx of Held. J. Physiol. *587*, 3009–3023.

Koizumi, A., Jakobs, T.C., and Masland, R.H. (2011). Regular mosaic of synaptic contacts among three retinal neurons. J. Comp. Neurol. *519*, 341–357.

Kostadinov, D., and Sanes, J.R. (2015). Protocadherin-dependent dendritic self-avoidance regulates neural connectivity and circuit function. Elife *4*, 1–23.

Lee, S., and Zhou, Z.J. (2006). The synaptic mechanism of direction selectivity in distal processes of starburst amacrine cells. Neuron *51*, 787–799.

Lee, S., Kim, K., and Zhou, Z.J. (2010). Role of ACh-GABA cotransmission in detecting image motion and motion direction. Neuron *68*, 1159–1172.

Morgan, J.L., and Kerschensteiner, D. (2012). Coating gold particles with DNA (biolistics). Cold Spring Harb. Protoc. *2012*, 114–117.

Morgan, J.L., Schubert, T., and Wong, R.O.L. (2008). Developmental patterning of glutamatergic synapses onto retinal ganglion cells. Neural Dev. *3*, 8.

Morrie, R.D., and Feller, M.B. (2015). An Asymmetric Increase in Inhibitory Synapse Number Underlies the Development of a Direction Selective Circuit in the Retina. J. Neurosci. *35*, 9281–9286.

Münch, T. a, and Werblin, F.S. (2006). Symmetric interactions within a homogeneous starburst cell network can lead to robust asymmetries in dendrites of starburst amacrine cells. J. Neurophysiol. *96*, 471–477.

Oesch, N.W., and Taylor, W.R. (2010). Tetrodotoxin-resistant sodium channels contribute to directional responses in starburst amacrine cells. PLoS One *5*, e12447.

Ozaita, A., Petit-Jacques, J., Völgyi, B., Ho, C.S., Joho, R.H., Bloomfield, S. a, and Rudy, B. (2004). A unique role for Kv3 voltage-gated potassium channels in starburst amacrine cell signaling in mouse retina. J. Neurosci. *24*, 7335–7343.

Park, S.J.H., Kim, I.-J., Looger, L.L., Demb, J.B., and Borghuis, B.G. (2014). Excitatory synaptic inputs to mouse on-off direction-selective retinal ganglion cells lack direction tuning. J. Neurosci. *34*, 3976–3981.

Pei, Z., Chen, Q., Koren, D., Giammarinaro, B., Acaron Ledesma, H., and Wei, W. (2015). Conditional Knock-Out of Vesicular GABA Transporter Gene from Starburst Amacrine Cells Reveals the Contributions of Multiple Synaptic Mechanisms Underlying Direction Selectivity in the Retina. J. Neurosci. *35*, 13219–13232.

Rall, W. (1964). Theoretical significance of dendritic trees for neuronal input-output relations. Neural Theory Model. 73–97.

Rall, W. (1967). Distinguishing theoretical synaptic potentials computed for different soma-dendritic distributions of synaptic input. J. Neurophysiol. *30*, 1138–1168.

Taylor, W.R., and Smith, R.G. (2012). The role of starburst amacrine cells in visual signal processing. Vis. Neurosci. *29*, 73–81.

Torborg, C.L., and Feller, M.B. (2004). Unbiased analysis of bulk axonal segregation patterns. J. Neurosci. Methods *135*, 17–26.

Tukker, J.J., Taylor, W.R., and Smith, R.G. (2004). Direction selectivity in a model of the starburst amacrine cell. Vis. Neurosci. *21*, 611–625.

Vaney, D.I., Sivyer, B., and Taylor, W.R. (2012). Direction selectivity in the retina: symmetry and asymmetry in structure and function. Nat. Rev. Neurosci. *13*, 194–208.

Vlasits, A.L., Bos, R., Morrie, R.D., Fortuny, C., Flannery, J.G., Feller, M.B., and Rivlin-Etzion, M. (2014). Visual Stimulation Switches the Polarity of Excitatory Input to Starburst Amacrine Cells. Neuron *83*, 1172–1184.

Wei, W., Elstrott, J., and Feller, M.B. (2010). Two-photon targeted recording of GFP-expressing neurons for light responses and live-cell imaging in the mouse retina. Nat. Protoc. *5*, 1347–1352.

Wei, W., Hamby, A.M., Zhou, K., and Feller, M.B. (2011). Development of asymmetric inhibition underlying direction selectivity in the retina. Nature *469*, 402–406.

Xu, H.., Zhao, J.., and Yang, X.. (2003). Cholinergic and dopaminergic amacrine cells differentially express calcium channel subunits in the rat retina. Neuroscience *118*, 763–768.

Yonehara, K., Balint, K., Noda, M., Nagel, G., Bamberg, E., and Roska, B. (2011). Spatially asymmetric reorganization of inhibition establishes a motion-sensitive circuit. Nature *469*, 407–410.

Yonehara, K., Farrow, K., Ghanem, A., Hillier, D., Balint, K., Teixeira, M., Jüttner, J., Noda, M., Neve, R.L., Conzelmann, K.-K., et al. (2013). The First Stage of Cardinal Direction Selectivity Is Localized to the Dendrites of Retinal Ganglion Cells. Neuron *79*, 1–8.

Yoshida, K., Watanabe, D., Ishikane, H., Tachibana, M., Pastan, I., and Nakanishi, S. (2001). A key role of starburst amacrine cells in originating retinal directional selectivity and optokinetic eye movement. Neuron *30*, 771–780.

Zheng, J., Lee, S., and Zhou, Z. (2004). A Developmental Switch in the Excitability and Function of the Starburst Network in the Mammalian Retina. Neuron *44*, 851–864.

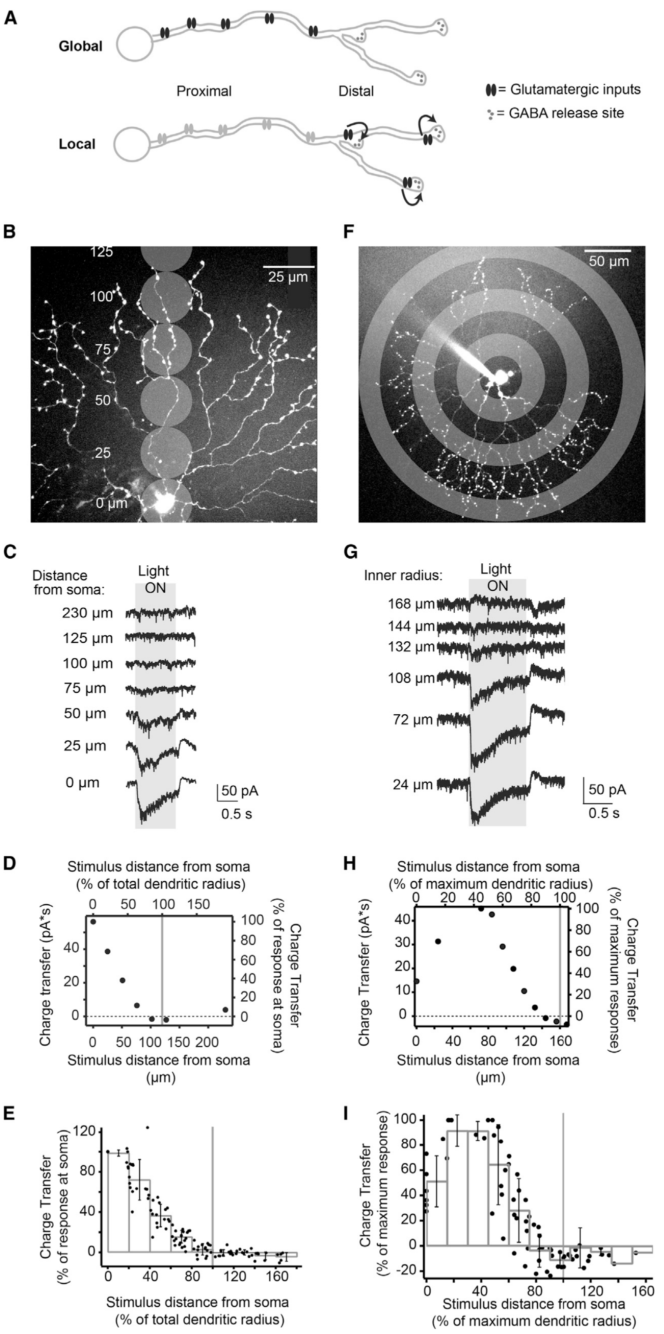

Figure 1. Starburst amacrine cell excitatory receptive field is smaller than dendritic field. **A**) Schematic of two distributions of glutamatergic inputs (ovals) and GABAergic release sites (outputs, small circles) on a SAC dendrite. The skewed distribution (top) produces a global computation where all inputs contribute, while the regular distribution produces primarily local computations, with receptors near outputs having a dominant effect on neurotransmitter release (arrows). **B**) Schematic showing locations of visual stimulation spots overlaid on a 2-photon fluorescence image of a SAC (z-projection). Distances are relative to the soma. **C**) Light-evoked current responses for illumination locations shown in **B** (holding potential = -72 mV). Grey box indicates the timing of the stimulus onset and offset. Traces are averages of 4 sweeps. **D**) Excitatory charge transfer as a function of distance from experiment in **C**. Right and top axes are normalized to the maximum charge transfer and maximum dendritic radius, respectively. Grey vertical line: the radius of the dendritic tree. **E**) Normalized excitatory charge transfer following visual stimulation as a function of distance from the soma (15 cells). Black dots: individual cells; grey bars: binned averages. Grey vertical line: 100% of the radius of the dendritic tree. Error bars = S.D. **F**) Schematic showing anatomical location of visual stimulation rings overlaid with 2-photon fluorescence projection of a SAC at low magnification. Rings shown have an inner radius of 24, 72, and 132 µm. The thickness of the rings was 24 µm. **G**) Voltage clamp recordings (holding potential = -72 mV) from the SAC in **F** during stimulation with stationary rings (width = 24 µm) with different inner radii. Averages of 4 sweeps. Grey box: the timing of the stimulus onset and offset. **H**) Excitatory charge transfer calculated from the recordings in **G** plotted as a function of the inner radius from the soma. Right and top axes are normalized to the maximum charge transfer and maximum dendritic radius, respectively. For this cell, the maximum dendritic radius was 160 µm. **I**) Excitatory charge transfer calculated for 6 cells plotted as a function of the length of the inner radius from the soma. Axes are normalized to the maximum charge transfer response and maximum dendritic radius, respectively. Black dots: measurements from each cell; grey bars: binned averages of these measurements; error bars: S.D.

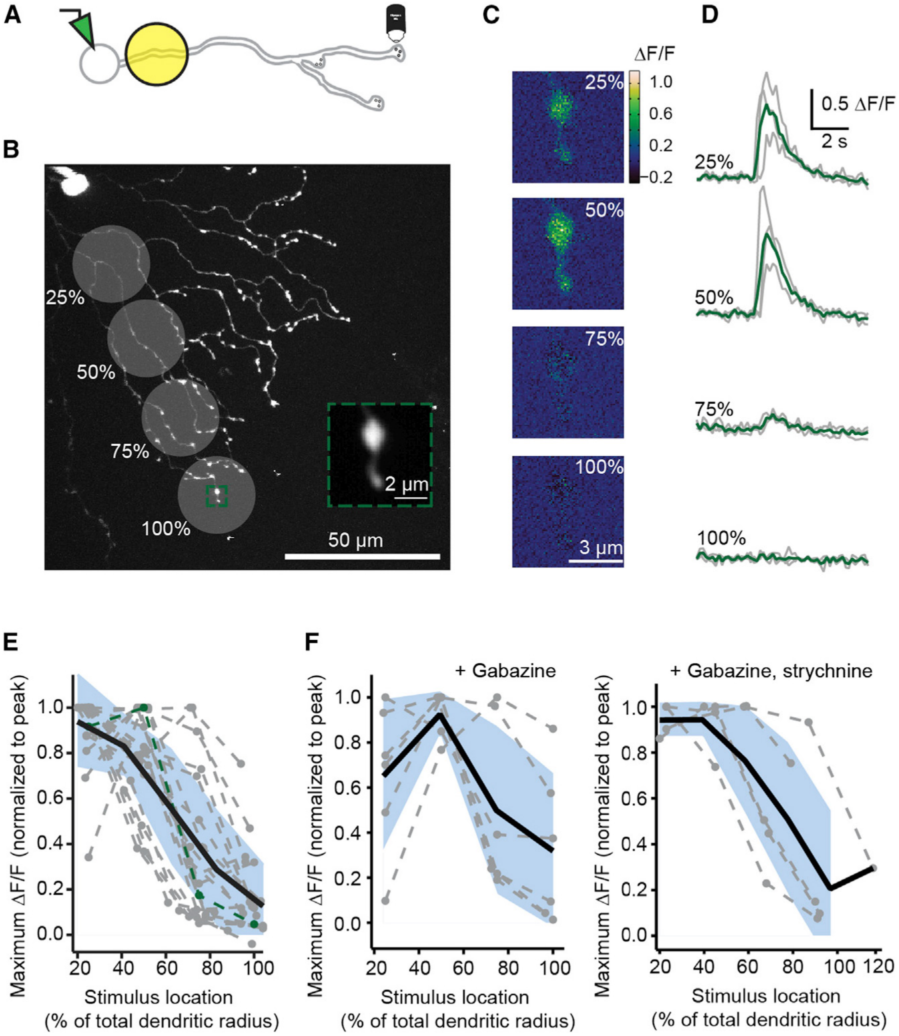

Figure 2. Ca^{2+} transients in varicosities are largest during proximal visual stimulation
A) Schematic displaying experiment to image a distal varicosity from a SAC filled with 150 µM OGB-1 during visual stimulation with 25 µm diameter spots. **B**) Location of visual stimulation spots overlaid with a 2-photon fluorescence image of a SAC filled with OGB-1 (z-projection). Visual stimuli were centered at indicated positions (25, 50, 75, 100%) after measuring the SAC dendritic radius along the axis of the varicosity being imaged. Green box: ROI used to image a distal varicosity. The soma and patch electrode are visible in the top left corner. Inset: average intensity projection of the fluorescent images acquired during visual stimulation. **C**) Maximal change in fluorescence (ΔF/F) responses of the ROI shown in **B** to one presentation of each spot located at the indicated % of the total dendritic radius along the axis of the varicosity being imaged. **D**) ΔF/F (grey lines) following visual stimulation centered at the % of the total dendritic radius for the varicosity in **B**. Green traces: the mean of three trials. **E**) Maximum ΔF/F normalized to the peak response for 15 varicosities measured from 15 cells in response to stimuli at four locations along their dendrites (grey dotted lines; green line = the cell in **B-D**). Black line: the average response of linear interpolations of each receptive field. Blue shading = S.D. **F**) Same as **E** but for varicosities in the presence of 5 µM gabazine (left; 5 cells) or 5 µM gabazine + 1 µM strychnine (right; 5 cells) to isolate the excitatory inputs.

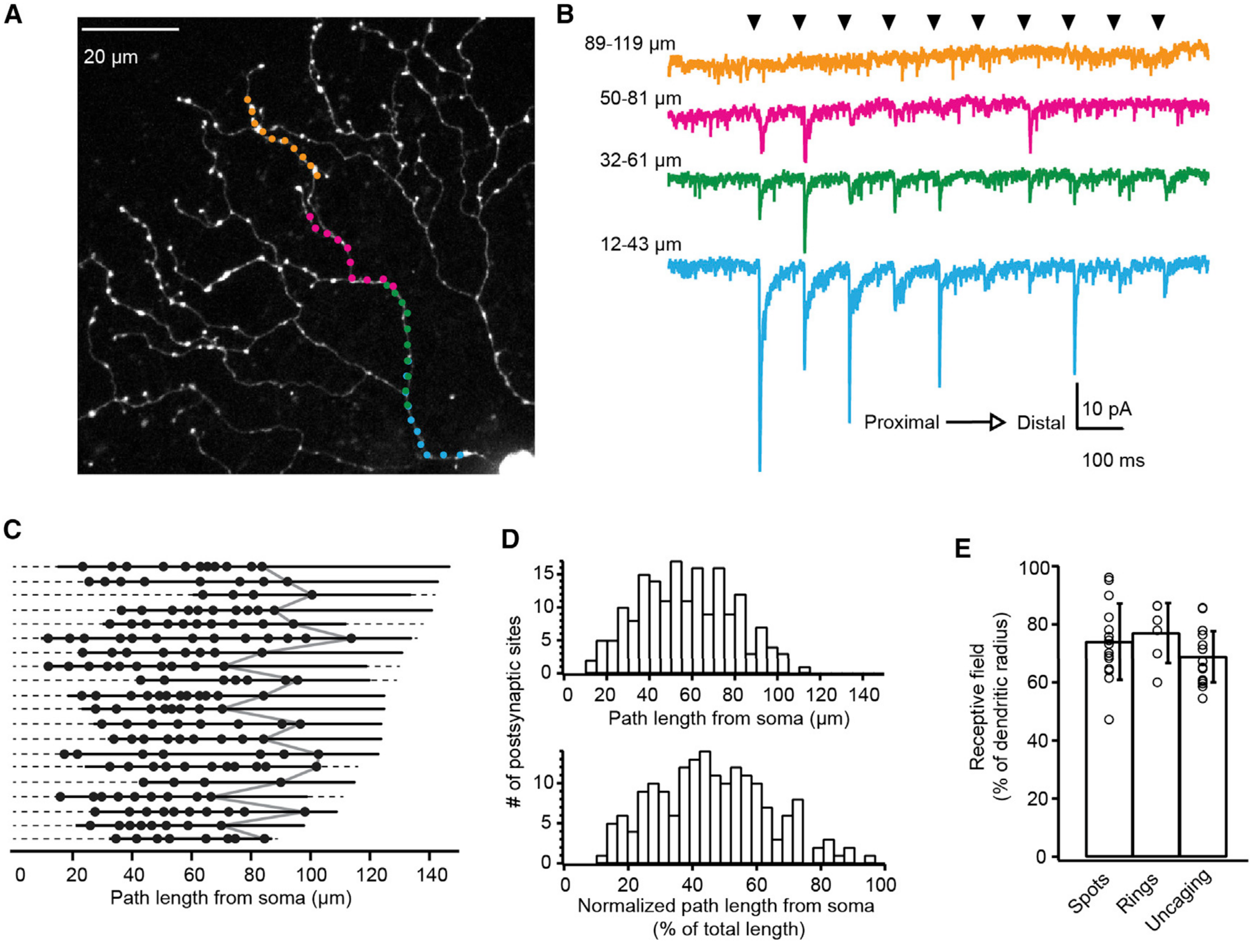

Figure 3. Glutamate receptors are absent from distal dendrites
A) 2-photon fluorescence image of a SAC (z-projection) with targeted locations of glutamate uncaging sites along one dendritic path. Colors correspond to current responses in **B**. **B**) Voltage clamp recordings (holding potential = -72 mV) from the cell in **A** in response to glutamate uncaging at 40 dendritic sites. Black arrowheads indicate the timing of the 100 µs laser uncaging pulses at different dendritic sites (moving outward from the soma to the distal dendrites from left to right and bottom to top). Traces are averages of 10 sweeps. **C**) Locations where uncaging-evoked EPSCs indicated the presence of putative postsynaptic sites (black dots). Each row represents a different dendrite (n = 20 dendrites from 15 cells). Dashed lines: the entire path lengths from the soma to the end of the dendrite; solid lines: the path lengths sampled by uncaging. Locations of the last synapses in each dendrite are connected by the grey line. **D**) Histograms of the putative postsynaptic sites as a function of path length (top) or path length normalized to the dendritic length of each dendrite. **E**) Starburst amacrine cell excitatory receptive field size determined using spot stimulation ('Spots'), ring stimulation ('Rings'), or glutamate uncaging ('Uncaging'). Error bars are S.D.

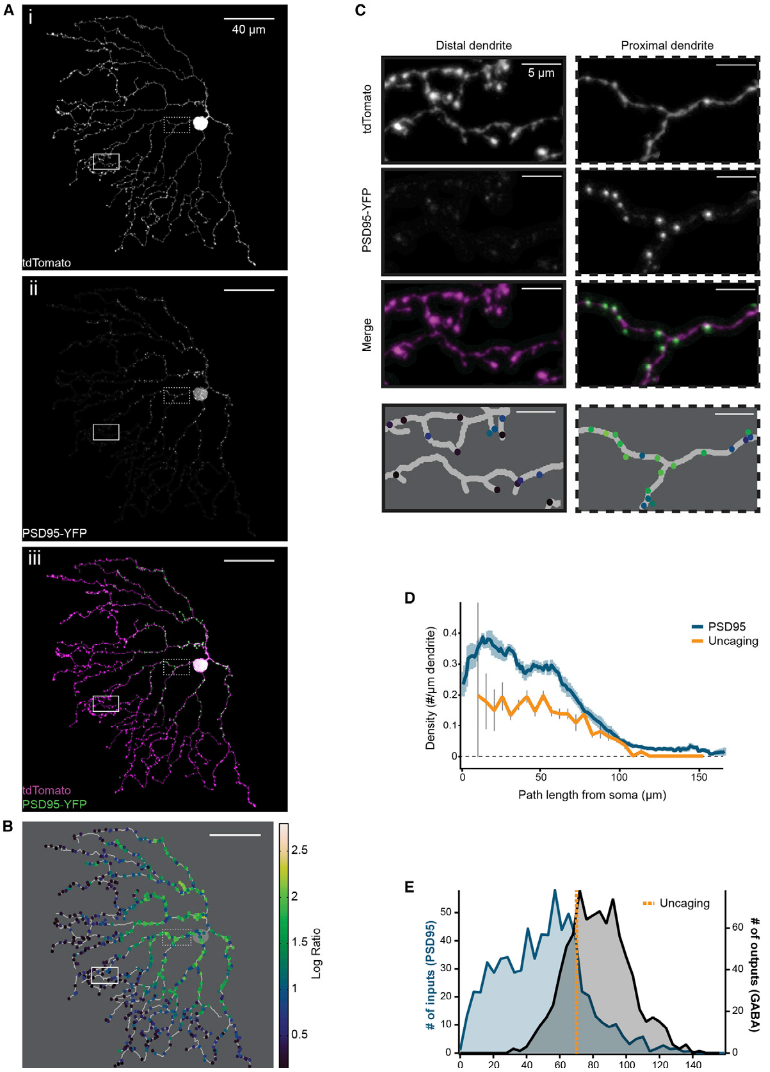

Figure 4. Distribution of putative postsynaptic sites is skewed away from output sites.
A) Projection image of the analyzed dendritic processes of a SAC expressing tdTomato (**i**) and PSD95-YFP (**ii**). **iii** is a merged image showing tdTomato in magenta and PSD95-YFP in green; in this image, contrast was adjusted to improve visibility for display. The image was masked to exclude dendritic branches that overlapped with other labeled cells to ensure that only PSD95 puncta from SACs were included in analysis. Magnified regions (dotted and solid boxes) correspond to example proximal and distal regions in **C**. **B**) Skeleton of cell from **A** with identified PSD95 puncta (colored dots). Colors represent the log ratio of the PSD95 to tdTomato fluorescence intensity within each puncta, which was used for thresholding puncta to include in subsequent analysis (see Methods). **C**) Examples of proximal (top) and distal (bottom) regions indicated by the dotted and solid boxes in **A**. Colors of identified puncta in the 4th column correspond to the heat map in **B**. **D**) Density of PSD95-YFP puncta or putative postsynaptic sites determined by uncaging (see **Fig. 3E**) as a function of dendritic path length from the soma. For PSD95, the average linear density of PSD95 puncta using a 10 µm sliding window is plotted using a threshold log ratio of 1.0 to select puncta to include (blue line; light blue shading = S.E.M, 8 cells). For uncaging, histogram of the average density of putative postsynaptic sites in 5 µm bins is plotted (orange line; grey bars = S.E.M, 23 dendrites). **E**) Histogram of PSD95 puncta from 8 SACs using a threshold log ratio of 1.0 (left axis, blue) as well as the synaptic contacts with DSGCs (outputs, right axis, black) as a function of radial distance from the soma. Orange dotted line: the mean radial distance of the last putative postsynaptic sites detected with uncaging (see **Fig. 3E**). Outputs were determined from electron microscopy reconstructions of 24 SACs (Briggman et al., 2011) and analyzed as a function of radial distance to compare with PSD95 locations.

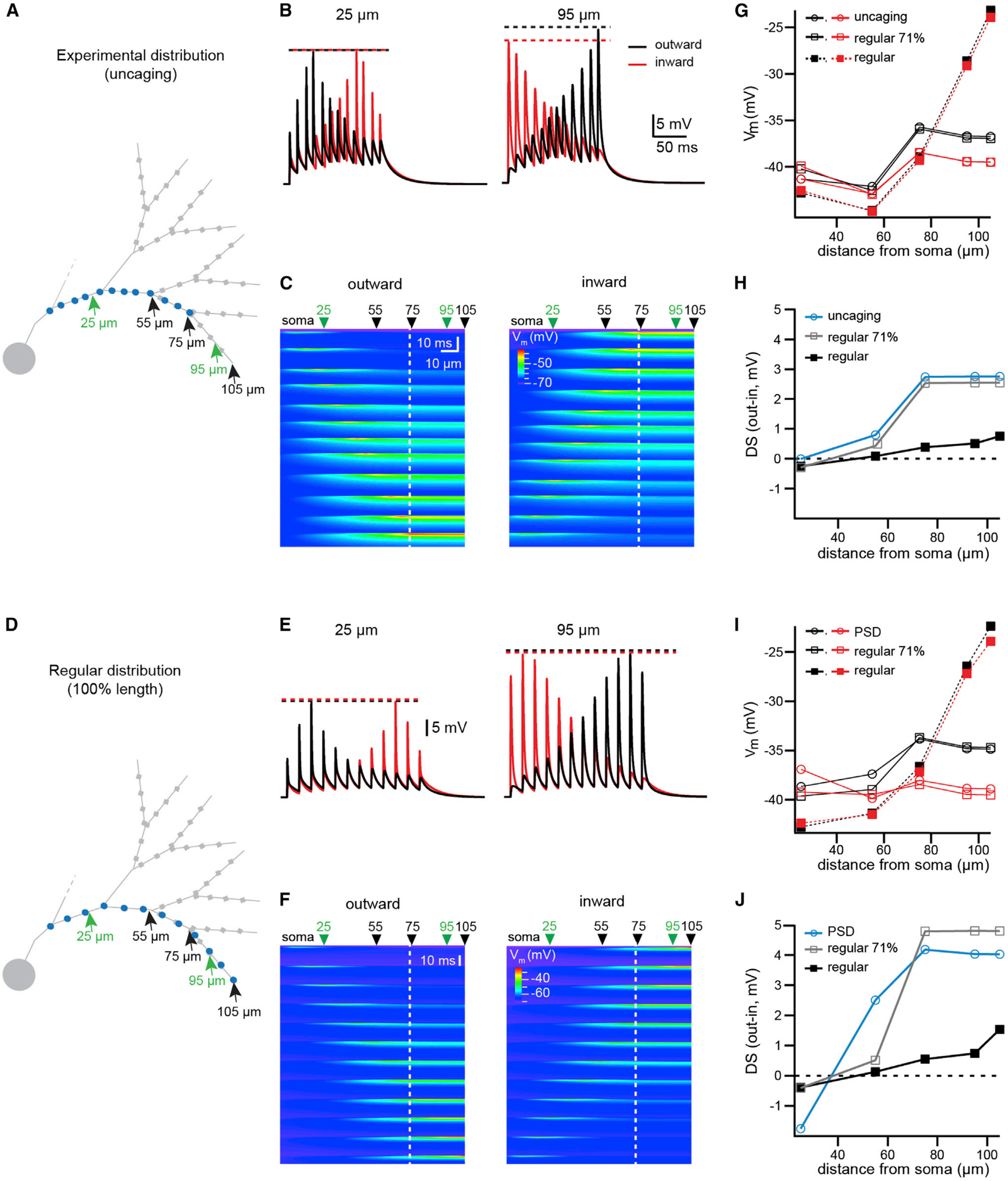

A
Experimental distribution (uncaging)
25 µm
55 µm
75 µm
95 µm
105 µm
B
25 µm
95 µm
outward
inward
5 mV
50 ms
C
outward
inward
soma
25
55
75
95
105
10 ms
10 µm
V_m (mV)
-50
-70
G
uncaging
regular 71%
regular
-25
-30
-35
-40
V_m (mV)
40
60
80
100
distance from soma (µm)
H
uncaging
regular 71%
regular
DS (out-in, mV)
5
4
3
2
1
0
-1
40
60
80
100
distance from soma (µm)
D
Regular distribution (100% length)
25 µm
55 µm
75 µm
95 µm
105 µm
E
25 µm
95 µm
5 mV
F
outward
inward
soma
25
55
75
95
105
10 ms
V_m (mV)
-40
-60
I
PSD
regular 71%
regular
-25
-30
-35
-40
V_m (mV)
40
60
80
100
distance from soma (µm)
J
PSD
regular 71%
regular
DS (out-in, mV)
5
4
3
2
1
0
-1
40
60
80
100
distance from soma (µm)

Figure 5. Synaptic input distribution supports DS of simulated dendritic voltage.
A) Ball-and-stick representation of a partial SAC dendritic tree, used for simulations of dendritic integration in a passive model. Blue circles: the location of synapses used in simulations, corresponding to the average location of putative synapses determined from uncaging. Green arrows: locations where the dendritic voltage is plotted in **B**; black arrows: locations where the peak of the dendritic voltage is plotted in the summary in **G-H**. Grey squares: wider compartments of the distal dendrite representing varicosities. **B**) Simulated dendritic voltage at two locations (indicated by green arrows in **A**), in response to the outward (black traces) or inward (red traces) activation of the synapses displayed in **A** at a speed of 500 µm/s. Dotted lines: amplitude of the peak of the synaptic response in each condition. **C**) Heat map of simulated dendritic voltage measured along the entire dendritic branch containing the activated synapses (x-axis) for the duration of the stimulus (y-axis). The color scale depicts the peak amplitude of the depolarization. *Left plot*: response to outward stimulation. *Right plot*: response to inward stimulation. At the peak of the activation of each synapse, the local voltage propagates with little electrotonic attenuation to the dendritic tip due to the end effect of the electrical cable. Green arrows: the two positions along the dendrite corresponding to the traces in **B** (25 and 95 µm from the soma); black arrows: locations where the peak of the dendritic voltage is plotted in the summary in **G-H**. The white dotted line indicates the location of the most distal synapse. **D**) Same as **A**, but blue circles indicate the location of regularly distributed synapses, the most distal synapse being located at the tip of the dendrite. For the regular distributions, the average density is the same as the experimental distribution determined with uncaging (0.09/µm). **E**) Same as **B**, for the gradient of regular synapses stopping at 100% of the dendritic length (displayed in **D)**. **F**) Same as **C**, for the gradient of regular synapses stopping at 100% of the dendritic length (displayed in **D)**. **G**) Plot of the maximum simulated dendritic voltage during inward (red) or outward (black) activation of synapses, measured at several dendritic locations, for the experimental distribution of synapses (circles, solid lines), a distribution of regularly spaced synapses with the most distal synapse located at 71% of the length of the dendrite as in the experimental distribution (open squares, solid lines), and the regular distribution stopping at the tip of the dendrite (closed squares, dotted lines). **H**) Summary plot showing the DS (defined as the difference of the peak dendritic voltage measured during outward and inward activation of inputs) at various dendritic locations for the different synaptic distributions (experimental distribution of synapses, circles, light blue; regularly spaced synapses with the most distal synapse located at 71% of the dendritic length, open squares, grey; regular distribution stopping at the tip of the dendrite, closed squared, black). **I**) Same as **G**, using synapse gradients determined from the average locations of PSD95 labeling (see **Fig. S5**). The regular distributions in this plot have the same average synaptic density as the experimental distribution from PSD95 labeling (0.2/µm). **J**) Same as **H**, using synapse gradients determined from the average locations of putative PSDs.

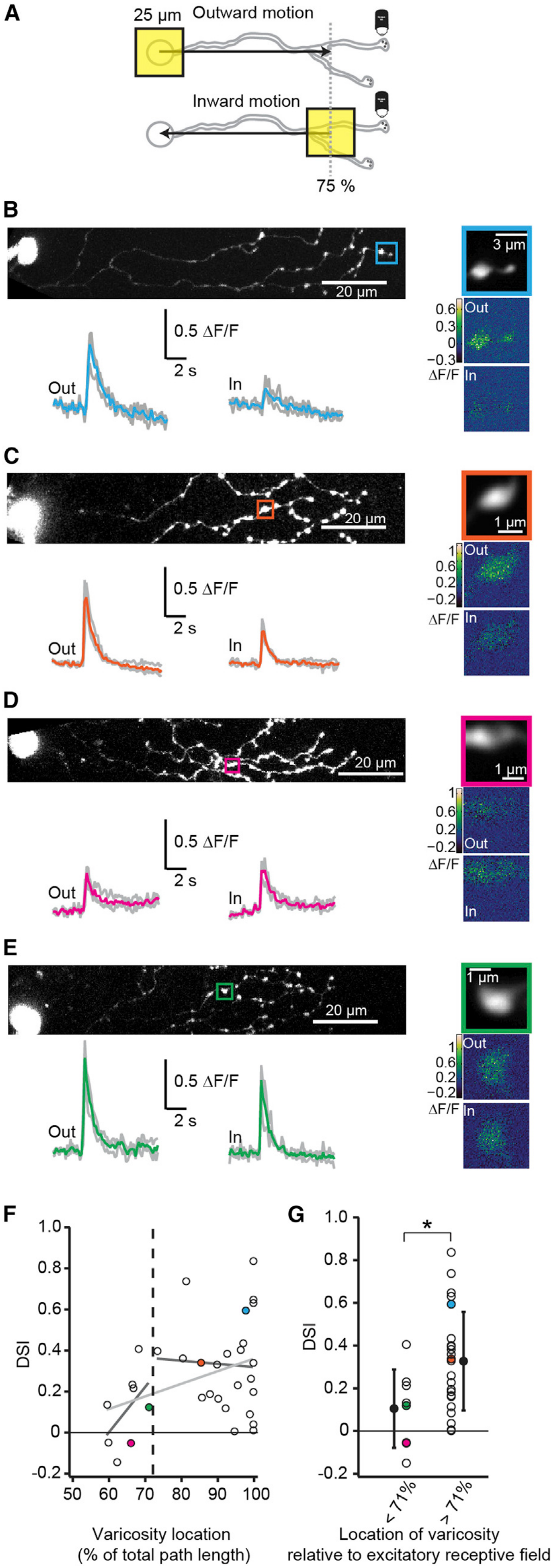

Figure 6. DS of varicosities depends on varicosity location
A) Schematic showing imaging of a distal varicosity from an OGB-1-filled SAC presented with a 25 μm square of light moving either outward from the soma toward the distal dendrites or inward from the distal dendrites toward the soma. The stimulus was restricted to 75% of the dendritic radius (grey dotted line). **B-E**) Four examples of Ca^{2+} responses to stimulation with moving squares. **B** is an example of an outward-preferring varicosity near the end of the dendrite. **C** is an example of a more proximal varicosity that is strongly direction selective for outward motion. **D** is an example of a slightly inward-preferring varicosity. **E** is an example of an untuned varicosity.
Top left: 2-photon fluorescence image of SAC filled with OGB-1 (z-projection). The square indicates the imaged varicosity. The soma is on the left.
Top right: Average intensity projection of the imaged varicosity during the entire experiment.
Bottom left: ΔF/F (grey) following visual stimulation with a 25 μm moving square either outward from the soma toward the end of the dendrites ("out") or inward from the distal dendrites toward the soma ("in"). Colored traces: averages of the three trials.
Bottom right: Maximal ΔF/F responses of the imaged varicosities to a single presentation of the moving square moving outward ("out") or inward ("in") along the dendritic radius. **F**) Direction selective index (DSI) for varicosities from 33 cells in response to inward vs. outward moving squares (black circles) as a function of the varicosity location normalized to the path length of the dendrite. A positive value for the DSI indicates a larger response for outward motion compared to inward motion. Colored dots are the DSIs for the example cells in **B-E.** Black dotted line: average length of the excitatory receptive field predicted from uncaging (see **Fig. 3**). Light grey line is a linear fit to the entire data set (slope = 0.006, r2 = 0.134) while dark grey lines are fits to the varicosities inside vs. outside of the receptive field detected from uncaging (inside: slope = 0.022, r2=0.248; outside: slope = -0.002, r2 = 0.002). **G**) DSI for varicosities from 33 cells (black circles) sorted by whether they are within (< 71%; 8 cells) or outside (> 71%; 25 cells) of the mean excitatory receptive field predicted from uncaging (black dotted line in **F**). Colored dots are the DSIs for the example cells in **B-E.** Open circles = means; error bars = S.D. * = $p < 0.05$, Student's t-test.

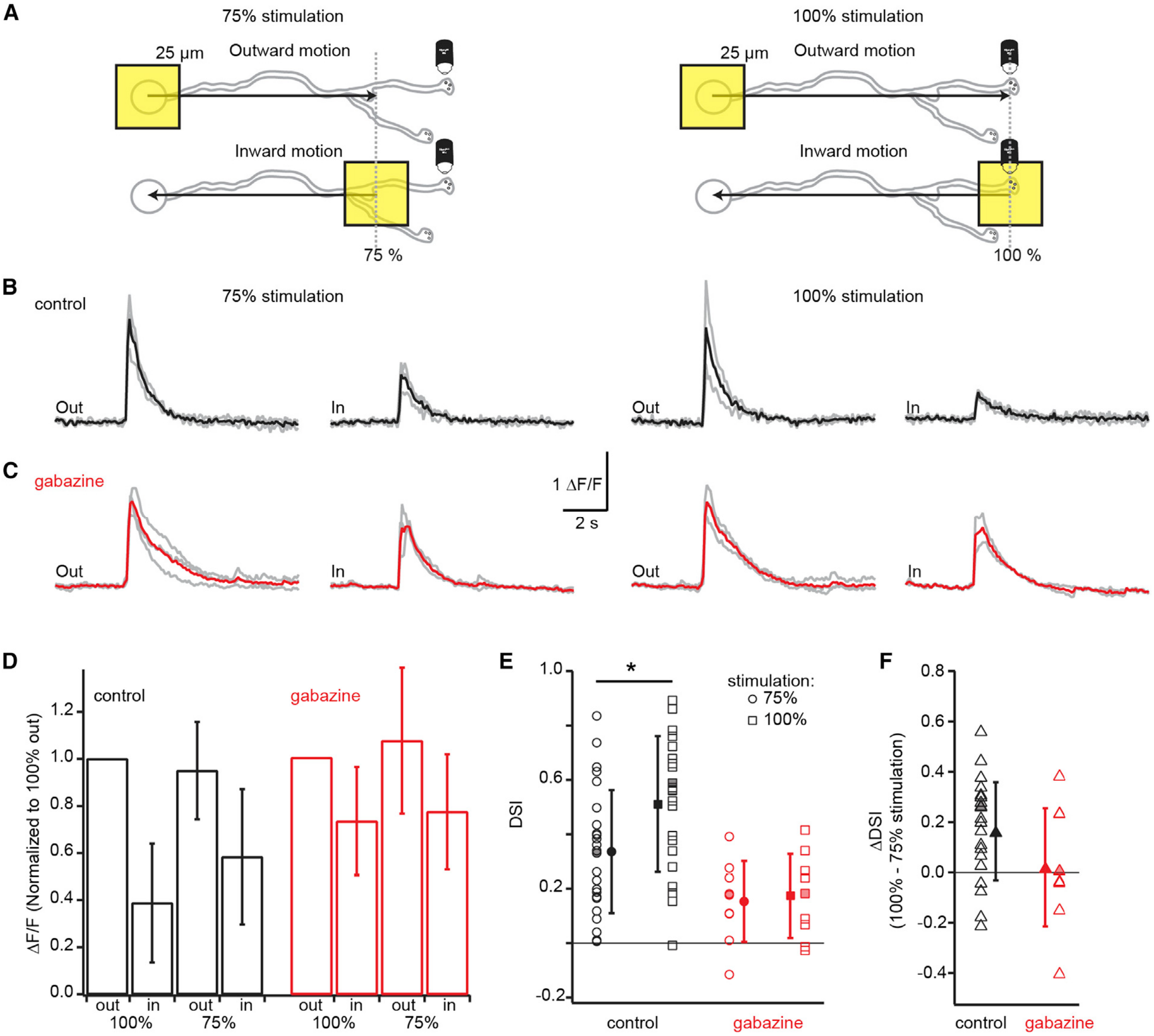

Figure 7. GABAergic lateral inhibition enhances DS

A) Schematic showing imaging of a distal varicosity from an OGB-1-filled SAC presented with a 25 µm square of light moving either outward from the soma toward the distal dendrites or inward from the distal dendrites toward the soma. *Left*: Visual stimulation restricted to 75% of the dendritic radius (grey dotted line), which activated less of the lateral inhibition from neighboring SACs. *Right*: Visual stimulation of 100% of the dendritic radius (grey dotted line), which activated more of the lateral inhibition. **B**) Ca^{2+} responses (ΔF/F, grey) from a single varicosity following visual stimulation with a 25 µm moving square either outward from the soma toward the end of the dendrites ("out") or inward from the distal dendrites toward the soma ("in") in response to either the 75% stimulation (left traces) or the 100% stimulation (right traces) depicted in **A**. Black traces: averages of three trials. **C**) Same as **B** but showing the responses of a different varicosity from a different cell in the presence of 5 µm gabazine to block $GABA_a$ receptors. Red traces: averages of the three trials. **D**) The average maximum ΔF/F for varicosities in control conditions (black bars) in response to 100% (23 cells) or 75% (26 cells) outward and inward stimulation normalized to the response to 100% outward stimulation and in 5 µm gabazine (red, 9 cells for both 75% and 100% stimulation). The control and gabazine populations are separate. Error bars = S.D. **E**) Direction selective index (DSI) for the varicosities in **D** in response to 75% stimulation (circles) or 100% stimulation (squares) in control conditions (black) or 5 µM gabazine (red). Solid symbols = mean; error bars = S.D. * = paired t-test: $p<0.05$, n=22 varicosities for which both 75% and 100% stimulation was measured. Shaded-in symbols: example cells in **B** and **C**. **F**) The ΔDSI showing the difference between the DSI in response to 100% vs 75% stimulation in varicosities in control conditions (black triangles, 22 cells) and in 5 µm gabazine (red triangles, 9 cells). Solid triangles: means; error bars = S.D. Shaded-in symbols: example cells in **B** and **C**.

Figure S1 (DiGregorio, Feller)

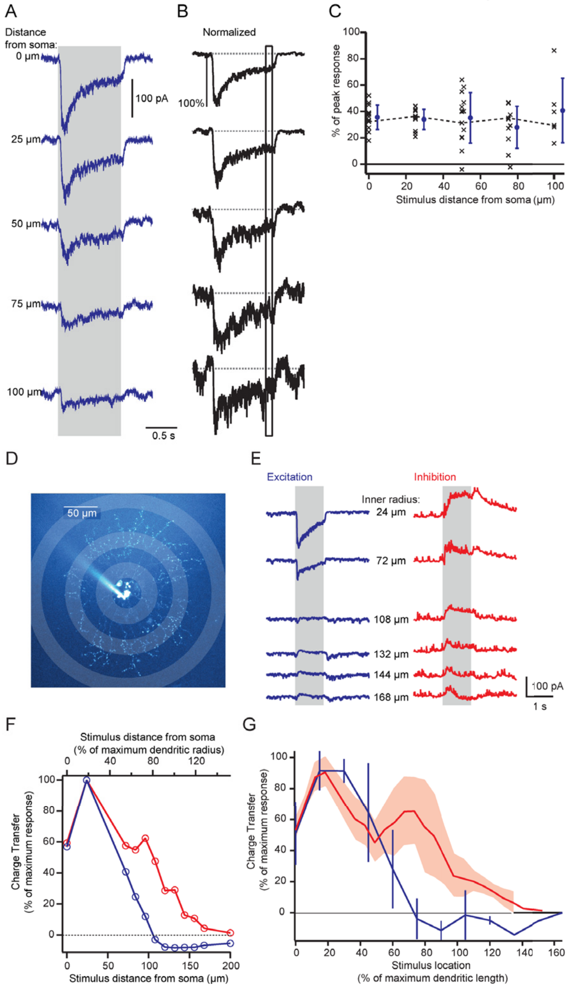

Figure S1. Kinetics of bipolar cell release onto SAC dendrites do not vary based on input location and inhibitory receptive field is larger than dendritic field. Related to Figure 1

A) Voltage clamp recordings (holding potential = -72 mV) in response to stimulation with 25 µm diameter spots centered at different distances from the soma. Grey box indicates the timing of the light stimulus. Traces are averages of 3 responses. **B**) The same responses as in **A** normalized to the maximum amplitude (averaged over 50 ms window) during the first 300 ms of the response. The box indicates the period of time used to assess the sustained component of the response in **C**. Grey dotted lines mark the baseline. **C**) Plot showing the amplitude of the sustained component of the response to spots at different distances from the soma as a percentage of the maximum amplitude. Black x are individual cells, blue dots are averages, error bar = S.D. Dotted line connects responses for the cell in **A** and **B**. N = 14 cells. **D**) Schematic showing anatomical location of visual stimulation rings overlaid with 2-photon fluorescence projection of a SAC at low magnification (20x). Rings shown have an inner radius of 24, 72, and 132 µm. Ring thickness was 24 µm. **E**) Voltage clamp recordings (holding potentials = -72 mV (blue) and 0 mV (red)) from the SAC in **D** during stimulation with stationary rings with different inner radii. Traces are averages of 4 sweeps. Grey box indicates the timing of stimulus presentation. **F**) Excitatory and inhibitory charge transfers calculated from the recordings in **E** and normalized to the maximum charge transfers plotted as a function of the distance from the inner radius of the ring stimulation to the soma. Blue trace is the excitatory receptive field and red trace is the inhibitory receptive field. Top axes show ring inner radius distance normalized to the maximum dendritic radius. For this cell, the maximum dendritic radius was 130 µm. **G**) Excitatory charge transfer calculated for 4 cells plotted as a function of the length of the inner radius of the stimulus from the soma. Axes are normalized to the maximum charge transfer response and maximum dendritic radius, respectively. Blue and red lines are binned averages of the responses from each cell for excitation and inhibition, respectively; error bars/shading are S.D.

Figure S2 (DiGregorio, Feller)

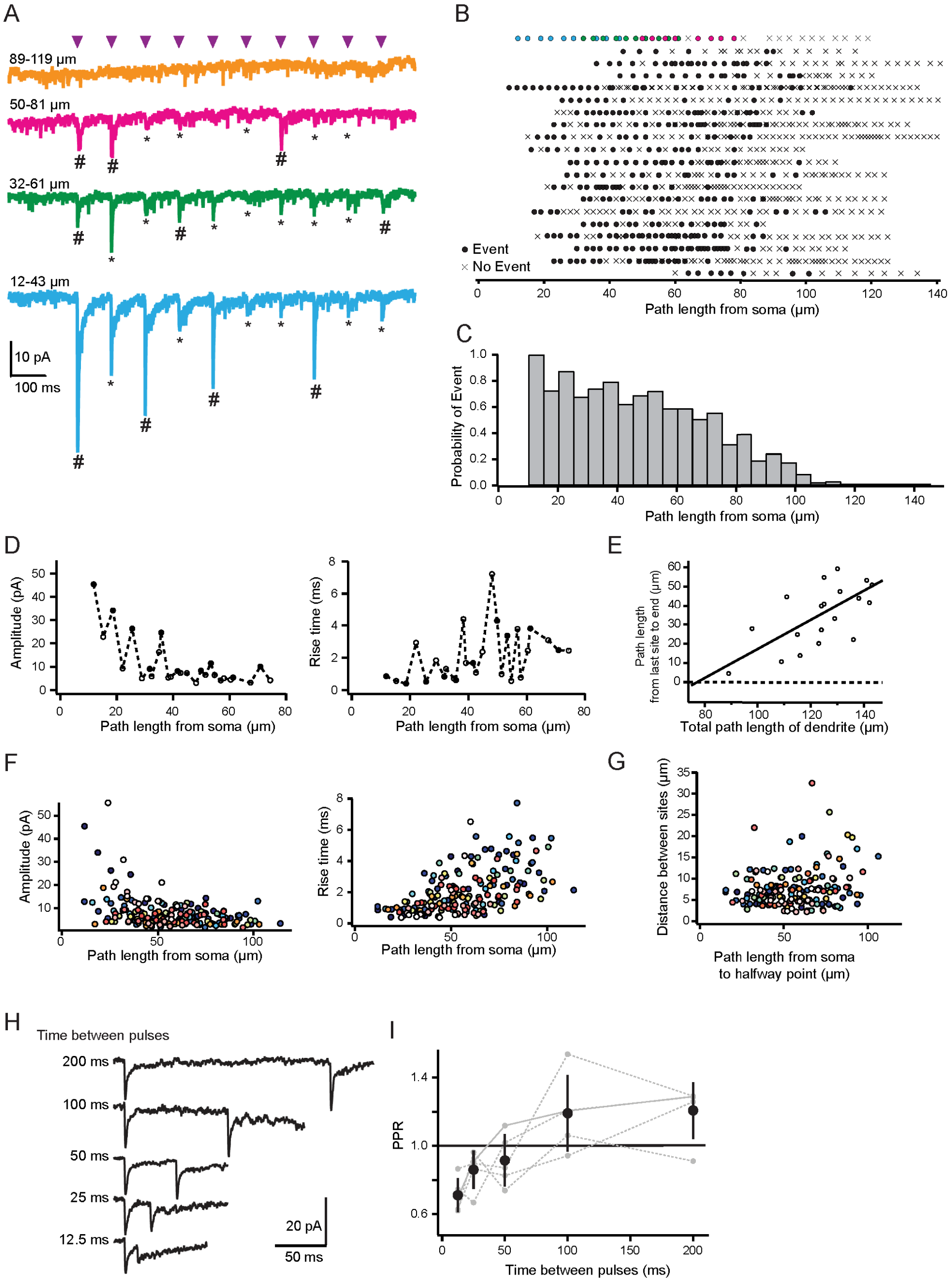

Figure S2. Procedure for determining locations of putative postsynaptic sites using kinetics of uncaging evoked events. Related to Figure 3.
We used event detection combined with selection of uncaging-evoked EPSCs with locally-maximal amplitudes to determine the location of putative postsynaptic sites.
A) Same recordings as in **Figure 3B** showing dendritic locations of detected uncaging-evoked events (*) and events further determined to be the sites of putative postsynaptic sites (#). For event detection, uncaging-evoked events were included if the amplitude was greater than 6 times the S.D of the baseline noise, measured during the 3 ms prior to uncaging. This conservative threshold was necessary because of the large amount of spontaneous activity in SACs. To determine putative postsynaptic sites, we identified locations along the dendrite in which the amplitude of uncaging-evoked currents were maximal relative to its neighbors within 5 µm (local maximum). This strategy minimized double counting, but could also lead to undercounting of putative postsynaptic sites for dendritic segments with high synapse density. **B**) Dendritic locations of uncaging-evoked events. Each row is a different dendrite (n = 20 dendrites from 15 cells). The top row shows the event locations color-coded to match the traces in **A**. **C**) Probability histogram of detecting events from **B** in 5 µm bins as a function of the path length from the soma. **D**) Amplitude and rise time of uncaging-evoked events from the cell in **A** as a function of path length from the soma to the uncaging site. Putative postsynaptic sites were selected from uncaging-evoked events based on the amplitude of the events. Putative postsynaptic sites were defined as locally maximal in amplitude (filled circles) and the other events (open circles) were discarded. For well space-clamped locations proximal to the soma, the location of locally maximal amplitude almost always had locally minimal rise times, confirming the presence of a postsynaptic site. For distal locations, we did not observe the amplitude-rise time correlation, presumably due to dendritic filtering. **E**) The path length for dendrites in **Figure 3C** from the most distal detected putative postsynaptic site ("last site") to the end of the dendrite plotted as a function of the total path length of the dendrite. The black line is a linear fit with $r^2 = 0.48$. **F**) Rise time and amplitude of the uncaging-evoked events from putative postsynaptic sites from **Figure 3C-D** plotted as a function of path length from the soma. **G**) The distance between pairs of adjacent putative postsynaptic sites from **Figure 3C-D** plotted as a function of the path length from the soma to the halfway point between each pair of putative postsynaptic sites.

To determine the minimum time between uncaging pulses to avoid uncaging when receptors were desensitized, we performed a paired-pulse experiment. We uncaged at the exact same location over a putative postsynaptic site and varied the interval between pulses to measure the desensitization period of the receptors.
H) Voltage clamp recordings (holding potential = -72 mV) from a SAC in response to glutamate uncaging at a single dendritic site. The time between pairs of uncaging pulses was varied and is listed to the left of each trace. Traces are averages of 10 sweeps. **I**) Paired pulse ratio (PPR) as a function of the time between pulses for 5 dendritic sites from 3 cells. Grey lines = individual sites; solid grey line = the cell in **H**; black spots = the mean PPR across sites; error bars = S.D.
For 5 cells, we found a PPR equal to or greater than 1 when the time between uncaging pulses was 100 ms or more. Thus, we used intervals of 100 or 200 ms to map the uncaging responses.

Figure S3 (DiGregorio, Feller)

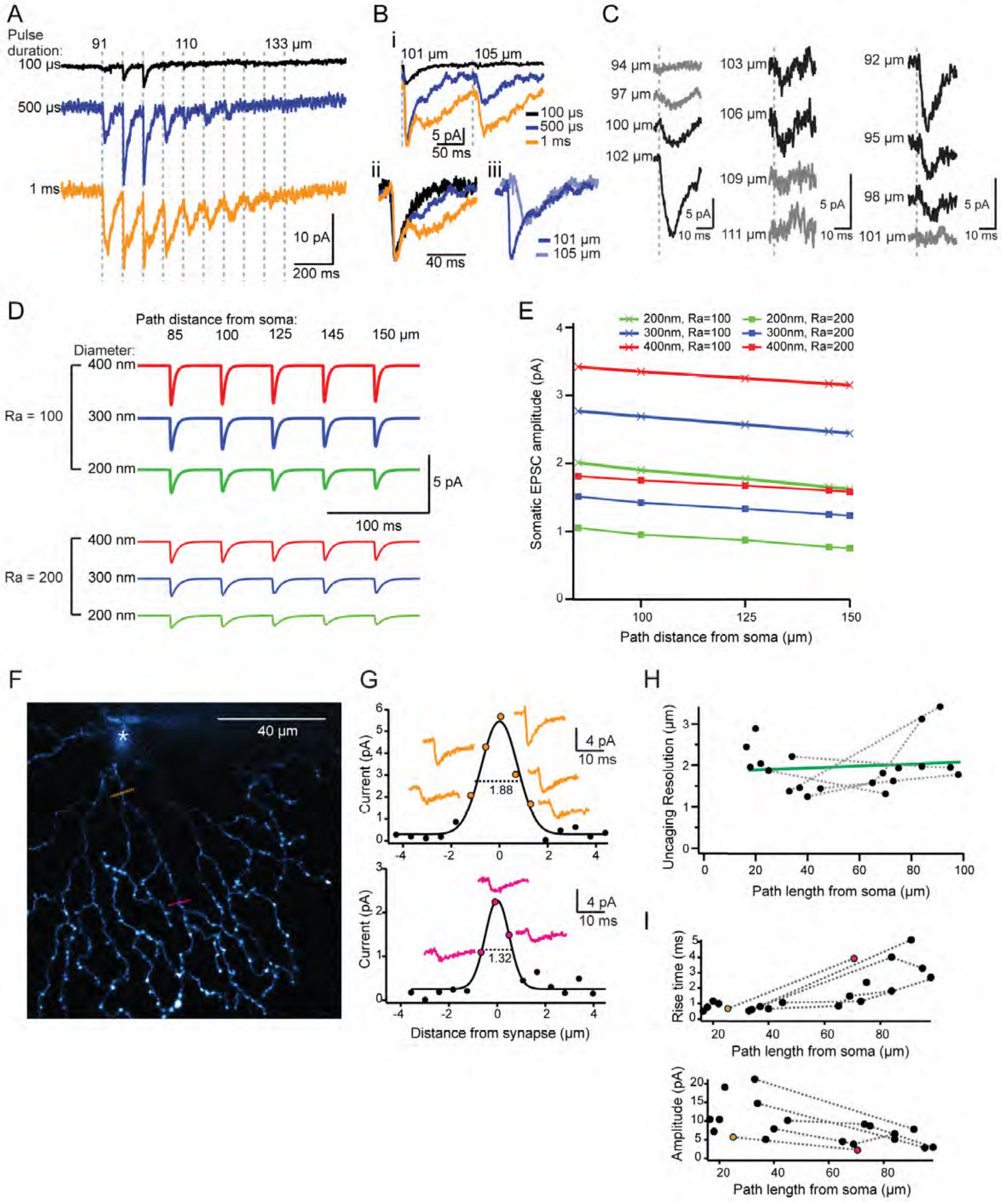

Figure S3. Glutamate uncaging duration and resolution are sufficient to detect postsynaptic sites in distal dendrites if postsynaptic sites are present. Related to Figure 3.

We wanted to determine whether an absence of uncaging-evoked events in distal sites was due to an absence of receptors or the inability to record these currents from the soma. To test this, we performed two experiments. First, we increased the uncaging laser pulse duration while uncaging over distal dendrites to reveal the presence of AMPARs with a larger dose of glutamate.

A) SAC current responses (holding potential = -72 mV) to glutamate uncaging at 10 different dendritic sites (path length from soma indicated above traces) with three different laser pulse durations. The start of laser pulse illumination is indicated by the grey dashed lines. For part **A-C**, all traces are averages of 10 sweeps. **B**) **i**: Expanded timescale of currents evoked at two adjacent dendritic sites from **A**. **ii:** Normalized uncaging-evoked currents at 101 µm show that a fast-rising response is detected at all laser pulse durations. **iii**: Responses to 500 µs uncaging pulse at the two adjacent sites from **i** overlaid to demonstrate that sites not showing a response at short laser pulse durations never evoke fast-rising events, as would be expected if a prominent number of AMPARs were present at the site of uncaging. Note that because of the close location of the two sites, dendritic filtering also cannot account for the difference (see below for more detail). **C**) Voltage clamp recordings (holding potential = -72 mV) from three cells in response to glutamate uncaging at very distal dendritic sites (path length from soma indicated to the left of the trace) using a 100 µs uncaging laser pulse demonstrating detection of glutamate receptors. Black traces were events detected using event detection criteria (see Methods), while adjacent grey traces were concluded to have no event. We found that, while new events emerged when the pulse duration increased (**A**), these events display the typical kinetics of glutamate spillover (DiGregorio et al., 2007) (**B**, events recorded at >105 µm from soma), while synaptic sites showed a fast and slow phase typical of on-synapse activation followed by glutamate spillover onto the same synapse (events at <105 µm from the soma). Based on this experiment, we determined that the 100 µs uncaging laser pulse duration was sufficient for detection of distal synapses (**C**) while optimizing resolution and avoiding spillover.

Second, we examined theoretically whether there could be a decreased chance of detecting distal AMPAR clusters due to dendritic filtering.

D) and **E**) Numerical simulations of somatic EPSCs in a passive neuron under voltage-clamp (with C_m =1 pF/cm^2, R_m = 21700 Ω-cm^2, R_a = 100 Ω-cm or 200 Ω-cm. The amplitude of g_{syn} was set to reproduce experimental miniature EPSCs recorded from SACs (data not shown). Passive properties were assumed uniform across the cell. Pipette resistance was set at 20 MΩ. The idealized SAC dendritic morphology has a uniform diameter of 0.2 -0.4 µm (green, blue, and red traces), 3 dendritic branch points, and a maximum length of 150 µm. **D**) Traces of simulated EPSCs in response to an evoked conductance (g_{syn}) at input locations at different path distances from the soma. **E**) The peak amplitude of somatic EPSCs in response to a simulated evoked conductance at different path distances from the soma.

This simulation revealed that dendritic filtering, while present at distal sites, does not increase dramatically across the region of dendrite where the most distal synapses were observed, even for diameters as narrow as 0.2 µm. Thus we predict that currents arising from distal synapses should be detectable.

To determine whether the uncaging resolution is affected by the dendritic location of the uncaging site, we uncaged along lines perpendicular to sites previously determined to contain putative postsynaptic sites at different distances from the SAC soma. We determined the effective uncaging resolution by fitting the maximal responses to a Gaussian distribution and measuring the full-width half maximum (FWHM).

F) 2-photon fluorescence z-projection of a SAC showing locations of uncaging sites used to determine uncaging resolution (orange and pink lines). White asterisk = location of cell soma. **G**) Amplitude of uncaging-evoked current as a function of the distance from the putative postsynaptic site to the uncaging site for the cell in **F**. Colored traces are voltage clamp recordings (holding potential = -72 mV) showing events detected by uncaging (averages of 10 sweeps). Solid black line is the Gaussian fit; the dotted line is the full-width half-max (FWHM) of the fit in microns. **H**) The uncaging resolution (FWHM of the Gaussian fits determined as in **G**) as a function of the path length from the soma. The mean uncaging resolution was 2±0.6 µm (n=20 measurements from 11 dendrites in 8 cells). Grey dotted lines connect measurements from different sites on the same dendrite. Green line is a linear fit (slope = 0.002, r^2=0.013). **I**) Rise time and amplitude of uncaging evoked events from dendritic locations in **H** plotted as a function of path length from the soma (n=20 measurements from 11 dendrites in 8 cells). Events shown were found to be closest to the peak amplitude of the Gaussian fits used to determine the uncaging resolution; colors correspond to the traces in that figure. Dotted lines connect samples measured from the same dendrite.

Figure S4 (DiGregorio, Feller)

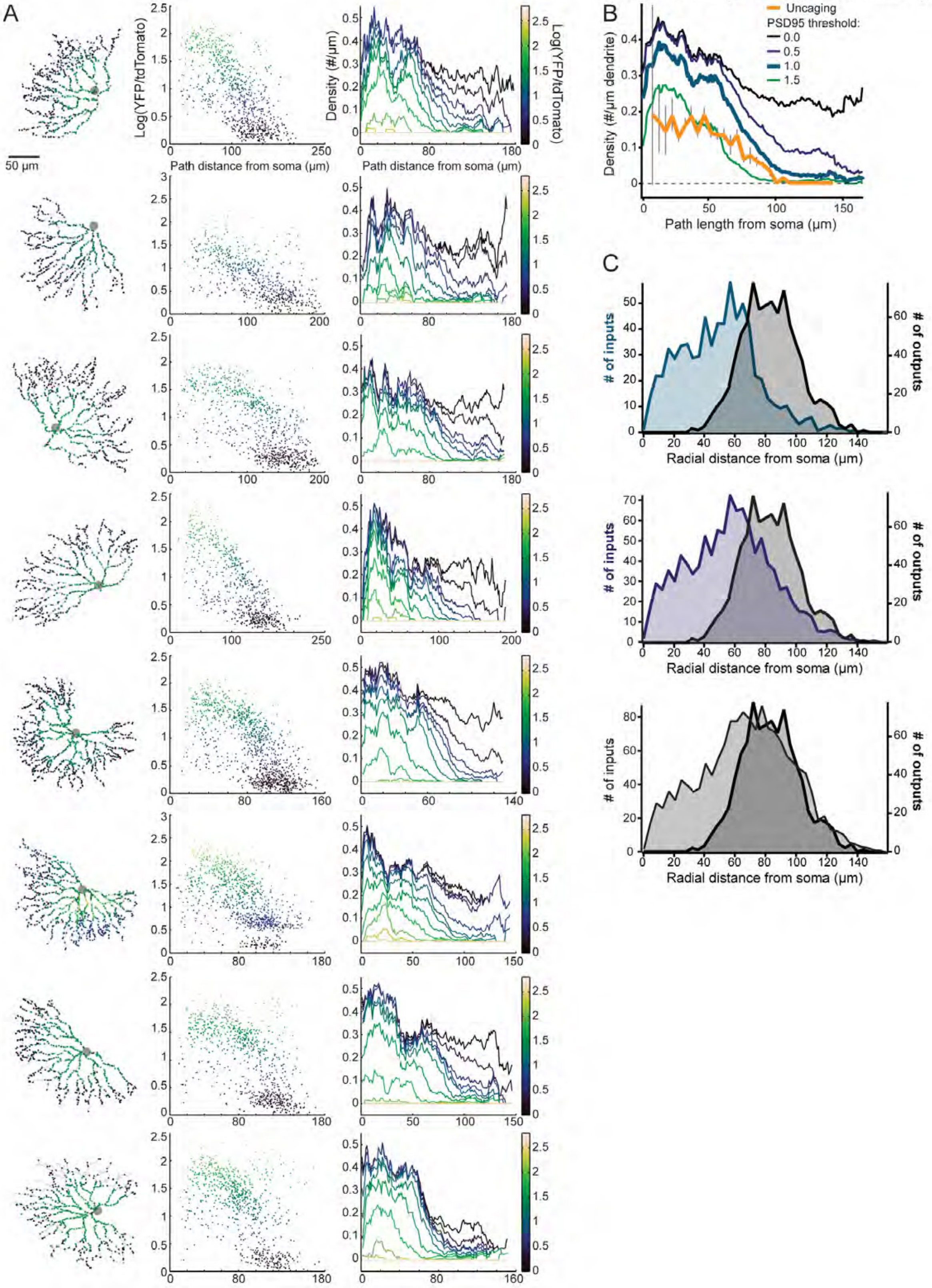

Figure S4. Effect of threshold on puncta detected from eight SACs labeled with PSD95-YFP. Related to Figure 4.
To identify PSD95 puncta, we computed the log ratio of the intensity of YFP fluorescence to tdTomato fluorescence for each pixel, $R=\log(F_{YFP}/F_{tdTomato})$. Variations in R are independent of imaging conditions that linearly scale the ratio of F_{YFP} and $F_{tdTomato}$ and help to normalize for bleed-through from the tdTomato channel into the YFP channel, which is more substantial in distal dendrites (see example images in **Figure 4C**). PSD95 puncta were subsequently identified using a segmentation algorithm that detected spatial variations of R. We systematically varied the threshold value of R to determine the effect of this value on the distribution of puncta as a function of distance along the dendrite. Across all cells, a threshold of $R=1$ represented a transition—a range of higher thresholds did not vary the distributions substantially while lower thresholds greatly increased the number of distal puncta. In addition, values of $R<1$ corresponded to F_{YFP} that was indistinguishable from $F_{tdTomato}$ bleedthrough (see example in **Figure 4A,C**).

A) First column: Skeleton analyzed dendritic arbors of all 8 cells with identified PSD95 puncta used for analysis (colored dots). Colors represent $R = \log(F_{YFP}/F_{tdTomato})$ within each punctum, which was used for thresholding puncta to include in subsequent analysis. Second column: For each cell, the R value within each punctum (dots) is plotted as a function of path distance from the soma. Third column: For each cell, the average linear density of PSD95 puncta as a function of path length from the soma is plotted using increasing thresholds of R to determine puncta to include in analysis. All colors correspond to the colormap on the right. **B**) This plot is the same as the plot in **Figure 4D** with the addition of three density lines showing additional threshold log ratios (green = 1.5; indigo = 0.5; black = 0.0), which demonstrate the average linear density of PSD95 puncta as a function of path length from the soma in 8 cells. **C**) Histogram of PSD95 puncta (left axis) from 8 cells using a threshold log ratio of 1.0 (top; same as **Fig. 4E displayed for comparison**), 0.5 (middle), or 0.0 (bottom), as well as the synaptic contacts with DSGCs (right axis, black), as a function of radial distance from the soma. Radial distances of synaptic contacts with DSGCs were measured from electron microscopy reconstructions of 24 SACs (Briggman et al., 2011).

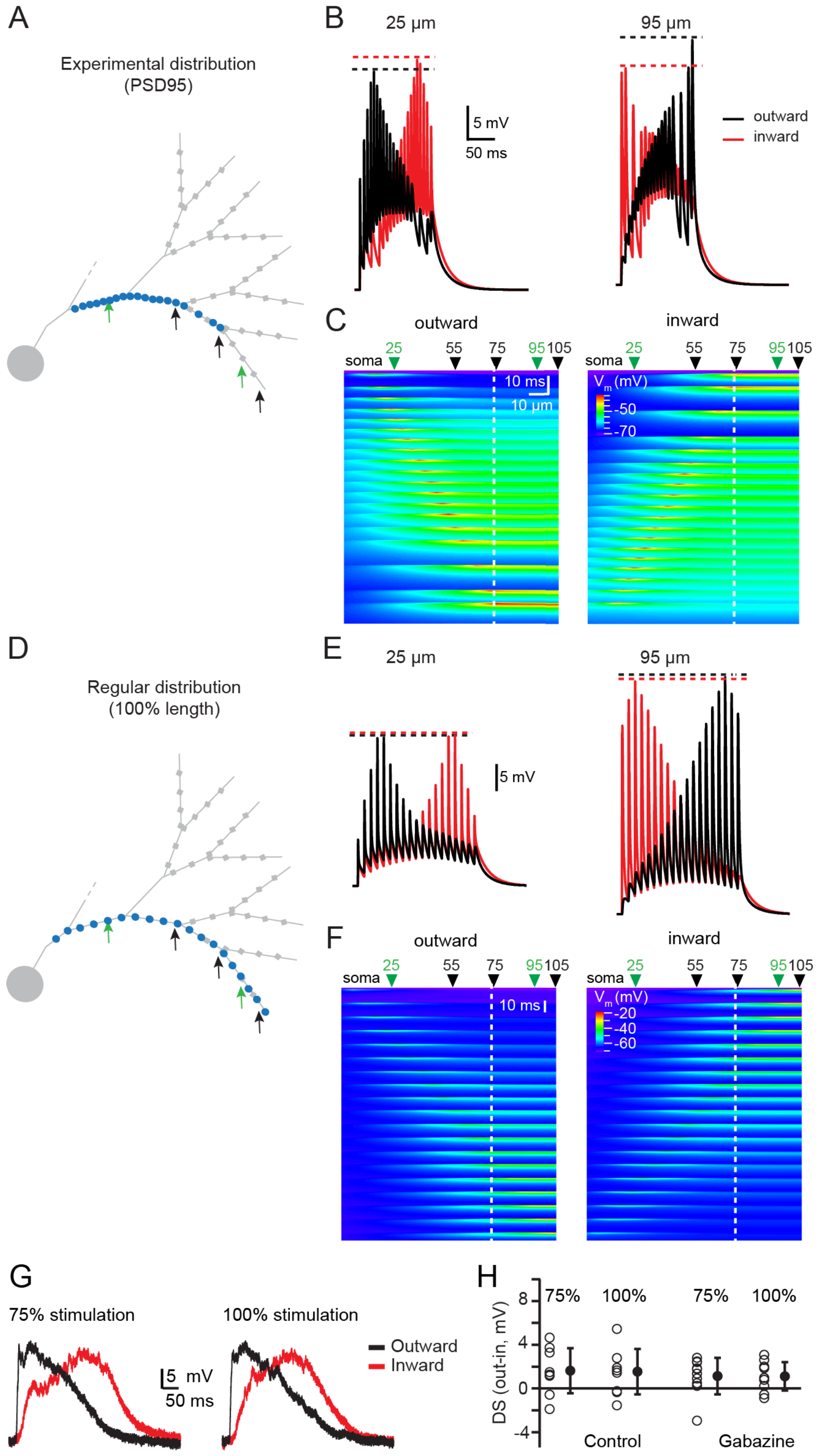
A
Experimental distribution
(PSD95)
B
25 µm
95 µm
5 mV
50 ms
outward
inward
C
outward
inward
soma
25
55
75
95
105
10 ms
10 µm
V_m (mV)
-50
-70
D
Regular distribution
(100% length)
E
25 µm
95 µm
5 mV
F
outward
inward
soma
25
55
75
95
105
10 ms
V_m (mV)
-20
-40
-60
G
75% stimulation
100% stimulation
Outward
Inward
5 mV
50 ms
H
75%
100%
75%
100%
DS (out-in, mV)
8
4
0
-4
Control
Gabazine

Figure S5. Synaptic input distribution supports direction selectivity of simulated dendritic voltage (PSD95 gradient). Related to Figure 5.

A) Ball-and-stick model of a partial SAC dendritic tree used for numerical simulations of dendritic integration. Blue circles indicate the location of synapses based on the distribution determined with PSD95 labeling (**Fig. 4**). Green arrows indicate locations where the dendritic voltage is measured. **B**) Dendritic voltage at two of the locations indicated by the green arrows in **A**, in response to the outward (black traces) or inward (red traces) activation of the synapses displayed in **A** at a speed of 500 µm/s. Dotted lines indicate the amplitude of the peak of the synaptic response in each condition. **C**) Heat map of dendritic voltage measured along the entire dendritic branch (x-axis) for the duration of the stimulus (y-axis) during which synapses, placed according to the average location of putative synapses determined from PSD95 labeling, are activated. The color scale depicts the amplitude of the depolarization. The left plot represents the response to outward stimulation, and the right plot the response to inward stimulation. At the peak of the activation of each synapse, the local voltage propagates with little electrotonic attenuation to the dendritic tip due to the end effect of the electrical cable. The green arrows above the plot indicate the two positions along the dendrite corresponding to the traces in **B** (25 and 95 µm from the soma), and the black arrows indicate the other locations where peak dendritic voltage is plotted on the summary plot (**Fig. 5I-J**). **D**) Same as **A**, but blue circles indicate the location of regularly distributed synapses with the same average density as in A, the most distal synapse being located at the tip of the dendrite. **E**) Same as **B**, but for the regular distribution of synapses extending to the tip of the dendrite, as displayed in **D**. **F**) Same as **C**, but for the regular distribution of synapses extending to the tip of the dendrite, as displayed in **D**. **G**) Somatic current clamp recordings from SACs during stimulation with moving squares presented over 75% (left) or 100% (right) of the dendritic radius. Responses to motion outward from the soma to the distal dendrites (black) and inward from the distal dendrites to the soma (red) are shown.

H) DS of the peak somatic voltage measured in current clamp during visual stimulation with moving squares traversing 75% or 100% of the dendritic radius. Data are from 9 cells in control conditions and 10 cells in the presence of 5 µM gabazine. Note the similarity between these recordings and the simulations of the voltage at 25 µm from the soma in **B**. Also note that the results shown in **G** and **H** here suggest that the SAC is not a passive cell, but rather has active conductances that alter the direction preference recorded at the soma.

Varicosities outside the excitatory receptive field

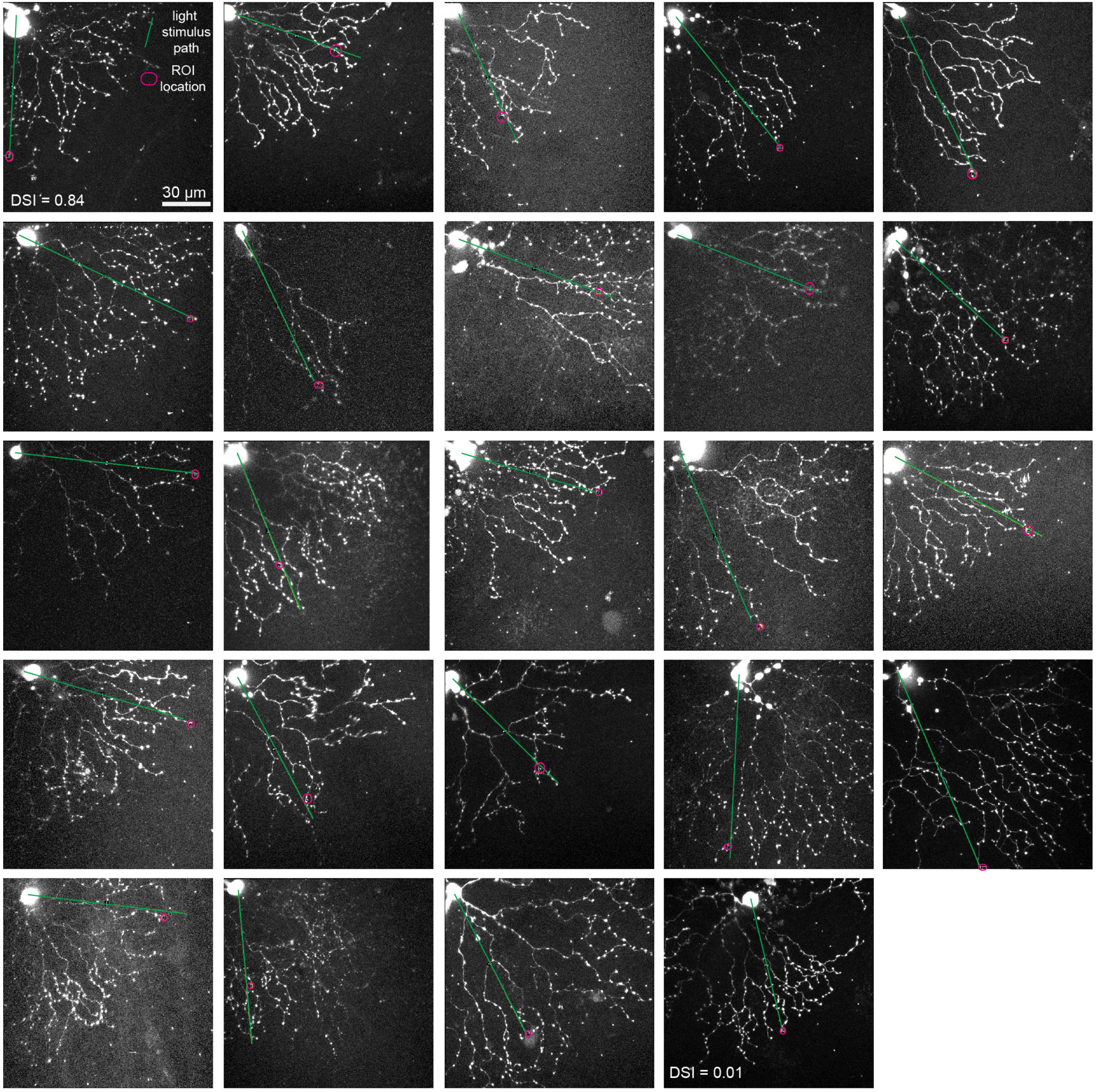

Varicosities within the excitatory receptive field

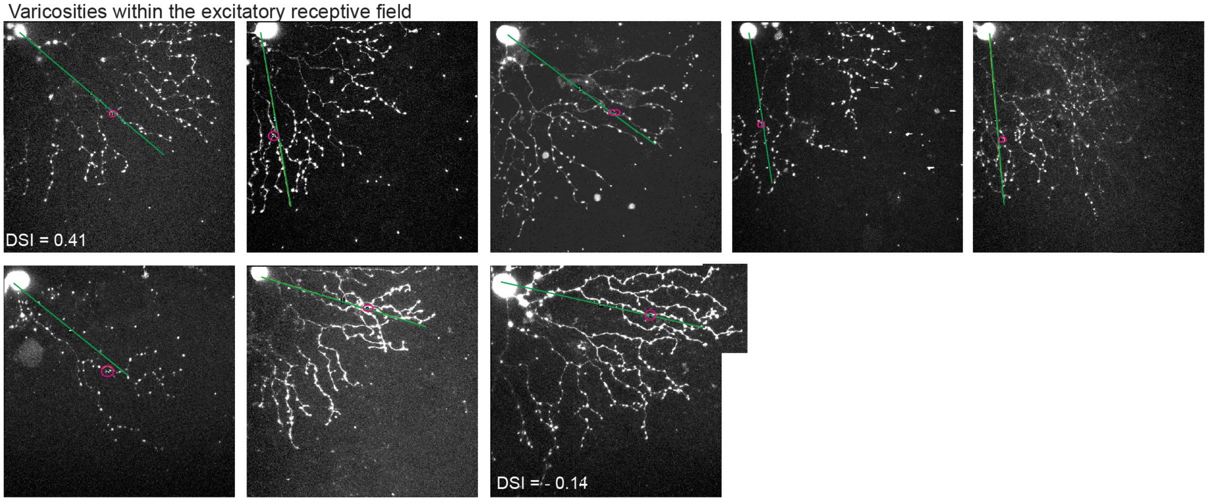

Figure S6. Locations of visual stimulation and imaged varicosities. Related to Figure 6.

Maximum intensity z-projections of 2-photon images of SACs filled with OGB-1 with the laser tuned to 800 nm. Images were acquired after measuring Ca^{2+} transients in the varicosities indicated (magenta circles) in response to visual stimulation (see **Fig. 6**). Squares of light (25 µm) were projected on the retina along either 75 or 100% (**Fig. 7)** of the path indicated in green. The exact extent of stimulation relative to the SAC arbor was determined post-hoc from these images and corrected if necessary (e.g. SAC #8 below). Images are divided into two groups: SACs for which the imaged varicosity was located outside of the SAC's predicted excitatory receptive field (**top**) and SACs for which the imaged varicosity was within the SAC's predicted excitatory receptive field (**bottom**). Images within groups are ordered from left to right by the DSI of the indicated varicosity, starting with the varicosity with the strongest preference for outward motion at the top left.

The DS of varicosities was variable, as observed in previous studies (Euler et al., 2002; Hausselt et al., 2007; Lee and Zhou, 2006; Yonehara et al., 2013) (**Fig 6.**), which may arise from the following factors: 1) inability to optimally stimulate along the SAC dendritic path due to sometimes tortuous dendritic morphology (see SAC #18 below) and 2) limiting the stimulation to inward vs. outward may sub-optimally activate a varicosity whose preferred direction is slightly off this axis, as seen in other studies (Euler et al., 2002; Yonehara et al., 2013).

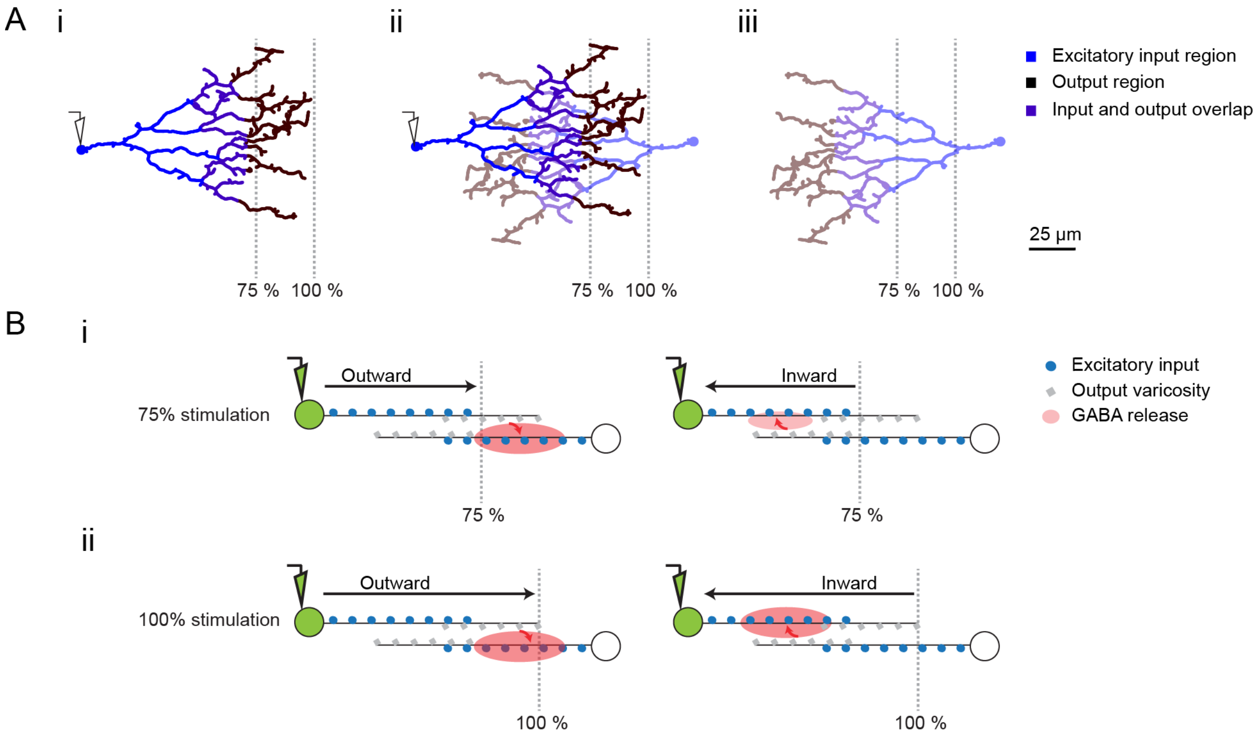
A
i
ii
iii
Excitatory input region
Output region
Input and output overlap
25 µm
75 %
100 %
75 %
100 %
75 %
100 %
B
i
75% stimulation
Outward
Inward
75 %
75 %
Excitatory input
Output varicosity
GABA release
ii
100% stimulation
Outward
Inward
100 %
100 %

Figure S7. **Schematic of dendrite-autonomous contribution to circuit-level computation of motion direction. Related to Figure 7.**

A) i) Partial skeleton of a SAC showing the locations of the excitatory input region predicted from uncaging (blue), the varicosity-rich GABAergic output region (dark brown) and the overlapping region containing inputs and outputs (purple). The grey dotted lines show 75% and 100% of the dendritic radius. The details of this skeleton are based on reconstructions of starburst cells and therefore accurately reflect the dendritic features.
ii) The dendrite in **i** overlaid with a neighboring SAC dendrite (the same dendrite rotated 180°), with somas offset by 150 μm. The output regions of the two SACs overlap and provide opportunities for lateral inhibition between neighboring SACs.
iii) The grey dotted lines are in the same positions as in **i** and **ii**, demonstrating the regions of the neighboring SAC stimulated when the SAC in **i** is stimulated over 75% vs. 100% of its dendritic radius. A much larger region of the neighboring SAC is stimulated during 100% stimulation, which could produce an increase in lateral inhibition for the recorded cell, particularly during inward stimulation (inward relative to the recorded cell).

B) Schematic describing the enhancement of direction selectivity in SAC dendrites through SAC-SAC inhibitory interactions. Green cell indicates SAC filled with OGB via patch pipette (the recorded cell). White cell is a neighboring SAC. Excitatory bipolar cell inputs to SACs are blue circles, presynaptic GABA release sites on SACs are grey squares, and extent and direction of GABA release is indicated by size of red cloud and direction of red arrow, respectively. Extent of GABA release is assumed to correlate with the amplitudes of Ca^{2+} transients in putative release sites.
<u>**i)** SAC-SAC interactions minimally affect SAC intrinsic direction selectivity during 75% stimulation</u>.
Left: Outward stimulation of the recorded SAC produces a large calcium transient in its varicosities resulting in GABA release onto neighboring SACs. In contrast, the neighboring SAC experiences little excitation from this “inward” stimulation, which minimally enters its excitatory receptive field and does not induce strong summation of excitatory potentials at its varicosities. Therefore, no GABA is released onto the recorded SAC from the neighboring SAC and therefore there is minimal lateral inhibition.
Right: Inward stimulation of the recorded SAC reduces summation of excitatory potentials in its varicosities, resulting in a smaller calcium transient compared to outward stimulation. In addition, despite the stimulation minimally entering the excitatory receptive field of the neighboring SAC**,** the neighboring SAC experiences greater summation of excitatory potentials due to the “outward” stimulation it receives, resulting in a small release of GABA onto the recorded SAC. The small GABA release suppresses the calcium response in the varicosities of the recorded SAC, increasing its direction selectivity.
<u>**ii)** SAC-SAC interactions enhance intrinsic SAC direction selectivity during 100% stimulation</u>.
Left: Outward stimulation of the recorded SAC produces a large calcium transient in its varicosities, resulting in GABA release onto neighboring SACs. In contrast, outward stimulation also enters a large portion of the neighboring SAC’s excitatory receptive field**,** but the “inward” stimulation does not induce strong summation of excitatory potentials at its varicosities and inhibition from antiparallel SACs further suppresses the response. Therefore, even though the 100% stimulus causes increased excitation onto the neighboring SAC compared to the 75% stimulus, the varicosities of the neighboring SAC still do not have enough Ca^{2+} influx to cause significant release of GABA onto the recorded SAC.
Right: Inward stimulation of the recorded SAC reduces summation of excitatory potentials in its varicosities, resulting in a smaller Ca2+ transient compared to outward stimulation. In addition, the stimulation activates a larger portion of the neighboring SACs excitatory receptive field than during the 75% stimulation. This increased outward stimulation of the neighboring SAC results in a large release of GABA onto the recorded SAC. The large GABA release further reduces the Ca^{2+} response in the varicosities of the recorded SAC, enhancing its direction selectivity about two-fold **(Figure 7)**.

In summary, SAC-SAC interactions serve to enhance the dendrite autonomous preference for outward motion we observe in SAC varicosities **(Figure 6)**. Importantly, dendrite autonomous direction selectivity also increases the importance of circuit level interactions; without the dendrite autonomous component of SAC direction selectivity, SAC-SAC signaling would cause GABA release onto a SAC even during outward motion, resulting in an overall reduction in SAC Ca^{2+} entry and a reduced preference for outward motion.

Chapter IV

A Dense Starburst Plexus is Critical for Generating Direction Selectivity

This chapter is a full reprint of Morrie & Feller, *Current Biology* (2018), in which I was the primary author. This work is included with permission from all authors.

Relevant Publication:
Morrie, R. D., & Feller, M. B. (2018). A Dense Starburst Plexus Is Critical for Generating Direction Selectivity. *Current Biology*, *28*(8), 1204–1212.

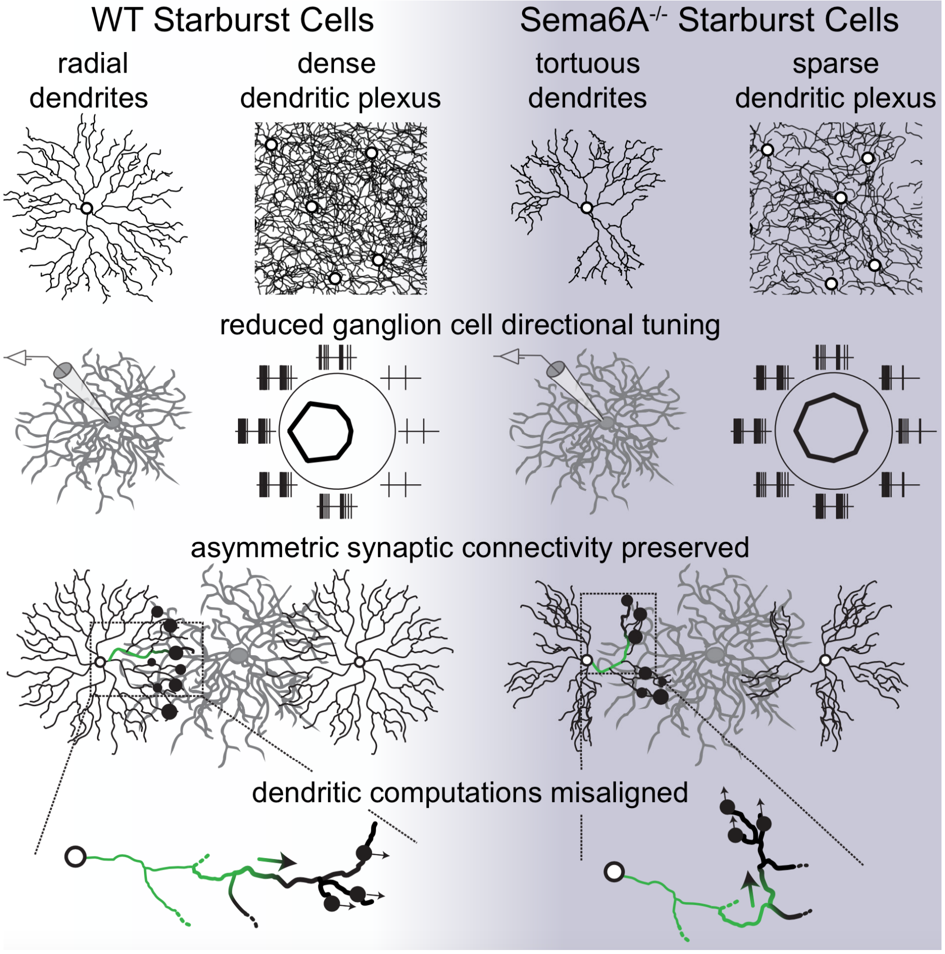

Abstract

Starburst amacrine cell (SAC) morphology is considered central to retinal direction selectivity. In *Sema6A*$^{-/-}$ mice, SAC dendritic arbors are smaller and no longer radially symmetric, leading to a reduction in SAC dendritic plexus density. *Sema6A*$^{-/-}$ mice also have a dramatic reduction in the directional tuning of retinal direction-selective ganglion cells (DSGCs). Here we show that the loss of DSGC tuning in *Sema6A*$^{-/-}$ mice is due to reduced null direction inhibition, even though strong asymmetric SAC-DSGC connectivity and SAC dendritic direction selectivity are maintained. Hence, the reduced coverage factor of SAC dendrites leads specifically to a loss of null direction inhibition. Moreover, SAC dendrites are no longer strictly tuned to centrifugal motion, indicating that SAC morphology is critical in coordinating synaptic connectivity and dendritic integration to generate direction selectivity.

Introduction

Starburst amacrine cells (SACs) have provided a rich model to analyze the relationship between neuronal morphology and circuit computations. SACs are radially symmetric retinal interneurons whose neurites function as both dendrites and axons, with pre-synaptic release sites restricted to the distal third and post-synaptic structures to the inner two-thirds of the neurite in mice [1-3] or along the entire neurite in rabbits [4, 5]. While most retinal neuron types tile the retina, SACs neurites, which we will henceforth refer to as dendrites, overlap extensively, forming a thick plexus of highly fasiculated processes across the inner retina. Furthermore, unlike other retinal interneurons whose arbors also form a highly overlapping plexus to serve a neuromodulatory role, such as dopaminergic amacrine cells, (reviewed in [6]), SACs contribute to direction selectivity, a precise circuit computation, via several subcellular features (reviewed in [7, 8]). First, SACs synapse onto direction selective ganglion cells (DSGCs) with subcellular precision – individual SAC dendrites form GABAergic synaptic connections with DSGC subtypes when the SAC dendrite is oriented in the DSGCs' null direction [9-11]. Second, individual SAC dendrites have direction selective Ca^{2+} responses in which motion away from the soma, termed centrifugal motion, generates a larger calcium transient in the distal release sites than motion toward the soma [1, 5, 12, 13].

To what extent are these synaptic and dendritic properties dependent on the density and radial symmetry of the SAC arbor? Two gene families have been identified as critical for SAC morphology. One is the protocadherin-γ (*Pcdhg*) cluster [14]. Each SAC expresses a single protocadherin isoform, leading to homotypic dendritic self-avoidance in individual SACs but synaptic connections between different SACs [14, 15]. Deletion of the entire *Pcdhg* cluster in SACs causes a collapse of the SAC structure [14], dramatically reducing direction selectivity in DSGCs, and alters the spatial pattern of inter-SAC inhibitory synaptic signaling [15]. However, whether the absence of DSGC direction selectivity directly results from changes in SAC-DSGC synaptic connectivity or SAC dendritic direction selective computations has not been explored.

A second gene family implicated in SAC dendritic development is semaphorins, a class of transmembrane proteins with multiple roles in synapse development, axon guidance, and laminar specification, especially within the retina (reviewed in [16]). SEMA6A is essential for the ON/OFF segregation found in the inner plexiform layer of the retina, and signals repulsively through PLEXINA2 to achieve proper lamination of ON and OFF SAC dendrites [17]. In addition, in *Sema6A*$^{-/-}$ mice, ON, but not OFF, SACs lose their radial morphological symmetry, appearing as if pie slices have been removed from their circular shape. In contrast to the *Pcdhg*$^{-/-}$ SAC phenotype, in which SAC dendrites fail to exhibit self-avoidance beginning at the soma, *Sema6A*$^{-/-}$ SAC phenotypes are milder, with SACs only failing to exhibit self-avoidance at the distal third of their dendrites [17]. Despite this more moderate phenotype in SACs, DSGCs in *Sema6A*$^{-/-}$ mice exhibit the same dramatic degree of reduced direction selective tuning as in *Pcdhg*$^{-/-}$ mice [15, 17].

Here, we take advantage of the altered SAC morphology in *Sema6A*$^{-/-}$ mice to determine how SAC dendritic architecture instructs synaptic wiring and subcellular computations in the direction selective circuit.

Results

DSGCs in Sema6A$^{-/-}$ *mice receive weak and symmetric ON response inhibition.*

Sema6A is expressed in ON, but not OFF, SACs and thus the *Sema6A*^{lacZ} allele in the gene-trap *Sema6A*$^{-/-}$ mouse [18] leads to a reduction specifically in ON SAC dendritic length and coverage, creating large gaps in the SAC plexus in the ON, but not OFF, sublamina of the IPL. These phenotypes were correlated with a significant decrease in DSGC tuning for ON, but not OFF, responses in these mice [17], but the underlying synaptic basis for this loss of direction selectivity remained unknown.

To determine whether SAC mediated inhibition onto DSGCs was affected in *Sema6A*$^{-/-}$ mice, we first performed targeted cell attached recordings from genetically identified DSGCs and stimulated them with moving bars. We observed a striking decrease in ON response direction selectivity due to an increase in null direction evoked firing (Figure 1A,B,E, Figure S1D), consistent with [17]. We then performed whole cell voltage clamp recordings from DSGCs, and observed a corresponding decrease in null direction evoked inhibition (Figure 1C,D,F) but not an increase in null direction evoked excitation (Figure S1A-C). We also observed a slight decrease in OFF direction selectivity, (Figure 1A,B, Figure S1D), but not in null direction evoked OFF inhibitory responses (Figure 1C,D, Figure S1E), indicating that the small changes in OFF spiking likely arise from the reduced laminar segregation of ON and OFF SAC dendrites in the *Sema6A*$^{-/-}$ mouse [17].

DSGCs receive inhibition from two sources – symmetric input from non-SAC GABAergic interneurons [19], and asymmetric input from SACs, in which most SAC mediated inhibition onto DSGCs occurs during null direction stimulation [20]. Therefore, we directly compared DSGC spike tuning to the amount of asymmetric SAC mediated inhibitory input, which we estimated by computing the difference in inhibition along the nasal-temporal axis, which is the preferred-null axis for the Control GFP^{+} DSGCs in this study. We found that, regardless of genotype or luminance change direction, DSGC tuning increased with increased SAC synaptic input (Figure 1G). Overall, these results indicate that the reduction in directional tuning in DSGCs in *Sema6A*$^{-/-}$ mice is due to a loss of asymmetric SAC-mediated inhibitory input.

SAC-DSGC synaptic strength and asymmetric wiring is preserved in Sema6A$^{-/-}$ *mice.*

One possible source of reduced SAC-mediated input to DSGCs in *Sema6A*$^{-/-}$ mice is a failure to form strong synaptic connections with DSGCs. Yet, paired recordings between SACs and DSGCs revealed that SAC-DSGC synaptogenesis and asymmetric connectivity were preserved in *Sema6A*$^{-/-}$ mice (Fig. 2A-E, compare with [11]). Furthermore, inhibitory conductance peaks and time courses between null side Control and *Sema6A*$^{-/-}$ pairs were not significantly different (Figure 2D,E). Note, we chose *Sema6A*$^{-/-}$ SACs close to the DSGC soma to ensure dendritic overlap. Therefore, we normalized the recorded conductances to the number of putative null-oriented synapses [9] and again found no significant difference in the relative strength per synaptic connection between Control and *Sema6A*$^{-/-}$ pairs (Figure 2F). These data indicate that subcellular SAC-DSGC synaptic specificity is unperturbed in *Sema6A*$^{-/-}$ mice, demonstrating that the developmental processes governing asymmetric SAC-DSGC wiring are independent of the morphology of the distal SAC dendritic arbor and SEMA6A signaling.

Sema6A$^{-/-}$ *SAC varicosities maintain direction selectivity*

Asymmetric inhibition from SACs to DSGCs requires not only asymmetric wiring, but also a centrifugal motion preference of SAC GABA release sites at distal dendritic varicosities [13]. Therefore, we tested whether the decrease in null direction evoked inhibition measured in DSGCs of *Sema6A*$^{-/-}$ mice resulted from changes in the response properties of SAC varicosities to visual stimuli. First, voltage clamp recordings showed that light flashes evoked similar peak excitatory and inhibitory conductances in Control and *Sema6A*$^{-/-}$ SACs (Figure S2A,B). Second, two photon Ca^{2+} imaging revealed that *Sema6A*$^{-/-}$ SACs maintain the skewed distribution of excitatory inputs thought to underlie SAC varicosity direction selectivity (Figure S2C,D, [1, 5]). Third, varicosity Ca^{2+} responses to motion stimulation in *Sema6A*$^{-/-}$ SACs were equally as strong (Figure 3B), and, surprisingly, could be even more narrowly tuned (Figure 3A,C) than in Control SACs. Together, these data indicate that despite the shorter dendritic lengths (Figure S3D) of *Sema6A*$^{-/-}$ SAC dendrites, direction selective computational abilities were preserved.

Sema6A$^{-/-}$ *SAC varicosities are not necessarily tuned to centrifugal motion*

The antiparallel alignment of the preferred directions of SAC varicosities and their postsynaptic DSGCs is essential for generating tuned inhibitory input. Thus, although asymmetric SAC-DSGC wiring and direction selectivity in SAC dendrites are maintained in *Sema6A*$^{-/-}$ mice, we hypothesized that the increased dendritic tortuosity ([17], Figure 4A,E) in *Sema6A*$^{-/-}$ SACs may affect the interplay of these two circuit components. Therefore, we analyzed the direction selective tuning of varicosities in *Sema6A*$^{-/-}$ and Control SACs (Figure 4A) along the preferred-null axis (defined by the orientation of the vector sum of the tuning curve) and along the soma-varicosity, or centrifugal, axis, which determines SAC wiring with DSGC subtypes. For Control SAC varicosities, direction selective tuning was equally strong along the soma-varicosity and preferred-null axes (Figure 4B,D), as expected by the radial symmetry of the dendrites. In contrast, for *Sema6A*$^{-/-}$ SACs, there was a significant difference in tuning between the two axes (Figure 4D). Varicosity directional tuning along the preferred-null axis was larger than that in Control SAC varicosities, while varicosity directional tuning along the soma-varicosity axis was significantly reduced compared to Control SAC varicosities (Figure 4B). This difference in *Sema6A*$^{-/-}$ SAC tuning was due to decreased Ca^{2+} transient amplitudes in response to centrifugal stimulation compared to responses during preferred direction stimulation (Figure 4C). Overall, the greater degree of dendritic tortuosity in *Sema6A*$^{-/-}$ SACs led to a significantly larger misalignment between the functional preferred-null axis and the anatomical soma-varicosity axis (Figure 4E). These results indicate that SACs in *Sema6A*$^{-/-}$ mice may no longer maximally release GABA in response to motion in their postsynaptic DSGCs' null direction.

Loss of inhibitory directional tuning in Sema6A$^{-/-}$ mice results primarily from reduced SAC dendritic density.

Thus far, we have shown that SACs in *Sema6A$^{-/-}$* mice synapse asymmetrically onto DSGCs and have directionally tuned dendrites, but that these processes are not always aligned. In addition, the reduced dendritic length of SACs in *Sema6A$^{-/-}$* mice leads to a reduction of dendritic coverage (cell density x field area) from around 30 [17] to roughly 11 (Figure 5A). Does the loss of SAC dendritic coverage or the misalignment between functional and anatomical axes in *Sema6A$^{-/-}$* SACs contribute more to the reduction in DSGC IPSC tuning? Using a simulation that accounted for the symmetric inhibitory contribution from non-SAC GABAergic amacrine cells [19, 20], we found that decreasing SAC dendritic coverage to *Sema6A$^{-/-}$* SAC levels led to a large reduction in the asymmetric inhibitory inputs onto the DSGC that closely mimicked IPSC amplitudes recorded in *Sema6A$^{-/-}$* mice (Figure 5B,C). Simulations in which SAC dendrites tiled the retina led to a complete abolishment of directional inhibitory input (Figure 5A-C). These results indicate that the loss in coverage factor alone would be sufficient to prevent direction selective signaling.

We then estimated how increasing the misalignment between the SAC-DSGC wiring axis and varicosity preferred directions contributes to a reduction in IPSC tuning at both WT and *Sema6A$^{-/-}$* SAC coverage levels. When we assumed a random alignment between these two circuit components IPSC directional tuning was completely abolished at all SAC coverage factors (Figures 5D–5F). However, simulations using the experimentally observed differences in *Sema6A$^{-/-}$* mice between the two axes (Figure 4), resulted in a smaller, but still significant, reduction in IPSC directional tuning (Figure 5D-F). Thus, we conclude that in *Sema6A$^{-/-}$* mice the loss of DSGC directional tuning is explained primarily by the decreased SAC dendritic coverage [17], while synaptic input from varicosities on tortuous SAC dendritic arbors can further degrade the precise asymmetry of GABA release found in Control retinas.

SAC varicosity directional preferences determined near the end of the excitatory input distribution.

We next sought to use the increased dendritic tortuosity of *Sema6A$^{-/-}$* SAC dendrites to elucidate which portions of the SAC dendritic arbor were responsible for determining varicosity directional preference. Specifically, we compared varicosity preferred directions to the average dendritic orientations of different portions of the SAC dendrite, starting at the first branch from the soma (Figure 6A). The dendrites of Control SACs generally radiate straight out from the soma, and therefore Control SAC varicosity preferred directions aligned equally well with all average dendritic orientations calculated using segments distal to the first branch point (Figure 6A,B, gray). In contrast, for the more complex dendrites of *Sema6A$^{-/-}$* SACs (Figure 4E, S3F), varicosity preferred directions aligned best to dendritic orientations calculated with segments distal to the fourth branch point (Figure 6A,B blue). These results were consistent across varicosity tuning strengths (Figure S3A). The fourth branch point is 90-120 μm away from the soma (roughly 70% of the SAC dendrite), corresponding to the most distal extent of bipolar cell inputs onto the SAC dendrite as determined by glutamate uncaging [1] and electron microscopy [2, 5] (Figure S3D,E). Indeed, when individual branch angles were considered, the orientation of the 4th order dendritic segment was most responsible for varicosity directional preference (Figure 6B, Figure S3B,C), indicating that the directional preference of SAC varicosities is determined by the local orientation of the last dendritic segment with glutamate receptors (Figure 6C). The implications of these results on current models of SAC directional computations are discussed below.

Discussion

These results show that DSGCs in *Sema6A*$^{-/-}$ mice have reduced ON directional tuning directly resulting from changes in SAC morphology, but not SAC-DSGC wiring or SAC dendritic computations. First, DSGCs lack directional tuning due to a weaker and more symmetric synaptic inhibitory input in *Sema6A*$^{-/-}$ mice. Second, paired recordings between *Sema6A*$^{-/-}$ SACs and DSGCs show that asymmetric wiring is preserved. Third, two-photon Ca^{2+} imaging of *Sema6A*$^{-/-}$ SAC varicosities shows that the intrinsic direction selectivity of SAC dendrites is preserved. Hence, we conclude that SAC morphology and spacing is critical for generating a highly overlapping plexus of dendrites required for direction selective computations. Finally, the increased dendritic tortuosity in *Sema6A*$^{-/-}$ SACs allowed us to determine that a relatively short portion of the distal half of the SAC dendritic arbor is sufficient for determining varicosity directional preference.

Implications for direction selectivity mechanisms

Our finding that the loss of direction selectivity in *Sema6A*$^{-/-}$ mice is due to an overall loss of SAC coverage is surprising given that SACs are among the most over-represented cell types in the retina, with coverage factors from 25-35 depending on the mouse strain [21]. While there is a dramatic loss of ON SAC dendritic coverage in *Sema6A*$^{-/-}$ mice, ON SACs and DSGCs still cofasciculate strongly [17]. Thus, one may expect that the remaining inhibition from SAC dendrites would be sufficient to generate direction selective responses, especially since asymmetric wiring and SAC varicosity tuning are still present (Figures 2,3). Indeed, SAC mediated transmission alone is sufficient in WT mice to generate direction selective responses in DSGCs [22]. However, we found that this loss of coverage causes a significant reduction in IPSC asymmetry, likely disrupting the delicate balance between excitatory bipolar cell inputs and both inhibitory and excitatory SAC inputs onto DSGCs [22-24] leading to an increase in null direction evoked DSGC spiking.

In contrast, using a simple simulation, we found that the misalignment between the functional preferred-null axis and the anatomical soma-varicosity axis minimally impacted IPSC tuning in DSGCs of *Sema6A*$^{-/-}$ mice. However, when we repeated the simulation using a broader range of angles, we observed a dramatic loss of IPSC tuning (Figure 5). We postulate that this greater loss of IPSC tuning may in part explain the reduced IPSC tuning in Pcdhg$^{-/-}$ mice, which have even more tortuous SAC dendrites but no reduction in coverage factor [14]. Hence, different manipulations of SAC morphology can impact direction selective computations via distinct mechanisms.

Implications for dendritic tuning

The subcellular directional computation in SAC dendrites emerges from the interplay of three potential mechanisms. The first mechanism is based on a proximally skewed distribution of excitatory bipolar cell inputs combined with the electronic properties of the thin SAC cable [1, 5] and assumes that SAC processes are electrically isolated from each other, a requirement recently proven critical for direction selectivity generation [12]. In this model, temporal summation of closely spaced glutamatergic inputs during motion towards the varicosities leads to a slightly larger membrane depolarization at distal dendrites than during motion towards the soma, in a manner first described by Rall [25]. This small difference is greatly amplified by the presence of nonlinear conductances located in the distal portion of the dendrite [12, 26, 27].

How much dendrite is necessary to perform this computation? By comparing SAC dendritic segment orientations to varicosity preferred directions, we found that the dendritic segment best aligned to varicosity preferred directions was distal to the fourth branch point (Figure 6), corresponding to the location of the most distal glutamatergic bipolar cell inputs onto the SAC (Figure S3E). These data suggest that sequential summation over only a small segment of glutamate receptors is sufficient to generate a depolarization difference that differentiates centrifugal from centripetal stimulation. Our results also suggest that the nonlinear conductance underlying the conversion of a weak directional voltage difference to a strong dendritic directional preference is located distal to the glutamate receptors but proximal to most of the release sites. This configuration ensures a consistent level of direction selectivity over all varicosities due to the dendritic end effect [1].

The second mechanism for SAC dendritic direction selectivity is based on lateral inhibition between SACs [28]. This mutual inhibition enhances the directionality of SAC dendrites [1, 15, 29], but is not the primary component of the computation [13], playing a more critical role under conditions of high contrast [5] or noisy backgrounds [30]. Since SAC-SAC connections are formed in proximal dendritic segments [5], only the distal third of SAC dendrites in *Sema6A*$^{-/-}$ SACs fail to exhibit self-avoidance, inhibitory conductances in *Sema6A*$^{-/-}$ SACs are the same as in Controls, and *Sema6A*$^{-/-}$ SAC varicosities are well tuned (Figure 3), inhibitory SAC-SAC connections are not likely to be a major factor in affecting direction selectivity in *Sema6A*$^{-/-}$ mice.

The third mechanism is based on the arrangement of pre-synaptic bipolar cells with different kinetics. Disruption of bipolar cell wiring onto SACs certainly reduces direction selectivity in DSGCs [31, 32], but the presence of distance dependent differences in excitatory input kinetics required for “space-time wiring” in ON SACs has remained controversial [2, 5, 33, 34]. Two of our findings in *Sema6A*$^{-/-}$ mice suggest this model is not a major contributor in the ON pathway. First, bipolar kinetics vary with IPL lamination [35, 36] and *Sema6A*$^{-/-}$ SACs no longer stratify in a single layer ([17], Figure S2A,B), but strong SAC dendritic direction selectivity is maintained (Figure 3). Second, the “space-time” model requires both proximal and distal excitatory inputs to generate direction selectivity, but we find that SAC tuning is most well aligned with the orientation of distal dendritic branches (Figure 6) that are not likely to receive spatially offset inputs from two different bipolar cell subtypes.

In conclusion, our results reveal a central role for the high SAC coverage factor in generating direction selectivity. Understanding the genetic basis [37] and cellular mechanisms [38, 39] underlying the creation of the dense SAC plexus may shed light on why some cell classes are overrepresented in the retina and other brain regions. Moreover, the altered morphology of *Sema6A*$^{-/-}$ SACs has revealed a dissociation within the SAC arbor between connectivity and intrinsic directional preference. While asymmetric wiring with DSGCs is likely instructed by the segregation of different signaling molecules at proximal SAC dendrites [40, 41], we find that the directional preferences of varicosities on that dendrite are determined at a more distal location. Further functional analysis of morphological alterations in SACs [15, 42] and other neurons [14, 43] can help elucidate the underlying cellular and molecular mechanisms that link dendritic structure, wiring, and computation.

References

1. Vlasits, A. L., Morrie, R. D., Tran-Van-Minh, A., Bleckert, A., Gainer, C. F., DiGregorio, D. A., and Feller, M. B. (2016). A Role for Synaptic Input Distribution in a Dendritic Computation of Motion Direction in the Retina. Neuron *89*, 1317–1330.
2. Greene, M. J., Kim, J. S., Seung, H. S., EyeWirers (2016). Analogous Convergence of Sustained and Transient Inputs in Parallel On and Off Pathways for Retinal Motion Computation. CellReports *14*, 1892–1900.
3. Kim, J. S., Greene, M. J., Zlateski, A., Lee, K., Richardson, M., Turaga, S. C., Purcaro, M., Balkam, M., Robinson, A., Behabadi, B. F., et al. (2014). Space-time wiring specificity supports direction selectivity in the retina. Nature *509*, 331–336.
4. Famiglietti, E. V. (1991). Synaptic organization of starburst amacrine cells in rabbit retina: analysis of serial thin sections by electron microscopy and graphic reconstruction. J. Comp. Neurol. *309*, 40–70.
5. Ding, H., Smith, R. G., Poleg-Polsky, A., Diamond, J. S., and Briggman, K. L. (2016). Species-specific wiring for direction selectivity in the mammalian retina. Nature *535*, 105–110.
6. Reese, B. E., and Keeley, P. W. (2015). Design principles and developmental mechanisms underlying retinal mosaics. Biological Reviews *90*, 854–876.
7. Mauss, A. S., vlasits, A., Borst, A., and Feller, M. (2017). Visual Circuits for Direction Selectivity. Annu. Rev. Neurosci. *40*, 211–230.
8. Vaney, D. I., Sivyer, B., and Taylor, W. R. (2012). Direction selectivity in the retina: symmetry and asymmetry in structure and function. Nat Rev Neurosci *13*, 194–208.
9. Briggman, K. L., Helmstaedter, M., and Denk, W. (2011). Wiring specificity in the direction-selectivity circuit of the retina. Nature *471*, 183–188.
10. Morrie, R. D., and Feller, M. B. (2015). An Asymmetric Increase in Inhibitory Synapse Number Underlies the Development of a Direction Selective Circuit in the Retina. J. Neurosci. *35*, 9281–9286.
11. Wei, W., Hamby, A. M., Zhou, K., and Feller, M. B. (2011). Development of asymmetric inhibition underlying direction selectivity in the retina. Nature *469*, 402–406.
12. Koren, D., Grove, J. C. R., and Wei, W. (2017). Cross-compartmental Modulation of Dendritic Signals for Retinal Direction Selectivity. Neuron *95*, 914–927.e4.
13. Euler, T., Detwiler, P. B., and Denk, W. (2002). Directionally selective calcium signals in dendrites of starburst amacrine cells. Nature *418*, 845–852.
14. Lefebvre, J. L., Kostadinov, D., Chen, W. V., Maniatis, T., and Sanes, J. R. (2012). Protocadherins mediate dendritic self-avoidance in the mammalian nervous system. Nature *488*, 517–521.
15. Kostadinov, D., and Sanes, J. R. (2015). Protocadherin-dependent dendritic self-avoidance regulates neural connectivity and circuit function. Elife *4*.
16. Koropouli, E., and Kolodkin, A. L. (2014). Semaphorins and the dynamic regulation of synapse assembly, refinement, and function. Current Opinion in Neurobiology *27C*, 1–7.

17. Sun, L. O., Jiang, Z., Rivlin-Etzion, M., Hand, R., Brady, C. M., Matsuoka, R. L., Yau, K. W., Feller, M. B., and Kolodkin, A. L. (2013). On and Off Retinal Circuit Assembly by Divergent Molecular Mechanisms. Science *342*, 1241974–1241974.
18. Leighton, P. A., Mitchell, K. J., Goodrich, L. V., Lu, X., Pinson, K., Scherz, P., Skarnes, W. C., and Tessier-Lavigne, M. (2001). Defining brain wiring patterns and mechanisms through gene trapping in mice. Nature *410*, 174–179.
19. Park, S. J. H., Borghuis, B. G., Rahmani, P., Zeng, Q., Kim, I.-J., and Demb, J. B. (2015). Function and Circuitry of VIP+ Interneurons in the Mouse Retina. J. Neurosci. *35*, 10685–10700.
20. Pei, Z., Chen, Q., Koren, D., Giammarinaro, B., Ledesma, H. A., and Wei, W. (2015). Conditional Knock-Out of Vesicular GABA Transporter Gene from Starburst Amacrine Cells Reveals the Contributions of Multiple Synaptic Mechanisms Underlying Direction Selectivity in the Retina. J. Neurosci. *35*, 13219–13232.
21. Keeley, P. W., Whitney, I. E., Raven, M. A., and Reese, B. E. (2007). Dendritic spread and functional coverage of starburst amacrine cells. J. Comp. Neurol. *505*, 539–546.
22. Sethuramanujam, S., McLaughlin, A. J., deRosenroll, G., Hoggarth, A., Schwab, D. J., and Awatramani, G. B. (2016). A Central Role for Mixed Acetylcholine/GABA Transmission in Direction Coding in the Retina. Neuron *90*, 1243–1256.
23. Sethuramanujam, S., Yao, X., deRosenroll, G., Briggman, K. L., Field, G. D., and Awatramani, G. B. (2017). “Silent” NMDA Synapses Enhance Motion Sensitivity in a Mature Retinal Circuit. Neuron *96*, 1099–1111.e3.
24. Poleg-Polsky, A., and Diamond, J. S. (2016). Retinal Circuitry Balances Contrast Tuning of Excitation and Inhibition to Enable Reliable Computation of Direction Selectivity. J. Neurosci. *36*, 5861–5876.
25. Rall, W. (1967). Distinguishing theoretical synaptic potentials computed for different soma-dendritic distributions of synaptic input. J. Neurophysiol. *30*, 1138–1168.
26. Lee, S., Kim, K., and Zhou, Z. J. (2010). Role of ACh-GABA cotransmission in detecting image motion and motion direction. Neuron *68*, 1159–1172.
27. Oesch, N. W., and Taylor, W. R. (2010). Tetrodotoxin-resistant sodium channels contribute to directional responses in starburst amacrine cells. PLoS ONE *5*, e12447.
28. Lee, S., and Zhou, Z. J. (2006). The synaptic mechanism of direction selectivity in distal processes of starburst amacrine cells. Neuron *51*, 787–799.
29. Poleg-Polsky, A., Ding, H., and Diamond, J. S. (2018). Functional Compartmentalization within Starburst Amacrine Cell Dendrites in the Retina. CellReports *22*, 2898–2908.
30. Chen, Q., Pei, Z., Koren, D., and Wei, W. (2016). Stimulus-dependent recruitment of lateral inhibition underlies retinal direction selectivity. Elife *5*, 4481.
31. Shi, Z., Trenholm, S., Zhu, M., Buddingh, S., Star, E. N., Awatramani, G. B., and Chow, R. L. (2011). Vsx1 Regulates Terminal Differentiation of Type 7 ON Bipolar Cells. J. Neurosci. *31*, 13118–13127.
32. Duan, X., Krishnaswamy, A., la Huerta, De, I., and Sanes, J. R. (2014). Type II Cadherins Guide Assembly of a Direction-Selective Retinal Circuit. Cell *158*, 793–807.
33. Fransen, J. W., and Borghuis, B. G. (2017). Temporally Diverse Excitation Generates Direction-Selective Responses in ON- and OFF-Type Retinal Starburst Amacrine Cells. Cell Reports *18*, 1356–1365.

34. Stincic, T., Smith, R. G., and Taylor, W. R. (2016). Time course of EPSCs in ON-type starburst amacrine cells is independent of dendritic location. The Journal of Physiology *594*, 5685–5694.
35. Borghuis, B. G., Marvin, J. S., Looger, L. L., and Demb, J. B. (2013). Two-photon imaging of nonlinear glutamate release dynamics at bipolar cell synapses in the mouse retina. J. Neurosci. *33*, 10972–10985.
36. Baden, T., Berens, P., Bethge, M., and Euler, T. (2013). Spikes in Mammalian Bipolar Cells Support Temporal Layering of the Inner Retina. Current Biology *23*, 48–52.
37. Whitney, I. E., Keeley, P. W., St John, A. J., Kautzman, A. G., Kay, J. N., and Reese, B. E. (2014). Sox2 regulates cholinergic amacrine cell positioning and dendritic stratification in the retina. J. Neurosci. *34*, 10109–10121.
38. Farajian, R., Raven, M. A., Cusato, K., and Reese, B. E. (2004). Cellular positioning and dendritic field size of cholinergic amacrine cells are impervious to early ablation of neighboring cells in the mouse retina. Vis. Neurosci. *21*, 13–22.
39. Kay, J. N., Chu, M. W., and Sanes, J. R. (2012). MEGF10 and MEGF11 mediate homotypic interactions required for mosaic spacing of retinal neurons. Nature *483*, 465–469.
40. Morrie, R. D., and Feller, M. B. (2016). Development of synaptic connectivity in the retinal direction selective circuit. Current Opinion in Neurobiology *40*, 45–52.
41. Yonehara, K., Fiscella, M., Drinnenberg, A., Esposti, F., Trenholm, S., Krol, J., Franke, F., Scherf, B. G., Kusnyerik, A., Müller, J., et al. (2016). Congenital Nystagmus Gene FRMD7 Is Necessary for Establishing a Neuronal Circuit Asymmetry for Direction Selectivity. Neuron *89*, 177–193.
42. Ing-Esteves, S., Kostadinov, D., Marocha, J., Sing, A. D., Joseph, K. S., Laboulaye, M. A., Sanes, J. R., and Lefebvre, J. L. (2018). Combinatorial Effects of Alpha- and Gamma-Protocadherins on Neuronal Survival and Dendritic Self-Avoidance. J. Neurosci. *38*, 2713–2729.
43. Joo, W., Hippenmeyer, S., and Luo, L. (2014). Dendrite morphogenesis depends on relative levels of NT-3/TrkC signaling. Science *346*, 626–629.
44. Gong, S., Zheng, C., Doughty, M. L., Losos, K., Didkovsky, N., Schambra, U. B., Nowak, N. J., Joyner, A., Leblanc, G., Hatten, M. E., et al. (2003). A gene expression atlas of the central nervous system based on bacterial artificial chromosomes. Nature *425*, 917–925.
45. Rivlin-Etzion, M., Zhou, K., Wei, W., Elstrott, J., Nguyen, P. L., Barres, B. A., Huberman, A. D., and Feller, M. B. (2011). Transgenic mice reveal unexpected diversity of on-off direction-selective retinal ganglion cell subtypes and brain structures involved in motion processing. J. Neurosci. *31*, 8760–8769.
46. Mitchell, K. J., Pinson, K. I., Kelly, O. G., Brennan, J., Zupicich, J., Scherz, P., Leighton, P. A., Goodrich, L. V., Lu, X., Avery, B. J., et al. (2001). Functional analysis of secreted and transmembrane proteins critical to mouse development. Nat Genet *28*, 241–249.
47. Wei, W., Elstrott, J., and Feller, M. B. (2010). Two-photon targeted recording of GFP-expressing neurons for light responses and live-cell imaging in the mouse retina. Nat Protoc *5*, 1347–1352.
48. Hoggarth, A., McLaughlin, A. J., Ronellenfitch, K., Trenholm, S., Vasandani, R., Sethuramanujam, S., Schwab, D., Briggman, K. L., and Awatramani, G. B. (2015). Specific Wiring of Distinct Amacrine Cells in the Directionally Selective Retinal Circuit Permits Independent Coding of Direction and Size. Neuron *86*, 276–291.

49. Denk, W., and Detwiler, P. B. (1999). Optical recording of light-evoked calcium signals in the functionally intact retina. Proc. Natl. Acad. Sci. U.S.A. *96*, 7035–7040.
50. Cuntz, H., Forstner, F., Borst, A., and Häusser, M. (2010). One Rule to Grow Them All: A General Theory of Neuronal Branching and Its Practical Application. PLoS Comput Biol *6*, e1000877.
51. Cuntz, H., Forstner, F., Borst, A., and Häusser, M. (2011). The TREES toolbox--probing the basis of axonal and dendritic branching. Neuroinform *9*, 91–96.
52. Taylor, W. R., and Vaney, D. I. (2002). Diverse synaptic mechanisms generate direction selectivity in the rabbit retina. J. Neurosci. *22*, 7712–7720.
53. Wehr, M., and Zador, A. M. (2003). Balanced inhibition underlies tuning and sharpens spike timing in auditory cortex. Nature *426*, 442–446.
54. Berens, P. (2009). CircStat: a MATLAB toolbox for circular statistics. Journal of Statistical Software *31*, 1–21.

STAR Methods

Contact For Reagent and Resource Sharing

Further information and requests for reagents may be directed and will be fulfilled by the Lead Contact and corresponding author Marla B. Feller (mfeller@berkeley.edu).

Experimental Model and Subject Details

Animals

Mice used in this study were aged from p25-120 and were of both sexes. To target DSGCs and SACs, ChAT-Cre/nGFP/TrHr (CNT) mice were generated by crossing together three mouse lines: (1) B6.129S6-ChATtm1(cre)lowl/J (Jackson Laboratories), with Cre driven by the endogenous choline acetyltransferase promoter, (2) B6.129-Gt(ROSA)26Sor^{tm1Joe}/J (Jackson Laboratories), with a nuclear-localized GFP-lacZ function protein downstream of a loxP-flanked STOP sequence, and (3) TrHr-GFP mice [44], which express GFP in nasal preferring DSGCs [45]. CNT mice then were crossed to a *Sema6A* gene trap mouse [18, 46] in which a PLAP secretory trap vector was inserted at the codon for amino acid 473 in the semaphorin domain. For all experiments, Control animals were CNT*Sema6A*$^{+/+}$ or CNT*Sema6A*$^{+/-}$ littermates of CNT*Sema6A*$^{-/-}$ animals. All experiments involved recording from 1-5 cells or cell pairs from at least 3 animals of either sex for each genotype. All animal procedures were approved by the UC Berkeley Institutional Animal Care and Use Committee and conformed to the NIH *Guide for the Care and Use of Laboratory Animals*, the Public Health Service Policy, and the SFN Policy on the Use of Animals in Neuroscience Research.

Method Details

Retina Preparation

Mice were anesthetized with isoflurane and decapitated. Retinas were dissected from enucleated eyes in oxygenated (95% O2/ 5% CO2) Ames' media (Sigma) for light responses or ACSF (in mM, 119 NaCl, 2.5 KCl, 1.3 $MgCl_2$, 1 K_2HPO_4, 26.2 $NaHCO_3$, 11 D-glucose, and 2.5 $CaCl_2$) for paired recordings. Retinal orientation was determined as described previously [47]. Isolated retinas were cut into dorsal and ventral halves, mounted over a 1–2 mm^2 hole in nitrocellulose filter paper (Millipore) with the photoreceptor layer side down, and stored in oxygenated Ames' media or ACSF until use (maximum 10 h). Filter paper mounted retinas in which dorsal-ventral orientation was tracked will be referred to as oriented retinas.

2P targeted recordings and visual stimulation

Oriented retinas were placed under the microscope in oxygenated Ames' medium at 32–34°C. Identification and recordings from GFP$^+$ cells were performed as described previously [47]. In brief, GFP$^+$ cells were identified using a custom-modified two-photon microscope (Fluoview 300; Olympus America) tuned to 920 nm to minimize bleaching of photoreceptors. The inner limiting membrane above the targeted cell was dissected using a glass electrode. Cell attached voltage clamp recordings were performed with a new glass electrode (4-5 MΩ) filled with internal solution containing the following (in mM): 110 $CsMeSO_4$, 2.8 NaCl, 20 HEPES, 4 EGTA, 5 TEA-Cl, 4 Mg-ATP, 0.3 Na_3GTP, 10 Na_2Phosphocreatine, 5 QX-Cl (pH = 7.2 with CsOH, osmolarity = 290, E_{Cl^-} = -60 mV). After cell attached recordings of spikes, whole cell recordings were performed with the same pipette after obtaining a GΩ seal. Holding voltages for measuring excitation and inhibition after correction for the liquid junction potential (-10 mV) were 0 mV and -60 mV, respectively. Signals were acquired using pCLAMP 9 recording software and a Multiclamp 700A amplifier (Molecular Devices), sampled at 20 kHz, and low-pass filtered at 6 kHz.

For visual stimulation of DSGCs, broad-band visible light ranging from 470 to 620 nm was generated using an OLED display (SVGA Rev2 OLED-XL; eMagin) displaying custom stimuli created using MATLAB software with the Psychophysics Toolbox. These images were projected onto the photoreceptor layer through the same 60x objective used to target cells (Olympus LUMPlanFl/IR 360/0.90W), which was focused onto the photoreceptor layer once the cell attached recording configuration was achieved. The illumination radius on the retina was ~300 µm, which was significantly smaller than in previous recordings from DSGCs in *Sema6A*$^{-/-}$ mice [17] to limit the modulation of DSGC responses by inhibitory wide-field amacrine cells [48]. Moving bars (320 x 650 µm) were presented to the cell with both positive and negative contrasts at 500 µm/sec in three trials of eight pseudorandomized directions parallel to the longer axis of the bar.

Paired voltage clamp recordings and imaging

Oriented retinas were placed under the microscope in oxygenated ACSF containing the following excitatory neurotransmitter blockers (in mM): 0.05 AP5, 0.02 DNQX and 0.008 DHβE. GFP^{+} DSGCs and nGFP^{+} SACs were identified under 2 photon illumination and targeted as above. Whole cell voltage clamp recordings were achieved for a given DSGC before targeting SACs. Note, we targeted SACs in *Sema6A*$^{-/-}$ mice with small inter-soma distances with the patched DSGC to ensure some degree of dendritic overlap and thus synaptic connectivity. Recordings from DSGCs were performed with glass electrodes (3-5 MΩ) filled with internal solution containing the following (in mM): 110 $CsMeSO_4$, 2.8 NaCl, 20 HEPES, 4 EGTA, 5 TEA-Cl, 4 Mg-ATP, 0.3 Na_3GTP, 10 Na_2Phosphocreatine, 0.025 AlexaFluor488 (pH = 7.2 with CsOH, osmolarity = 290, ECl^{-} = -74 mV). Recordings from SACs were performed similarly, except the internal solution EGTA concentration was 0.1 mM [10] and AlexaFluor594 was used. To calculate SAC-DSGC synaptic conductances, DSGC were held at voltage potentials ranging from -100 mV to +20 mV while SACs were depolarized three times from the holding potential (-70 mV) to 0 mV for 50 ms. After recording synaptic currents, 2 photon 1024x1024 image stacks of the dye filled cells were acquired with 780 nm excitation, using a 0.5 µm step size.

Imaged cells were manually reconstructed using the FIJI plugin Simple Neurite Tracer. After cells were traced, the ‘fill out’ function was used until a volume rendering of the entire cell was created. The resulting volumes for the two cells were exported as .tif image stacks and then imported into Imaris 9 (Bitplane), where the colocalization between the two volumes was calculated and the results were used to create a new colocalization channel. The ‘Spots’ function of Imaris was used on this colocalization channel to identify sites of overlap. To identify putative synaptic sites, we manually selected Spots on the outer third of SAC dendrites located within 67° on either side of the null direction (vertex at the SAC soma) [9]. The number of these putative synapses were then compared to the calculated conductances using regression analysis.

SAC Light Responses

Filter paper mounted retinas were placed under a custom 2-photon microscope [1] in oxygenated Ames’ medium at 32–34°C. nGFP^{+} SACs were identified under 2 photon illumination (930 nm) or by their small round somas, characteristic responses to voltage steps, and/or post-hoc imaging.

For voltage clamp experiments, glass electrodes (3-5 MΩ) filled with internal solution containing the following (in mM): 110 $CsMeSO_4$, 2.8 NaCl, 20 HEPES, 4 EGTA, 5 TEA-Cl, 4 Mg-ATP, 0.3 Na_3GTP, 10 Na_2Phosphocreatine, 0.025 AlexaFluor594 (pH = 7.2 with CsOH, osmolarity = 290, ECl^- = -73 mV) were used to target SACs identified under a 40x ACHROPLAN water immersion objective (0.80 NA, Zeiss). Light response recordings were performed with at least 5 different holding potentials ranging from -100 to +20 mV after correction for the liquid junction potential (-12mV). Visual stimuli were created on a 670 x 550 µm patch of retina by projecting an LED light source (M470L2, Thorlabs, Inc.) through a DMD (Cell5500-Fiber, Digital Light Innovations) controlled by custom software (Psychophysics Toolbox) that were focused through the condenser lens onto the photoreceptors. Prior to each experiment, visual stimuli were aligned to the middle of the 2-photon imaging field and the photoreceptors by inserting a pipette filled with Alexa Flour 594 and positioning it at the focal plane of the photoreceptors (measured by IR imaging) and the middle of the 2-photon imaging window. A small spot (5 µm radius) was projected and aligned to the tip of the pipette via focusing or shifting the condenser in the XY plane. SACs were presented with three repetitions of a 400 µm diameter spot centered on the SAC soma at each holding potential. After recording, full field (196 x 196 µm) images of SAC morphology (512 x 512, 8ms/line, bidirectional scanning) were obtained by tuning the laser to 850 nm to analyze SAC dendritic arbor length.

For Ca^{2+} imaging experiments, SACs were filled with Oregon Green 488 BAPTA-1 (OGB1, Life Technologies) via a sharp electrode as per [5]. Briefly, borosilicate glass (I.D.=1.1, O.D.=1.5 mm) electrodes were first pulled to a resistance of 100-150 MΩ and then were bent (such that electrode tips were perpendicular to the retinal surface when inserted into the headstage) by placing the electrode tangentially to a water bubble and heating it with a microforge. Bent electrodes were filled with 15 mM OGB1 and placed above the targeted SAC under infrared illumination. 2 photon illumination was used to guide the electrode tip through the inner limiting membrane into the targeted SAC and visualize cell filling. Ionotophoresis of OGB1 was achieved with negative current pulses (-10 to -20 nA, 500 ms) and electrodes were withdrawn as cell bodies began to fill. Filled SACs were left to recover for 30-60 minutes before imaging. Multiple, non-overlapping SACs were often filled within the same filter paper hole.

Simultaneous Ca^{2+} imaging and visual stimulation were performed generally as in [1] under a 60x LUMPlanFL N water immersion objective (1.00 NA, Olympus).

For spot response receptive field mapping experiments, visual stimuli were aligned to the center of the 2-photon imaging field. Spot positions were defined by taking a low intensity z-stack (930 nm) of the filled SAC, picking a varicosity at the end of a dendrite for imaging, and then identifying five points along that dendrite roughly corresponding to 0, 25, 50, 75, and 100% of total dendritic length. Visual stimuli were presented after 20 s of imaging to allow photoreceptors to adapt to the scanning laser [49]. Three trials of 12.5 µm radius spots centered at each of these points were presented in pseudorandom order for 1 sec each with 6 s in between. SAC varicosities were imaged using a 930nm excitation wavelength and images were acquired at 11.84 Hz (64 x 64 pixels, 1ms/line, bidirectional scanning).

For direction selectivity experiments visual stimuli were aligned to the top left corner of the 2-photon imaging field. After filled SACs recovered, cells were positioned with their soma at the center of the stimulus field and 26 x 26 µm ROIs were selected at various positions along the SAC arbor. SAC dendrites were imaged using a 930 nm excitation wavelength and images were acquired at 7.58 Hz (256 x 100 pixels, 1ms/line, bidirectional scanning). Visual stimuli consisted of 3 trials of moving bars (400 x 200 μm) moving at 500 μm/sec in eight pseudorandomized directions parallel to the shorter axis of the bar across the entire stimulus plane. SACs that did not exhibit Ca^{2+} responses to initial laser scanning were excluded from further experimentation.

For all Ca^{2+} imaging experiments, after functional imaging, full field (131 x 131 μm), high resolution images of SAC morphology (512 x 512, 4ms/line, bidirectional scanning) were obtained by tuning the laser to 800 nm to increase OGB1 excitation. The objective was moved and multiple images were acquired and stitched together using 3D stitching (FIJI), if required, to trace imaged varicosities back to the soma. Dendritic morphology was manually reconstructed using Simple Neurite Tracer (FIJI). Imaged varicosities and the cell soma were labeled on the Simple Neurite tracing of each SAC with SWC identifiers. Cell reconstructions were exported as .SWC files and imported into the TREES toolbox [50, 51] in Matlab for further analysis.

IPSC simulation

To simulate directional SAC-DSGC inhibitory synaptic transmission we first assigned pre-synaptic SAC release sites to a location on the null half of the SAC arbor (-90° to 90° with 0° representing the DSGC's null direction). The number of SAC release sites varied from 1-100, with 1 representing tiled SAC input and 100 representing the endogenous SAC coverage factor of 30 (Figure 5A). The direction of maximal GABA release for each simulated varicosity was then offset from its anatomical angle by randomly drawing, with replacement, from the experimentally observed differences between preferred-null (PN) and soma-varicosity (SV) axes orientations for Control or *Sema6A*$^{-/-}$ SAC (Figure 4). Varicosity synaptic release directions (anatomical angle + PN-SV axes offset) were binned into 45 degree increments to simulate the highest resolution possible in our experiments using 8 directions of stimulus motion. Synaptic release from each varicosity caused a 18 pA current in the simulated DSGC, based on quantal recordings [10] and our normalization of inhibitory conductances to putative release sites (Figure 2F). Synaptic currents magnitudes were then summed across bins and added to a radially symmetric 400 pA current from non-SAC GABAergic amacrine cells [19, 20] to create a synaptic release tuning curve. This simulation was repeated 1000 times to generate the average tuning curves and the distributions of normalized tuning curve vector sums in Figure 5. For the Random simulation, PN-SV axes offsets were randomly drawn, with replacement, from the distribution of all angles ranging from -359° to 359°.

Quantification and Statistical Analysis

DSGC Light Responses

For cell attached DSGC recordings, spike counts were calculated by bandpass filtering traces (0.08-2 kHz) and manually identifying a threshold value for spikes on the filtered traces. Local minima below threshold that did not violate refractory period criteria (0.001 s) were counted as spikes. ON and OFF responses were defined as spikes occurring within a 900 ms time window starting right before the presentation of the leading or trailing edge of the stimulus. The average spike counts across the 3 trials were used to calculate the vector sum of the spike responses. Preferred directions for both ON and OFF responses used to calculate average spike counts in Figure S1 were defined as the angle of the vector sum of spike responses for the OFF response.

For voltage clamp DSGC recordings, traces were first average across the 3 trials for each direction and inspected to ensure consistency of responses. Average traces were baseline subtracted based on the last 500 ms of recording or a user defined interval after manual inspection. Peak currents were calculated from average baseline subtracted traces and were the maximal (IPSC) or minimal (EPSC) points during the 900 ms window described above. Charge transfers were calculated as the integral of the average baselined traces during the 900 ms window. The peak currents were used to calculate the vector sum of the current responses. Preferred directions for both ON and OFF responses used to calculate peak responses reported in Supplementary Figure 1 were defined as 180^o + the angle of the vector sum of OFF peak IPSCs, or the angle of the vector sum of OFF peak EPSCs if IPSCs were not recorded in that cell.

Paired Recordings

Inhibitory conductance analysis of paired SAC-DSGC recordings was performed in IGOR Pro using the algorithm described in [52]. Briefly, sweeps at each DSGC holding potential were averaged and then the baseline holding current (defined as the average current prior to SAC stimulation) was subtracted from each average trace. We compensated for the series resistance (R_s) by measuring the series and input resistance (R_{in}) from a -5 mV pulse at the end of each trace. We used the following equations for compensation of the recorded current (I_m) and the holding potential (V_h):

(1) $I_{syn}(t) = (R_{in} + R_s)/R_{in} * I_m(t)$

(2) $V(t) = V_h - I_m(t)*R_s$

Then we fit a line to the IV data (I_{syn} vs.V) for the various holding potentials at each time point (t) in the trace. The slopes and intercepts of these lines were used to calculate the inhibitory conductance gT (the slope) and the reversal potential Vrev (-intercept/slope). We controlled for quality of recording by requiring an R^2 value for the linear fit of the IV data above 0.85.

SAC Light Response Recordings

Conductance analysis of SAC light responses was performed similarly using a custom written script in Matlab based off of [53]. Briefly, sweeps at each SAC holding potential were averaged and then the baseline holding current (200ms before light stimulation) was subtracted from each average trace. We compensated for the series resistance (R_s) and input resistance (R_{in}) from a -5 mV pulse at the end of each trace as above. The total conductance gT and reversal potential Vrev were calculated based on the IV data as above and recording quality was controlled by requiring an R^2 value for the linear fit of the IV data above 0.9.

Inhbitiory (gI) and excitatory conductances (gE) were separated based on the reversal potentials for inhibition (Vi = -73 mV) and excitation (Ve = 0 mV) using the following equations:

(3) $gI(t) = [gT(t)*(Vrev(t)-Ve)]/(Vi-Ve)$

(4) $gE(t) = [gT(t)*(Vrev(t)-Vi)]/(Ve-Vi)$

SAC Ca^{2+} Light Responses and morphology

For spot response receptive field mapping experiments, SAC varicosity ROIs were identified using a custom macro (FIJI). A summed intensity projection was created from the movie of the imaged varicosity, a Gaussian blur was applied to remove sharp edges (sigma = 1.5), and the ROI center was selected using the default thresholding algorithm. This ROI mask was dilated twice to ensure even sampling throughout the movie. Background ROIs were selected on the same Gaussian blurred image, but using the triangle threshold algorithm. SAC varicosity Ca^{2+} responses were analyzed with custom Matlab scripts. Average fluorescence intensity (F) was calculated for each ROI and background subtracted using the average intensity of the background ROI defined above for each frame. Background subtracted F traces were segmented by stimulus presentations. ΔF/F traces for each stimulus were calculated using the fluorescence intensity during the last half of the inter-trial period before the stimulus (3 s) and averaged together based on stimulus location. Stimulus center positions were matched to the closest point on the imported SAC dendrite reconstruction using custom Matlab scripts. Moving averages and standard deviations were calculated using the Average Waves function in Igor Pro.

For direction selectivity experiments, SAC varicosity ROIs were identified using a custom macro (FIJI). Images were 3D median filtered to denoise, baseline subtracted via a 100-frame z median filter, and then bandpass filtered (2-15 pixels). The processed image was thresholded via the Triangle algorithm, with upper and lower bounds manually defined, and the background was subtracted. Potential individual varicosities were identified as local maxima on the average projection of the background-subtracted stack via a user defined threshold level and a subsequent watershed step filled them out. The resulting varicosity and background ROI masks were imported into Matlab for further processing.

SAC varicosity Ca^{2+} responses were analyzed with custom Matlab scripts. Average fluorescence intensity (F) was calculated for each ROI and background subtracted using the average intensity of the background ROI defined above for each frame. Background subtracted F traces for each ROI were segmented by stimulus presentations and the F traces for each stimulus direction were averaged together. ΔF/F traces were calculated using the fluorescence intensity during the first 2/5 of the time in between stimulus presentations as the baseline. Ca^{2+} responses to a given stimulus were defined as the maximal ΔF/F during stimulus presentation. ROIs were excluded from further analysis if their baseline background-subtracted fluorescence was <1 or the maximal responses to ≥4 stimulus presentations was not >2.5 standard deviations of the total ΔF/F trace for that stimulus direction. Vector sums were calculated from these maximal ΔF/F values for each ROI, with the preferred direction defined as the angle of the vector sum. Direction selective indices were calculated using the formula:

$$(3)\ DSI = \frac{(preferred - null)}{preferred}$$

where preferred is the peak Ca^{2+} transient in response to the stimulus moving in the direction closest to the preferred direction and null is the Ca^{2+} transient in response to the stimulus moving oppositely. For outward vs. inward calculation, preferred direction corresponded to the stimulus moving in the direction closest to that of the Euclidean angle described below.

Imaged ROIs were matched to their respective locations on the imported SAC reconstruction using custom Matlab scripts utilizing the TREES toolbox [50, 51]. For each imaged varicosity, the Euclidean angle from the SAC soma to that varicosity was calculated using the point of transition from soma to dendrites in the tree. Average dendritic angles were calculated by first calculating the angle and distance from a dendritic branch point to the next branch point along that path, and then taking a vector sum of these angles and distances. Tortuosity was computed as the path length from the soma to a varicosity divided by the length of the Euclidean distance from soma to varicosity.

To determine how much of the variance in the varicosity directional preference is explained by different SAC dendritic branches we used a series of restricted linear regression models in which one dendritic branch was allowed to vary while holding the other branch angles at their median. Linear regressions were performed individually on the sine and cosine of dendritic branch and varicosity directional preference data and the inverse tangent of the resulting predictors were used to compute circular correlations [54] between the predicted and measured varicosity directional preferences. Regression models were validated with 10-fold cross validation by using a random sample of 90% of the data to fit the linear regression models and the remaining 10% of the data to calculate circular correlations. The model was bootstrapped 5000 times to get confidence intervals of the cross-validated circular correlations.

Statistics

Statistical tests used are indicated in the figure legends. All tests were two-sided. We report exact p values for all tests in which $p > 0.001$.

Data and Software Availability

The datasets generated during and/or analyzed during the current study and all custom scripts and functions generated or used during the current study are available from the corresponding author on request.

KEY RESOURCES TABLE

REAGENT or RESOURCE	SOURCE	IDENTIFIER
Antibodies		
Bacterial and Virus Strains		
Biological Samples		
Chemicals, Peptides, and Recombinant Proteins		
Ames' Media	Sigma	A1420-10X1L
Oregon Green BAPTA-1 Hexapotassium Salt	Life Technologies	O6806
Critical Commercial Assays		
Deposited Data		
Experimental Models: Cell Lines		
Experimental Models: Organisms/Strains		
Mouse: B6;FVB-Tg(Trhr-EGFP)HU193Gsat/Mmucd	MMRRC	RRID:MMRRC_030036-UCD
Mouse: B6.129S6-ChATtm1(cre)lowl/J	The Jackson Laboratory	RRID:IMST_JAX:018957
Mouse: B6.129-Gt(ROSA)26Sor^{tm1Joe}/J	The Jackson Laboratory	RRID:IMST_JAX:026005
Mouse: *Sema6A* Gene Trap	[18, 46]	N/A
Oligonucleotides		
Recombinant DNA		
Software and Algorithms		
Trees Toolbox	[50]	http://www.treestoolbox.org/
Segmentation Simple Neurite Tracer ImageJ plugin	NIH	http://imagej.net/Simple_Neurite_Tracer
Image J	NIH	https://imagej.nih.gov/ij/
Matlab	Mathworks	https://www.mathworks.com/products/matlab.html
Igor Pro	WaveMetrics	https://www.wavemetrics.com/products/igorpro/igorpro.htm
Imaris	Bitplane	http://www.bitplane.com/imaris/imaris
Pairwise Stitching Image J Plugin	NIH	http://imagej.net/Image_Stitching
Other		

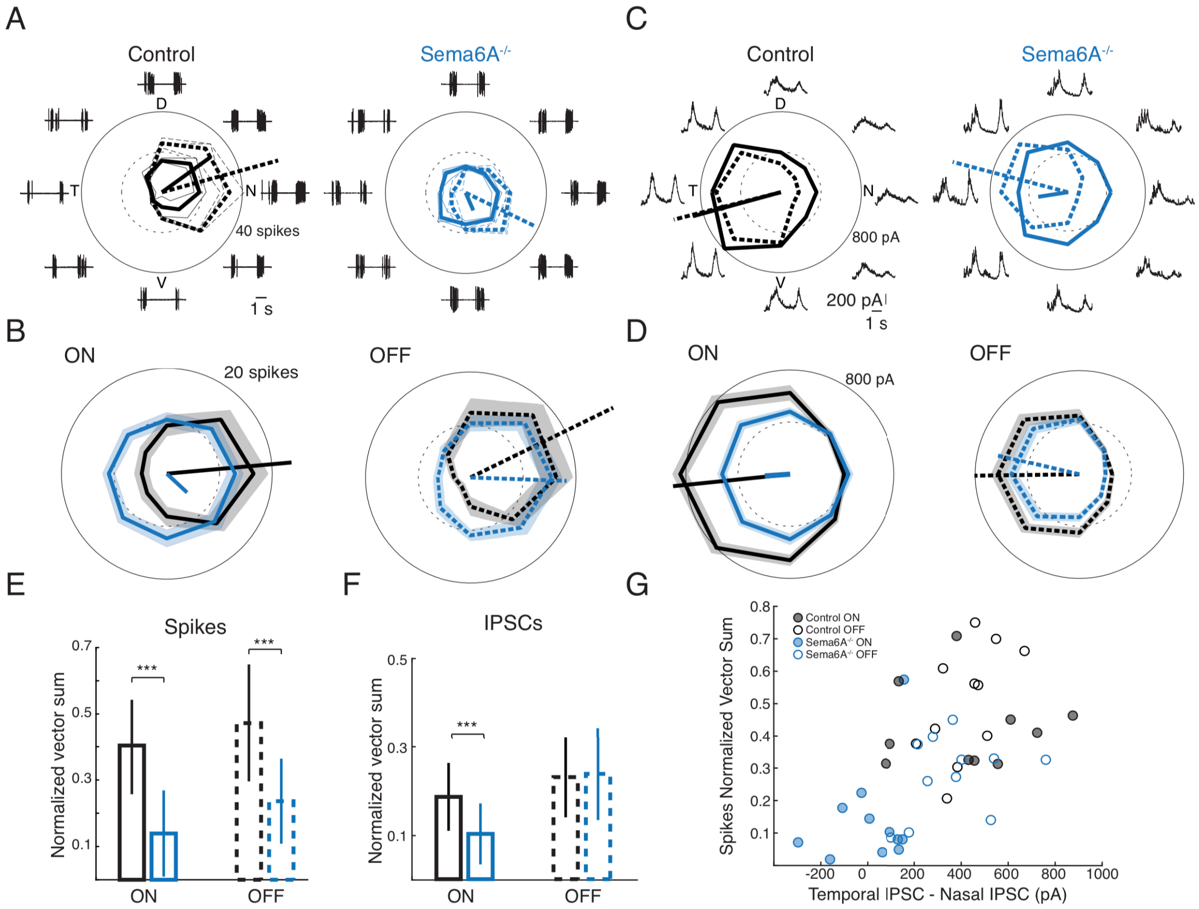

Figure 1. DSGCs in *Sema6A*$^{-/-}$ mice receive weak and symmetric inhibition.
A. Example DSGC spikes to moving bars in eight directions. Tuning curves of mean spike counts for ON (solid) and OFF (dotted) responses are shown with respective vector sums. Thin lines are spike counts of individual trials. D,T,V,N = motion towards dorsal, temporal, ventral, or nasal retinal locations, respectively.
B. Average spike tuning curves across all DSGCs (n=13 littermate Controls, 17 *Sema6A*$^{-/-}$) ± sem.
C,D. Same as *A,B* for peak IPSCs. Individual trials were averaged before calculating peaks (n=15 Control, 21 *Sema6A*$^{-/-}$).
E,F. Normalized vector sums of tuning curves for ON and OFF responses ± SD for spikes (E) and IPSCs (F). 1 way ANOVA, Tukey-Kramer post-hoc, ***$p < 0.001$.
G. Spike tuning increases with greater SAC-mediated inhibition for DSGC ON and OFF responses in both Control and *Sema6A*$^{-/-}$ mice.
See also Figure S1.

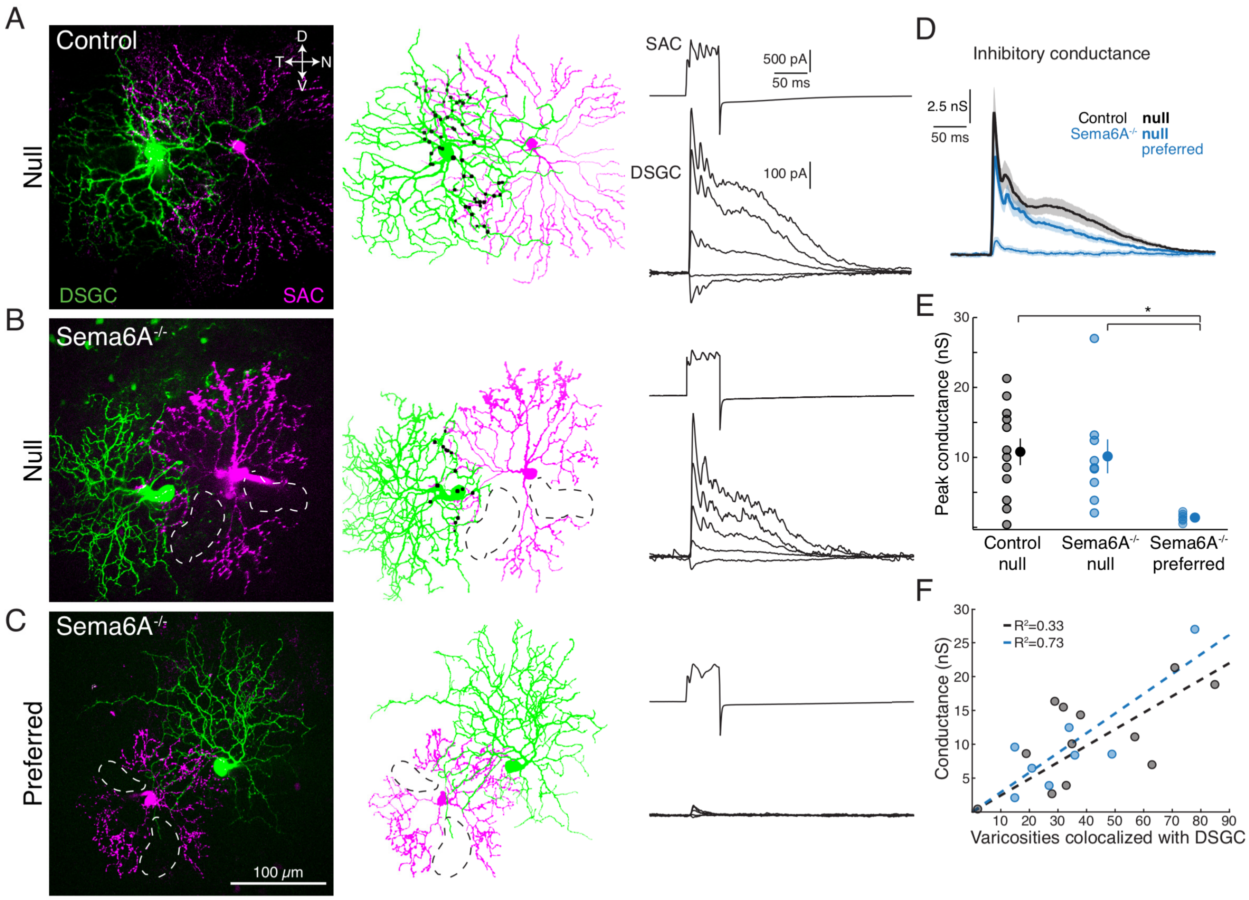

Figure 2. SAC-DSGC synaptic strength and asymmetric wiring is preserved in *Sema6A*$^{-/-}$ mice.
A-C. Examples of paired recordings between DSGCs and null side control (A), null side *Sema6A*$^{-/-}$ (B) and preferred side *Sema6A*$^{-/-}$ (C) SACs. (left) Projections of 2-photon images, (middle) reconstructions with putative synaptic sites in black [9], and (right) inhibitory synaptic recordings from SAC-DSGC pairs. SAC capacitive transients are clipped. Dotted lines are missing portions of *Sema6A*$^{-/-}$ SAC dendritic arbors. D,T,V,N are retinal coordinates as in Figure 1.
D. Average inhibitory conductance traces ± sem for SAC-DSGC pairs. (n=12 Control, 9 *Sema6A*$^{-/-}$ null, 6 *Sema6A*$^{-/-}$ preferred).
E. Average peak inhibitory conductance ± sem. 1-way ANOVA $p < 0.0135$, Tukey-Kramer post-hoc, $*p = 0.014$ Control vs *Sema6A*$^{-/-}$ preferred, $*p = 0.032$ *Sema6A*$^{-/-}$ null vs preferred.
F. SAC-DSGC inhibitory conductance increases with the number of putative synaptic sites from null oriented SAC dendrites [9].

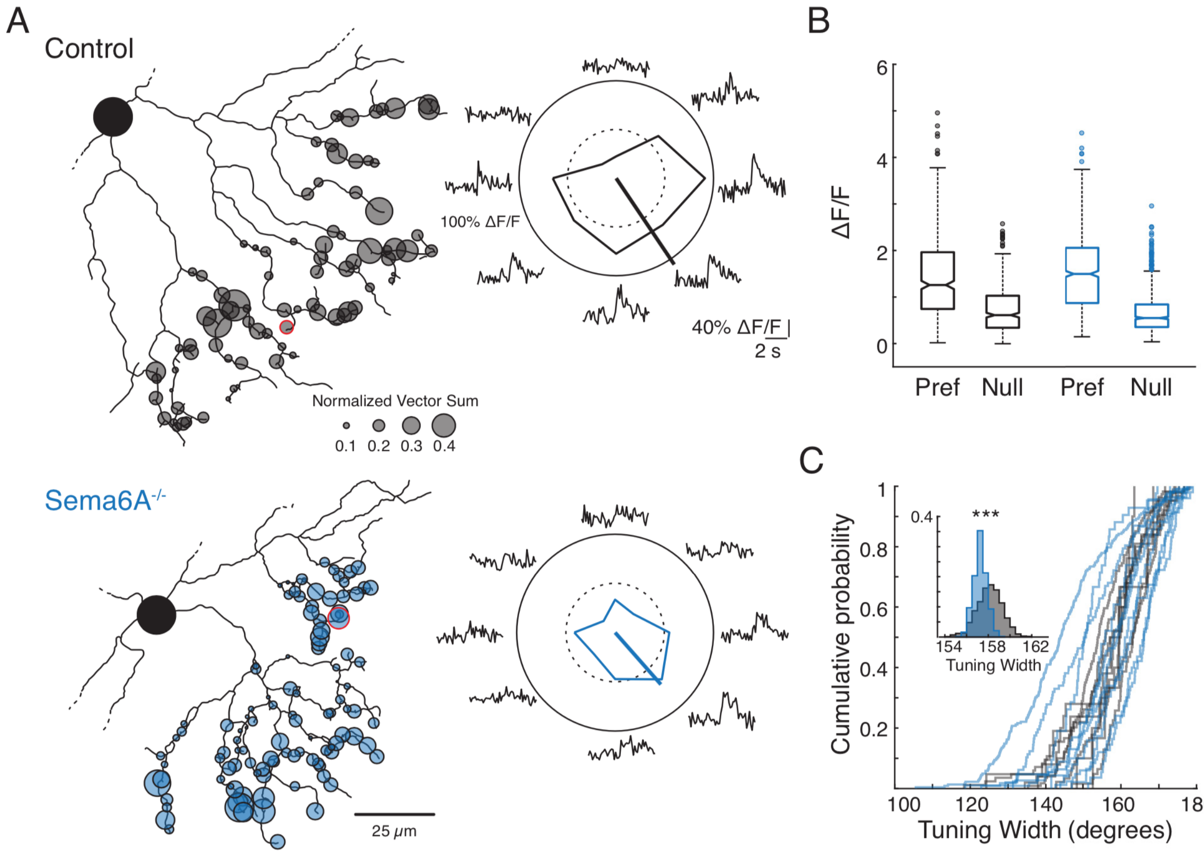

Figure 3. SAC varicosity direction selectivity is preserved in *Sema6A*$^{-/-}$ mice.
A. (left) Reconstructions of Control (top) and *Sema6A*$^{-/-}$ (bottom) SACs with imaged varicosities denoted by semi-transparent circles. Circle diameter represents Ca^{2+} response tuning curve normalized vector sum magnitude, a measure of directional tuning. (right) Average Ca^{2+} responses (□F/F_O) and corresponding tuning curves of two example varicosities (red circles, left). The straight lines inside the polar plots indicate the vector sums.
B. Peak Ca^{2+} increases for Control or *Sema6A*$^{-/-}$ varicosities in response to stimulation along the preferred-null axis (n = 462 Control, 840 *Sema6A*$^{-/-}$ varicosities). Preferred responses are significantly different than null responses for both Control and *Sema6A*$^{-/-}$ SAC varicosities. Kruskal-Wallis, Tukey-Kramer post-hoc, $p < 0.001$.
C. Cumulative distributions for each SAC of varicosity Ca^{2+} response tuning widths. Inset: Probability distribution of mean tuning width for Control and *Sema6A*$^{-/-}$ varicosities after randomly sampling the same number of varicosities from each SAC. *Sema6A*$^{-/-}$ SAC varicosities have slightly smaller tuning widths, t-test ***$p < 0.001$. See also Figure S2.

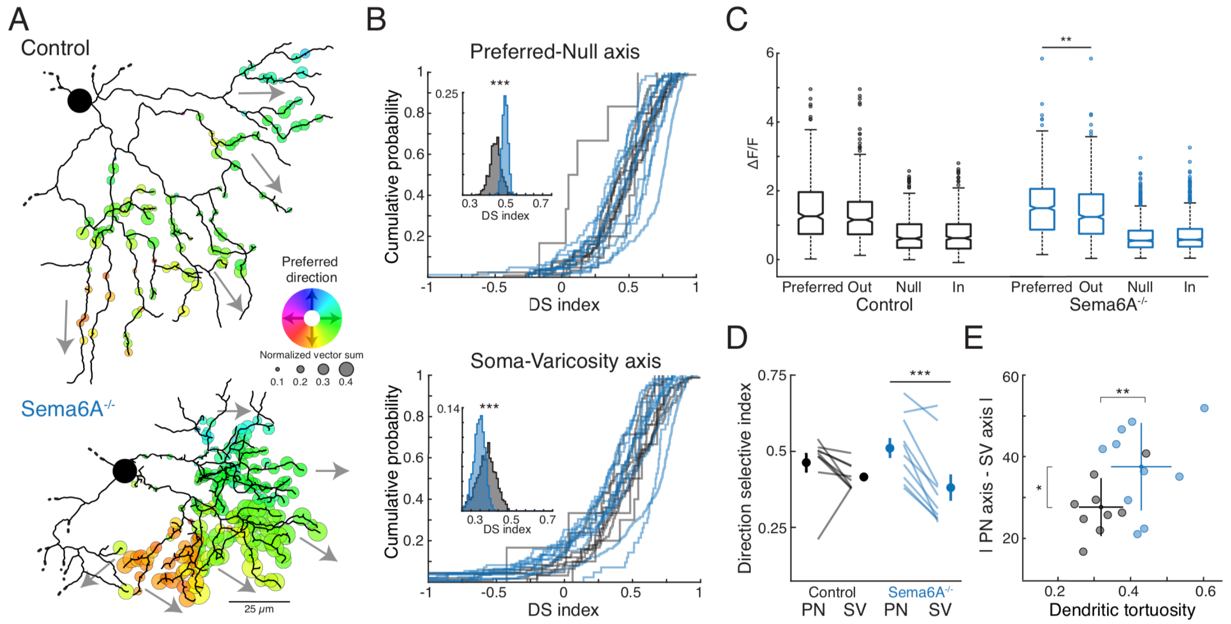

Figure 4. *Sema6A*$^{-/-}$ SAC varicosities are not necessarily tuned to centrifugal motion

A. Reconstructions of Control (top) and *Sema6A*$^{-/-}$ (bottom) SACs with imaged varicosities denoted by colored circles. Gray arrows indicate orientation of the proximal portion of the dendrite on which the surrounding varicosities are located. Inset: color code for varicosity preferred directions.

B. Cumulative distributions for each SAC (n = 9 Control, 10 *Sema6A*$^{-/-}$) of varicosity direction selectivity indices (see Methods) calculated along the preferred-null axis (top), defined by the orientation of the tuning curve vector sum for each varicosity, and along the soma-varicosity axis (bottom), defined by the anatomical angle from the SAC soma to each varicosity. Inset: Probability distribution of mean direction selective index for Control and *Sema6A*$^{-/-}$ varicosities after randomly sampling the same number of varicosities from each SAC. *Sema6A*$^{-/-}$ SAC varicosities have slightly higher DSIs along the preferred-null axis, t-test ***$p < 0.001$, and slightly lower DSIs along the soma varicosity axis, t-test ***$p < 0.001$.

C. Peak Ca^{2+} increases for Control (left) or *Sema6A*$^{-/-}$ (right) varicosities in response to different motion directions (n = 462 Control, 840 *Sema6A*$^{-/-}$ varicosities). Preferred and null are the responses along the preferred-null axis, and out and in are responses along the soma-varicosity axis. *Sema6A*$^{-/-}$ varicosities have a significant reduction in peak Ca^{2+} responses to outward motion compared to responses to preferred direction motion. All preferred and outward responses are significantly different than all null and inward responses, Kruskal-Wallis, Dunn-Sidák post-hoc, $p < 0.001$, **$p = 0.0016$.

D. Average varicosity direction selective index (see Methods) for each imaged SAC. Indices were calculated using Ca^{2+} responses along the preferred-null axis (PN) or along the soma-varicosity axis (SV). Paired t-test, ***$p = 0.17$ Control, $p < 0.001$ *Sema6A*$^{-/-}$.

E. Average absolute angular difference between the preferred-null axis and the soma-varicosity axis for the varicosities on each SAC as a function of average dendritic tortuosity (see Methods). t-test, *$p = 0.032$ angular difference, **$p = 0.005$ tortuosity.

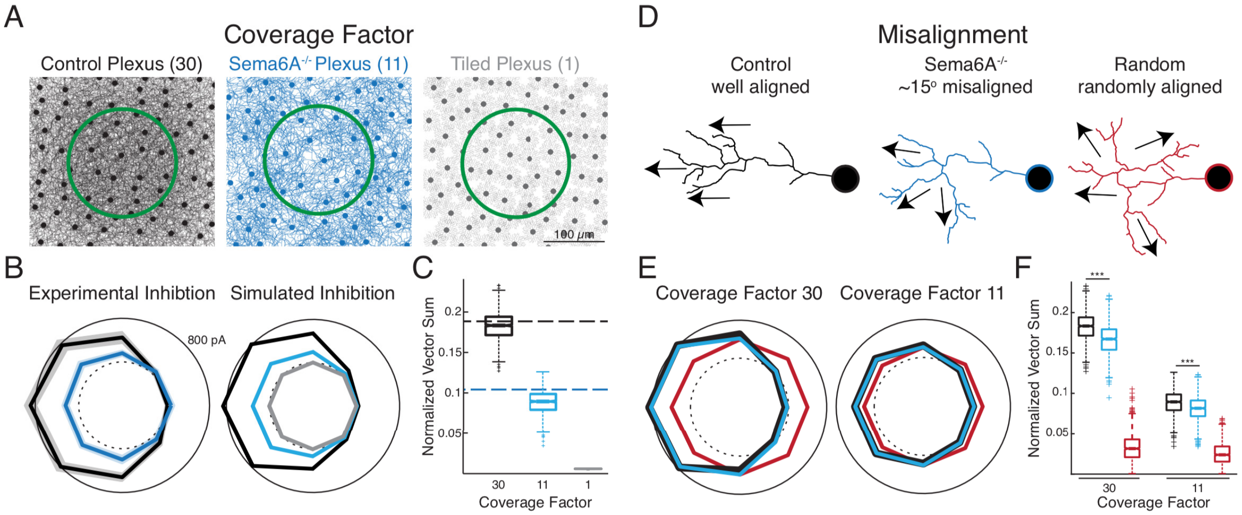

Figure 5. Reduced SAC dendritic coverage in *Sema6A*$^{-/-}$ mice leads to weak and symmetric inhibition in DSGCs.

A. Schematic depicting differences in the SAC coverage factor between Control retinas, *Sema6A*$^{-/-}$ retinas, and retinas with a SAC coverage factor of 1. Green circle indicates extent of DSGC dendritic arbor. The shorter dendrites in *Sema6A*$^{-/-}$ SACs leads to a 63% reduction in dendritic coverage (see [17]).

B. (left) Average ON response IPSC tuning curves ± sem for DSGCs in Control (black) and *Sema6A*$^{-/-}$ (blue) mice in response to moving bar stimulation (see Figure 1D). Accounting for the symmetric inhibitory contribution from non-SAC GABAergic amacrine cells [19, 20], there is a 67% reduction in SAC-mediated inhibition for DSGCs in *Sema6A*$^{-/-}$ mice compared to Control. (right) Simulated IPSC tuning curves for DSGCs based on SAC coverage factors in Control (black), *Sema6A*$^{-/-}$ (blue), and coverage factor 1 (grey) conditions.

C. Normalized vector sum magnitudes for IPSC tuning curves from experimental (dotted lines) and simulated (boxplots) data in B. The simulated inhibition based on the *Sema6A*$^{-/-}$ SAC coverage factor leads to a reduction in overall IPSC directional tuning matching the experimental data.

D. Schematic depicting alignment between soma-varicosity angles and varicosity preferred directions used in the simulation in E,F (see Figure 4).

E. Simulated IPSC tuning curves for DSGCs at Control (30) and *Sema6A*$^{-/-}$ (11) SAC coverage factors in which angular differences between SAC varicosity anatomical and functional axes were randomly drawn from the experimental Control (black) and *Sema6A*$^{-/-}$ (blue) data (Figure 4E). The same simulation was also performed using randomly drawn differences between anatomical and functional axes from -359 to 359 degrees (red).

F. Normalized vector sum magnitudes for IPSC tuning curves from simulated data in E. The misalignment between the SAC-DSGC wiring axis and varicosity preferred directions in *Sema6A*$^{-/-}$ mice leads to a significant reduction in IPSC tuning, with larger reductions occurring at denser SAC coverages. DSGCs would experience symmetric inhibitory input with a complete loss of alignment in more tortuous SAC dendrites (red). Kruskal-Wallis, Tukey-Kramer post-hoc,*** $p < 0.001$.

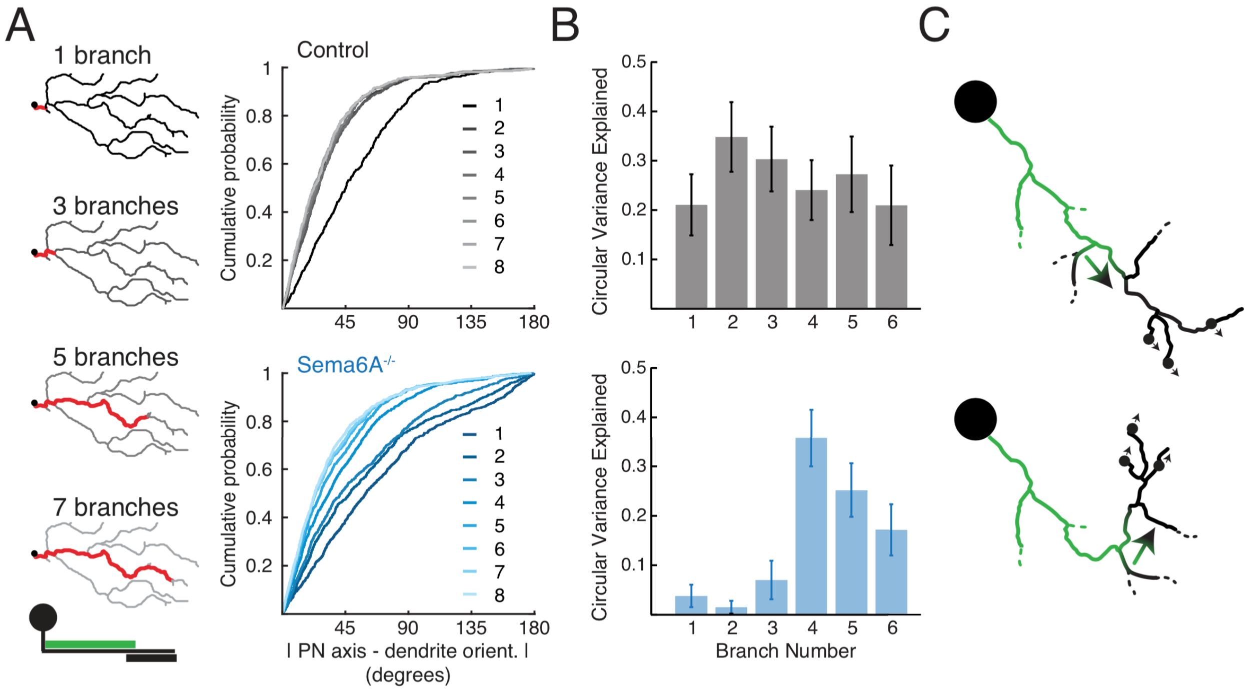

Figure 6. Varicosity preferred directions are determined by the angle of the SAC dendrite at the end of the bipolar cell input distribution.

A. (left) Schematics showing the portion of the dendrite used for determining average dendritic orientation. (bottom) Schematic depicting average location of glutamatergic inputs (green) and release sites (black) on a SAC process [1, 5]. (right) Cumulative distributions of absolute angular differences between the orientation of Ca^{2+} response tuning curve vector sums for each varicosity and the average orientations of portions of the dendrite on which the varicosity is located. Lighter lines indicate angular differences computed using dendritic orientations of portions of the SAC dendrite farther from the soma as indicated by the legend (n = 462 Control varicosities, 840 *Sema6A*$^{-/-}$ varicosities).
B. Bootstrapped circular regression analysis shows that the variance in varicosity preferred directions is best explained by the angle of the 4th branch order SAC dendritic segment. Error bars are 95% confidence intervals.
C. Schematic depicting Control (top) and *Sema6A*$^{-/-}$ (bottom) SACs. Varicosity (black circle) preferred directions are determined by the angle of the SAC dendrite at the end of the bipolar cell input distribution (green).
See also Figure S3.

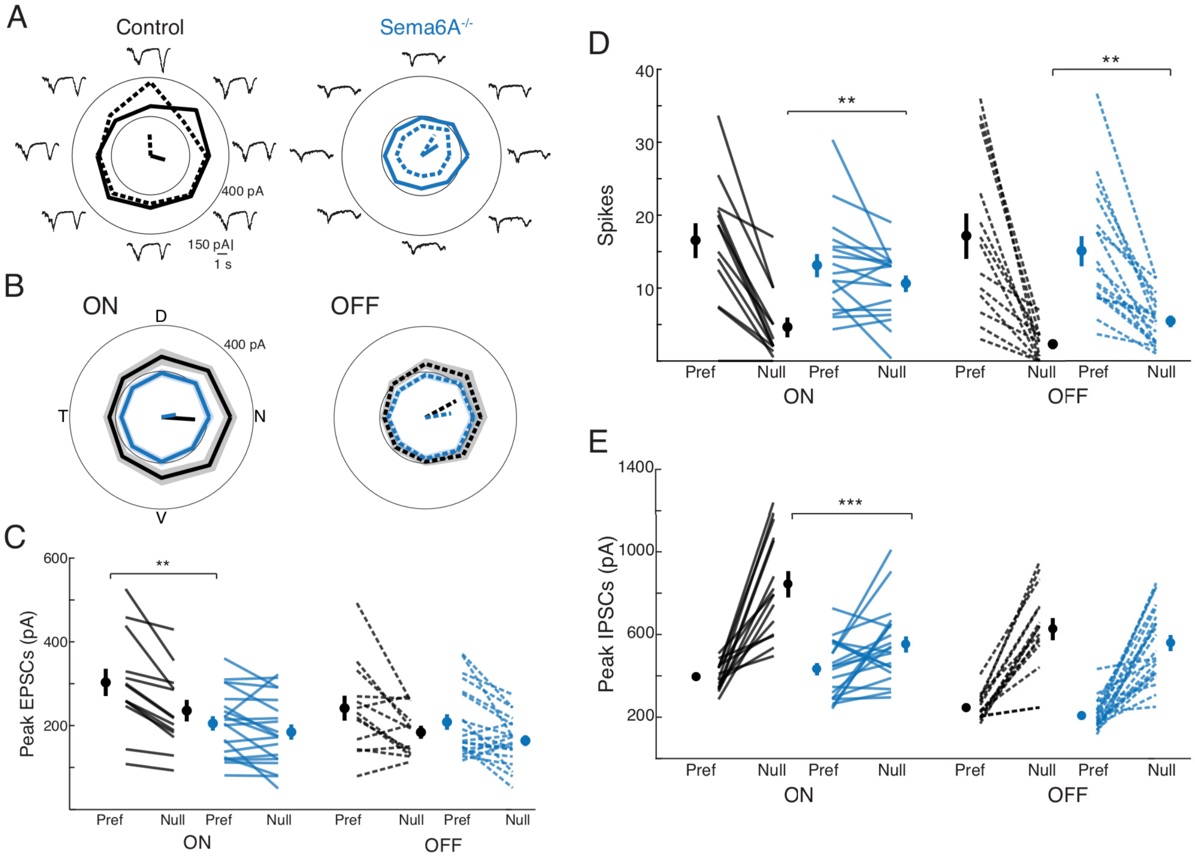

Figure S1. Related to Figure 1. nDSGCs in Control and Sema6A$^{-/-}$ mice receive the same amount of excitatory synaptic input during null direction stimulation.

A. Example DSGC EPSC responses to moving bars of light in eight different directions. Average tuning curves for ON (solid line) and OFF (dotted line) responses are shown with respective vector sums.

B. Average EPSC tuning curves across all nDSGCs (n=15 Control, 21 Sema6A$^{-/-}$) ± sem.

C. Peak EPSCs to preferred and null direction stimulation. t-test, $p = 0.007$.

D. Spike responses to preferred and null direction stimulation. t-test, $p = 0.002$ ON, $p = 0.007$ OFF. Note, the decrease in DSGC OFF spike tuning in Sema6A$^{-/-}$ is likely due to aberrant innervation of the OFF synaptic layers of the retina by ON SACs [17], which is evident in the small OFF evoked excitatory conductance in some Sema6A-/- ON SACs (Supplementary Figure 2). Indeed, a similar, but not significant, decrease in DSGC OFF tuning in Sema6A$^{-/-}$ mice was also observed in a previous study, which used a much larger stimulus area [17]. The smaller stimulus area used in our study also reduces the contribution of surround inhibitory inputs to the DS circuit [48]. Together, these factors may have enabled the small but significant increase in null direction OFF spiking we observed (Figure. 1C), reducing the directional tuning.

E. Peak IPSCs to preferred and null direction stimulation. t-test, $p < 0.001$.

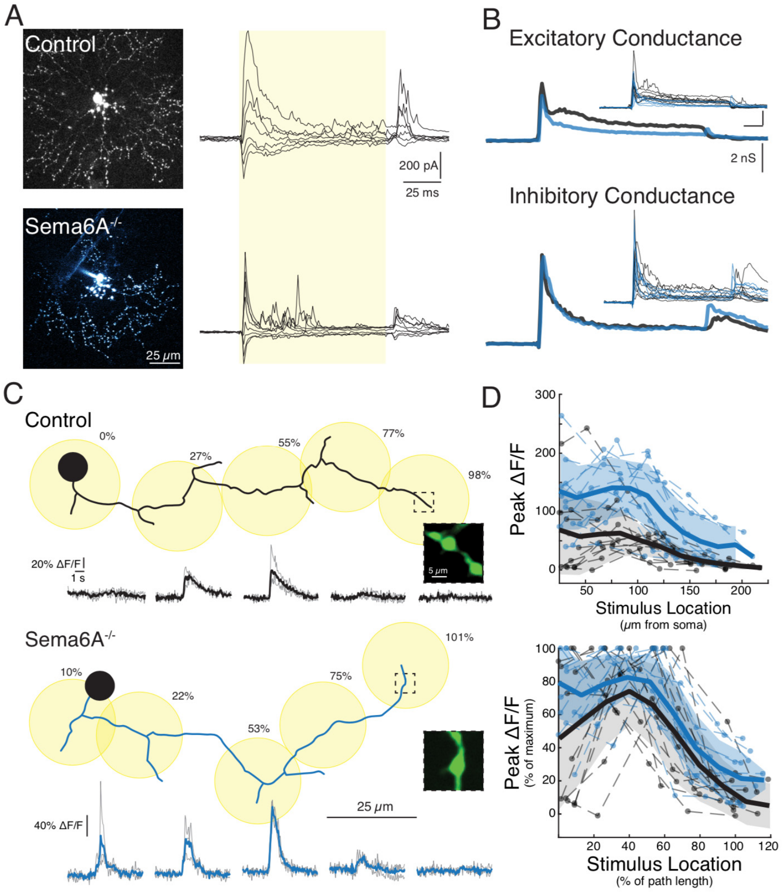

Figure S2. Related to Figure 3. Postsynaptic responses and input distributions are preserved in Sema6A$^{-/-}$ SACs.
A. (left) Max intensity projections of 2 photon image stacks of dye filled Control and Sema6A$^{-/-}$ SACs. (right) Synaptic currents recorded in pictured SACs at various holding potentials (-100, -80, -60, -40, -20, 0, 20 mV) in response a 400 µm diameter flash of light centered on the soma. Note the small excitatory OFF response in the Sema6A$^{-/-}$ SAC that is absent from the Control SAC.
B. Average excitatory and inhibitory conductance traces measured in Control (black) and Sema6A$^{-/-}$ (blue) SACs in response to light flashes. Excitatory currents are more transient in Sema6A$^{-/-}$ SACs and some SACs have a small OFF excitatory component. Unlike in [17], we observed no difference in ON inhibitory light responses in Sema6A$^{-/-}$ SACs, although the small OFF inhibitory response is larger and has a shorter latency. Inset: Excitatory and inhibitory conductance traces for each recorded cell (n = 9 Control, 6 Sema6A$^{-/-}$ SACs).
C. Example Control and Sema6A$^{-/-}$ SAC reconstructions with locations of visual stimulation spots and varicosity light responses. Percentages indicate the relative path distance of the closest point on the SAC dendrite to the center of the spot. Note, the final spot can be centered beyond the end of the dendrite (>100% path length). Grey traces are the individual ΔF/F responses following the visual simulation above each trace. Thick lines are mean of the three trials. Insets: Summed intensity projections of the imaged varicosities in the areas indicated by the dotted boxes.
D. (top) Peak ΔF/F responses for each imaged varicosity (n = 12 varicosities from 6 SACs, Control; n = 13 varicosities from 5 SACs Sema6A$^{-/-}$) in response to different visual stimulation locations (dots) connected by dotted lines. Thick lines are means with ± s.d. shading. Sema6A$^{-/-}$ SACs have larger Ca^{2+} responses than Control SACs. (bottom) Ca^{2+} transients in Control and Sema6A$^{-/-}$ SACs are largest during proximal visual stimulation. Normalized ΔF/F responses for each imaged varicosity as a function of relative stimulus location. Ca^{2+} transients are largest during visual stimulation centered at 20-60% of total dendritic length, while decreases in Ca^{2+} responses occur with stimuli centered at > 80% of total dendritic length, where excitatory postsynaptic structures are generally absent (see [1]).

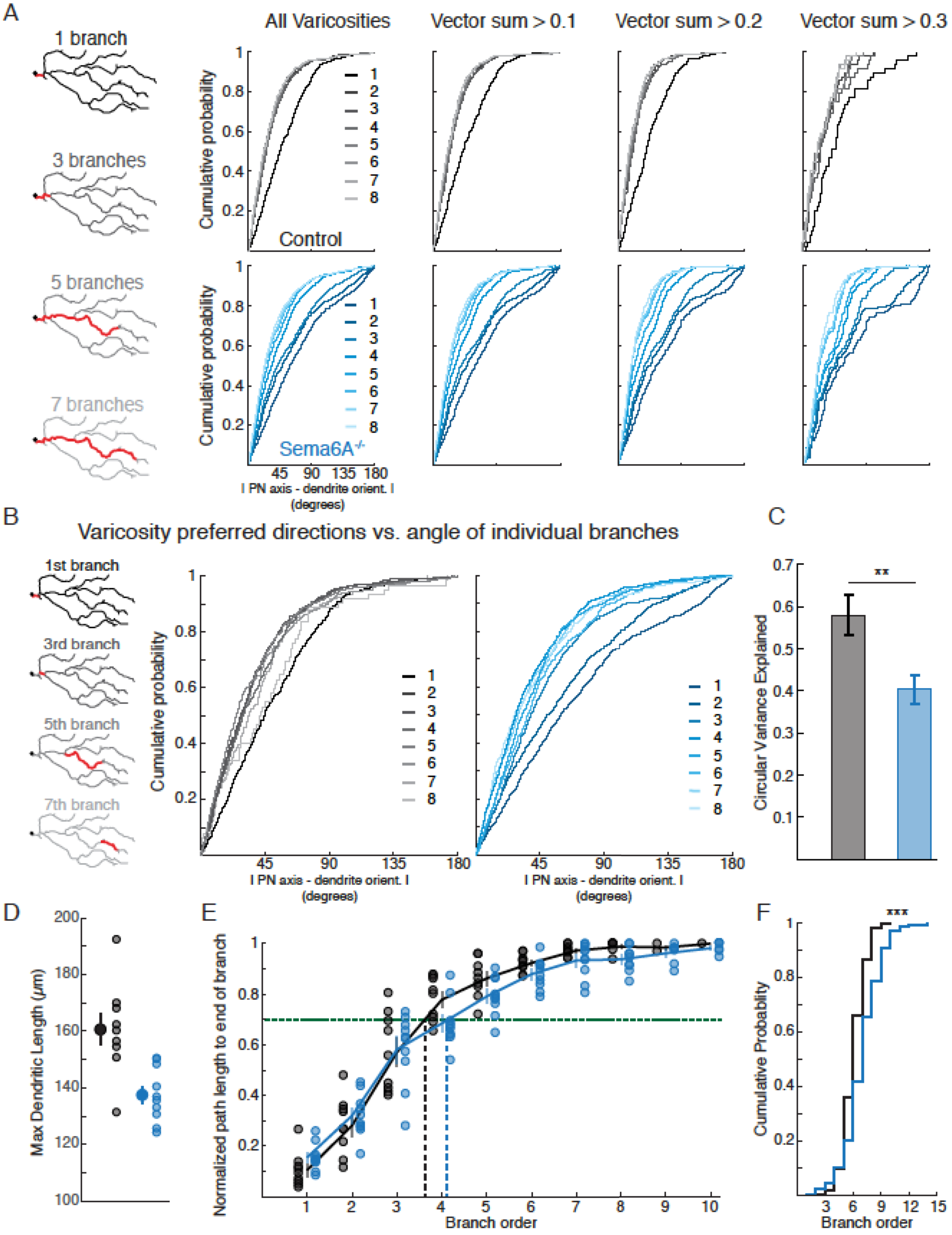

Figure S3. Related for Figure 4. SACs boutons define their directional preference by the angle of the 4th and 5th branch order dendrites.

A. Varicosity preferred directions are determined by the angle of the dendrites after the 4th branch order regardless of the degree of varicosity direction selectivity. Cumulative distributions of angular differences between the orientation of the vector sum of the Ca^{2+} response tuning curve for each varicosity and the average orientations of portions of the dendrite on which the varicosity is located (as in Figure 4). Vector sum magnitude cutoffs are indicated at the top of each column.
B. Cumulative distributions of angular differences between the orientation of the vector sum of the Ca^{2+} response tuning curve for each varicosity and the orientations of specific branch order segments of the dendrite on which the varicosity is located. Lighter lines indicate angular differences computed using dendritic orientations calculated with portions of the SAC dendrite farther from the soma as indicated by the legend. Angular differences are smallest in $Sema6A^{-/-}$ SACs when computed with the orientation of the 4th or 5th branch order dendrites.
C. Percent of the variance in varicosity preferred directions explained by dendritic orientations in a series of restricted circular regression models. Control dendrites are better overall predictors of varicosity preferred directions due to the lower variance in dendritic angles between segments. ** $p = 0.0013$, 2 sample z test.
D. Maximum dendritic length for each imaged SAC. Individual $Sema6A^{-/-}$ SAC dendrites are ~ 20 µm shorter than Control SACs dendrites.
E. Average normalized path lengths along dendrites at the end of the indicated branch order. Individual data points are average normalized path lengths of all fully reconstructed dendrites for each imaged SAC ($n = 9$ Control, 10 $Sema6A^{-/-}$ SACs). Green dotted line indicates 71% path length, corresponding to the average extent of bipolar cell input onto the SAC dendrite as determined by glutamate uncaging [1] and electron microscopy [2, 5]. Vertical dotted lines show that bipolar cells inputs extend to about the end of the 4th branch order SAC dendrites in both Control and $Sema6A^{-/-}$ SACs.
F. Distribution of branch orders that imaged varicosities were located on in $Sema6A^{-/-}$ and Control SACs. $Sema6A^{-/-}$ SACs had slightly increased branching, causing imaged varicosities to be located on 1 higher branch order on average. ($n=462$ Control, 840 $Sema6A^{-/-}$ varicosities). Kolmogorov-Smirnov, ***$p < 0.001$.

Chapter V

A Gene Expression Screen to Identify Genetic Determinants of Asymmetric Synaptogenesis Between Starburst Amacrine Cells and Direction Selective Ganglion Cells

This chapter comprises previously unpublished data.

Shaw Hsu performed the experiments and analyzed the data for SAC morphology across development (Figure 1E,F).

Introduction

For nervous systems to produce the appropriate sensory perceptions and motor outputs, neurons must identify the correct pre- and post-synaptic partners. Thus, understanding how the nearly 10^{12} synaptic connections in the mouse brain are instructed is a fundamental goal of developmental neuroscience. Importantly, the processes that govern neuronal connectivity are born out at multiple levels, from connections between different brain regions to the subcellular localization of specific synapses on dendrites and axons (Swanson and Lichtman, 2016). The retina, due to its highly laminated structure and accessibility to study, has served as a prime model system for elucidating the rules of synaptic targeting (reviewed in (Zhang et al., 2016)). However, while much progress has occurred in identifying the genetic basis for laminar targeting of dendritic processes in the retina (e.g. (Duan et al., 2014; Sun et al., 2013; Visser et al., 2015)), few studies have assigned roles to molecules involved in establishing the subcellular synaptic specificity that is beginning to be mapped out anatomically (Briggman et al., 2011; Helmstaedter et al., 2013) within the dense milieu of neurites in each laminal layer.

The direction selective circuit provides an intriguing circuit model for determining the molecular underpinnings regulating subcellular synaptic localization. As described in other chapters, starburst amacrine cells (SAC) dendrites from a thick plexus within two layers of the retinal inner plexiform layer (S2 and S4), and this degree of overlap is required to provide enough asymmetric inhibition onto the DSGC to generate direction selectivity (Chapter IV). However, how SAC dendrites are able to identify the correct post-synaptic DSGC within this neurite forest is still unknown (reviewed in (Morrie and Feller, 2016), Chapter I). The asymmetric SAC-DSGC wiring scheme (Briggman et al., 2011) is established by a highly stereotyped synaptogenic program that does not appear to undergo pruning (Morrie and Feller, 2015) (Chapter II) and it is thus hypothesized that particular transmembrane signaling molecules are differentially trafficked to the four different ‘quadrants’ of the starburst cell dendrites, presumably via the starburst cell reading out local gradients that are present within the retina (reviewed in (Hoon et al., 2014)). These gradients are predicted to emanate from singularities at different points in the retinal hemisphere, corresponding to the centers of expansion or contraction of the visual field as the animal undergoes translatory motion (Sabbah et al., 2017). The SAC signaling molecules are then hypothesized to recognize complementary proteins expressed on the DSGC cell surface.

In support of the aforementioned hypothesis, loss of *FRMD7* in SACs leads to a loss of direction selectivity in DSGCs preferring horizontal directions, but vertical preferring DSGC direction selectivity is unaffected (Yonehara et al., 2016), indicating synaptogenic signaling cues along the two different singularity axes are independent. The loss of direction selectivity along the horizontal axes in *FRMD7*$^{-/-}$ mice results from the emergence of symmetry in the inhibitory input from SACs onto DSGCs, without decreasing the total amount of inhibition the DSGC experiences when summing input from all stimulus directions. Thus, FRMD7, a known intracellular trafficking protein, is hypothesized to differentially traffic SAC proteins along the horizontally oriented dendrites in SACs, although FRMD7 itself is expressed symmetrically within the SAC arbor (Yonehara et al., 2016). These results also indicate that the asymmetric wiring scheme may result from an asymmetric distribution of repulsive signals that prevent preferred oriented SAC dendrites from synapsing onto DSGCs, rather than signals promoting synaptic contacts from null oriented dendrites.

Although the aforementioned results support the idea of a molecular determination of direction selective circuit wiring, the molecules mediating this process have yet to be identified. In addition, while specific DSGC populations are labeled in many transgenic mouse lines (Dhande et al., 2013; Huberman et al., 2009; Kay et al., 2011; Rivlin-Etzion et al., 2011; Trenholm et al., 2011) and some of their genetic signatures have been identified (Kay et al., 2011; Peng et al., 2017) a comprehensive differential expression analysis using RNA sequencing has yet to be completed using these labeled lines. In addition, to what extent these molecular markers label specific or multiple DSGC populations remains unknown. Finally, many gene expression studies in DSGCs and SACs have used mice that are younger (p5-6) (Kay et al., 2011) or older (~P66) (Siegert et al., 2012) than the critical time window within the second postnatal week when asymmetric SAC-DSGC connectivity is established (Wei et al., 2011).

To begin to identify differentially expressed genes responsible for asymmetric synaptic connectivity, we first identified P10 as the age when null oriented SAC dendrites dramatically increase the number of synapses formed with DSGCs. We then isolated transgenically identified DSGCs at P10 from three different mouse lines representing two orthogonal preferred directions. By performing RNA-seq on cDNA libraries created from these sorted populations, we hope to generate a list of putative genes involved in repulsive subcellular SAC-DSGC synaptic signaling.

Results

Null oriented SAC processes rapidly form synapses with DSGCs beginning at P10

Paired recordings revealed that SACs undergo a dramatic increase in asymmetric synaptic connections with ON-OFF DSGCs between P7 and P14 (Wei et al., 2011), while optogenetic experiments showed that the emergence of asymmetric connections from SACs to ON DSGCs occurs around P8-9 (Yonehara et al., 2011). To ensure that RNA-seq samples would identify differentially expressed synaptic markers, we sought to identify a time point in development in which asymmetric connectivity was present but had not yet matured to adult levels using two different metrics.

First, we used paired recordings to directly assay SAC-DSGC connectivity (Figure 1A,B). As in (Morrie and Feller, 2015) we sequentially patched onto multiple SACs surrounding a single DSGC, enabling us to construct spatial maps of overall inhibitory conductance (Figure 1C). We found that while paired recordings at P9 revealed small inhibitory SAC-DSGC conductances and fairly symmetric connectivity, inhibitory conductances at P10 increased for null side pairs, leading to a significant asymmetry in total inhibition (Figure S1, Figure 1C,D). Thus, asymmetric connectivity is established by P10, although inhibitory conductances from null oriented SACs to DSGCs are still smaller than in adult animals (Figure 1D).

Second, we utilized the unique morphology of the SAC to analyze formation of presynaptic structures during development. Specifically, during the first two postnatal weeks SACs undergo a large morphological shift in their distal dendrites in which filopodial structures give way to thin dendrites with swellings, termed varicosities (Zheng et al., 2004). EM reconstructions of the direction selective circuit have identified these swelling as presynaptic GABA release sites (Briggman et al., 2011; Famiglietti, 1991). To determine when these structures emerge on the SAC dendrite during development, we sparsely labeled SACs using an inducible Chat::Cre^{ER} x LSL-TdTomato mouse and low doses of tamoxifen. After amplifying the TdTomato signal via immunohistochemistry, high resolution confocal imaging enabled precise reconstructions of SAC arbors throughout development (Figure 1E). By counting varicosities on

SACs from P7 – P14, we found that varicosities begin to emerge at P10, reaching mature levels by P12 (Figure 1F) and that varicosities appear symmetrically on the SACs. Thus, our morphological correlate of synaptogenesis corroborates our physiologically identified time point of P10 as the beginning of null oriented SAC dendrite synaptogenesis with DSGCs.

Isolation of transgenically identified DSGC populations for RNA sequencing

We next sought to isolate specific DSGC populations at P10 to probe what genetic differences existed that might instruct wiring with SACs. To do so, we took advantage of three well characterized BAC-GFP transgenic mouse lines: DRD4 (Huberman et al., 2009), TrHr (Rivlin-Etzion et al., 2011), and HB9 (Trenholm et al., 2011) (Figure 1A). The DRD4 and TrHr GFP lines label potentially non-overlapping populations of nasal preferring DSGCs (Rivlin-Etzion et al., 2011), while the HB9-GFP line labels ventral preferring DSGCs (Figure 1B). Thus, in comparing the transcriptional profiles of these populations, we can determine the extent to which Drd4 and TrHr populations are similar and what genes differentiate nasal and ventral preferring populations. Using retinas from three or more P10 mice of each transgenic line, we dissociated the tissue and isolated the DSGC populations using FACS (Figure 1C). This scheme was straightforward for the Drd4 mouse line (Figure 1D), in which we isolated 227 ± 84 GFP^+ cells from each set of littermate retinas, because Drd4 GFP^+ DSGCs are the only GFP^+ cells in the retinas of these mice. However, as discussed below, additional transgenic lines were necessary to isolate TrHr-GFP and Hb9-GFP DSGCs.

Both TrHr-GFP and HB9-GFP mouse lines express GFP in a subtype of DSGCs as well as other cells within the retina. TrHr-GFP mice express GFP in a large population of amacrine cells in the INL (Rivlin-Etzion et al., 2011) (Figure 3A,B). These amacrine cells are not GABAergic (Figure S2) but their neurotransmitter identity remains unknown. HB9-GFP mice express GFP in a population of cones photoreceptors (Figure 3D,E). These cones are found in a dorsal to ventral gradient across the retina, opposite that of s-cones (Figure S3). Some rare HB9-GFP^+ cones express S-opsin, while many, but not all, HB9-GFP^+ cones express M-opsin (Figure S3). Together, these results indicate that HB9-GFP^+ cones likely comprise both S- and M-coexpressing cones (which are the largest cone population in the mouse retina), as well as some of the exclusive S-opsin expressing cones (Haverkamp et al., 2005).

The presence of these non-DSGC GFP^+ cells, which greatly outnumbered GFP^+ DSGCs, within retinas from TrHr-GFP and Hb9-GFP mice precluded high confidence separation of DSGCs with FACS, even after selecting for the largest cells. Therefore, to avoid contaminating our RNA-seq analysis with transcripts from these amacrine and cone populations, we co-labeled our DSGCs with TdTomato by crossing TrHr-GFP and HB9-GFP mice to VGlut2-Cre x LSL-TdTomato mice (TVT or HVT mice) (Figure B,E). VGlut2 is expressed by all RGCs (Johnson et al., 2003) and within the GCL the VGlut2-Cre mouse line exclusively labels RGCs (Ellis et al., 2016). To confirm this specificity, we stained retinas from VGlut2-Cre x LSL-TdTomato mice with the pan-RGC marker RBPMS (Rodriguez et al., 2014) and TdTomato (Figure S4). There was nearly a 1:1 correspondence between TdTomato and RPBMS labeling, even for the few displaced ganglion cells in the INL (Figure S4). Thus, we conclude that within the GCL, all TdTomato labeled cells are RGCs. In addition to RGCs, VGlut2-Cre x LSL-TdTomato mice also label some horizontal cells (Martersteck et al., 2017) and cone photoreceptors. The labeled cones are likely to be the $VGlut2^+$ cones expressed in an even density throughout the retina (Wässle et al., 2006) and overlap minimally with the HB9-GFP^+ cones, ranging from 0-8% co-localization depending upon HB9-GFP cone density (Figure S5).

The colabeling of DSGCs with TdTomato and GFP in HVT and TVT mice enabled us to confidently isolate DSGC populations from these mouse lines using FACS (Figure 3C,F). TdTomato$^+$ RGCs were much brighter than their cone and horizontal cell counterparts, likely due to their larger size and/or greater VGlut2 expression. This was confirmed by first gating cells based on TdTomato fluorescence. The brightest TdTomato group were of larger size, and therefore RGCs, in the FSC/SSC plot (data not shown). Importantly, this meant that the small percentage of TdTomato and GFP co-expressing cones in the HVT mouse also separated well from the HB9-GFP$^+$ DSGCs (Figure 3F). Overall, these results indicate that GFP$^+$ DSGCs from Drd4, TrHr, and HB9-GFP mouse lines were selectively isolated from dissociated retinas, providing a highly purified population for subsequent RNA-sequencing analysis.

Confirmation of cDNA library quality

To determine whether cDNA libraries constructed from the bulk RNA of our samples was derived from a pure population of DSGCs we performed PCR using primers for genes known to be expressed in all or certain subtypes of DSGCs. For example, CART is a marker expressed in all but anterior preferring DSGCs (Dhande et al., 2013; Kay et al., 2011; Sabbah et al., 2017). PCR using primers specific for CART cDNA amplified an appropriately sized product from all our DSGC samples (Figure 4A). MMP17 is a more specific marker known to be expressed in Drd4-GFP$^+$ DSGCs but not in vertically preferring DSGCs (Kay et al., 2011). PCR using primers specific for MMP17 cDNA amplified an appropriately sized product from a Drd4 sample, as well as from our TrHr samples, albeit at lower expression levels (Figure 4B). Importantly, no MMP17 expression was detected in cDNA samples from the vertically preferring Hb9-GFP$^+$ DSGCs. Further quality control analysis using this technique with primers for both genes expressed in DSGCs and non-DSGC populations can be performed to further validate the isolation of specific DSGC populations using this technique.

CART and Cdh6 Cre mouse lines label vertically preferring DSGC populations

In addition to the VGlut2-Cre line, additional mouse lines were assayed in our screen to identify a TdTomato co-label for TrhR and Hb9-GFP$^+$ DSGCs. Cart is expressed in both TrHr and HB9 populations (Kay et al., 2011; Peng et al., 2017). Therefore, we crossed Cart-IRES-Cre (Cart-Cre) mice to LSL-TdTomato mice to label DSGCs. At P10 we found TdTomato expression in astrocytes in the inner limiting membrane, cells in the GCL, and amacrine cells in the INL (Figure 5A). When we crossed these mice into the TrHr line, we were surprised to find that very few GFP$^+$ DSGCs coexpressed TdTom, regardless of age of analysis (Figure 5B,C). In contrast, while GFP$^+$ DSGCs in the HB9 line coexpressed TdTom at low levels around P10, > 90% of GFP$^+$ DSGCs also expressed TdTom in adult animals (Figure 5B,D). Thus, the lack of co-labeling precluded the use of Cart-Cre mice for sorting HB9 and TrHr GFP$^+$ DSGC populations at P10, but Cart-Cre does provide genetic access to HB9-GFP$^+$ DSGCs in adult animals.

To determine the response properties of TdTomato$^+$ GCL cells labeled in the Cart-Cre mouse, we performed two photon population Ca^{2+} imaging (Bos et al., 2016; Briggman and Euler, 2011) on Cart-Cre TdTomato retinas electroporated with Cal 520 (Figure 5E). By simultaneously imaging and presenting the retina with a drifting bar stimulus, we found that some TdTomato$^+$ cells were direction selective (DSI > 0.15, 72/230, 31%), and of those that were directionally selective, most preferred bars moving in one of the two vertical directions on the retina (Figure 5F,G). However, not all TdTomato$^+$ cells in the GCL displayed ON-OFF responses to light flashes or moving bars, and many cells in the INL are labeled in the Cart-Cre mouse, indicating that Cart expression is not specific to DSGCs within the retina. Overall, these preliminary results, combined with a high degree of Hb9-GFP$^+$ DSGC labeling, indicate that of the DSGC populations labeled in the Cart-Cre TdTomato mouse in retinas from adult animals, the majority are vertically preferring ON-OFF DSGCs.

Cdh6 is also expressed by vertically preferring DSGCs and Cdh6-Cre^{ER} mice label DSGCs when crossed with a Thy1-GFP reporter (Kay et al., 2011). To determine whether HB9-GFP$^+$ DSGCs express cre in the Cdh6-Cre^{ER} mouse we crossed mice with these two alleles to the LSL-TdTomato reporter mouse. Injection of large doses of tamoxifen (1mg) in young animals led almost 40% of Hb9-GFP$^+$ DSGC to express TdTomato at P11 (Figure 6A,B). While this specificity would have worked for FACS sorting, the smaller percentage of cells labeled due to the inducible nature of the cre led us to pursue the use of the VGlut2-Cre line to isolate this rare population of cells. In addition, these results indicate that Cdh6-Cre is useful mouse line in which to drive expression of cre in HB9-GFP$^+$ DSGCs, as it is expresses cre earlier than the Cart-Cre mouse (Figure 5B), does not cause labeling of inner limiting membrane cells, and tamoxifen titers can be tested to induce sparse expression. However, Cdh6-Cre^{ER} also is expressed in SACs (Kay et al., 2011)data not shown) which may complicate experiments in which only HB9-GFP$^+$ DSGCs should be affected.

Discussion

These preliminary results provide the framework on which to conduct a screen to identify the molecular determinants of SAC-DSGC wiring. To construct a list of putative wiring genes, differential gene expression analysis will have to be performed on RNA-sequencing results, and then curated to identify cell surface proteins using the GO term ‘plasma membrane’. Using cre lines or other genetic tools (Tang et al., 2015) to selectively perturb the expression of these putative wiring genes in DSGCs, possibly via a CRISPR-Cas9 based mutagenesis screen (Sarin et al., 2018), will hopefully help elucidate how SAC dendrites find the correct postsynaptic partners.

To isolate GFP$^+$ DSGC populations many mouse lines were created by crossing various Cre, BAC, and reporter alleles. The following table summarizes the expression patterns of these mice and the extent that they label DSGCs.

	GCL	INL	ONL	DSGCs labeled (and %)
Hb9-GFP	v-DSGCs	-	Unidentified cone population	v-DSGCs (<100%?)
TrHr-GFP	n-DSGCs	GABA negative amacrine cells	-	n-DSGCs (<100%)
Drd4-GFP	nDSGCs	-	-	n-DSGCs (<100%)
VGlut2-Cre x Ai9	All RGCs	Displaced RGCs; horizontal cells?	VGlut2+ cones	All DSGCs labeled
Cart-Cre (Jax 028533) x Ai9	Astrocytes? Some DSGCs; unidentified RGCs	Unidentified amacrine cells	-	>90% Hb9-GFP DSGCs in adult ~10% of TrHr-GFP DSGCs Other vertical preferring DSGCs?
Cdh6-Cre^{ER} x Ai9	Vertical preferring DSGCs; SACs	SACs	-	~40% of HB9-GFP DSGCs (dependent on Tamoxifen dose)

Methods

Paired recordings

Paired recording were performed as previously described (Morrie and Feller, 2015), using Ca^{2+}-ACSF. SACs were depolarized from -70 to 0 mV for 50 ms to evoke GABA release. Conductance measurements were calculated for SAC-DSGC pairs as in Chapter IV.

Anatomic reconstructions of SACs

To induce sparse TdTomato expression in SACs, tamoxifen (Sigma) was delivered to CharCreER/TdTomato mice via intraperitoneal injection at a dose of 200µg in 125µL sunflower oil at postnatal day 4.

Mice were anesthetized with isoflurane and decapitated. The eyes were enucleated and the retinas dissected out from eyecup in bicarbonate buffered artificial cerebrospinal fluid (ACSF) solution. The orientations of the retinas were determined from landmarks on the pigment epithelium and marked by a cut in the ventral direction (Wei et al, 2010). Whole mount retinas were transferred onto filter papers and fixed in 4% paraformaldehyde (PFA) solution for 20 min at room temperature, then washed in block solution (2% donkey serum, 2% bovine serum albumin (BSA), 0.3% Triton-X in PBS, 0.2% sodium azide, 5 × 20 min) at room temperature. Next, retinas were incubated in primary antibody (1:500 rabbit anti-DsRed) for 72 hours at 4^oC, then washed in block solution for 72 hours at 4^oC. The retinas were then incubated in secondary antibody (1:1000 goat anti-rabbit Alexa 488, 1:1000 goat anti-rabbit Alexa 594) for 72 hours at 4^oC and washed in block solution for 72 hours at 4^oC. Then the retinas were mounted onto slides and cover-slipped with fluoromount-G (SouthernBiotech).

Starburst amacrine cells were imaged using a Zeiss LSM AxioObserver laser scanning confocal microscope with Zen 2010 software located at the University of California, Berkeley Molecular Imaging Center. Fluorescent confocal image stacks of starburst amacrine cells were acquired with a Plan-Apochromat 40x (NA = 1.4) or a Plan-Apochromat 60x (NA = 1.4) oil immersion objective and Immersol 518F oil (Figure 1E). Alexa Fluor 488 was excited using Argon 488 laser at around 15% transmission, and emission was detected from 493nm-630nm. Alexa Fluor 594 was excited using HeNe 594 laser at around 20% transmission, and emission was detected from 599nm-734nm. Images were taken at frame size of 2048x2048 pixel with a pixel size of around 100nm and a pixel dwell time of around 3.15µsec. Pinhole size was set to 1 Airy unit.

Starburst amacrine cell image stacks acquired from confocal microscopy were imported into Imaris software (Bitplane) and the dendritic processes and soma were reconstructed in three dimensions using the filament function under the Surpass mode (Figure 1E). Varicosities on starburst amacrine cell reconstructed filaments were marked manually using the draw spine feature, and the location and diameter of varicosities were exported using built-in Imaris statistical tools. Dendritic branch point number, dendritic segment number, dendritic branch depth, and dendritic arbor diameter analysis were also done using built-in Imaris statistical tools and exported. Exported data was analyzed using Igor-Pro (WaveMetrics).

FAC sorting of DSGCs

Dissocation of P10 retinas was carried out as in (Kay et al., 2011) with some modifications. Prior to retinal dissection, 80 µl of papain suspension (Worthington) was activated in 5 mL of HBSS + HEPES (10mM) by adding DNase and L-cysteine (C1276, Sigma).

The sterile filtered solution was left at 37°C while retinas were dissected. Retinal dissections took place in cold HBSS + HEPES. Whole retinal cups were transferred to HBSS + HEPES on a cold block until all retinas were dissected, and then transferred to the activated papain solution. Papain digestion occurred for 21 minutes at 37°C, gently shaking the retinas every 7 minutes to ensure even coating of the enzyme. Retinas were spun for 1.5 minutes at 200 g and then papain solution was aspirated and replaced with 2 mL of lo ovomocoid solution. Retinas were broken up with trituration using a p1000 tip, spun for 20 seconds at 200 g, the single cell supernatant was transferred to a new tube, and an additional 1mL of lo ovomocoid solution was added. This trituration process was repeated until all tissue was dissociated into a single cell suspension. Single cell suspensions were then passed through a 70 μm filter and spun down at 375 g for 10 minutes. After aspiration of the lo ovomocoid solution, cells were resuspended in 2 mL of MEM-B.

GFP^+ DSGCs were isolated using FACS. To draw gates, a GFP negative sample was run through the machine and > 1,000,000 events were recorded. Cells were selected based on size (largest cells for RGCs), then doublets were excluded, and GFP^+ cells were collected based on the aforementioned gate. For TVT or HVT mouse lines, double negative, GFP only, and VGlut2-TdTomato only samples were run first to ensure accurate gating. Cells were sorted into 500 μL of Trizol-LS and cDNA libraries were prepared using Smart-Seq technology by the Berkeley Functional Genomics Laboratory.

PCR of DSGC genes

PCR of cDNA was performed using primers created by qPrimerDepot (Cui et al., 2007) and illustra PuReTaq Ready-To-Go PCR Beads (GE). Thermocycler settings were 5 minutes 95° C digest, and then forty amplifications steps of 30 seconds 95° C, 30 seconds, 60° C, and 30 seconds 72° C. A 3 minutes elongation step was included after all cycles completed. Primers for Cart amplification were:
GTCGTCCCTTCACAAGCACT
ACGAGAAGAAGTACGGCCAA
Primers for MMP17 amplification were:
GCAGGTAGCCAAACCTGCT
GCTGCTTGTACTGGCGCT

Immunohistochemistry and data analysis

S- and M- opsin staining was carried out as previously described (Rosa et al., 2016). For all other staining procedures, filter paper mounted retinas were fixed for 20 minutes in 4% PFA at room temperature, rinsed three times 20 minutes with blocking buffer (2% Donkey Serum, 2% bovine serum albumin (BSA), 0.3% Triton-X, 0.2% Sodium Azide), and left in primary antibody diluted in blocking buffer overnight at 4°C. Retinas were then rinsed five times 20 minutes with blocking buffer and left in secondary antibody diluted overnight in blocking buffer at 4°C. Stained retinas were rinsed twice with blocking buffer and twice with PBS + 0.3% Triton-X, then mounted with Fluoromount-G and coverslipped. Primary antibodies used were rabbit anti-GFP (A11122), chick anti-GFP (ab13970), goat anti-TdTom (AB8181), rabbit anti-TdTom (632496), rabbit anti-GABA (2052), and rabbit anti-RBPMS (1830). Secondary donkey anti rabbit and goat antibodies were conjugated to Alexa Fluor 488 or 594. Images were taken with a Zeiss LSM AxioObserver laser scanning confocal microscope with Zen 2010 software using a 20x air objective.

Colocalization analysis on somas was performed with a custom Matlab script. First, a mask in the GFP channel was created by thresholding a maximum intensity projection into 5 bins and segmenting the top threshold bin into individual cells. The intensity of the other channel through all z-slices was then plotted for each masked soma with an area greater than 25 pixels. A user defined threshold was then established to distinguish marker positive cells.

Population Imaging

Population calcium imaging of electroporated retinas was performed as described in (Bos et al., 2016). Retinas were electroporated with 5 mM Cal520. TdTomato positive cell ROIs were constructed using a user defined threshold.

References

Bos, R., Gainer, C., and Feller, M.B. (2016). Role for Visual Experience in the Development of Direction-Selective Circuits. Current Biology.

Briggman, K.L., and Euler, T. (2011). Bulk electroporation and population calcium imaging in the adult mammalian retina. J. Neurophysiol. *105*, 2601–2609.

Briggman, K.L., Helmstaedter, M., and Denk, W. (2011). Wiring specificity in the direction-selectivity circuit of the retina. Nature *471*, 183–188.

Cui, W., Taub, D.D., and Gardner, K. (2007). qPrimerDepot: a primer database for quantitative real time PCR. Nucleic Acids Res. *35*, D805–D809.

Dhande, O.S., Estevez, M.E., Quattrochi, L.E., El-Danaf, R.N., Nguyen, P.L., Berson, D.M., and Huberman, A.D. (2013). Genetic Dissection of Retinal Inputs to Brainstem Nuclei Controlling Image Stabilization. J. Neurosci. *33*, 17797–17813.

Duan, X., Krishnaswamy, A., la Huerta, De, I., and Sanes, J.R. (2014). Type II Cadherins Guide Assembly of a Direction-Selective Retinal Circuit. Cell *158*, 793–807.

Ellis, E.M., Gauvain, G., Sivyer, B., and Murphy, G.J. (2016). Shared and distinct retinal input to the mouse superior colliculus and dorsal lateral geniculate nucleus. J. Neurophysiol. *116*, 602–610.

Famiglietti, E.V. (1991). Synaptic organization of starburst amacrine cells in rabbit retina: analysis of serial thin sections by electron microscopy and graphic reconstruction. J. Comp. Neurol. *309*, 40–70.

Haverkamp, S., Wässle, H., Duebel, J., Kuner, T., Augustine, G.J., Feng, G., and Euler, T. (2005). The Primordial, Blue-Cone Color System of the Mouse Retina. J. Neurosci. *25*, 5438–5445.

Helmstaedter, M., Briggman, K.L., Turaga, S.C., Jain, V., Seung, H.S., and Denk, W. (2013). Connectomic reconstruction of the inner plexiform layer in the mouse retina. Nature *500*, 168–174.

Hoon, M., Okawa, H., Santina, Della, L., and Wong, R.O.L. (2014). Progress in Retinal and Eye Research. Progress in Retinal and Eye Research *42*, 44–84.

Huberman, A.D., Wei, W., Elstrott, J., Stafford, B.K., Feller, M.B., and Barres, B.A. (2009). Genetic identification of an On-Off direction-selective retinal ganglion cell subtype reveals a layer-specific subcortical map of posterior motion. Neuron *62*, 327–334.

Johnson, J., Tian, N., Caywood, M.S., Reimer, R.J., Edwards, R.H., and Copenhagen, D.R. (2003). Vesicular neurotransmitter transporter expression in developing postnatal rodent retina: GABA and glycine precede glutamate. J. Neurosci. *23*, 518–529.

Kay, J.N., la Huerta, De, I., Kim, I.-J., Zhang, Y., Yamagata, M., Chu, M.W., Meister, M., and Sanes, J.R. (2011). Retinal ganglion cells with distinct directional preferences differ in molecular identity, structure, and central projections. J. Neurosci. *31*, 7753–7762.

Martersteck, E.M., Hirokawa, K.E., Evarts, M., Bernard, A., Duan, X., Li, Y., Ng, L., Oh, S.W., Ouellette, B., Royall, J.J., et al. (2017). Diverse Central Projection Patterns of Retinal Ganglion Cells. Cell Reports *18*, 2058–2072.

Morrie, R.D., and Feller, M.B. (2015). An Asymmetric Increase in Inhibitory Synapse Number Underlies the Development of a Direction Selective Circuit in the Retina. J. Neurosci. *35*, 9281–9286.

Morrie, R.D., and Feller, M.B. (2016). Development of synaptic connectivity in the retinal direction selective circuit. Current Opinion in Neurobiology *40*, 45–52.

Peng, Y.-R., Tran, N.M., Krishnaswamy, A., Kostadinov, D., Martersteck, E.M., and Sanes, J.R. (2017). Satb1 Regulates Contactin 5 to Pattern Dendrites of a Mammalian Retinal Ganglion Cell. Neuron *95*, 869–883.e6.

Rivlin-Etzion, M., Zhou, K., Wei, W., Elstrott, J., Nguyen, P.L., Barres, B.A., Huberman, A.D., and Feller, M.B. (2011). Transgenic mice reveal unexpected diversity of on-off direction-selective retinal ganglion cell subtypes and brain structures involved in motion processing. J. Neurosci. *31*, 8760–8769.

Rodriguez, A.R., de Sevilla Müller, L.P., and Brecha, N.C. (2014). The RNA binding protein RBPMS is a selective marker of ganglion cells in the mammalian retina. J. Comp. Neurol. *522*, 1411–1443.

Rosa, J.M., Morrie, R.D., Baertsch, H.C., and Feller, M.B. (2016). Contributions of Rod and Cone Pathways to Retinal Direction Selectivity Through Development. J. Neurosci. *36*, 9683–9695.

Sabbah, S., Gemmer, J.A., Bhatia-Lin, A., Manoff, G., Castro, G., Siegel, J.K., Jeffery, N., and Berson, D.M. (2017). A retinal code for motion along the gravitational and body axes. Nature *546*, 492.

Sarin, S., Zuniga-Sanchez, E., Kurmangaliyev, Y.Z., Cousins, H., Patel, M., Hernandez, J., Zhang, K.X., Samuel, M.A., Morey, M., Sanes, J.R., et al. (2018). Role for Wnt Signaling in Retinal Neuropil Development: Analysis via RNA-Seq and In Vivo Somatic CRISPR Mutagenesis. Neuron *0*.

Siegert, S., Cabuy, E., Scherf, B.G., Kohler, H., Panda, S., Le, Y.-Z., Fehling, H.J., Gaidatzis, D., Stadler, M.B., and Roska, B. (2012). Transcriptional code and disease map for adult retinal cell types. Nat Neurosci *15*, 487–495.

Sun, L.O., Jiang, Z., Rivlin-Etzion, M., Hand, R., Brady, C.M., Matsuoka, R.L., Yau, K.W., Feller, M.B., and Kolodkin, A.L. (2013). On and Off Retinal Circuit Assembly by Divergent Molecular Mechanisms. Science *342*, 1241974–1241974.

Swanson, L.W., and Lichtman, J.W. (2016). From Cajal to Connectome and Beyond. Annu. Rev. Neurosci. *39*, 197–216.

Tang, J.C.Y., Rudolph, S., Dhande, O.S., Abraira, V.E., Choi, S., Lapan, S.W., Drew, I.R., Drokhlyansky, E., Huberman, A.D., Regehr, W.G., et al. (2015). Cell type–specific manipulation with GFP-dependent Cre recombinase. Nat Neurosci *18*, 1334–1341.

Trenholm, S., Johnson, K., Li, X., Smith, R.G., and Awatramani, G.B. (2011). Parallel mechanisms encode direction in the retina. Neuron *71*, 683–694.

Visser, J.J., Cheng, Y., Perry, S.C., Chastain, A.B., Parsa, B., Masri, S.S., Ray, T.A., Kay, J.N., and Wojtowicz, W.M. (2015). An extracellular biochemical screen reveals that FLRTs and Unc5s mediate neuronal subtype recognition in the retina. Elife *4*, e08149.

Wässle, H., Regus-Leidig, H., and Haverkamp, S. (2006). Expression of the vesicular glutamate transporter vGluT2 in a subset of cones of the mouse retina. J. Comp. Neurol. *496*, 544–555.

Wei, W., Hamby, A.M., Zhou, K., and Feller, M.B. (2011). Development of asymmetric inhibition underlying direction selectivity in the retina. Nature *469*, 402–406.

Yonehara, K., Balint, K., Noda, M., Nagel, G., Bamberg, E., and Roska, B. (2011). Spatially asymmetric reorganization of inhibition establishes a motion-sensitive circuit. Nature *469*, 407–410.

Yonehara, K., Fiscella, M., Drinnenberg, A., Esposti, F., Trenholm, S., Krol, J., Franke, F., Scherf, B.G., Kusnyerik, A., Müller, J., et al. (2016). Congenital Nystagmus Gene FRMD7 Is Necessary for Establishing a Neuronal Circuit Asymmetry for Direction Selectivity. Neuron *89*, 177–193.

Zhang, C., Kolodkin, A.L., Wong, R.O., and James, R.E. (2016). Establishing Wiring Specificity in Visual System Circuits: From the Retina to the Brain. Annu. Rev. Neurosci. *40*, annurev–neuro–072116–031607.

Zheng, J.-J., Lee, S., and Zhou, Z.J. (2004). A Developmental Switch in the Excitability and Function of the Starburst Network in the Mammalian Retina. Neuron *44*, 851–864.

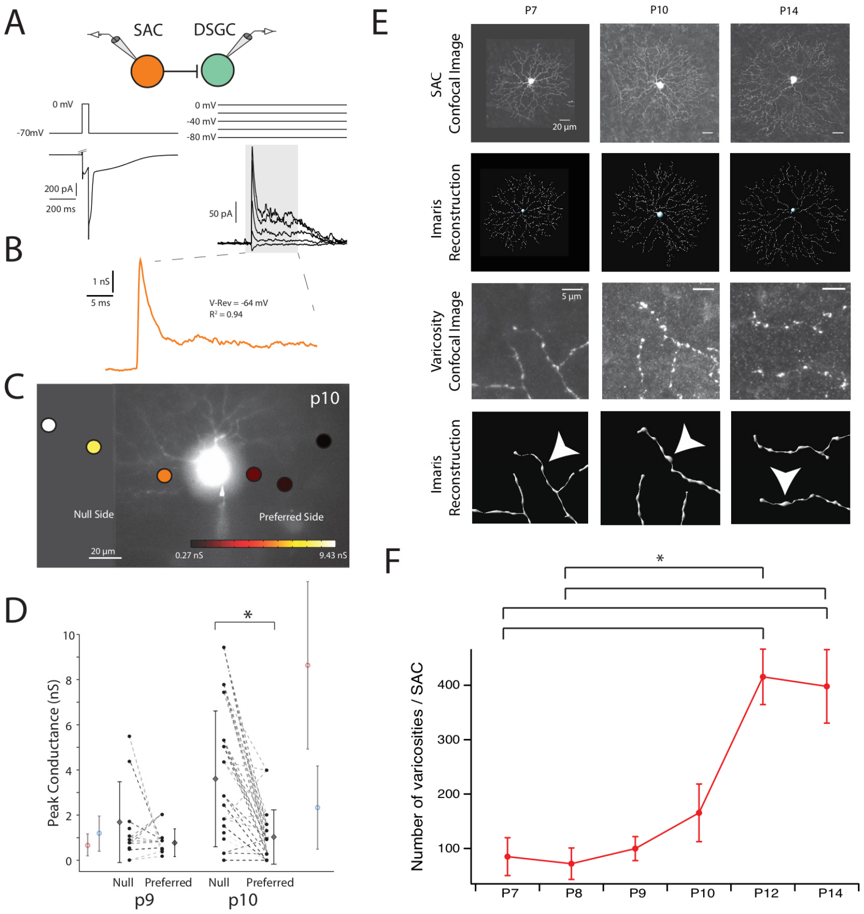

Figure 1. Asymmetric inhibitory SAC-DSGC synaptogenesis emerges beginning at P10.

A) Schematic showing paired recording between a SAC and DSGC (top). SACs were depolarized repeatedly while holding DSGCs at the varying potentials indicated. Corresponding currents recorded in the SAC (left) and DSGC (right) are shown below the voltage steps. The capacitive transient at SAC depolarization onset has been clipped for visualization purposes. Depolarization of the SAC induces release of GABA onto the DSGC throughout the duration of the depolarization and also during the subsequent tail current in the SAC upon hyper-repolarization. DSGC currents have been leak subtracted.

B) Inhibitory conductance trace calculated from slope of the IV curve through every time point for the DSGC currents in the shaded area of **A**. The average reversal potential and r-squared values for the IV curve in the shaded area of **A** are indicated.

C) Epifluorescent image of a DSGC filled with Alexa 488 with SAC somata (circles) overlaid to indicate their position relative to the DSGC. SAC somata are colored coded by the maximum inhibitory conductance recorded in the DSGC upon depolarization of that SAC.

D) Peak inhibitory conductances at P9 and P10 for null and preferred side SAC-DSGC pairs. Inhibitory conductances are small at P9 for all SAC-DSGC pairs, while by P10 null side SAC-DSGC pairs exhibit an increased inhibitory conductance while preferred side pairs do not. SAC-DSGC conductances recorded in the same DSGC are connected via dotted lines of the same color. ($n = 4$ DSGCs at P9, $n = 5$ DSGCs at P10). Peak inhibitory conductances from P7 (left) and P14-48 (right) null and preferred side pairs (red,blue respectively) (Wei et al., 2011) are shown outside of the P9 and P10 data points. T-test *$p = 0.014$.

E) (top) Z-projections of confocal image stacks of SACs stained for TdTomato and Imaris reconstructions. (bottom) Zoomed in image of dendritic processes of SACs and Imaris reconstructions. Arrowheads indicate a manually identified varicosity.

F) Number of manually identified varicosities per SAC during the second postnatal week. $n = 5$ SACs per age. Dunn-Holland-Wolfe, *$p < 0.05$.

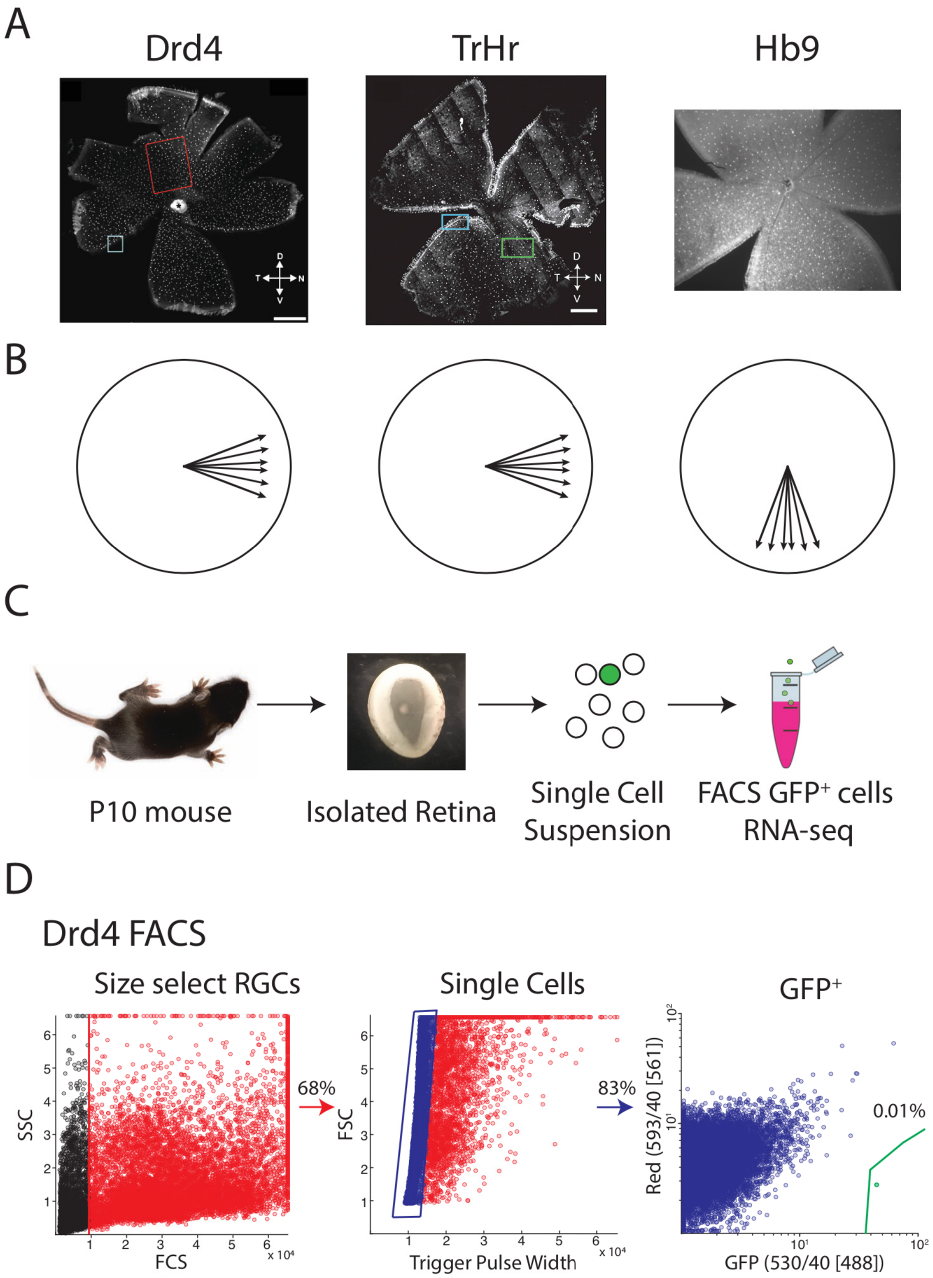

Figure 2. Strategy for RNA-sequencing gene expression screen of DSGC populations.
A) Epifluorescent images of whole mount retinas stained for GFP showing the distribution of GFP^{+} DSGCs in the Drd4-, TrHr-, and Hb9-GFP BAC transgenic mouse lines. Drd4 and TrHr images are from (Huberman et al., 2009) and (Rivlin-Etzion et al., 2011), respectively.
B) Schematic showing preferred directions of Drd4-, TrHr-, and Hb9-GFP^{+} DSGCs. Drd4- and TrHr-GFP^{+} DSGCs prefer nasal motion (retinal coordinates), while Hb9-GFP^{+} DSGCs prefer ventral motion.
C) Pipeline for collecting RNA from GFP^{+} DSGCs. Retinas were dissected from P10 mice, digested with papain to create a single cell suspension, and FAC sorted into Trizol-LS for RNA extraction.
D) Example flow cytometry plots for Drd4-GFP^{+} DSGC isolation. All events were first size selected for larger cells (68% of total), cell doublets were excluded (83% of large cells remained), and finally gated by GFP expression (0.01% of all single cells). GFP gates were determined by first recording > 1,000,000 events from Drd4-GFP negative mice.

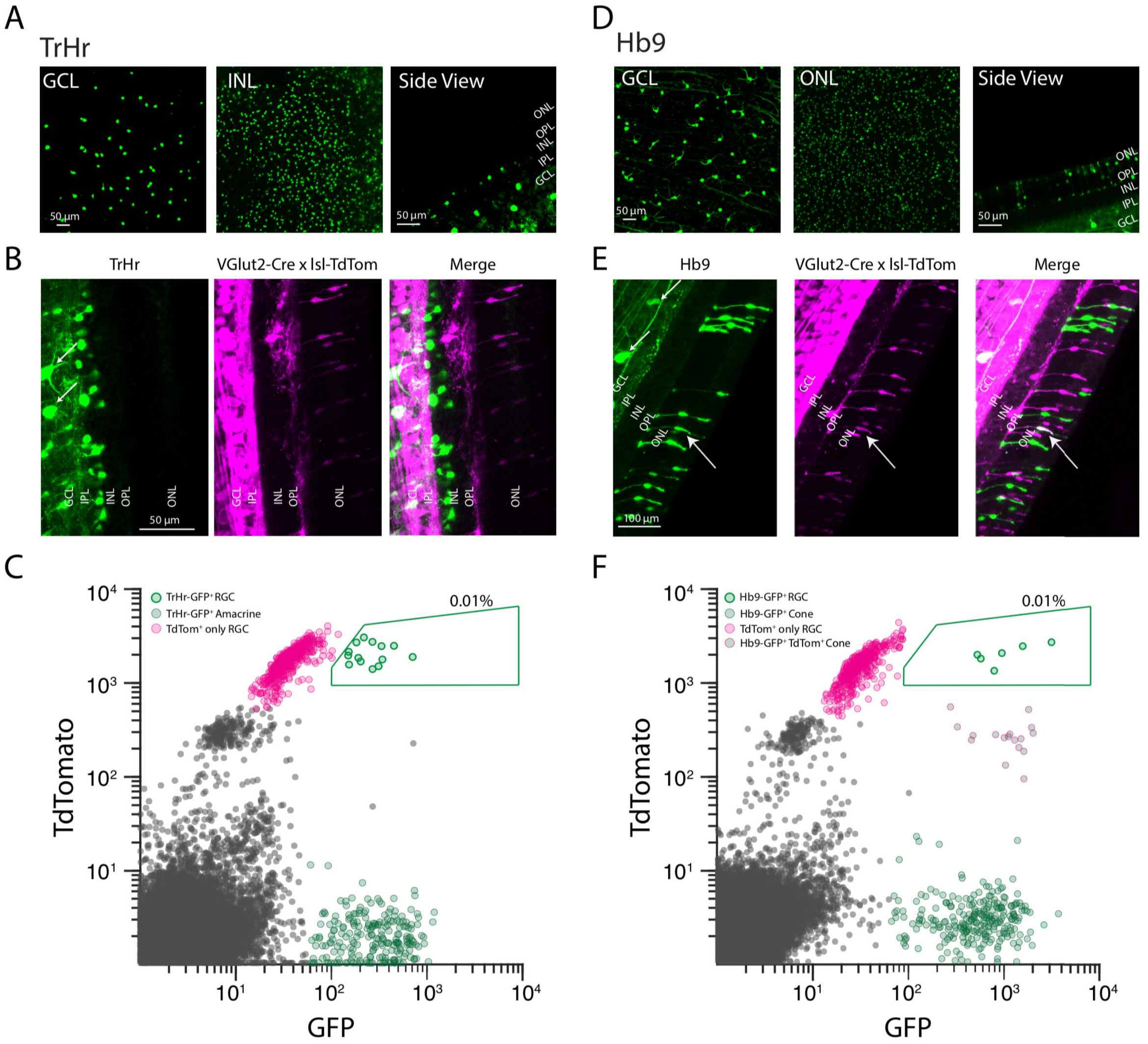

Figure 3. Isolation of TrHr- and Hb9-GFP$^+$ DSGC populations.

A) Confocal images of retinas stained for GFP in the TrHr-GFP mouse line. In addition to GFP$^+$ DSGCs in the GCL, many amacrine cells are also labeled with GFP in the INL. ONL = outer nuclear layer, OPL = outer plexiform layer, INL = inner nuclear layer, IPL = inner plexiform layer, GCL = ganglion cell layer.

B) Confocal images of a retinal optical cross section stained for GFP and TdTomato in the TVT mouse line. Arrows indicate GFP$^+$ DSGCs. GFP$^+$ amacrine cells are not co-labeled with TdTomato, while GFP$^+$ DSGCs are.

C) Example flow cytometry plot showing the first 100,000 events recorded for TrHr-GFP$^+$ DSGC isolation in the TVT mouse. RGCs are the brightest cluster of TdTomato expressing cells. TrHr-GFP$^+$ DSGCs are easily distinguished from GFP$^+$ amacrine cells based on co-expression of TdTomato.

D) Confocal images of retinas stained for GFP in the Hb9-GFP mouse line. In addition to GFP$^+$ DSGCs in the GCL, many cone photoreceptors are also labeled in the ONL.

E) Confocal images of a retinal optical cross section stained for GFP and TdTomato in the HVT mouse line. Small arrows indicate GFP$^+$ DSGCs. Most GFP$^+$ cones are not co-labeled with TdTomato, while GFP$^+$ DSGCs are. Large arrow indicates a rare cone co-expressing GFP and TdTomato.

F) Example flow cytometry plot showing the first 100,000 events recorded for Hb9-GFP$^+$ DSGC isolation in the HVT mouse. RGCs are the brightest cluster of TdTomato expressing cells. Hb9-GFP$^+$ DSGCs are easily distinguished from GFP$^+$ cones based on co-expression of TdTomato and from GFP$^+$/TdTomato$^+$ cones based on brighter TdTomato expression.

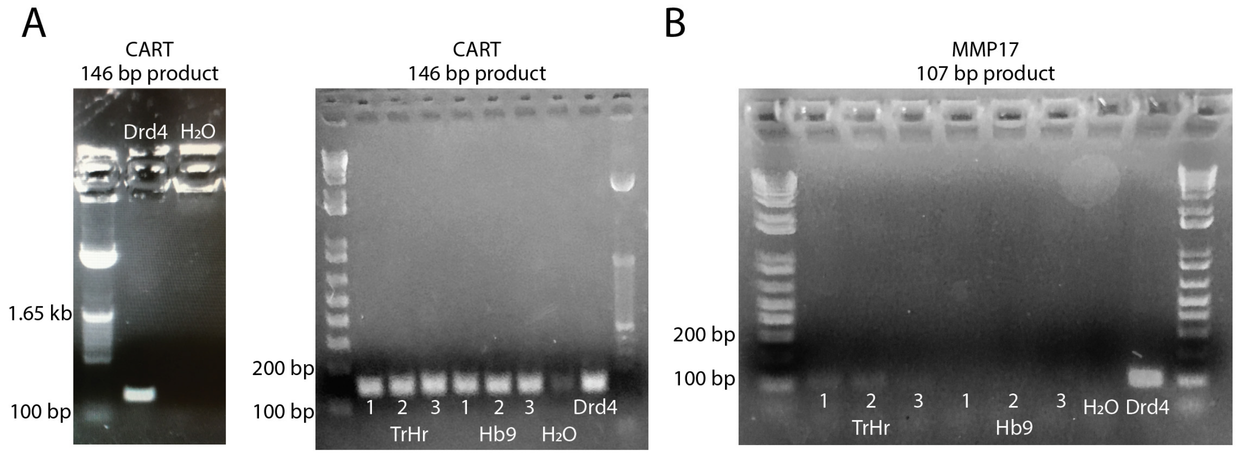

Figure 4. cDNA from isolated GFP$^+$ DSGC populations contain expected genes.

A) PCR using primers for Cart, a gene known to be expressed in DSGCs, amplifies the expected size band from our cDNA samples.

B) PCR using primers for MMP17, a gene known to be expressed in Drd4-GFP$^+$ DSGCs, amplifies the expected size band from our Drd4 and TrHr DSGC cDNA samples. No band is detected in the ventrally preferring Hb9 samples, which are known not to express MMP17 (Kay et al., 2011)**.**

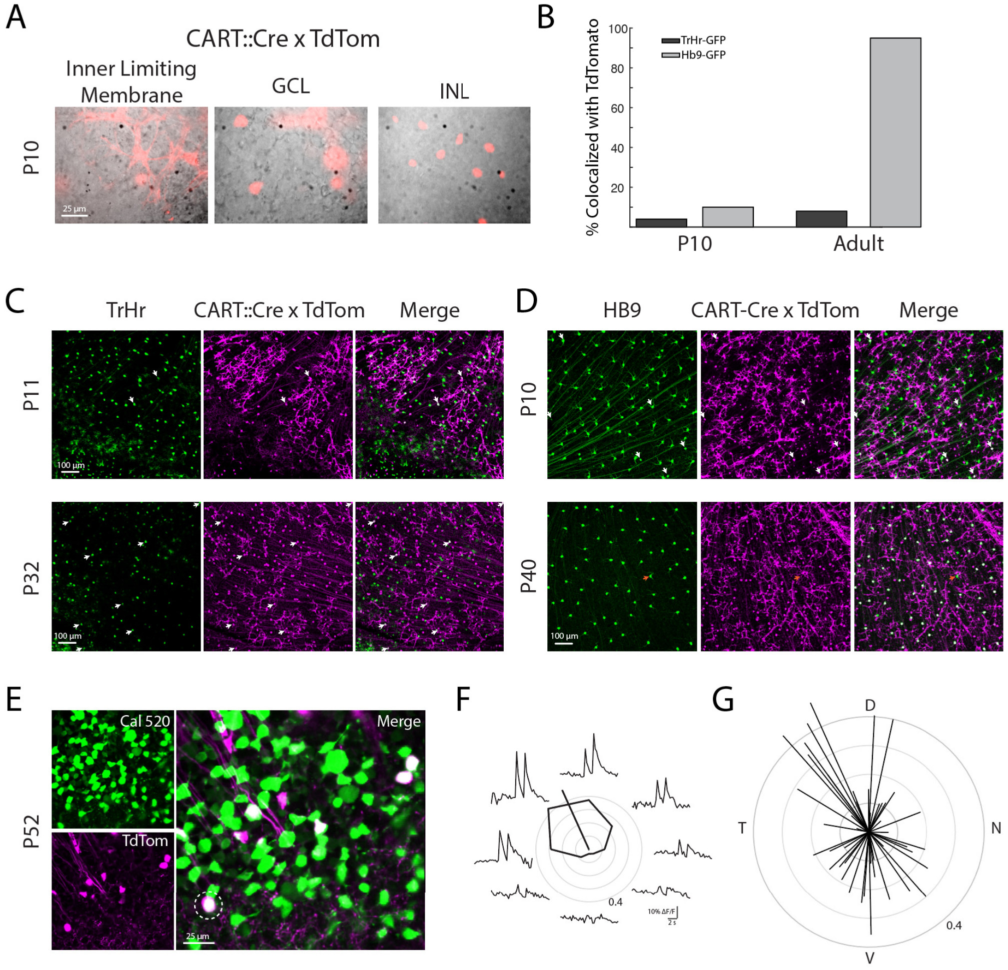

Figure 5. Cart-Cre mouse line preferentially labels vertically preferring DSGCs.

A) Brightfield images of a Cart-Cre x TdTomato retina overlaid with epiflourescent images showing TdTomato expression. Astrocytes are labeled in the inner limiting membrane, RGCs in the ganglion cell layer, and amacrine cells in the inner nuclear layer are labeled with TdTomato.

B) Quantification of TrHr- or Hb9-GFP$^+$ DSGCs colabeled with TdTomato at different developmental ages. TrHr-GFP$^+$ DSGCs show little labeling in the Cart-Cre line, while Hb9-GFP$^+$ DSGCs are well labeled only in adult Cart-Cre animals.

C) Confocal images of the GCL of retinas stained for GFP and TdTomato in the TrHr-GFP Cart-Cre TdTomato mouse. Arrows indicate GFP$^+$/TdTomato$^+$ DSGCs.

D) Confocal images of the GCL of retinas stained for GFP and TdTomato in the Hb9-GFP Cart-Cre TdTomato mouse. White arrows indicate GFP$^+$/TdTomato$^+$ DSGCs in images of P10 retinas. All GFP$^+$ DSGCs express TdTomato in P40 retina except the one indicated by the orange arrow.

E) 2 photon images showing Cal520 dye filling and TdTomato expression of cells in the GCL of a Cart-Cre TdTomato retina. Merged image shows good labeling of TdTomato$^+$ cells with Cal520. Circle indicates example cell in (**F**).

F) Example Ca^{2+} responses to bars of light moving in the eight directions indicated by the position around the polar plot for the circled cell in (**E**). The TdTomato cells exhibited directionally tuned ON and OFF responses characteristic of a DSGC. Polar plot shows maximal Ca^{2+} responses to each stimulus direction and the vector sum of this tuning curve.

G) Combined normalized vector sums of tuning curves in response to moving bars from all TdTomato$^+$ cells in a field of view from the left and retina retinas. TdTomato$^+$ cells that are strongly direction selective mostly prefer either dorsal or ventral motion on the retina.

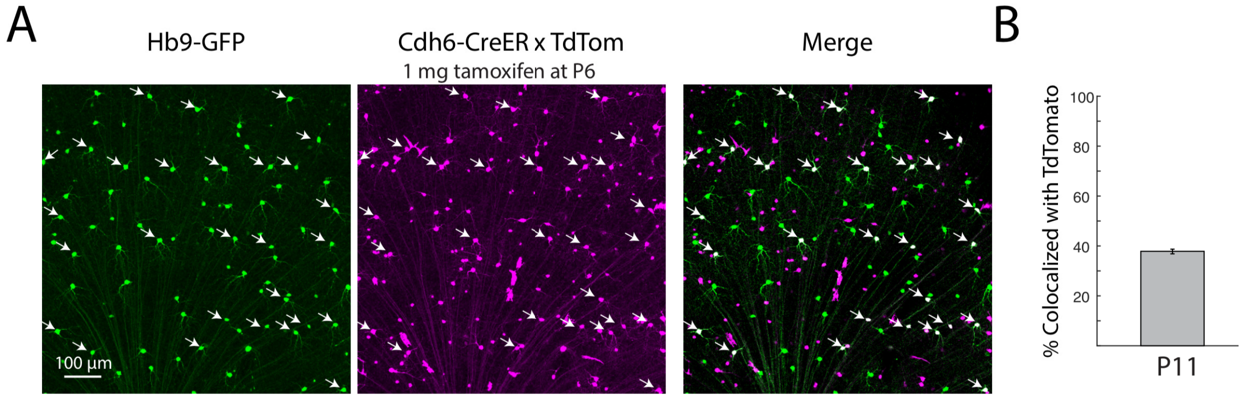

Figure 6. Cdh6-CreER mouse line expresses Cre in Hb9-GFP$^+$ DSGCs.
A) Confocal images of the GCL of retinas stained for GFP and TdTomato in the Hb9-GFP Cdh6-CreER TdTomato mouse. White arrows indicate GFP$^+$/TdTomato$^+$ DSGCs.
B) Quantification of Hb9-GFP$^+$ DSGCs colabeled with TdTomato.

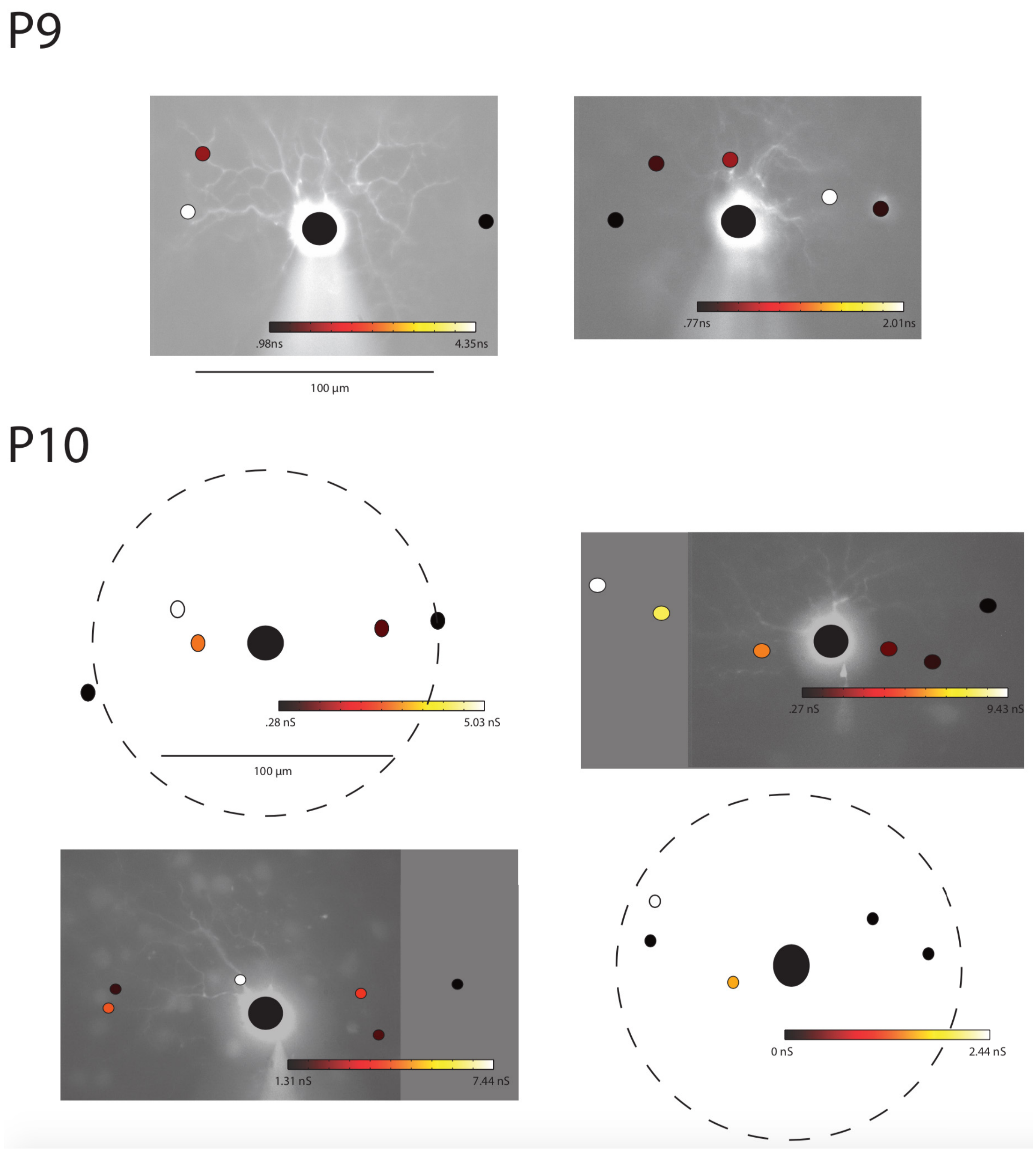

Figure S1. Asymmetric SAC-DSGC inhibition emerges beginning at P10.
Examples of SAC-DSGC inhibitory conductance maps for summary in Figure 1D. Epifluorescent images of DSGCs filled with Alexa 488 are overlaid with SAC somata (circles) to indicate their position relative to the DSGC. SAC somata are colored coded by the maximum inhibitory conductance recorded in the DSGC upon depolarization of that SAC, with color scale indicated on each connectivity map. Large black circles denote DSGC soma location. For inhibition maps in which the DSGC was not filled with fluorescent dye, dotted lines have been added to estimate DSGC dendritic extent. Maps at P10 are more asymmetric than maps at P9.

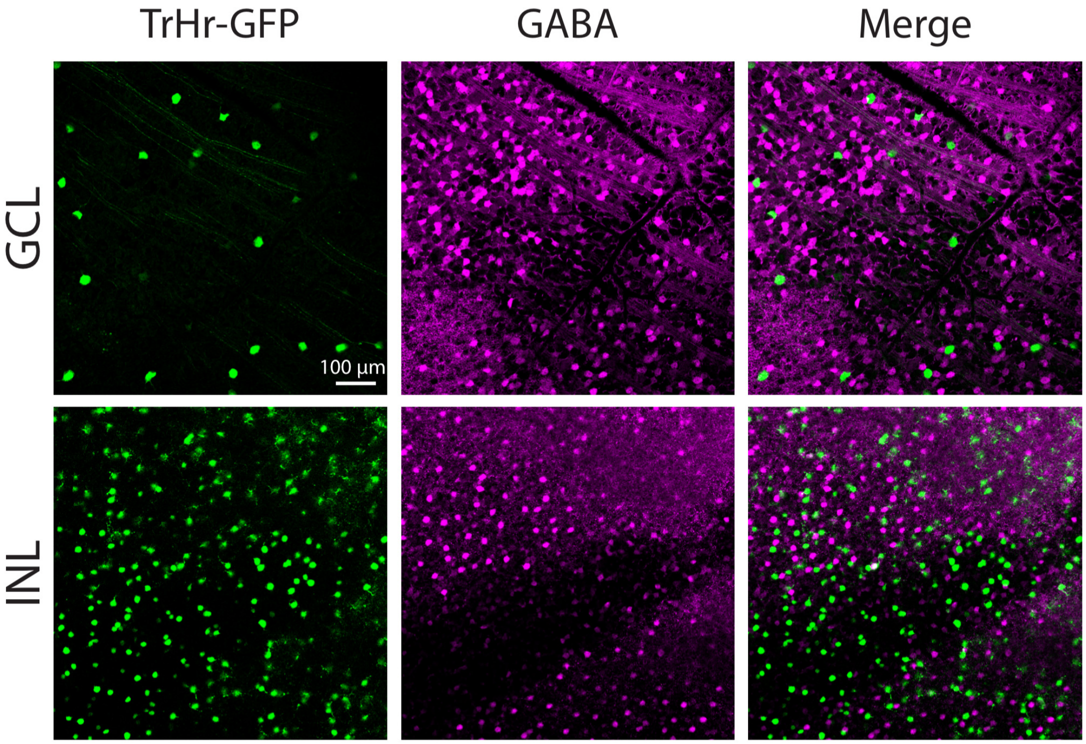

Figure S2. TrHr-GFP$^+$ amacrine cells are not GABAergic.
Confocal images of a TrHr-GFP retina stained for GFP and GABA. There is no overlap in GFP and GABA expression in the GCL or in the INL.

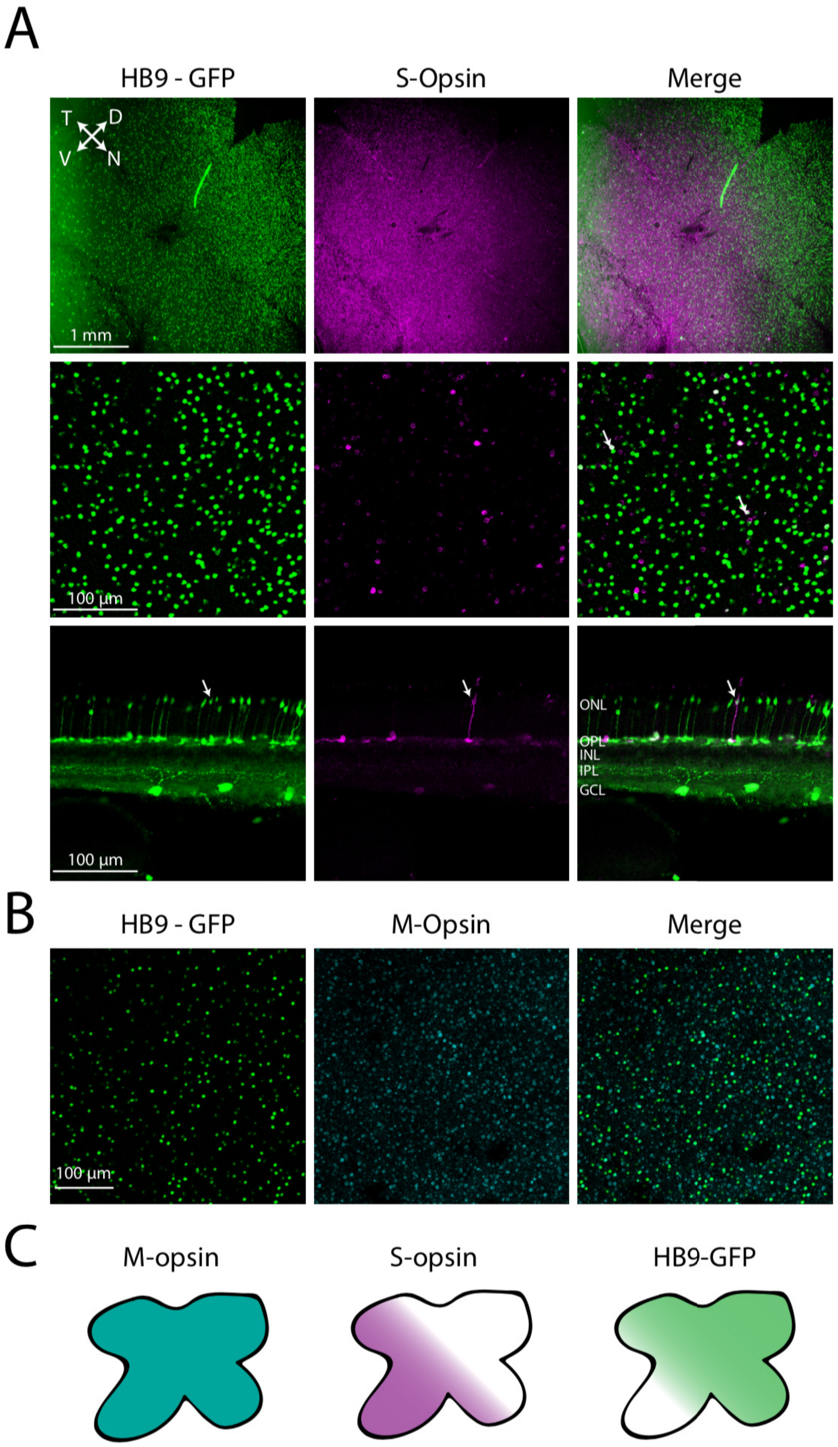

Figure S3. Hb9-GFP$^+$ cones are not exclusively M- or S-cones.
A) (top and middle) Confocal images of the ONL of retinas stained for GFP and S-opsin in the Hb9-GFP mouse. (bottom) Optical cross section view of the same retina. White arrows indicate GFP$^+$/S-opsin$^+$ cones in all images.
B) Confocal images of ONL of retinas stained for GFP and M-opsin in the Hb9-GFP mouse. Most Hb9-GFP$^+$ cones also express some level of M-opsin, although not all M-opsin cones express GFP.

C) Schematic showing the distribution of different cone types across the retina. M-opsin expression is found throughout the retina, S-opsin is expressed in a ventral to dorsal gradients, and HB9-GFP+ cones are found in a dorsal to ventral gradient.

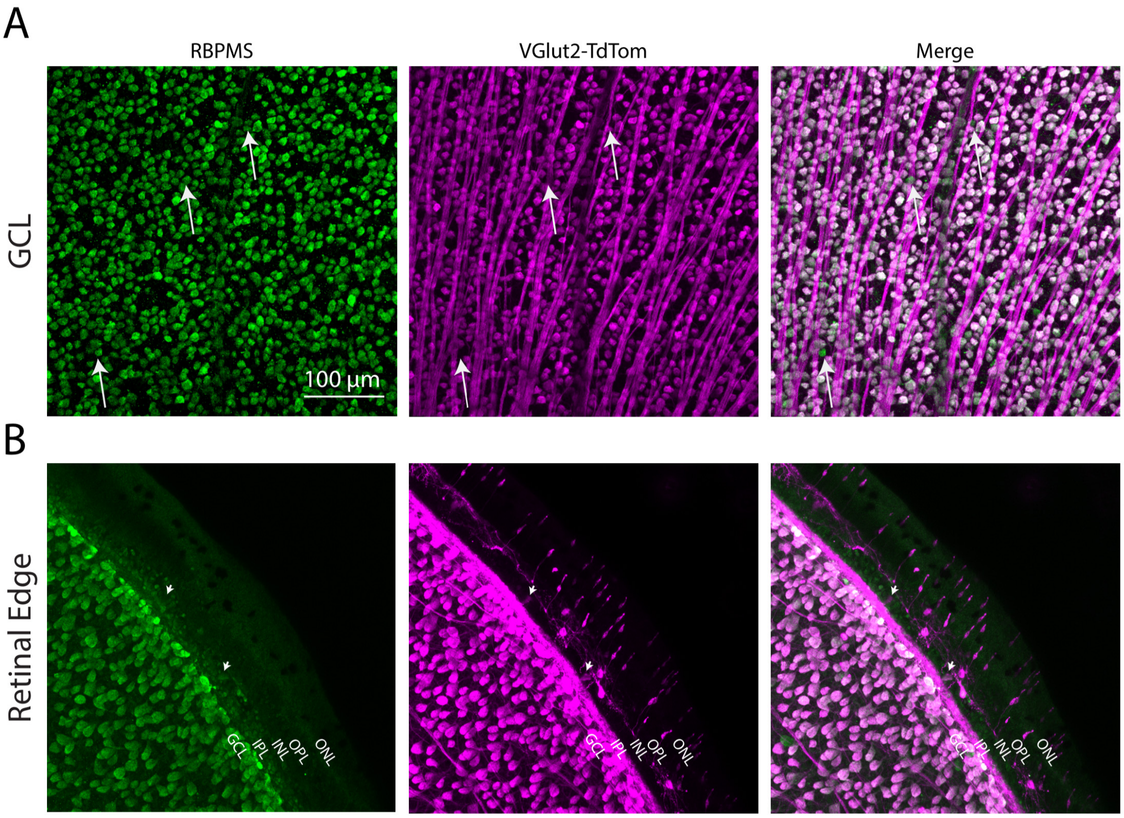

Figure S4. VGlut2-Cre mice express Cre in almost all RGCs.

A) Confocal images of the GCL of retinas stained for TdTomato and the pan-RGC marker RBPMS in the VGlut2-Cre TdTomato mouse. White arrows indicate RBPMS$^+$/TdTomato$^-$ RGCs.

B) Confocal images of the edge of a retinal whole mount stained for TdTomato and the pan-RGC marker RBPMS in the VGlut2-Cre TdTomato mouse. White arrows indicate RBPMS$^+$/TdTomato$^+$ cells in the INL.

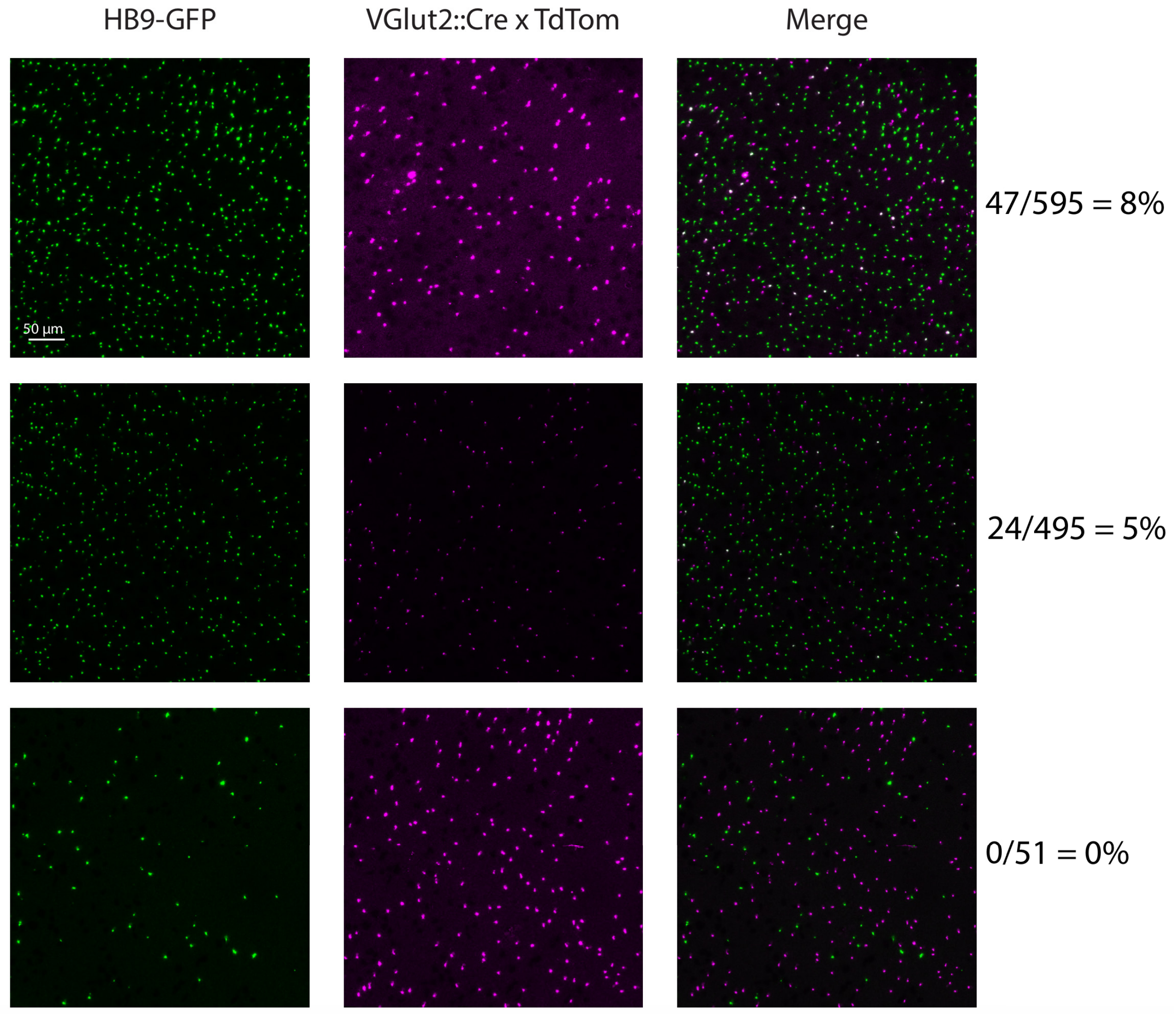

Figure S5. Hb9-GFP$^+$ cones have sparse overlap with VGlut2-Cre expressing cones.
Confocal images of the ONL a retina stained for GFP and TdTomato in the HVT mouse. Images are presented in a dorsal to ventral pattern from top to bottom. Areas of the highest Hb9-GFP$^+$ cone density (dorsal retina) have about 8% co-expression of TdTomato, while areas of sparser Hb9-GFP$^+$ cones density (ventral retina) do not show any overlap with TdTomato$^+$ cones. TdTomato$^+$ cones do not show a location dependent change in density (Wässle et al., 2006).